

# Microinstability in the Pedestal



Jason Francis Parisi  
Merton College  
University of Oxford

A thesis submitted for the degree of  
*Doctor of Philosophy in Theoretical Physics*

Trinity Term 2020

# Microinstability in the Pedestal

Jason Francis Parisi

Merton College, University of Oxford

*Submitted for the degree of Doctor of Philosophy in Theoretical Physics*

Trinity Term 2020

The pedestal is a region of increased equilibrium pressure gradients near the edge of high performance toroidal plasmas. While the MHD properties of this region have been fairly well-characterized, pedestal microinstabilities and turbulence remain relatively unexplored, particularly in steep gradient regions. In this thesis, we describe a new microinstability caused by the steep equilibrium temperature gradients and complex magnetic geometry. This instability has a critical temperature gradient that is much higher than core temperature gradients, and hence likely exists only in pedestals. Basic analytic arguments show that in the presence of magnetic shear and steep temperature gradients, this mode must be one of the fastest growing modes. In realistic magnetic equilibria that we study, it is the fastest growing mode at almost all scales comparable to ion and electron gyroradii. Therefore, it is a robust feature of pedestal microinstability.

We also investigate nonlinear pedestal microturbulence. We find the turbulent saturated state to be inhomogeneous in the poloidal angle, in strong contrast to core microturbulence that is typically well-correlated for long distances along magnetic field lines. Turbulence is particularly strong in poloidal regions of (i) weaker local magnetic shear and (ii) shorter distances between flux surfaces. These two effects cause the perpendicular wavenumber of the turbulence to have a particularly strong poloidal angle dependence, which results in the turbulence being strongly damped by finite Larmor radius effects in certain poloidal regions, hence causing the turbulent poloidal inhomogeneity. While we find that the linear instabilities caused by magnetic drifts are the fastest growing modes, nonlinear simulations appear to reach a quasi-steady state insensitive to these drifts and dominated by the branch of electron temperature gradient turbulence caused by parallel streaming. The heat flux in this quasi-steady state is roughly constant in time, but some modes that appear to be driven by magnetic drifts have not yet saturated.

## Acknowledgements

First and foremost, I would like to thank my advisor, Felix Parra. Felix's generosity and kindness has made the PhD process more enjoyable and smooth than it otherwise would have been. Finishing a PhD during a global pandemic is quite an undertaking, and Felix's support has been instrumental in completing this thesis. Thank you, Felix.

Thank you also to my Culham advisor Colin Roach, whose enthusiasm and difficult questions kept me on my toes. I am grateful to those in our research group at Oxford and beyond; thanks to Ian Abel, Michael Barnes, Steve Cowley, Bill Dorland, Carine Giroud, David Hatch, and Alex Schekochihin, and thanks to my examiners Paul Dellar and Walter Guttenfelder. I would be remiss to omit the 'Plasmaniacs' in our Oxford research group. Whether it was exploring a city during a conference, a last minute practice talk, or simply having lunch together, your friendship has made the past four years even more memorable; thank you Mantas Abazorius, Toby Adkins, Ollie Beeke, Nicolas Christen, Alessandro Geraldini, Valerian Hall-Chen, Plamen Ivanov, Yohei Kawazura, Javier Maurino, Adnane Osmane, Juan Ruiz Ruiz, Denis St-Onge, Marek Strumik, and Alexander von Boetticher! Particular thanks to Justin Ball and Michael Hardman for graciously tolerating my questions. I am grateful to Priya Natarajan and David Poland for their guidance.

Last but not least, I would like to thank my loving parents, family, and friends. In particular, Lukas for bike rides, Glenn for tiramisu, Philipp for thought experiments, Scott for the all the fish, and Spence for brotherhood. I reserve special thanks to Muni for her love, patience, and encouragement. It has been an immense pleasure and privilege to have shared worldlines with you all; I look forward to many more adventures together.

*The author is supported by EPSRC Scholarship No 3000207032. Computational time was provided by Plasma HEC Consortium EPSRC (grant number EP/L000237/1). This work has been carried out within the framework of the EUROfusion Consortium and has received funding from the Euratom research and training programme 2014-2018 and 2019-2020 under grant agreement No 633053 and from the RCUK Energy Programme (grant number EP/T012250/1 and EP/P012450/1). Withal, this work has been carried out within the framework of the Contract for the Operation of the JET Facilities and has received funding from the European Union's Horizon 2020 research and innovation programme. The views and opinions expressed herein do not necessarily reflect those of the European Commission. The author acknowledges EUROfusion, the EUROfusion High Performance Computer (Marconi-Fusion), the use of ARCHER through the Plasma HEC Consortium EPSRC grant numbers EP/L000237/1 and EP/R029148/1 under the projects e281-gs2, and software support from Joseph Parker through the Plasma-CCP Network under EPSRC grant number EP/M022463/1. This work also received computational support from Joseph Parker of CoSeC (the Computational Science Centre for Research Communities), funded through CCP-Plasma/Plasma-HEC EPSRC grants EP/R029148/1 and EP/M022463/1. The author acknowledges travel support from Merton College, Oxford, and is grateful for the hospitality of the Wolfgang Pauli Institute, University of Vienna.*

# Contents

<b>1</b>	<b>Introduction</b>	<b>7</b>
1.1	Plasma Microturbulence . . . . .	11
1.2	Pedestals . . . . .	12
1.3	Microinstability Characteristics . . . . .	15
1.3.1	FLR Effects . . . . .	18
1.3.2	Magnetic Shear . . . . .	19
1.3.3	Pedestal Temperature Gradients . . . . .	21
1.4	Thesis Outline . . . . .	22
<b>2</b>	<b>Overview of Gyrokinetics</b>	<b>25</b>
<b>I</b>	<b>Linear Physics</b>	<b>30</b>
<b>3</b>	<b>Pedestal Gyrokinetic Simulations of JET Shot 92174</b>	<b>31</b>
3.1	JET-ILW Profiles . . . . .	32
3.2	Gyrokinetic Simulation Results . . . . .	35
3.3	Linear Features of the Electrostatic Pedestal . . . . .	39
<b>4</b>	<b>Linear Gyrokinetics With Large Gradients</b>	<b>42</b>
4.1	Electrostatic Collisionless Local Limit . . . . .	43
4.2	Slab Versus Toroidal ETG In Large Gradient Regions . . . . .	44
4.3	ETG Dispersion Relation . . . . .	51
<b>5</b>	<b>ETG Stability in the Pedestal</b>	<b>55</b>
5.1	Toroidal ETG Versus Slab ETG Instability . . . . .	55
5.2	Location And Width Of The Toroidal ETG Mode . . . . .	63
5.3	Effects of $\theta_0$ . . . . .	71

5.4	Critical $R_0/L_{Te}$ . . . . .	78
<b>6</b>	<b>ITG Stability in the Pedestal</b>	<b>85</b>
<b>7</b>	<b>Flow Shear</b>	<b>90</b>
<b>8</b>	<b>Linear Physics Discussion</b>	<b>95</b>
<b>II</b>	<b>Nonlinear Physics</b>	<b>97</b>
<b>9</b>	<b>Nonlinear Simulations</b>	<b>98</b>
9.1	Resolving Toroidal and Slab ETG Turbulence . . . . .	100
9.2	Hyperviscosity . . . . .	105
9.3	Numerical Results . . . . .	107
9.3.1	Hero Simulation . . . . .	110
<b>10</b>	<b>Magnetic Drifts and FLR Effects in Pedestal ETG Turbulence</b>	<b>116</b>
10.1	The Effect of Magnetic Drifts . . . . .	118
10.2	FLR Effects in Pedestal Turbulence . . . . .	119
10.2.1	Heat Flux Poloidal Distribution . . . . .	131
10.3	Toroidal ETG Turbulent State . . . . .	131
10.4	Discussion . . . . .	134
<b>11</b>	<b>Conclusions</b>	<b>135</b>
<b>A</b>	<b>Other Discharges</b>	<b>137</b>
<b>B</b>	<b>Electrostatic modes at <math>k_y \rho_i \lesssim 1.0</math></b>	<b>140</b>
<b>C</b>	<b>Full Dispersion Relation</b>	<b>143</b>
<b>D</b>	<b>Nonlinear Simulations Parameters</b>	<b>146</b>
	<b>References</b>	<b>148</b>

# Chapter 1

## Introduction

Fusion fuels have the highest extractable energy per unit mass of any known substance, with the exception of the matter-anti-matter annihilation reaction. As an energy source, nuclear fusion has many attractive properties: in addition to its high specific energy, there is a bounteous availability of fusion fuels, it has a tolerable environmental impact, the fueling system is resistant to nuclear proliferation, and reactors could provide a weather-independent, baseload energy source. These factors make controlled nuclear fusion a prime candidate for the production of useful energy. Indeed, nature has already provided a sublime example of a nuclear fusion reactor: stars are powered by a range of nuclear fusion reactions that mainly turn hydrogen into helium. However, the physics understanding required to realize controlled commercially-viable nuclear fusion on machines on Earth is rather different.

In stars, gravitational wells provide the confinement needed for nuclear fusion, albeit with fusion reaction rates much slower than would be acceptable for controlled terrestrial fusion. Furthermore, due to the relative weakness of gravity, on Earth it is not possible to realize a gravitationally-bound fusion device. Therefore, the challenge is to build a fusion reactor with reaction rates orders of magnitude higher than in stars, and to confine the plasma without gravity's assistance. Because of the temperatures required for significant fusion reaction rates, gases used for nuclear fusion are plasmas. However, the Coulomb collisions that occur in these plasmas are typically orders of magnitude more likely than fusion reactions, and hence, we must build machines that can confine the plasma for many Coulomb scattering times. Due to its relatively high cross section,

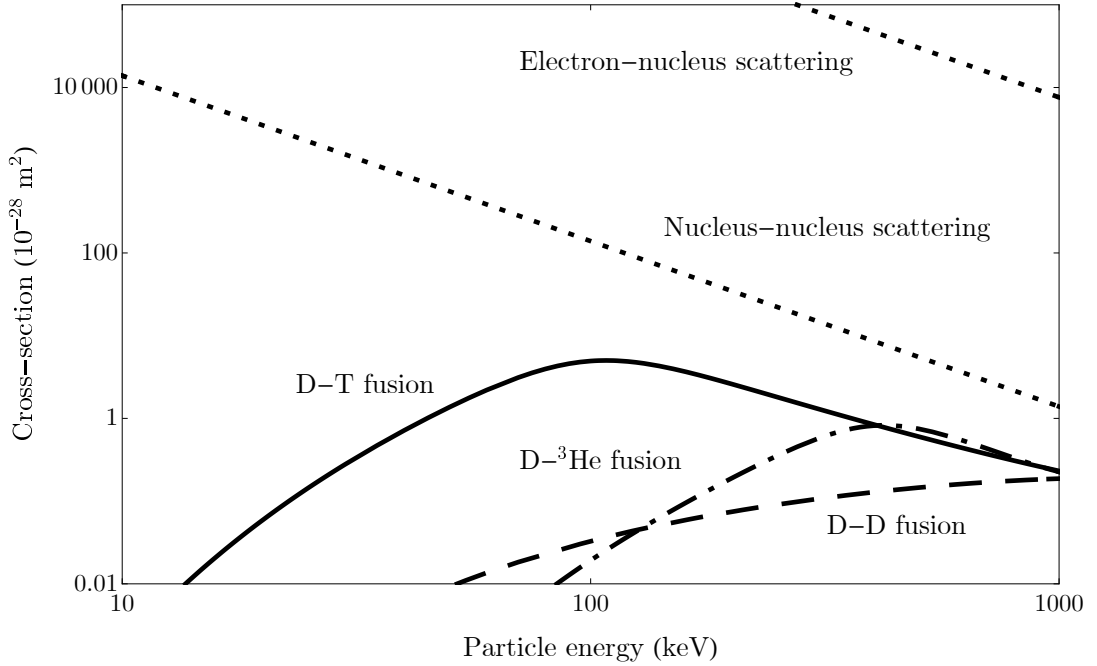


Figure 1.1: Cross sections for Coulomb scattering and fusion processes as a function of the particle energy. Adapted from [1].

deuterium-tritium (D-T) is the preferred fuel for first generation fusion reactors (see Figure 1.1).

There are two mainstream fusion research efforts. The first, inertial confinement fusion, uses the fusion fuel's inertia to confine it for sufficiently long to produce substantial fusion power. The second, magnetic confinement fusion, uses powerful magnetic fields to confine the plasma for many collision times. This thesis addresses exclusively the latter technique. In particular, we will focus on the physics of magnetic toroidal confinement devices called tokamaks. The governing principle is to confine charged particles' motion to nested toroidal magnetic 'flux surfaces,' which are formed by ergodic magnetic field lines winding around the torus (see Figure 1.2(a)). As a consequence of the Lorentz force, charged particles will execute Larmor motion perpendicular to field lines, but are free to stream rapidly along field lines. Thus, charged particles tend to sample a flux surface as they move along a field line. One can therefore define 'flux functions,' which are functions that are constant on magnetic flux surfaces. For example, the dominant contributions to the equilibrium temperature, density, and electrostatic potential are flux functions. Particles move at thermal velocities along field lines, but because the strong

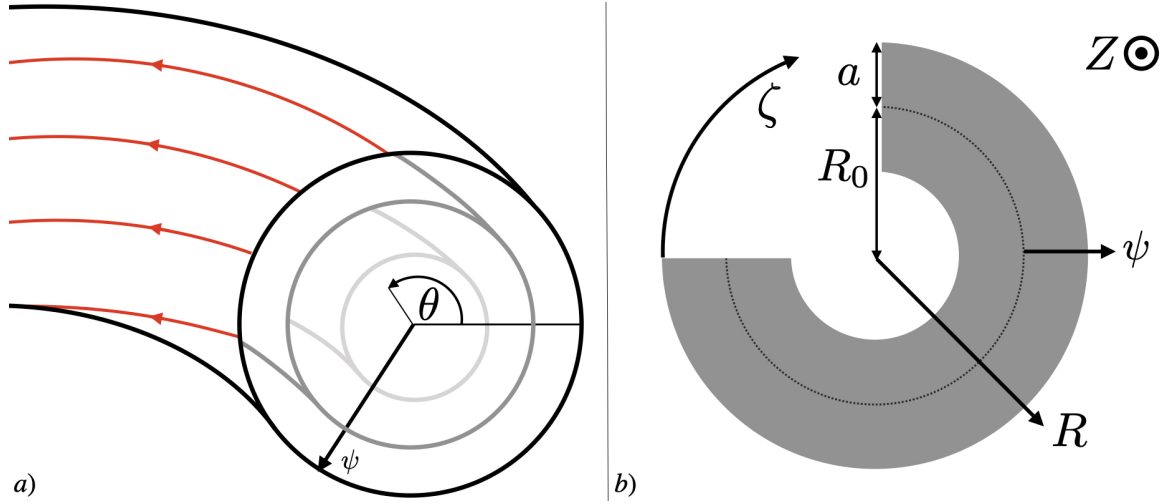


Figure 1.2: (a): Three nested magnetic flux surfaces. The red lines on the outermost surface represent a field line sampling the surface. The angle  $\theta$  is a poloidal angle and  $\psi$  is the poloidal flux divided by  $2\pi$ . (b): Bird's eye view of a tokamak;  $R$  is the major radial coordinate,  $Z$  is the axial coordinate,  $\zeta$  is the toroidal angle,  $R_0$  is the  $R$  location of the LCFS, and  $a$  is the minor radius.

magnetic field causes the gyroradius to be small relative to the system size, they drift much more slowly across field lines. Due to the relatively slow perpendicular particle motion, flux surfaces are an effective tool for confining charged particles in collisionless non-turbulent plasma, therefore reducing perpendicular heat fluxes. A torus can be covered by a nonzero magnetic field at every point [2]; this keeps heat fluxes to tolerable levels as particles are unable to rapidly carry heat flux to the walls. The outermost flux surface created by closed field lines is called the last closed flux surface (LCFS). Beyond this, all field lines are in contact with the wall.

In order to describe physical phenomena in tokamaks, it will be useful to introduce two coordinate systems, shown in Figure 1.2(a) and (b):

1. Cylindrical coordinates  $(R, Z, \zeta)$ , where  $R$  is the major radial coordinate,  $Z$  is the axial coordinate, and  $\zeta$  is the toroidal angle. Using  $\nabla \cdot \mathbf{B} = 0$  and that  $\mathbf{B}$  is axisymmetric, one can show that there exists a flux function  $\psi(R, Z)$  that satisfies  $\mathbf{B} \cdot \nabla \psi = 0$ . It is customary to define  $\psi$  as the poloidal flux divided by  $2\pi$ . Here,  $\mathbf{B}$  is the leading order equilibrium magnetic field, which can be split into a toroidal and poloidal component, where the poloidal magnetic field can be written as  $\mathbf{B}_P = \nabla \zeta \times \nabla \psi$ . Using  $(\nabla \times \mathbf{B}) \cdot \nabla \psi = 0$ , we find that the poloidal

current  $I(\psi(R, Z)) = RB_T$  is a flux function, where  $B_T$  is the toroidal component of the magnetic field. Therefore, we can write the leading order magnetic field in a tokamak as

$$\mathbf{B} = I\nabla\zeta + \nabla\zeta \times \nabla\psi. \quad (1.1)$$

2. Flux coordinates  $(\psi, \theta, \zeta)$  form a convenient coordinate system that takes advantage of the magnetic flux surfaces to write certain expressions in a convenient form. The quantity  $\theta$  is a poloidal angle that can be defined in many different ways.

Other useful quantities are  $a$ , the minor radius, and  $R_0$ , the  $R$  location of the LCFS.

Magnetic confinement, however, is nontrivial. Large scale magnetohydrodynamic (MHD) forces conspire to disrupt magnetic field lines, causing massive plasma leakage [3]. These forces constrain tokamak operation through plasma pressure [4], density [5, 6], current [7], and pressure gradient limits [8, 9]. While many MHD instabilities have been well-understood and mitigated for decades, there are still several outstanding issues, including disruptions [10, 11], just a couple of which could disable ITER's vacuum chamber<sup>1</sup>. In addition to MHD phenomena, classical [12], neoclassical [13], and turbulent transport [14] serve to diffuse heat from hot to cold regions. Classical transport is caused by collisions that disrupt the Larmor motion. Neoclassical transport is also caused by collisions, but it is due to the interruption of drift orbits. Turbulent transport is caused by turbulent plasma fluctuations that form eddies, which can ruin confinement in a fusion reactor by rapidly transporting heat from the core to the edge. Early, optimistic transport calculations such as Braginskii's [12] did not include neoclassical and turbulent contributions, and hence anticipated excellent confinement times, and placing a fully-fledged reactor well within reach. As fusion reactor performance improved, neoclassical and turbulent transport worsened, giving rise to an ongoing research effort to tame them. While neoclassical transport is an important and active area of tokamak and stellarator research, this thesis focuses primarily on the physics that gives rise to turbulence, although the two can affect one another [15, 16]. While turbulent transport tends to be responsible for most of the heat loss in tokamaks, both neoclassical and turbulent effects can often cause comparable transport in stellarators [17].

---

<sup>1</sup>ITER is the world's largest fusion experiment, and is currently scheduled to have its first plasma in December 2025.

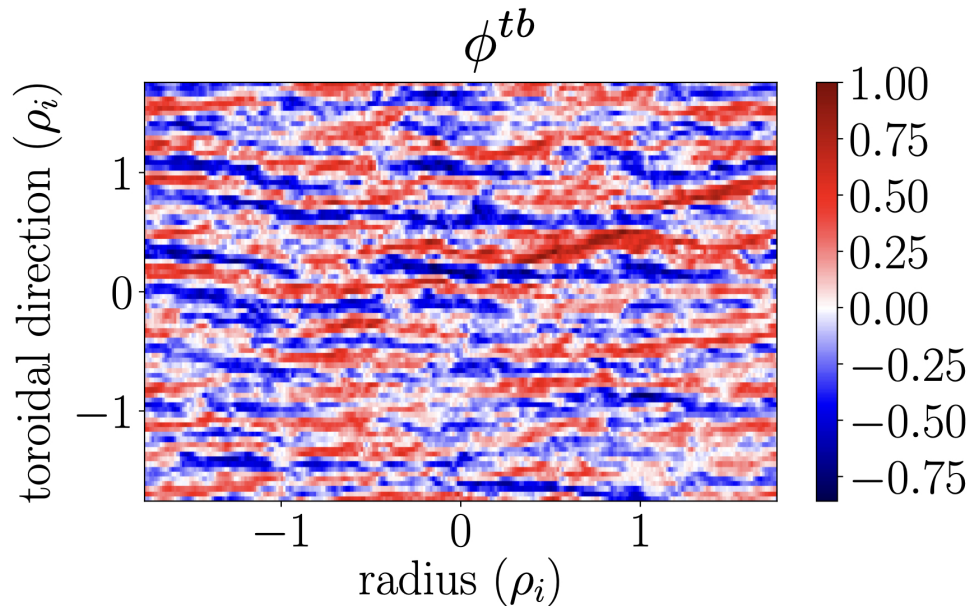


Figure 1.3: Typical electron temperature gradient streamer turbulence at the outboard midplane using Cyclone Base Case-like parameters [18]. The turbulent electrostatic potential,  $\phi^{tb}$ , is normalized to its maximum amplitude in the box.

## 1.1 Plasma Microturbulence

In tokamaks, cross-field particle and heat transport is typically dominated by turbulence [18–25]. This turbulence is caused by temperature gradient instabilities at various scales, although density gradient driven instabilities are also possible. Due to these instabilities, initially infinitesimal perturbations grow to become sufficiently large such that nonlinear interactions between different turbulent wavenumbers become non-negligible. Once these interactions are sufficiently strong, the system exhibits turbulent characteristics.

The steep gradients in density and temperature drive a range of instabilities. The equilibrium ion temperature gradient can drive the ion temperature gradient (ITG) instability, typically at ion gyroradius scales [26–30]. The equilibrium electron temperature gradient can drive the electron temperature gradient (ETG) instability, typically at electron gyroradius scales [23, 31–33]. A resonance of trapped electrons can also destabilize a drift wave, giving rise to a trapped electron mode (TEM) at ion gyroradius scales [34–36]. If the plasma is sufficiently collisional, a micro-tearing mode (MTM) can become unstable at ion gyroradius scales [37–39]. A kinetic ballooning mode (KBM), a ballooning mode [40] with kinetic corrections [41], can be made unstable due to both electron and

ion pressure gradients. A density gradient driven ‘universal’ instability can destabilize a drift wave at sub ion gyroradius scales when the magnetic shear is sufficiently weak [42, 43].

In fusion plasmas, the turbulence is typically on spatial scales comparable to ion and electron gyroradii; due to these relatively small spatial scales (small relative to the device size), fusion plasma turbulence is often referred to as *micro*turbulence. An image of simulated ETG turbulence in the core is shown in Figure 1.3, where  $\rho_s$  is the gyroradius for a species  $s$ . The linear growth rate of microinstabilities typically scales inversely with the perpendicular spatial scale. This is because the ITG and ETG instabilities are driven by advection due to a turbulent  $\mathbf{E}^{tb} \times \mathbf{B}$  drift,  $\mathbf{v}_E^{tb} = c\mathbf{E}^{tb} \times \mathbf{B}/B^2$ . Here,  $c$  is the speed of light, and  $\mathbf{E}^{tb}$  is the turbulent electric field. Since the perpendicular gradients of the turbulent fluctuations scale like  $1/\rho_s$ , the curl in the induction equation is large giving  $c|\nabla \times \mathbf{E}^{tb}| \gg |\partial \mathbf{B}^{tb}/\partial t|$ , where  $\mathbf{B}^{tb}$  is the turbulent magnetic field, which means that  $\mathbf{E}^{tb}$  can be written as a gradient of an electrostatic potential,  $\mathbf{E}^{tb} = -\nabla_{\perp} \phi^{tb}$ . Thus, for a given Fourier mode, the turbulent  $\mathbf{E}^{tb} \times \mathbf{B}$  drift is proportional to a perpendicular wavenumber. Because the steepest equilibrium gradients are in the radial direction, the advection of the equilibrium by the  $\mathbf{E}^{tb} \times \mathbf{B}$  drift is therefore directly proportional to the wavevector that is oriented perpendicular to the magnetic field and parallel to the flux surface. This wavevector will usually have a radial component. The growth rate of these instabilities therefore typically scales with wavenumber and the equilibrium temperature gradient.

## 1.2 Pedestals

In the core of fusion devices, it has been observed that temperature gradients tend to stay close to a microstability threshold, while in the deep core near the magnetic axis, MHD instabilities clamp the pressure profile [44, 45]. Thus, it is possible that core temperature profiles can be somewhat constrained by the ITG and ETG stability thresholds. If the temperature steepens, the relevant instability becomes unstable, it transports some heat, and hence flattens the temperature gradient to roughly the linear stability threshold. The ‘stiffness’ of a temperature profile measures how much heat flux is produced by a small

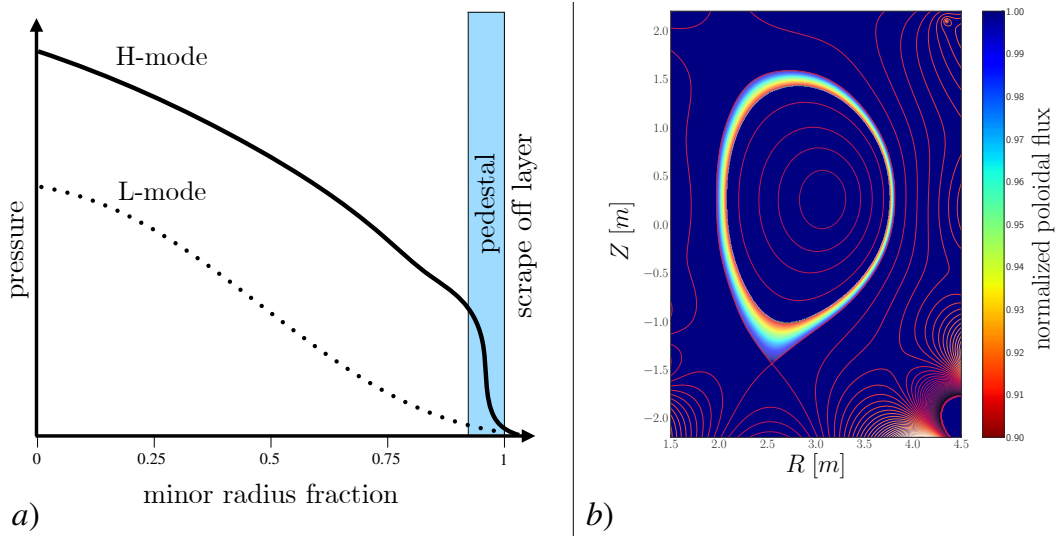


Figure 1.4: (a): Inter-ELM (Edge-localized mode) pressure profile for L-mode and H-mode. (b): Flux surfaces for a JET-ILW (Joint European Torus ITER-like-wall) discharge. The pedestal region at the plasma edge is given its own colorbar. All other regions have the same color. Each contour line represents  $\Delta\psi_N = 0.2$ , where  $\psi_N$  is the poloidal flux normalized to 1 at the last closed flux surface.

increase in the temperature gradient above the stability threshold. A profile that is relatively close to the stability boundary at all radial locations is known as an ‘L-mode’ plasma [46], shown in Figure 1.4(a).

However, away from the core towards the last closed flux surface, when the heating power exceeds a certain threshold [47, 48], there appears a region where temperature gradients are increased by at least an order of magnitude compared with the core. These steep gradients are far above the ITG and ETG core linear stability thresholds [33, 49]. This region, shown in Figure 1.4(a) and (b), is called the pedestal. Because the fusion reaction rate scales with the core temperature and density, a temperature and density pedestal is a substantial prize for a fusion reactor. Indeed, transport studies have found that the fusion power generated by burning plasmas can scale with the pedestal height, even as favorably as proportional to the square of the pedestal height [50]. Thus, if a stiff core profile is assumed, understanding the physics determining the pedestal dynamics is particularly important for realizing fusion power. By stiff, we mean that the gradients are close to the linear stability boundary, and that the transport scales strongly with the gradient. Plasmas with a pedestal are typically referred to as ‘H-mode’ (high performance-mode) plasmas.

H-mode was first discovered in ASDEX [47], and subsequently in most other tokamaks [51–54]. H-mode is characterized by the presence of a pedestal with decreased turbulent particle and heat diffusivities, and therefore significantly increased equilibrium gradients. These increased gradients drive MHD instabilities, which set hard limits on the maximum achievable pressure gradient [55–58].

Despite the pedestal being discovered nearly four decades ago, many aspects of pedestal physics are poorly-understood. One model that stands out in its predictive capacity is EPED, a predictive tool for the pedestal height and width [9, 59]. The EPED model assumes that once the plasma has transitioned into H-mode, the gradients will continue to steepen until the KBM becomes unstable. Once the gradients become sufficiently steep to trigger the KBM, the pedestal stays at a fairly constant pressure gradient, while increasing the pedestal current density until the peeling ballooning mode (PBM) [56, 60, 61] becomes unstable. As the PBM critical current density is reached, the model assumes that an edge localized mode (ELM) occurs, carrying heat and particles that degrade the pedestal, resetting the cycle [59]. The term ‘ELM’ refers to a set of MHD instabilities that occur in the edge of H-mode plasmas [8].

While the EPED model has a powerful predictive capacity, there are several factors that motivate studying pedestal dynamics from a non-MHD perspective. First, MHD dynamics does not distinguish between the density and temperature profiles. Many pedestals’ density and temperature profiles vary significantly [62], and hence understanding turbulent dynamics could be crucial for understanding such an asymmetry. Furthermore, while MHD analysis might determine pedestal stability, it does not predict the heating power and fueling required to sustain it. Additionally, MHD analysis has not yet explained why a pedestal appears in the first place; the EPED model, for example, assumes H-mode [59] and proceeds. Turbulent transport caused by microinstabilities driven unstable by equilibrium gradients that steepen during the inter-ELM period [63] can constrain other pedestal dynamics such as MHD stability [64, 65], scrape off layer and divertor physics [66], and neoclassical transport [67]. Finally, as a matter of theoretical inquiry, we will see that the steep temperature gradients, complex magnetic geometry, and finite gyroradius (FLR) effects — three essential components of a pedestal — give

rise to fascinating new microinstability physics, and hence the pedestal is an intriguing physical system in its own right, lying in an interesting parameter regime.

### 1.3 Microinstability Characteristics

In this section, we highlight some of the key properties of plasma microinstabilities that will be relevant to this thesis. In toroidal devices, there are three main particle drifts: parallel streaming, caused by particles following field lines, the magnetic drift, caused by magnetic geometry, and the  $\mathbf{E} \times \mathbf{B}$  drift, caused by electric and magnetic fields. These drifts, combined with a temperature gradient, can cause drift waves to go unstable. There are two main branches of ITG and ETG instability: toroidal and slab, though a mode can be a hybrid of both. The toroidal instability is caused by the magnetic drifts and the slab mode by the streaming of particles along magnetic field lines.

A further set of coordinates is particularly useful to describe microturbulence in tokamaks: flux tube coordinates. Microturbulence tends to be highly elongated along magnetic field lines, but narrow in extent across field lines [14]. Flux tube coordinates exploit the elongated nature of tokamak microturbulence: due to the relatively small perpendicular turbulent length scales, one can take a small region around a magnetic field line to examine the turbulence. We call this a flux tube because the perpendicular cut of the tube is chosen such that the magnetic flux through the perpendicular area is constant [68].

While similar to flux coordinates  $(\psi, \theta, \zeta)$ , flux tube coordinates  $(x, y, \theta)$  are field line following coordinates that measure the distance from the flux tube center  $\psi(r_c), \alpha_c$ , where the binormal coordinate  $\alpha$  labels the field line within a flux surface. By construction,  $\mathbf{B} \cdot \nabla \alpha = 0$ . Here,  $r_c$  and  $\alpha_c$  are the minor radial flux coordinate that is the half diameter of a flux surface at the midplane and the field line label coordinate, respectively, evaluated at the flux tube center. Using a flux function  $\psi$  and field line label  $\alpha$ , it is always possible to write the magnetic field as  $\mathbf{B} = \nabla \alpha \times \nabla \psi$ . It can be shown that for a magnetic field written in this way,  $\alpha = \zeta - q\theta + \nu$ , where  $q$  is the safety factor and  $\nu(\psi, \theta)$  is  $2\pi$  periodic in  $\theta$ , which we write explicitly in Equation (2.10). We have assumed that the toroidal

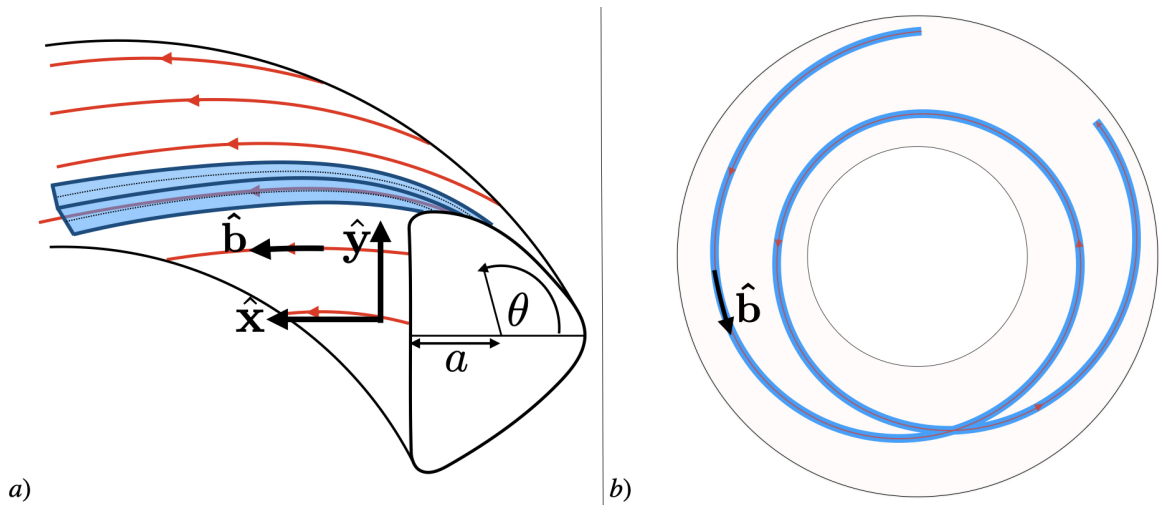


Figure 1.5: (a): Flux tube coordinates, where  $x$  is the radial flux coordinate,  $y$  is the field line label, and  $\hat{\mathbf{b}}$  is the unit vector along the magnetic field. (b) Bird's eye view of a flux tube in a tokamak.

system is axisymmetric, which makes  $\nu$  independent of  $\zeta$ . The flux coordinates  $x$  and  $y$  are given by

$$x = \frac{q_c}{r_c B_a} (\psi(r) - \psi(r_c)), \quad y = \frac{1}{B_a} \frac{\partial \psi}{\partial r} \Big|_{r_c} \alpha. \quad (1.2)$$

Here,  $B_a$  is the toroidal magnetic field strength evaluated at  $r_c$  and  $R_c$ , where  $R_c$  is the distance from the axis of symmetry of the tokamak to the center of the flux surface  $r_c$  at the midplane, and  $q_c = q(r_c)$ . We have chosen  $\alpha_c = 0$ . See Figure 1.5(a) and (b) for a diagram of the flux tube coordinate system and its physical extent in a tokamak. The flux tube prescription is useful as it is computationally efficient and the wavenumber  $k_y$  is constant along a magnetic field line.

Here, we provide a simple physical picture for the electrostatic toroidal ETG instability, which is shown in Figure 1.6. There are additional effects that we have neglected in this simple description; for example, parallel streaming, electromagnetic effects, FLR effects, and a radial wavenumber can change the character of the mode. We discuss some of these effects in the next section.

In Figure 1.6 (a), we show a wave at the outboard midplane with a poloidal wavenumber in the presence of a background temperature gradient. We represent peaks and troughs in the wave by red and blue horizontal ovals, depicting positive and negative electron temperature fluctuations, respectively. The temperature fluctuations due to

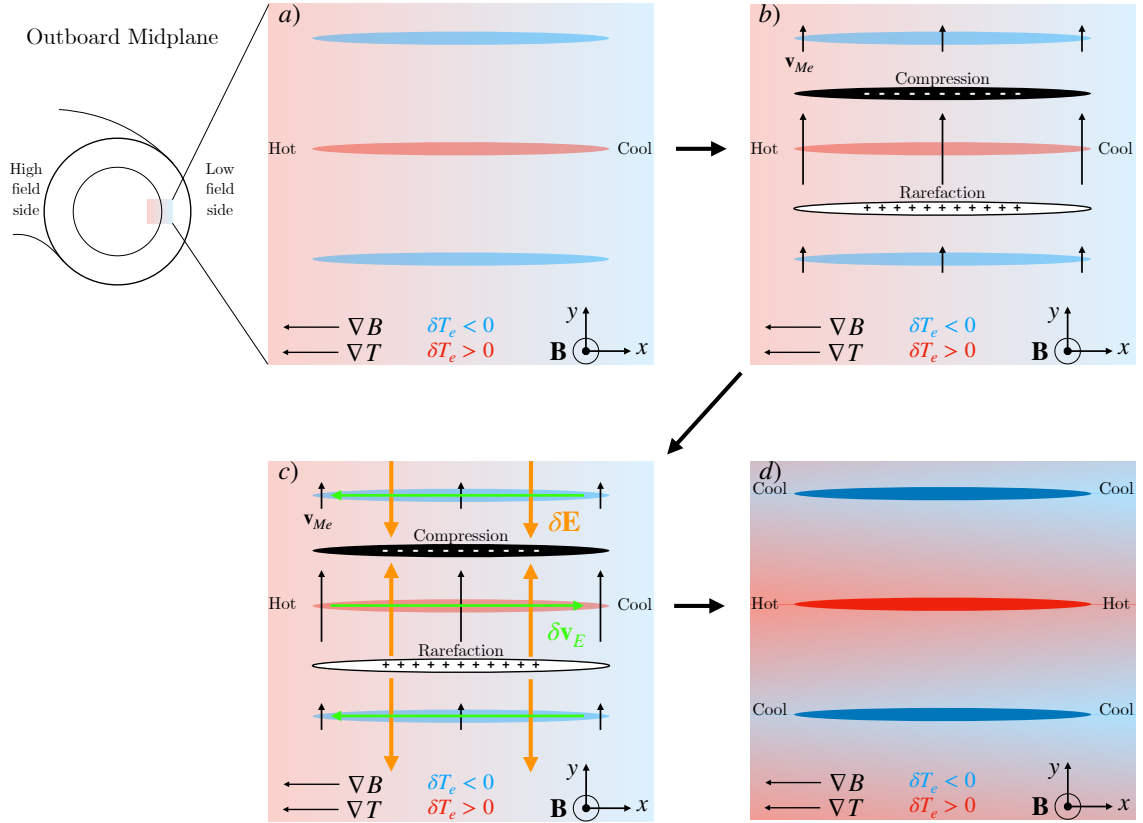


Figure 1.6: Mechanism for the standard toroidal ETG instability. (a): At the outboard midplane, consider a wave with a poloidal wavenumber, which creates regions of slightly hotter and colder temperature perturbations,  $\delta T_e$ , as shown by the red and blue contours. (b): The electron magnetic drift  $\mathbf{v}_{Me}$  is larger in the regions where  $\delta T_e > 0$  and smaller where  $\delta T_e < 0$ . This causes regions where the plasma is compressed and regions in which it is rarified. In compressed regions there will be a net negative electric charge and in rarified regions a net positive electric charge. (c): The charge overdensities and underdensities create a perturbed electric field  $\delta \mathbf{E}$ , which creates a perturbed  $\mathbf{E} \times \mathbf{B}$  drift,  $\delta \mathbf{v}_E$ . This causes hot plasma to be sucked into the regions where  $\delta T_e > 0$ , and cool plasma to be sucked into the regions where  $\delta T_e < 0$ , creating a positive feedback loop. This creates the unstable state in (d), which will become turbulent. The change in the total temperature due to the instability is exaggerated in (d).

the wave cause poloidal variations in the size of the electron magnetic particle drifts, shown in (b). Due to particle conservation, this causes electron density compressions and rarefactions, causing negative charge buildup and depletion, respectively. Shown in (c), this creates a perturbed electric field that also creates a perturbed  $\mathbf{E} \times \mathbf{B}$  drift. Due to the direction of the  $\mathbf{E} \times \mathbf{B}$  drift, hot plasma is sucked radially outwards from the core to where there are temperature overperturbations, and cold plasma is sucked radially inwards from the edge to where there are temperature underperturbations. This exacerbates the instability, whose amplitude might eventually grow sufficiently large to cause turbulence. Note that this mechanism does not drive instability at the inboard midplane, since the temperature gradient is in the opposite direction, which has a stabilizing effect when combined with the electron magnetic drifts.

In this simple picture, the toroidal ETG instability is most virulent when the magnetic curvature and temperature gradient are aligned, which occurs at the outboard midplane. However, as we will show in this thesis, both toroidal and slab ETG instability can be most virulent away from the outboard midplane, even for zero ballooning angle, the poloidal angle at which a mode has zero radial wavenumber. This linear physics can also manifest itself nonlinearly, with turbulence often peaking well away from the outboard midplane.

There are three effects that are particularly important for the pedestal microinstabilities described in this thesis: FLR effects, magnetic shear, and particularly steep temperature gradients. We introduce these below.

### 1.3.1 FLR Effects

FLR damping is one of the reasons that microinstabilities are most virulent at perpendicular wavenumbers comparable to the species gyroradius; that is,  $k_{\perp}\rho_i \sim 1$  and  $k_{\perp}\rho_e \sim 1$  for ITG and ETG instabilities, respectively. Here,  $k_{\perp}$  is the perpendicular turbulent wavenumber of the instability. FLR effects arise from a particle sampling different fluctuation amplitudes at different points in its gyromotion. For example, for  $k_{\perp}\rho_e \ll 1$ , if an electron samples a fairly constant fluctuation amplitude (see Figure 1.7 (a)), the growth rate of an instability such as ETG will be largely unaffected. However, once the wavelength is comparable to the gyroradius,  $k_{\perp}\rho_e \sim 1$ , the particle's sampling of several

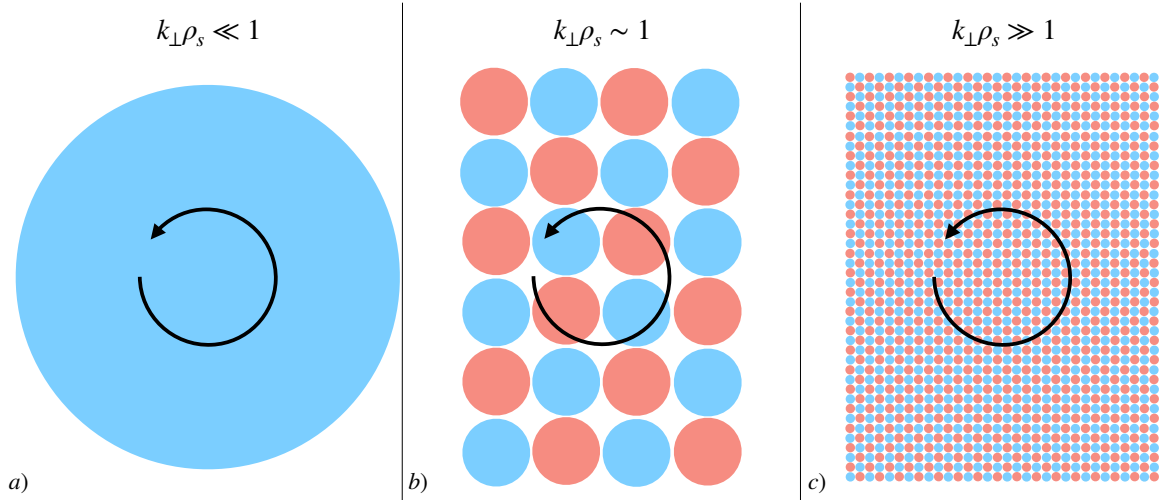


Figure 1.7: FLR effects at different perpendicular wavenumbers. Red and blue blobs represent turbulent overdensities and underdensities, respectively. Black arrows represent the particle's gyromotion. (a): The gyroradius is small compared with the turbulent wavelength and hence the particle sees a fairly constant density during a single gyroperiod. (b): The gyroradius is comparable to the turbulent wavelength and therefore the particle averages over several perturbations per gyroperiod, affecting its growth rate. (c): The gyroradius is large compared with the turbulent wavelength and hence the particle sees a rapidly changing turbulent density.

different fluctuations during a single gyromotion (see Figure 1.7 (b)) can start to reduce its growth rate. And if the particle's gyroradius is large compared with the turbulent wavelength, the particle averages over a large number of undulating fluctuations during its gyromotion (see Figure 1.7 (c)) and the instability growth rate decreases significantly. For ETG instability, usually  $k_{\perp}\rho_i \gg 1$ , and hence the ions are FLR damped and only respond adiabatically. While FLR damping decreases growth rates when  $k_{\perp}\rho_s \gtrsim 1$ , ITG and ETG growth rates can increase somewhat for moderate perpendicular wavenumber values [49].

### 1.3.2 Magnetic Shear

Magnetic shear arises from the magnetic field line pitch angle varying across flux surfaces and along field lines. The magnetic shear depends mainly on  $\psi$  for a circular flux surface. For realistic tokamak geometry, and particularly near the plasma edge, there is usually some local variation in the magnetic shear at different points along a field line. For a mode with some radial extent, the effect of magnetic shear is to increase the radial

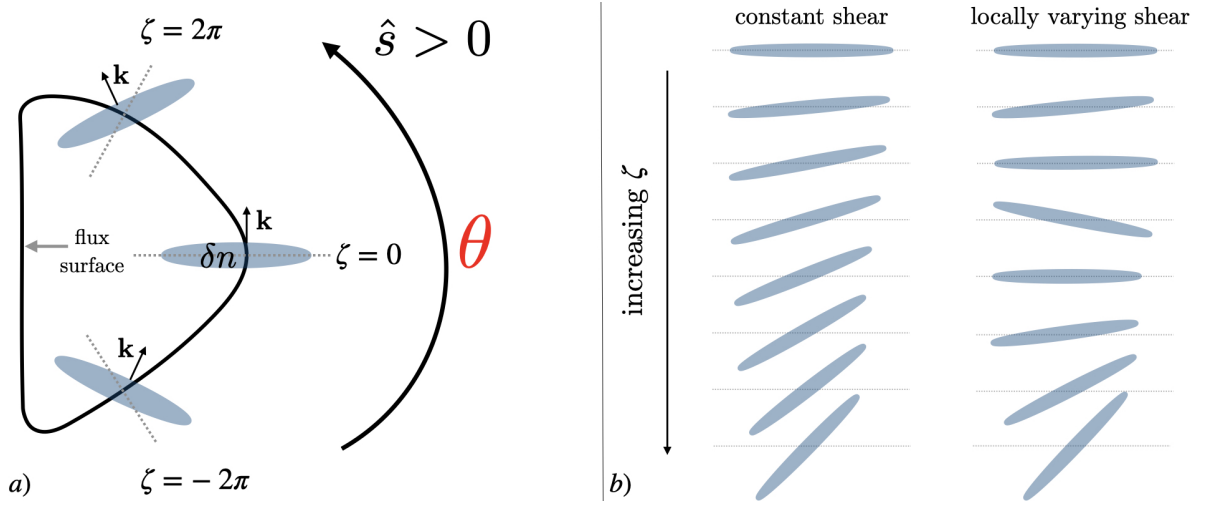


Figure 1.8: The effect of magnetic shear acting on a mode. The blue colored ovals represent wavefronts. (a): As a mode moves along a field line, its radial wavenumber increases. Here, the mode at  $\theta = 0$  has zero radial wavenumber. The quantity  $\mathbf{k}$  is the projection of the perpendicular wavenumber of the mode on the surface of constant toroidal angle  $\zeta \bmod 2\pi = 0$ . As the mode moves along a field line away from  $\theta = 0$ ,  $\mathbf{k}$  acquires a radial component. (b): The effect of magnetic shear on a perturbation that starts with zero radial wavenumber as it moves along a field line for two cases: with a constant magnetic shear (left column), and with a locally varying magnetic shear (right column).

wavenumber as the mode moves along a field line. In Figure 1.8 (a), we schematically show the effect of magnetic shear on a perturbation. The mode at  $\theta = \zeta = 0$  has zero radial wavenumber; the dotted grey line shows the zero radial wavenumber direction. Due to particles streaming rapidly along field lines, the mode will move in the toroidal direction. However, because the mode has some radial extent, the mode will sample different field line pitch angles at different radial locations. Therefore, as the mode moves along a field line it will become increasingly tilted due to its radial wave number increasing.

Heuristically, we can understand the mode tilting using an approximate form of  $\alpha$ , where  $\alpha \approx \zeta - q\theta$ . In the flux tube approximation, we Taylor expand the safety factor  $q \approx q_c + q'_c \Delta\psi$ , where  $\Delta\psi$  is the radial distance from the flux tube center, and  $q'_c$  is the derivative of the safety factor evaluated at the flux tube center, also known as the magnetic shear. By choosing a field line that satisfies  $\alpha = 0$ , we find an equation for the

toroidal angle,

$$\zeta = \theta (q_c + q'_c \Delta\psi), \quad (1.3)$$

According to Equation (1.3), at  $\theta = 0$ , all radial locations have the same value of  $\zeta$ . However, for  $\theta \neq 0$ , if  $q'_c \neq 0$ , the toroidal location for a mode has a radial dependence. Thus, as the mode completes a single toroidal turn, shown by the mode at  $\zeta = 2\pi$  in Figure 1.8 (a), its radial wavenumber increases due to the magnetic shear.

In Figure 1.8 (b), we show the effect of magnetic shear on an eddy for a constant magnetic shear (left column) and a locally varying magnetic shear (right column). Each row shows an eddy at a different  $(\theta, \zeta)$  location in the frame that rotates with the poloidal angle such that one of its axes aligns with the radial direction, indicated by the dotted grey line in Figure 1.8(b). In the left column, the radial wavenumber of the perturbation increases monotonically and uniformly with  $\theta$  as the mode moves along a field line. The right column shows the effect of local magnetic shear. Here, the eddy's radial wavenumber does not increase uniformly (or even necessarily monotonically): its rate of change of radial wavenumber varies locally in  $\theta$  because of differences in the magnetic shear at different poloidal locations.

Due to magnetic shear increasing a mode's radial wavenumber along a magnetic field line, a mode's growth rate can be decreased once  $k_\perp$  becomes sufficiently large and FLR effects start affecting the mode. Since both the global value of magnetic shear and local variations in the magnetic shear are typically very strong in the pedestal, we will see FLR damping caused by magnetic shear being important for pedestal microinstability physics.

### 1.3.3 Pedestal Temperature Gradients

Pedestal temperature gradients are particularly steep, which has consequences for ITG and ETG instabilities. The quantities  $L_{Te} = -(\partial_r \ln T_{0e})^{-1}$  and  $L_{Ti} = -(\partial_r \ln T_{0i})^{-1}$  measure the length scale associated with the equilibrium gradients. Here,  $T_{0s}$  is the leading order equilibrium temperature for a species  $s$ . The quantities  $R_0/L_{Te}$  and  $R_0/L_{Ti}$  are typically larger than  $\sqrt{m_i/m_e}$  in the pedestal's steep gradient region. One of the main consequences of  $R_0/L_{Te} \gg 1$  is that scale separation between linear ITG and ETG instability is no longer possible and that the usual pictures for ITG and ETG

instabilities that are valid in the tokamak core are now more complicated. In particular,  $R_0/L_{Te} \gtrsim \sqrt{m_i/m_e}$  means that the ETG instability can be strongly driven at ion Larmor scales, as discussed in Chapter 4. However, as shown in Chapter 9, it still appears that the nonlinear ETG turbulence has a maximum amplitude closer to the electron Larmor scale.

## 1.4 Thesis Outline

This thesis is separated into two parts. Part I is concerned with linear microinstability physics of the pedestal. Part II then explores pedestal microturbulence.

We study the stability of a JET ITER-like wall (JET-ILW) inter-ELM magnetic equilibrium with different ion and electron temperature profiles. The ion and electron temperatures are obtained using impurity charge exchange emission and Thomson scattering, respectively. Since  $\mathbf{E} \times \mathbf{B}$  shear is hypothesized to play a key role in pedestal formation [46, 69, 70], we focus on the radial region near the maximum value of the equilibrium  $\mathbf{E} \times \mathbf{B}$  shear. The region of maximum  $\mathbf{E} \times \mathbf{B}$  shear is estimated by balancing the radial electric field with the pressure gradient.

Gyrokinetic studies of pedestals have been performed before. Local gyrokinetic analysis of MAST found the main instabilities at  $k_\perp \rho_i \sim 1$  to be KBMs in the steep pressure gradient region and MTMs in the less steep pressure gradient region inside the pedestal top, throughout the inter-ELM recovery of the pedestal [71]. A follow up study using Doppler backscattering and cross-polarization scattering found that  $k_\perp \rho_i \approx 3 - 4$  turbulence at the pedestal top in MAST was most consistent with the ETG instability [72]. Using the Gyrokinetic Toroidal Code [73], PIC simulations in the steep gradient region of DIII-D discharges found electrostatic electron-driven modes peaking at poloidal angle  $\theta = \pm\pi/2$  [74]. More recently, in JET-ILW discharges where the ion temperature was not measured and was assumed to be equal to the measured electron temperature, nonlinear global gyrokinetic calculations were performed using the GENE code [33, 75]. These global simulations predict pedestal heat transport fluxes that are comparable with experiment, and suggest that pedestal fluxes will be increasingly dominated by ITG turbulence as the heating power increases [65]. Hatch et al. also proposed that impurity

seeding reduces ion-scale and ETG instability transport via ion-dilution and increased collisionality [65]. In [76], it was again demonstrated that the sum of neoclassical, MTM, and ETG turbulent transport was in good agreement with another JET-ILW pedestal measurement. Another recent work that used experimental ion temperature profiles found that ITG was suppressed in JET Carbon discharges, but not in JET-ILW cases, where ITG turbulence carried a substantial fraction of the total heat flux [77]. The difference between JET Carbon and JET-ILW was attributable to a decreased density gradient in JET-ILW discharges, which increased the growth rates of slab ITG and ETG instabilities.

In this work, we identify a novel type of toroidal ETG instability that appears in regions of steep equilibrium temperature gradients. These sub-ion Larmor scale modes have a radial wavenumber larger than its poloidal wavenumber, and have been observed (but not explained) in previous pedestal simulations [74, 78–82]. The particularly large radial wavenumber means that the radial magnetic drift plays an important role in these toroidal ETG modes. We find that this toroidal ETG has a large critical gradient threshold, which occurs due to the pedestal’s magnetic geometry and the radial magnetic drift. Moreover, because of the large equilibrium temperature gradients, we show theoretically and numerically that both toroidal and slab ETG modes are extended from perpendicular scales of  $k_y \rho_e \sim 1$  in the core, to  $k_y \rho_i \sim 1$  in the pedestal.

We primarily examine microinstability at a single radial location in the steep gradient region of JET-ILW shot 92714 [83], a highly-fueled deuterium discharge with deuterated ethylene ( $\text{C}_2\text{D}_4$ ) injection. For this discharge, at all scales where instability occurs —  $0.005 \lesssim k_y \rho_i \lesssim 400$  — we find that electron temperature gradient-driven modes are the fastest growing modes. For  $k_y \rho_i \gtrsim 1$ , the novel toroidal ETG mode is usually the fastest growing mode. We also show that the gradients of the measured ion temperature profiles are insufficiently steep to drive ITG instability. With the measured ion temperature profiles, the ion temperature gradient is close to the critical gradient needed for linear instability and hence ITG is subdominant. We also show that if ion temperature gradients are made sufficiently steep, toroidal and slab ITG modes become unstable at  $k_y \rho_i \ll 1$ , but are suppressed by  $\mathbf{E} \times \mathbf{B}$  shear. Our findings suggest that the toroidal and

slab ITG mode are stable in many radial pedestal locations, even in the steep gradient region that we examine.

We then proceed to examine nonlinear pedestal physics in Part II. Here, we find that pedestal ETG turbulence is statistically inhomogeneous, being divided up into distinct regions depending on the poloidal location of the turbulence. We show that the dual effects of a locally varying magnetic shear and a locally varying flux surface radial separation are responsible for this turbulence inhomogeneity; this is qualitatively different to the core, where the turbulence is homogenous in poloidal angle.

The layout of this work is as follows: we first introduce gyrokinetics and the notation used throughout this work in Chapter 2. We then present JET-ILW density, temperature, and rotation profiles from an inter-ELM pedestal in Chapter 3. Here, we also give a broad overview of the growth rates and unusual mode structures for the fastest growing modes in this pedestal, including a discussion of electromagnetic effects and  $\mathbf{E} \times \mathbf{B}$  shear. At a wide range of scales, we find an ETG mode with unusual character. This mode typically has a radial wavenumber that is significantly larger than the poloidal wavenumber, and is insensitive to finite  $\beta$  effects and  $\mathbf{E} \times \mathbf{B}$  shear. Motivated by the results of Chapter 3 and using the notation of Chapter 2, we then make analytic predictions about microinstability in steep gradient regions in Chapter 4. This theoretical analysis explains the existence of the novel toroidal ETG modes that we see in Chapter 3. We then examine ETG and ITG (or lack thereof) instability in linear gyrokinetic simulations in Chapters 5 and 6, respectively. The effect of  $\mathbf{E} \times \mathbf{B}$  shear is discussed further in Chapter 7. Nonlinear results are presented in Chapters 9 and 10, where we discuss the spatial inhomogeneity of the nonlinear state, which occurs due to the pedestal geometry. We conclude in Chapter 11.

Experimentally-minded readers might wish to jump to Chapters 3 and 5, while those more theoretically inclined and with a background in gyrokinetics might wish to begin at Chapter 4.

# Chapter 2

## Overview of Gyrokinetics

In this section, we introduce the system of gyrokinetic equations and notation used throughout this work. This section can be skipped for readers well-acquainted with gyrokinetics, or who mainly wish to see gyrokinetic simulation results in Chapters 3, 5 to 7, 9 and 10. Gyrokinetics [84–89] is used to investigate turbulence and transport using an asymptotic expansion in the ratio of  $\rho_{*s} \equiv \rho_s/L_{Ts} \ll 1$ . We express the gradients by the equilibrium length scales  $L_Q \equiv -(\partial \ln Q/\partial r)^{-1}$ , where  $Q$  can be the equilibrium density, temperature, or pressure. Assuming  $k_{\perp}\rho_i \sim 1$  and  $\omega \ll \Omega_s$ , gyrokinetics describes plasma behavior on spatial scales comparable to the ion gyroradius, and on timescales much longer than the gyro period. The quantity  $\omega$  is the frequency for turbulent quantities,  $\Omega_s = Z_s e B/m_s c$  is the gyrofrequency,  $Z_s$  is the charge number,  $e$  is the proton charge, and  $m_s$  is the species mass. The gyrokinetic ordering is  $\rho_{*s} \sim \omega/\Omega_s \sim \nu_s/\Omega_s \sim k_{\parallel}/k_{\perp} \ll 1$ , where  $\nu_s$  is a typical collision frequency for species  $s$ , and  $k_{\parallel}$  is the turbulent parallel wavenumber. To obtain a rough estimate for the radial electric field (see Equation (3.3)), we will impose that the radial electric field is comparable to the pressure gradient, which implies a low flow ordering [13, 16, 90] for the electric field,  $|\mathbf{E}| \sim T_{0e}/eL_{Te}$ , that is, the equilibrium  $\mathbf{E} \times \mathbf{B}$  drift is small compared with the thermal velocity  $v_{ts} = \sqrt{2T_{0s}/m_s}$  by a factor of  $\rho_{*s}$ .

We expand the magnetic field in  $\rho_{*s}$ ,  $\mathbf{B} + \mathbf{B}_1 + \mathbf{B}_2 + \dots$ , where  $\mathbf{B}_n = \rho_{*s}^n \mathbf{B}$  (note that we reserve  $\mathbf{B}$  for the leading order magnetic field, and do not explicitly use a symbol for the total magnetic field in this thesis). The lowest order magnetic field is given by Equation (1.1). For  $n \geq 1$ , we further split  $\mathbf{B}_n$  into long-wavelength and turbulent components,  $\mathbf{B}_n = \mathbf{B}_n^{lw} + \overline{\mathbf{B}}_n^{tb}$ . We reserve the overline notation for some of

these turbulent quantities because later we will write their Fourier components without an overline, which will keep the notation tidier. Long wavelength quantities,  $g^{lw}$ , spatially change on equilibrium length scales,  $\nabla g^{lw} \sim g^{lw}/L_{Ts}$ , and temporally change on slow time scales,  $\partial g^{lw}/\partial t \sim g^{lw}/\tau_E$ , where  $\tau_E$  is the energy confinement time and  $t$  is the time variable. Turbulent quantities,  $g^{tb}$ , spatially change on equilibrium length scales along the mean magnetic field,  $\hat{\mathbf{b}} \cdot \nabla g^{tb} \sim g^{tb}/L_{Ts}$ , but on gyroradius scales across the mean field,  $\nabla_{\perp} g^{tb} \sim g^{tb}/\rho_s$ , and temporally change on fast time scales,  $\partial g^{tb}/\partial t \sim \omega g^{tb}$ . Here,  $\hat{\mathbf{b}} = \mathbf{B}/B$ , and  $\nabla_{\perp}$  is a spatial derivative perpendicular to  $\mathbf{B}$ . We ignore the correction,  $\mathbf{B}_1^{lw}$ , which is mainly due to the effect of the neoclassical pressure anisotropy on the magnetic field. One can show that the turbulent component of  $\mathbf{B}_1$  can be written as  $\overline{\mathbf{B}}_1^{tb} = \nabla \overline{A}_{\parallel 1}^{tb} \times \hat{\mathbf{b}} + \overline{B}_{\parallel 1}^{tb} \hat{\mathbf{b}}$ , where  $\overline{B}_{\parallel 1}^{tb}$  and  $\overline{A}_{\parallel 1}^{tb}$  are the leading order parallel components of the turbulent magnetic field and magnetic vector potential, respectively.

We also expand the electric field  $\mathbf{E}$  in  $\rho_{*s}$ ,  $\mathbf{E} = \mathbf{E}_0 + \mathbf{E}_1 + \dots$ , where  $\mathbf{E}_n \sim \rho_{*s}^n T_{0s}/eL_{Ts}$ . We split  $\mathbf{E}_n$  into long wavelength and turbulent parts,  $\mathbf{E}_n = \mathbf{E}_n^{lw} + \overline{\mathbf{E}}_n^{tb}$ . To lowest order,  $\mathbf{E}_0$  is electrostatic;  $\mathbf{E}_0^{lw} = -\nabla \phi_0$ , and  $\overline{\mathbf{E}}_0^{tb} = -\nabla_{\perp} \overline{\phi}_1^{tb}$ . Here,  $\phi_0$  is the leading order electric potential and  $\overline{\phi}_1^{tb}$  is the leading order turbulent electric potential, where  $\overline{\phi}_1^{tb} \sim \rho_{*s} \phi_0$ . Since  $\phi_0$  is a flux function,  $\mathbf{E}_0 \cdot \hat{\mathbf{b}} = 0$ . To leading order, the parallel components of the electric field are  $E_{\parallel}^{lw} = -\hat{\mathbf{b}} \cdot \nabla \phi_1^{lw}$  and  $\overline{E}_{\parallel}^{tb} = -\hat{\mathbf{b}} \cdot \nabla \overline{\phi}_1^{tb} - (1/c)(\partial \overline{A}_{\parallel 1}^{tb}/\partial t)$ . The electrostatic potential  $\phi_1^{lw}$  is mainly due to neoclassical physics.

We expand the distribution function in  $\rho_{*s}$ ,  $f_s = F_{Ms} + f_{1s} + \dots$ , where the lowest order distribution function,  $F_{Ms}$ , is a stationary Maxwellian,

$$F_{Ms}(r, v) = n_{0s}(r) \left( \frac{m_s}{2\pi T_{0s}(r)} \right)^{3/2} \exp \left( - \frac{m_s v^2}{2T_{0s}(r)} \right), \quad (2.1)$$

with particle speed  $v$ , and flux functions  $n_{0s}$  and  $T_{0s}$ , where  $n_{0s}$  is the leading order density. The Maxwellian is stationary because the mean flow is subsonic. Higher order corrections to the distribution function can be split into long-wavelength and turbulent quantities,  $f_{ns} = f_{ns}^{lw} + f_{ns}^{tb}$ , where neoclassical corrections would be included in  $f_{ns}^{lw}$ .

To describe phase space, we will employ gyrokinetic variables. These are the guiding center,  $\mathbf{R}_s$ , the kinetic energy,  $\mathcal{E} = v^2/2$ , the magnetic moment,  $\mu = v_{\perp}^2/2B$  where  $\mathbf{v}_{\perp} = \mathbf{v} - \mathbf{v} \cdot \hat{\mathbf{b}} \hat{\mathbf{b}}$ , and the gyrophase,  $\varphi$ , which is a particle's angular location during its gyromotion. The guiding center is given by  $\mathbf{R}_s = \mathbf{r} - \boldsymbol{\rho}_s$ , the gyroradius position is given

by  $\boldsymbol{\rho}_s = \hat{\mathbf{b}} \times \mathbf{v}/\Omega_s$ , and the quantity  $\mathbf{r}$  is the particle position. The first order turbulent component of the distribution function can be written as

$$f_{1s}^{tb}(\mathbf{R}_s, \mathcal{E}, \mu, \varphi, t) = \bar{h}_s(\mathbf{R}_s, \mathcal{E}, \mu, t) - \frac{Z_s e \bar{\phi}_1^{tb}}{T_{0s}} F_{Ms}(\mathbf{r}, \mathcal{E}, t). \quad (2.2)$$

Note that the function  $\bar{h}_s$  is independent of the gyrophase — our task is to find an evolution equation for  $\bar{h}_s$ .

To find  $\bar{h}_s$ , we substitute Equation (2.2) into the first order Fokker-Planck equation. Because only the variable  $\varphi$  varies over a single gyroperiod, it is convenient to average the Fokker-Planck equation over the gyromotion using a gyroaverage, defined as  $\langle \dots \rangle = (1/2\pi) \int_0^{2\pi} \dots d\varphi|_{\mathbf{R}_s, \mathcal{E}, \mu}$ , evaluated at fixed  $\mathbf{R}_s, \mathcal{E}$ , and  $\mu$ . Gyroaveraging the first order Fokker-Planck equation given by

$$\begin{aligned} \frac{\partial \bar{h}_s}{\partial t} + \left( \frac{d\mathbf{R}_s}{dt} \cdot \nabla_{\mathbf{R}_s} + \frac{d\mathcal{E}}{dt} \frac{\partial}{\partial \mathcal{E}} + \frac{d\mu}{dt} \frac{\partial}{\partial \mu} \right) (F_{Ms} + f_{1s}^{lw} + \bar{h}_s) \\ = \frac{Z_s e}{T_{0s}} \frac{d}{dt} \left( \bar{\phi}_1^{tb} F_{Ms} \right) - \Omega_s \frac{\partial}{\partial \varphi} (f_{2s}^{lw} + f_{2s}^{tb}) - C_s, \end{aligned} \quad (2.3)$$

and taking its turbulent component, we obtain the low flow electromagnetic gyrokinetic equation,

$$\begin{aligned} \left( \frac{\partial}{\partial t} + \Omega_E \frac{\partial}{\partial \zeta} \right) \bar{h}_s + (v_{\parallel} \hat{\mathbf{b}} + \mathbf{v}_{Ms} + \langle \mathbf{v}_{\chi}^{tb} \rangle) \cdot \nabla_{\mathbf{R}_s} \bar{h}_s \\ = \frac{Z_s e F_{Ms}}{T_{0s}} \left( \frac{\partial}{\partial t} + \Omega_E \frac{\partial}{\partial \zeta} \right) \langle \bar{\chi}_1^{tb} \rangle - \langle \mathbf{v}_{\chi}^{tb} \rangle \cdot \nabla_{\mathbf{R}_s} F_{Ms} - \left\langle C_s^{(l)} \right\rangle, \end{aligned} \quad (2.4)$$

where  $d/dt$  is a full time derivative along a particle trajectory,  $\Omega_E(r) = -c\partial\phi_0/\partial\psi$  is the  $\mathbf{E} \times \mathbf{B}$  toroidal angular velocity,  $C_s$  is a Fokker-Planck collision operator,  $C_s^{(l)}$  is a linearized Fokker-Planck collision operator,  $\nabla_{\mathbf{R}_s} \equiv \partial/\partial\mathbf{R}_s$ , and the magnetic drift is

$$\mathbf{v}_{Ms} = \frac{\hat{\mathbf{b}}}{\Omega_s} \times \left[ \left( v_{\parallel}^2 + \frac{v_{\perp}^2}{2} \right) \nabla \ln B + v_{\parallel}^2 \frac{4\pi}{B^2} \frac{\partial p_0}{\partial r} \nabla r \right]. \quad (2.5)$$

Here,  $p_0 = \sum_s p_{0s}$  is the total pressure and  $p_{0s} = n_{0s} T_{0s}$  is the lowest order pressure of species  $s$ . The parallel velocity is  $v_{\parallel} = \mathbf{v} \cdot \hat{\mathbf{b}}$ , and the gyrokinetic drift is  $\mathbf{v}_{\chi}^{tb} = (c/B) \hat{\mathbf{b}} \times \nabla \bar{\chi}_1^{tb}$ . Here,  $\bar{\chi}_1^{tb}$  is the leading order turbulent gyrokinetic potential defined as

$$\bar{\chi}_1^{tb} = \bar{\phi}_1^{tb} - \frac{v_{\parallel} \bar{A}_{\parallel 1}^{tb}}{c} + \frac{m_s}{Z_s e} \int_0^{\mu} \bar{B}_{\parallel 1}^{tb}(\mathbf{R}_s + \boldsymbol{\rho}_s(\mu')) d\mu'. \quad (2.6)$$

In Equation (2.4),  $\Omega_E(r)$  can be approximated around the radial location  $r_c$  of interest by  $\Omega_E(r_c) + (r - r_c)(\partial\Omega_E/\partial r)$  because the characteristic size of the eddies is small

compared with  $L_{Te}$ . In the low flow ordering that we use, the term  $(r - r_c)(\partial\Omega_E/\partial r)$ , which represents the  $\mathbf{E} \times \mathbf{B}$  shear, should be neglected because it is of the same size as other terms that we have not kept. Even so, we perform some simulations with  $\mathbf{E} \times \mathbf{B}$  shear. We will justify using this small term in Chapter 7.

To close the system of equations, we need to find  $\bar{\phi}_1^{tb}$ ,  $\bar{A}_{\parallel 1}^{tb}$ , and  $\bar{B}_{\parallel 1}^{tb}$  using  $\bar{h}_s$ . To find  $\bar{\phi}_1^{tb}$ , we use the first order turbulent quasineutrality condition,

$$\sum_s \frac{Z_s^2 e^2 \bar{\phi}_1^{tb}}{T_{0s}} n_{0s} = \sum_s Z_s e \int \bar{h}_s(\mathbf{r} - \boldsymbol{\rho}_s, \mathcal{E}, \mu) d^3v. \quad (2.7)$$

The parallel vector potential,  $\bar{A}_{\parallel 1}^{tb}$ , is found using the parallel component of Ampère's law,

$$-\nabla_{\perp}^2 \bar{A}_{\parallel 1}^{tb} = \frac{4\pi e}{c} \sum_s Z_s \int v_{\parallel} \bar{h}_s(\mathbf{r} - \boldsymbol{\rho}_s, \mathcal{E}, \mu) d^3v. \quad (2.8)$$

Finally,  $\bar{B}_{\parallel 1}^{tb}$  is determined by perpendicular pressure balance,

$$\frac{B \bar{B}_{\parallel 1}^{tb}}{4\pi} + \sum_s \int m_s B \int_0^{\mu} \bar{h}_s(\mathbf{r} - \boldsymbol{\rho}_s(\mu'), \mathcal{E}, \mu) d\mu' d^3v = 0. \quad (2.9)$$

Note that the integral over  $\mu'$  only affects the  $\mu$  dependence of  $\boldsymbol{\rho}_s$ .

In the Part I of this thesis, we will examine the stability properties of the gyrokinetic equation in the local limit. To understand how these linear instabilities then cause turbulent transport, one needs to keep the nonlinear term of Equation (2.4), which we will initially neglect. In Part II of this thesis, we will include the nonlinearity.

To describe the properties of the turbulent pieces,  $\bar{\phi}_1^{tb}$ ,  $\bar{A}_{\parallel 1}^{tb}$ ,  $\bar{B}_{\parallel 1}^{tb}$ , and  $\bar{h}_s$ , we use the flux coordinates  $(x, y, \theta)$ , introduced in Equation (1.2). The function  $\nu(r, \theta)$  that enters the definition of  $y$  is  $2\pi$ -periodic in  $\theta$ ,

$$\nu(r, \theta) = -I(r) \left( \int_0^{\theta} d\theta' \left[ \frac{1}{R^2(\theta') \mathbf{B}(\theta') \cdot \nabla \theta'} - \frac{1}{2\pi} \oint \frac{d\theta''}{R^2(\theta'') \mathbf{B}(\theta'') \cdot \nabla \theta''} \right] \right). \quad (2.10)$$

The safety factor,  $q(r)$ , is given by  $2\pi q(r) = \oint I(r) d\theta / R^2 \mathbf{B} \cdot \nabla \theta$ . We choose to define the poloidal angle  $\theta$  as

$$\theta = 2\pi l / L_{\theta}, \quad (2.11)$$

where  $l$  is the arclength along the magnetic field, and  $L_{\theta}$  is the distance along a field line for one complete poloidal turn. In this thesis,  $\theta$  will refer to a 'ballooning' coordinate,

which takes values  $-\infty < \theta < \infty$ . For reasons that will become obvious, in the nonlinear simulations chapters, we will define another poloidal coordinate  $\tilde{\theta}$  that is bounded by  $-\pi$  and  $\pi$ .

If we choose to describe a sufficiently narrow perpendicular region of the plasma, we can assume that equilibrium quantities and their corresponding gradients are constant. Therefore, we expect that the turbulence is statistically identical at all perpendicular locations in our box. These conditions are satisfied in the local limit,  $k_{\perp}L_{Ts} \gg 1$ . This limit is useful for analytic treatment and numerically efficient simulations. Spatial anisotropy,  $k_{\perp}/k_{\parallel} \gg 1$ , implies that  $\partial/\partial x \sim \partial/\partial y \gg (2\pi/L_{\theta})\partial/\partial\theta$ , and therefore the local limit describes turbulence that can be extended along field lines but narrow across field lines. If  $k_{\perp}L_{Ts} \gg 1$ , modes can be Fourier analyzed in the perpendicular domain; for example, we Fourier analyze  $\bar{\phi}_1^{tb}$  locally in the perpendicular plane and in time,

$$\bar{\phi}_1^{tb}(x, y, \theta, t) = \sum_{k_x, k_y, \omega} \phi_1^{tb}(k_x, k_y, \theta, \omega) \exp(ik_x x + ik_y y - i\omega t). \quad (2.12)$$

The electromagnetic fluctuations  $\bar{A}_{\parallel}^{tb}$  and  $\bar{B}_{\parallel}^{tb}$  are Fourier analyzed in a similar way. It will also be useful to Fourier analyze  $\bar{h}_s$ ,

$$\bar{h}_s(X_s, Y_s, \theta, \mathcal{E}, \mu, t) = \sum_{k_x, k_y, \omega} h_s(k_x, k_y, \theta, \mathcal{E}, \mu, \omega) \exp(ik_x X_s + ik_y Y_s - i\omega t), \quad (2.13)$$

where  $X_s = x - \boldsymbol{\rho}_s \cdot \nabla x$  and  $Y_s = y - \boldsymbol{\rho}_s \cdot \nabla y$  are guiding center variables. In the main JET equilibrium we examine in this work, at the radial location of interest, we find that  $L_{Te} \simeq 0.02\text{m}$ , and thus the local approximation is good provided that  $k_{\perp}\rho_i \gg \rho_i/L_{Te} \simeq 0.12$ . Note that throughout this work, the quantity  $k_y\rho_i$  will be a deceptive measure of  $k_{\perp}\rho_i$ ; the modes that we find typically have a very large radial wavenumber compared to  $k_y\rho_i$ . Hence, these modes satisfy the relation  $k_{\perp}\rho_i \gg k_y\rho_i$ .

**Part I**  
**Linear Physics**

## Chapter 3

# Pedestal Gyrokinetic Simulations of JET Shot 92174

In this chapter, we present the significant linear microstability features of a single JET-ILW inter-ELM pedestal discharge at a single radial location. This equilibrium exhibits properties such as temperature, magnetic geometry, injected neutral beam power, and fueling that are typical for JET-ILW inter-ELM H-mode pedestals: key experimental parameters for this discharge are  $I_p = 1.4$  MA,  $B_{T0} = 1.9$  T,  $H_{98(y,2)} = 1.0$ ,  $n_G = 0.7$ ,  $P_{\text{NBI}} = 17.4$  MW,  $\beta_N = 2.5$ , and  $R_D = 0.9 \times 10^{22}$  electrons/s. Here,  $I_p$  is the poloidal current,  $B_{T0}$  is the toroidal magnetic field at  $R = 2.96$ m,  $H_{98(y,2)}$  is the H factor relative to the IPB98<sub>(y,2)</sub> scaling [91],  $n_G$  is the Greenwald density fraction [6] defined as the line averaged density divided by the Greenwald density limit,  $P_{\text{NBI}}$  is the neutral beam injection power,  $\beta_N$  is the normalized  $\beta$  factor [4], and  $R_D$  is the deuterium electron flow rate.

In Section 3.1, we show the pedestal equilibrium temperature, density, and flow profiles, which will have significant implications for microstability. In Section 3.2, we present an overview of linear results from gyrokinetic simulations, run both with and without finite  $\beta$  effects. From these results, we justify an electrostatic study. Here, we find a range of modes, including an unusual toroidal ETG instability that is driven at a very wide range of perpendicular scales, and has a radial wavenumber that is typically much larger than its poloidal wavenumber. A significant portion of the work will be devoted to understanding this mode. We show that this mode is largely unaffected by finite  $\beta$  effects and  $\mathbf{E} \times \mathbf{B}$  shear, and in subsequent sections, that a quasilinear estimate

for the heat flux carried by this mode is comparable to the slab ETG branch. Finally, in Section 3.3, we present the prominent features of the electrostatic growth rate spectrum.

### 3.1 JET-ILW Profiles

In this work, we focus on simulation results from JET shot 92174. We run gyrokinetic simulations with a single deuterium ion species and no impurities, assuming that  $n_{0e} = n_{0i}$  (note that experimentally  $Z_{\text{eff}} = 1.8$ , where  $Z_{\text{eff}} = \sum_i n_{0i} Z_i^2 / n_{0e}$ ). Three other pedestals that we have analyzed (82550, 92167, 92168) give qualitatively similar results, which is notable, given that the nature of these discharges varies quite significantly. The experimental and simulation parameters and linear gyrokinetic growth rates for these additional three discharges are shown in Appendix A.

The temperature and density profiles for shot 92174 and associated gradients, are shown in Figure 3.1(a) as functions of  $r/a$ . The distance  $a$  is the value of  $r$  at the last closed flux surface (LCFS). In Figure 3.1(d), we also show the toroidal velocity of  $\frac{1}{6}C^+$ ,  $u_{\zeta C}$ , at the outboard midplane, normalized by the ion thermal speed  $v_{ti} = \sqrt{2T_{0i}/m_i}$ . We assume that this velocity is a good proxy for the toroidal ion velocity,  $u_{\zeta i}$ . We normalize the gradient length scales using the major radius of the last closed flux surface,  $R_0$ , which is the radial distance to the center of the last closed flux surface at the midplane. The profiles in Figure 3.1 are consistent with an emerging JET-ILW pedestal paradigm [65, 77, 92, 93], whereby enhanced gas puffing reduces the edge density gradient [94] and shifts the density pedestal outwards [72, 95], making microinstabilities more virulent [96]. Weaker density gradients also reduce the  $\mathbf{E} \times \mathbf{B}$  shear, which has often been observed to be important for microinstability suppression in the pedestal [65, 77, 93]. It is hypothesized that heat transport from more strongly-driven microinstabilities with less shear suppression is responsible for a reduced temperature at the pedestal top [77].

In this work, the electron temperature and density are determined from the High Resolution Thomson Scattering profiles [97, 98]. To improve the data statistics, a composite profile is constructed from profiles collected in a time window of 80-99% in the ELM interval period. The profiles of the ion temperature and rotation are measured with the edge Charge Exchange Recombination Spectroscopy diagnostic [99] for fully stripped

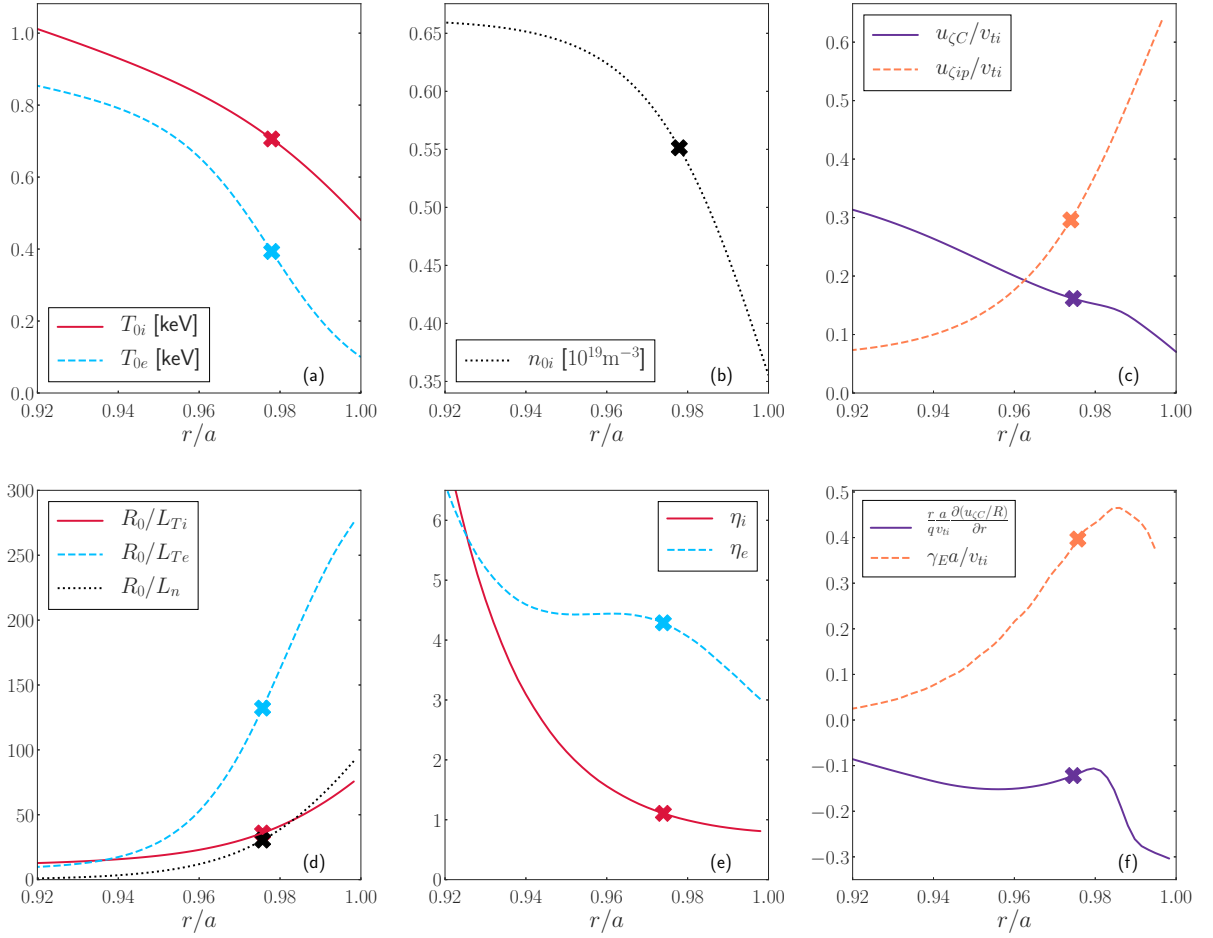


Figure 3.1: Pedestal profiles and their gradients for JET shot 92174. Crosses indicate simulation location of  $r/a = 0.9743$ . (a): Ion and electron temperatures profiles. (b): Density profiles. (c): Flow profiles for  $u_{zC}$ , the experimental value for the toroidal component of the  $^{12}\text{C}^+$  flow, and  $u_{zip}$ , the toroidal component of the ion diamagnetic flow, defined in Equation (3.2). (d): Temperature and density gradients profiles. (e):  $\eta_s$  profiles, where the parameter  $\eta_s$  is defined as  $\eta_s \equiv L_n/L_{Ts}$ . (f): Flow shear profiles.

carbon-12 ( $^{12}\text{C}^+$ ), with a time integration of 7.2ms. These ion profiles are collected on a longer 60-99 % ELM interval period time window. The  $^{12}\text{C}^+$  and ion temperature and rotation profiles in the pedestal can differ substantially, as found in some recent DIII-D experiments [100–102]. Since the ITG instability in Chapter 6 should be viewed in the context of potentially large uncertainties in ion temperature measurements, which might significantly underestimate the ion temperature gradient. For this reason, while we have mainly used  $T_{0i} > T_{0e}$  and  $R_0/L_{Te} > R_0/L_{Ti}$  in our simulations and theory, we have also explored the impact on gyrokinetic microinstabilities of assuming  $T_{0i} = T_{0e}$  and  $R_0/L_{Ti} = R_0/L_{Te}$ , which

can be found in Chapter 6. However, unless explicitly mentioned otherwise, we use the measured ion temperature profiles.

To obtain an estimate for the radial electric field, we use the most general ion flow [13, 90],

$$\mathbf{u}_i = -c \frac{\partial \phi_0}{\partial \psi} R^2 \nabla \zeta - \frac{c}{Z_i e n_{0i}} \frac{\partial p_{0i}}{\partial \psi} R^2 \nabla \zeta + \frac{\mathbf{B}}{n_{0i}} K_i(\psi) \frac{\partial T_{0i}}{\partial \psi}. \quad (3.1)$$

Here, the flux function,  $K_i(\psi)$ , is determined by neoclassical theory [13, 90]. Based on the experimental data in Figure 3.1, we find that  $u_{\zeta C} \lesssim (\rho_{Pi}/L_{Ti})v_{ti}$ . The quantity  $\rho_{Ps} = (B/B_P)\rho_s$  is the poloidal gyroradius for a species  $s$ , where  $B_P$  is the poloidal magnetic field strength. Thus, the flow velocity of the  $^{12}C^+$  impurity species is comparable to the size of the ion diamagnetic flow,  $u_{\zeta ip}$ ,

$$\frac{u_{\zeta ip}}{v_{ti}} = -\frac{Rc}{Z_i e n_{0i} v_{ti}} \frac{\partial p_{0i}}{\partial \psi} \sim \frac{\rho_{Pi}}{L_{pi}} \sim \frac{1}{3}. \quad (3.2)$$

Note that this implies that there are only several poloidal gyroradii in a pressure length scale,  $L_{pi}$ . To obtain a rough estimate of the radial electric field, we use the fact that the measurement of  $u_{\zeta i}$  suggests that the overall flow, the  $\mathbf{E} \times \mathbf{B}$  flow, the diamagnetic flow in Equation (3.2), and the term proportional to  $K_i(\psi)$  are all of the same order. Thus,

$$-\frac{\partial \phi_0}{\partial \psi} \approx \frac{1}{Z_i e n_{0i}} \frac{\partial p_{0i}}{\partial \psi}. \quad (3.3)$$

Then, the radial shear in the  $\mathbf{E} \times \mathbf{B}$  rotation,  $\gamma_E(\psi)$ , is approximately

$$\gamma_E \equiv -\frac{cr}{q} \frac{\partial}{\partial r} \left( \frac{\partial \phi_0}{\partial \psi} \right) \approx \frac{r}{q} \frac{\partial}{\partial r} \left( \frac{c}{Z_i e n_{0i}} \frac{\partial p_{0i}}{\partial \psi} \right). \quad (3.4)$$

The location of the simulations was chosen to have equilibrium length scales characteristic of the steep gradient region in the pedestal, and an  $\mathbf{E} \times \mathbf{B}$  shear value close to the maximum possible for a given equilibrium, using the estimate in Equation (3.4). The radial location for JET shot 92174, shown in Figure 3.1, is  $r/a = 0.9743$ . To simulate this discharge, we use the following simulation parameters:  $\rho_i = 0.27$  cm,  $\nu_{ee}a/v_{ti} = 0.83$ ,  $a/L_{Te} = 42$ ,  $a/L_{Ti} = 11$ ,  $a/L_n = 10$ ,  $\rho_i/L_{Te} = 0.12$ ,  $T_{0e}/T_{0i} = 0.56$ ,  $\hat{s} = 3.36$ ,  $q = 5.1$ ,  $R_0 = 2.86$  m,  $a = 0.91$  m,  $R_c = 2.91$  m, and  $r_c = 0.89$  m, where  $\nu_{ss'} = \sqrt{2\pi}n_{0s'}Z_s^2Z_{s'}^2e^4 \ln(\Lambda_{ss'})/\sqrt{m_s}T_{0s'}^{3/2}$ ,  $\ln(\Lambda_{ss'})$  is the Coulomb logarithm, and  $\hat{s} = (r/q)\partial q/\partial r$  is the magnetic shear. In the instances where we included  $\mathbf{E} \times \mathbf{B}$  shear and electromagnetic effects, we used  $\gamma_E a/v_{ti} = 0.56$  and  $\beta = 0.0031$ . Here, the quantity  $\beta = 8\pi(p_{0i} + p_{0e})/B_a^2$ , where  $B_a = 1.99$  T for this equilibrium.

## 3.2 Gyrokinetic Simulation Results

In this section, we present results obtained from linear gyrokinetic simulations (both electromagnetic and electrostatic) for this radial location and pedestal. For the chosen pedestal and radial location, we will establish that linear *electrostatic* simulations without  $\mathbf{E} \times \mathbf{B}$  shear give similar growth rate spectra to linear *electromagnetic* simulations with  $\mathbf{E} \times \mathbf{B}$  shear. The electrostatic limit of Equation (2.4) is taken by requiring that the turbulent electric field is primarily electrostatic,  $|\nabla \bar{\phi}_1^{tb}| \gg (1/c)|\partial \bar{A}_{\parallel 1}^{tb}/\partial t|$ , and that the turbulent magnetic field is small,  $|\mu \bar{B}_1^{tb}| \ll |Z_s \bar{\phi}_1^{tb}|e/m_s$ <sup>1</sup>. It is no coincidence that the electrostatic regime without  $\mathbf{E} \times \mathbf{B}$  shear and the electromagnetic case with  $\mathbf{E} \times \mathbf{B}$  shear give similar results; electromagnetic modes are suppressed by  $\mathbf{E} \times \mathbf{B}$  shear, leaving electrostatic modes that are unaffected by  $\mathbf{E} \times \mathbf{B}$  shear as the dominant instabilities. Therefore, it is reasonable to study this pedestal with linear electrostatic simulations without  $\mathbf{E} \times \mathbf{B}$  shear. We will choose to study the electrostatic limit without  $\mathbf{E} \times \mathbf{B}$  shear rather than an electromagnetic case with  $\mathbf{E} \times \mathbf{B}$  shear because the former is analytically and numerically simpler. We now proceed to give an overview of gyrokinetic results for the electrostatic pedestal.

We performed these local simulations in ballooning space, which can be represented in a flux-tube [68]. Because the novel toroidal ETG instability we have found is often driven at large distances along the field line from  $\theta = 0$ , we require a large range of  $\theta$  values, and hence we typically choose a flux-tube with 64 gridpoints in each  $2\pi$  period in  $\theta$ , with nine periods. This is equivalent to a ballooning space calculation extending to nine poloidal turns in the extended ballooning coordinate. The standard velocity space grid had 20 passing pitch angles, 33 trapped pitch angles, and 12 energy gridpoints [103]. Resolution scans were performed in all of these parameters by doubling each of them independently; there was no significant difference in the frequencies or the character of these modes.

While GS2 is capable of reading in numerical equilibria, we fit the magnetic equilibrium with Miller geometry. A Miller equilibrium is a prescription to generate flux

---

<sup>1</sup>Even though the last term in Equation (2.5) is formally small in  $\beta$  in the electrostatic limit, we keep it in all our electrostatic simulations because the large pressure gradients in the pedestal can make it important.

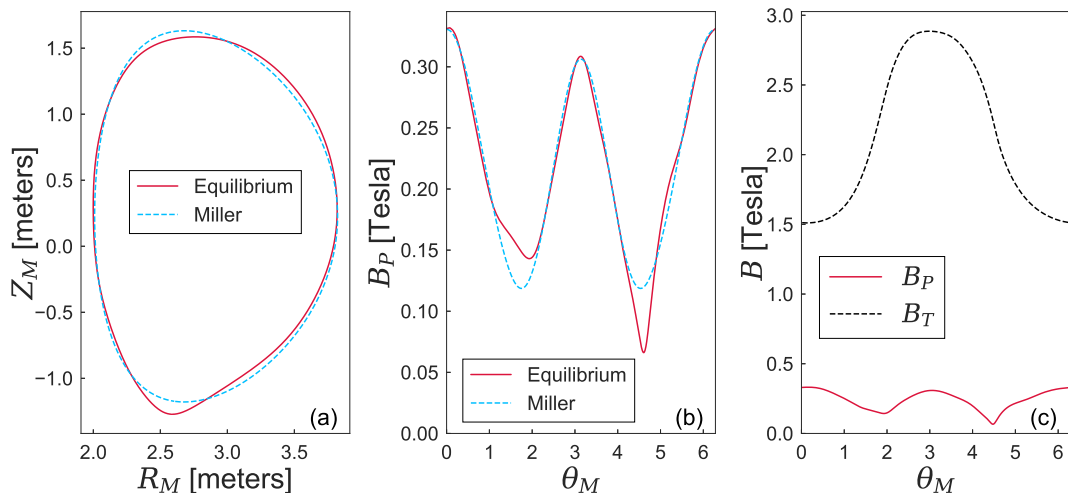


Figure 3.2: The Miller equilibrium and numerical equilibrium for JET shot 92174 used for gyrokinetic simulations. (a): Equilibrium and Miller flux surfaces in  $R_M, Z_M$  space, (b): Equilibrium and Miller poloidal magnetic field versus  $\theta_M$ , (c): Equilibrium toroidal and poloidal magnetic fields.

surfaces that satisfy the Grad–Shafranov equation locally by fitting to nine parameters [104]. The shape of the flux surface  $r_c$  and its neighbors is determined by  $R = R_M(r, \theta_M)$  and  $Z = Z_M(r, \theta_M)$ , where  $\theta_M$  is the Miller poloidal angle, which is in general not equal to the poloidal coordinate  $\theta$  defined in Equation (2.11). In Figure 3.2 we show the difference between the exact flux surface at  $r/a = 0.9743$  and the Miller fits that we use. The Miller parameters for this radial location are  $\Delta' = dR_c/dr = -0.345$ ,  $\kappa = 1.55$ ,  $a(d\kappa/dr) = 0.949$ ,  $\delta = 0.263$ ,  $a(d\delta/dr) = 0.737$ ,  $\beta' = \beta a(d \ln p_0/dr) = -0.161$ , where  $\delta$  is the triangularity.

Electromagnetic effects have been shown to be important for microinstability in the pedestal [65, 71, 76, 77, 82]. While we have neglected electromagnetic effects in most of this study, we have checked the potential effects of nonzero  $\beta$ . As an initial study, this is well-justified since we will show that a linear electromagnetic gyrokinetic simulation with  $\mathbf{E} \times \mathbf{B}$  shear gives similar results to a linear *electrostatic* gyrokinetic simulation without  $\mathbf{E} \times \mathbf{B}$  shear. To demonstrate this equivalence, we first show the results of gyrokinetic simulations with and without finite  $\beta$  effects in Figure 3.3. To include finite  $\beta$  effects, we included values of  $\beta$  and  $\beta'$  consistent with the Miller equilibrium.

In Figure 3.3, we show the effect of finite  $\beta$  on the growth rates (a), real frequencies (b), and eigenmodes (c) for  $\theta_0 = 0$ , where  $\theta_0$  is the ballooning angle, defined as  $\theta_0 =$

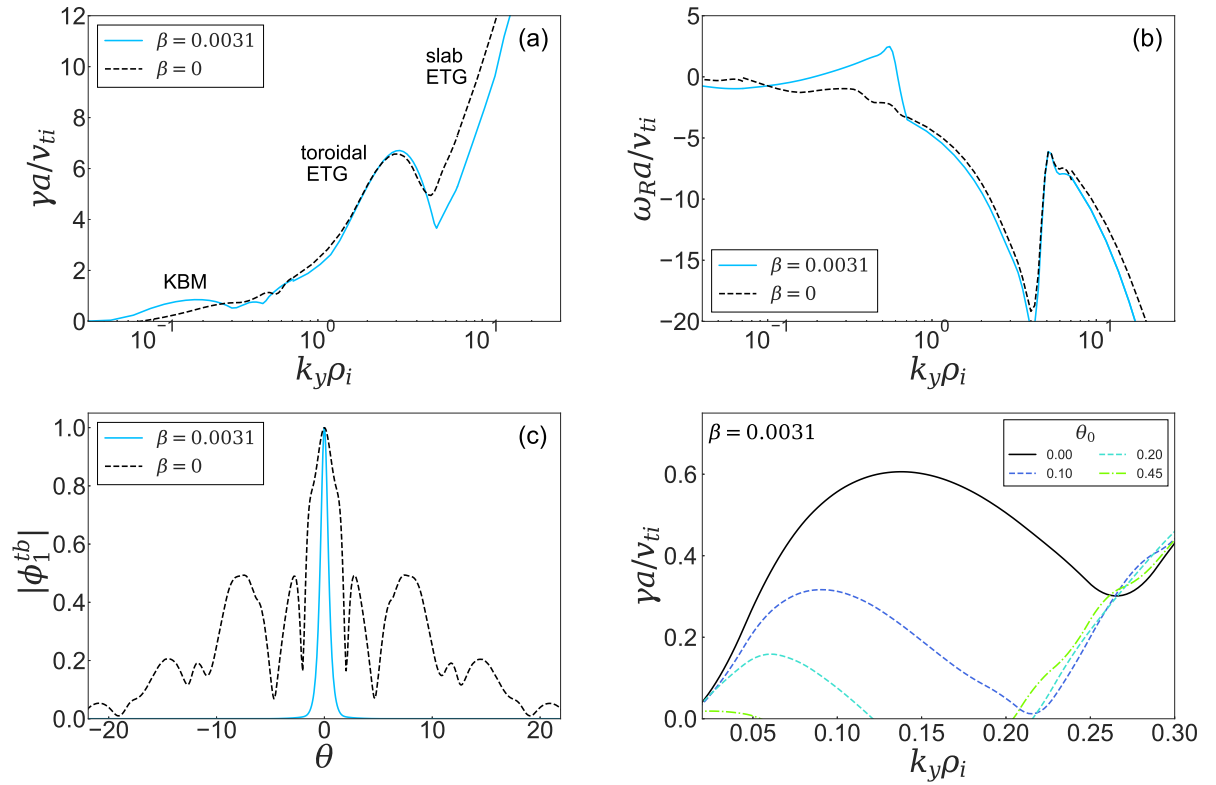


Figure 3.3: (a): GS2 growth rate ( $\gamma$ ) and (b): Real frequency ( $\omega_R$ ) for JET shot 92174 with  $\theta_0 = 0$  with and without finite  $\beta$ . (c): Eigenmodes for  $k_y \rho_i = 0.2$ . (d): Growth rates for an electromagnetic simulation with different  $\theta_0$  values at  $k_y \rho_i \sim 0.1$ . All of these simulations are performed without  $\mathbf{E} \times \mathbf{B}$  shear.

$k_x/\hat{s}k_y$ . Throughout this work, the eigenmodes are separately normalized such that  $|\phi_1^{tb}|$  has a maximum of 1. When finite  $\beta$  effects are included, a KBM appears, as shown by the small bump at  $k_y\rho_i \sim 0.1$  in Figure 3.3(a) of the growth rates. This KBM has a standard ballooning eigenmode structure, centered at  $\theta = \theta_0 = 0$ . However, when  $\beta = 0$ , there is no KBM, and instead at  $k_y\rho_i \sim 0.1$  there are modes with a much lower growth rate and a complicated mode structure in  $\theta$  (see Figure 3.3(c)). These eigenmodes tend to have maxima in bad curvature regions and can have either ballooning or tearing parity in both  $\text{Re}(\phi_1^{tb})$  and  $\text{Im}(\phi_1^{tb})$ . More details regarding these long wavelength electron modes can be found in Appendix B.

Much of the rest of the growth rate spectrum is quite unaffected by finite  $\beta$  effects. At  $k_y\rho_i \approx 1-5$  for  $\theta_0 = 0$ , there is a peculiar bump in Figure 3.3(a), whose corresponding instability will be the focus of much of this work. We identify this mode as toroidal ETG. We have undertaken extensive tests described later in Chapter 5 to confirm that it is a novel type of toroidal ETG; for now, we will refer to it as a toroidal ETG mode without justification. Finally, for  $k_y\rho_i \gtrsim 5$  and  $\theta_0 = 0$ , the fastest growing mode becomes a slab ETG mode, which again, we will justify later in Chapter 5. Clearly the toroidal ETG mode is almost entirely unaffected by finite  $\beta$ , and the slab ETG growth rates decrease by roughly 20%, but the mode structure is qualitatively the same. Thus, apart from the KBM, the electromagnetic and electrostatic growth rates and modes are very similar.

Once  $\mathbf{E} \times \mathbf{B}$  shear is included in the simulations, the electromagnetic and electrostatic growth rate spectra become qualitatively the same. This is because  $\mathbf{E} \times \mathbf{B}$  shear is found to easily suppress the KBM. Recall that the KBM is the main difference between the electromagnetic and electrostatic simulations without  $\mathbf{E} \times \mathbf{B}$  shear. Further evidence for the effectiveness of the  $\mathbf{E} \times \mathbf{B}$  shear for suppressing the KBM is that the KBM is stable for all  $|\theta_0| > \theta_{0c} \approx 0.5$ , as shown in Figure 3.3(d), where we show the growth rates for a range of  $\theta_0$  values at scales  $0.01 < k_y\rho_i < 0.3$  in a simulation with finite  $\beta$ . The dependence on  $\theta_0$  is important because  $\mathbf{E} \times \mathbf{B}$  shear causes a mode's radial wavenumber to vary with time as  $\Delta k_x = k_y\gamma_E t$ , giving a change in  $\theta_0$  of  $\Delta\theta_0 = \gamma_E t/\hat{s}$ . If a mode is shown to be unstable only for a very narrow range of  $\theta_0$  values,  $|\theta_0| < |\theta_{0c}|$ , it is highly susceptible to  $\mathbf{E} \times \mathbf{B}$  shear because in a time of order  $1/\gamma_E$  its  $\theta_0$  changes significantly. After a time  $t_C \sim \hat{s}\theta_{0c}/\gamma_E$ ,  $\mathbf{E} \times \mathbf{B}$  shear will have suppressed the KBM; in our simulations,

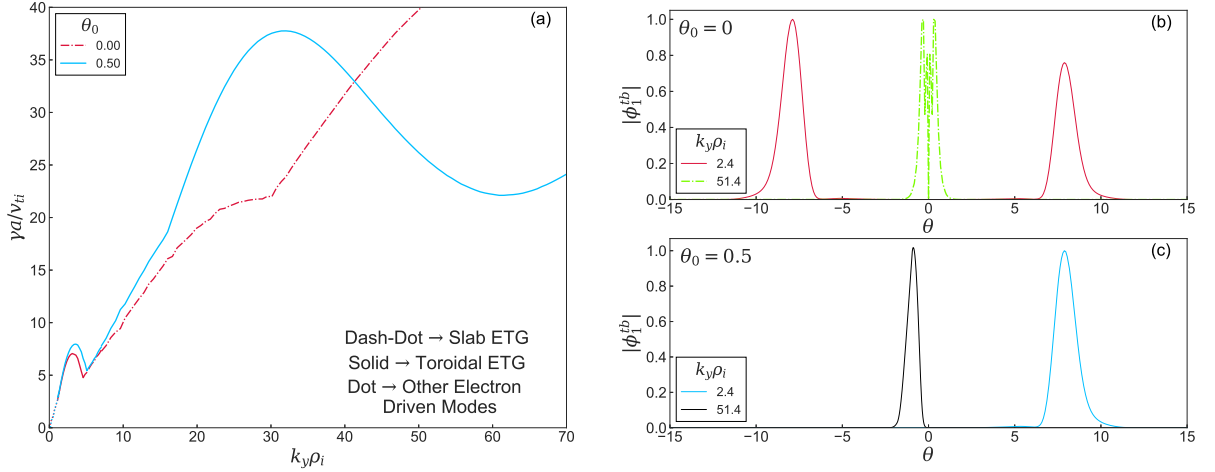


Figure 3.4: (a): Electrostatic growth rates for 2 values of  $\theta_0$ . (b): Eigenmodes for 2 values of  $k_y \rho_i$  at  $\theta_0 = 0$ . (c): Eigenmodes for 2 values of  $k_y \rho_i$  at  $\theta_0 = 0.5$ .

$t_C \approx 3$ . Thus, to suppress instability we require  $\gamma t_C \lesssim 1$ , leading to  $\gamma_E / \hat{s} \gamma \gtrsim \theta_{0c} \approx 0.5$ . We will discuss the  $\mathbf{E} \times \mathbf{B}$  shear and its effects on all the other instabilities we find in more detail in Chapter 7. Until then, all simulations are performed without  $\mathbf{E} \times \mathbf{B}$  shear.

Finally, the perpendicular wavenumber of the KBM is close to the limit where local simulations are valid, which is when  $k_\perp \rho_i \gg 0.12$ , and hence, results from our KBM simulations should be viewed in the context of uncertainties that are present due to the value of  $k_\perp \rho_i$  for the KBM being close to this limit.

### 3.3 Linear Features of the Electrostatic Pedestal

In this section, we describe the most prominent features of the electrostatic growth rate spectrum.

A notable feature of the growth rate spectrum shown earlier in Figure 3.3 is the bump at  $k_y \rho_i \approx 1 - 5$  in Figure 3.3(a), which we claimed was a novel toroidal ETG instability. In Figure 3.4(a), we show the growth rates for two values of  $\theta_0$ . Focusing first on  $\theta_0 = 0$ , we again identify the bump at  $k_y \rho_i \approx 1 - 5$ , which has a peak growth rate at  $k_y \rho_i \simeq 3$ . Once  $k_y \rho_i \gtrsim 5$ , the mode switches to a slab ETG instability. In Figure 3.4(b), we show the eigenmodes for two  $k_y \rho_i$  values in the  $\theta_0 = 0$  growth rate spectrum, one at  $k_y \rho_i = 2.4$  (near the top of the toroidal ETG bump) and one at  $k_y \rho_i = 51.4$ . The eigenmode associated with  $k_y \rho_i = 2.4$  is fairly localized at large  $\theta$ , whereas the eigenmode

associated with  $k_y \rho_i = 51.4$  is centered at  $\theta = 0$  and has a large parallel wavenumber. The  $k_y \rho_i = 2.4$  mode is the novel toroidal ETG mode, and the  $k_y \rho_i = 51.4$  mode is a slab ETG mode. In our up-down symmetric equilibrium fit, there is a subtlety for the novel toroidal ETG eigenmodes when  $\theta_0 = 0$ : there are two independent modes that grow at the same rate, and are localized at opposite signs of  $\theta$ . Indeed, for toroidal ETG, there must be two independent modes with  $\theta_0 = 0$ , since the linear gyrokinetic equation is invariant under the transformation  $\theta \rightarrow -\theta$ ,  $\theta_0 \rightarrow -\theta_0$  [105]. Thus, henceforth, when plotting the eigenmodes for  $\theta_0 \simeq 0$ , we choose a small value of  $\theta_0$ ,  $\theta_0 = 0.05$ , which causes the mode at one location to grow slightly faster than the mode at the other, but barely changes the growth rate compared with  $\theta_0 = 0$ . This results in a well-defined single eigenmode, like one we will show later in Figure 5.1(a), rather than two separate modes, like the ones shown in Figure 3.4(b). The relative size and phase of the modes at opposite values of  $\theta$  depend on the initial condition.

To distinguish between the toroidal and slab ETG modes in Figure 3.3(a) and Figure 3.4(a), we used a set of criteria discussed extensively in Section 5.1. Briefly, the toroidal ETG eigenmodes are localized far along the field line for smaller  $k_y \rho_i$  values, and are at a  $\theta$  location with the opposite sign of  $\theta_0$  for larger  $k_y \rho_i$  values. Sensitivity scans to equilibrium parameters, shown in Figure 5.3 (see Chapter 5), reveal that the slab and toroidal ETG branches have different dependences on parameters such as  $R_0/L_{Ti}$  and  $R_0/L_n$ . For a given  $k_y \rho_i$ , slab ETG modes also tend to have a much larger  $k_{\parallel}$  than toroidal ETG modes.

While the novel toroidal ETG mode is the fastest growing instability for  $1 \lesssim k_y \rho_i \lesssim 5$  when  $\theta_0 = 0$ , we find that when  $\theta_0$  differs slightly from 0, the toroidal ETG mode is the fastest growing for  $1 \lesssim k_y \rho_i \lesssim 400$ . We show a simple example of the growth rate spectrum for  $\theta_0 = 0.5$  in Figure 3.4(a), where the toroidal ETG mode is the fastest growing mode for that particular value of  $\theta_0$  for all  $k_y \rho_i \gtrsim 1$ . In Figure 3.4(c), we show the eigenmodes for  $\theta_0 = 0.5$  for  $k_y \rho_i = 2.4$  and  $k_y \rho_i = 51.4$ . For  $k_y \rho_i = 2.4$ , the eigenmodes for  $\theta_0 = 0$  and  $\theta_0 = 0.5$  have a similar structure, both being localized at  $|\theta| \simeq 8$ . However, the eigenmode at  $k_y \rho_i = 51.4$  is dramatically different to the  $\theta_0 = 0$  mode at  $k_y \rho_i = 51.4$ ; the eigenmode for  $\theta_0 = 0.5$  is localized at  $\theta \simeq -1$ , and has, in fact, the same novel toroidal ETG character we identified earlier. In Chapter 5 we will

explain these toroidal ETG modes in much more detail, including the reasons why they move in  $\theta$  for different values of  $k_y\rho_i$ , as evidenced by the eigenmodes for  $\theta_0 = 0.5$  at  $k_y\rho_i = 2.4$  and  $k_y\rho_i = 51.4$ .

For completeness, we briefly describe the modes we find at larger scales. For this JET discharge and the surface  $r/a = 0.9743$ , we find that the instabilities are electron-driven between  $0.005 \lesssim k_y\rho_i \lesssim 400$ . For  $0.005 \lesssim k_y\rho_i \lesssim 0.07$  the modes have electron tails similar to those described in [106], and for  $0.1 \lesssim k_y\rho_i \lesssim 1.0$ , there are complicated modes that appear to be a form of ETG we do not yet fully understand. Both the electron tails and complicated ETG modes will be excluded from in-depth analysis in the main text, but are described in Appendix B.

In the next chapter, we introduce the theory needed to understand these novel toroidal ETG modes as well as the slab ETG modes at  $k_y\rho_i \gtrsim 1$ . We will see that the existence of these modes follows naturally from the steep temperature gradients in pedestals.

# Chapter 4

## Linear Gyrokinetics With Large Gradients

In this section, we analyze the consequences of large equilibrium gradients for linear collisionless electrostatic gyrokinetic stability, which will considerably change the character of the toroidal ETG instability. We have already motivated the local and linear limits in Chapter 2, and the electrostatic limit in Section 3.2. We now motivate the collisionless limit of the electron gyrokinetic equation, which will be used for the theoretical analysis.

The collisionless limit for electrons is justified by the small electron collision frequency,  $\nu_{ee} \ll \gamma$ . For JET shot 92174 at  $r/a = 0.9743$ ,  $\nu_{ee} \simeq 2.4 \times 10^5$  Hz, and  $\gamma \simeq 1.6 \times 10^6$  Hz for  $k_y \rho_i = 2$ . In gyrokinetic simulations, we found ETG instabilities to be relatively insensitive to whether collisions are kept. However, for ITG scale instabilities at lower frequencies, electron collisions can decrease the ITG growth rates and cause electrons to be non-adiabatic, as we will see in Chapter 6.

Using the equations laid out in Chapter 2, we take the linear electrostatic collisionless local limit of the gyrokinetic equation in Section 4.1. Analytically and computationally, this limit is more straightforward, and includes key elements of the pedestal microinstability linear physics that we wish to explain. Motivated by the steep pedestal gradients, we explore the implications of steep equilibrium temperature gradients on ETG instability in Section 4.2. Simple arguments based on balancing terms with the same order of magnitude reveal how these steep gradients affect the perpendicular scales of the instability and how magnetic shear determines the parallel toroidal ETG mode structure, allowing the toroidal ETG mode to compete with the slab ETG mode. In Section 4.3, we

convert the gyrokinetic equation derived in Section 4.1 to an algebraic equation in order to analyze slab and toroidal ETG instabilities in the presence of large equilibrium gradients. This is then used to derive an analytical ETG dispersion relation that supports our simplified arguments.

## 4.1 Electrostatic Collisionless Local Limit

In this section, we take the electrostatic, linear, collisionless limit of the gyrokinetic equation. In this limit, Equation (2.4) is

$$\begin{aligned} \frac{\partial \bar{h}_s}{\partial t} + v_{\parallel} \hat{\mathbf{b}} \cdot \nabla_{\mathbf{R}_s} \bar{h}_s + \mathbf{v}_{Ms} \cdot \nabla_{\mathbf{R}_s} \bar{h}_s &= \frac{Z_s e F_{Ms}}{T_{0s}} \frac{\partial \langle \bar{\phi}_1^{tb} \rangle}{\partial t} \\ &+ \frac{c}{B} (\nabla_{\mathbf{R}_s} \langle \bar{\phi}_1^{tb} \rangle \times \hat{\mathbf{b}}) \cdot \nabla r \left[ \frac{\partial \ln n_s}{\partial r} + \frac{\partial \ln T_s}{\partial r} \left( \frac{m_s \mathcal{E}}{T_{0s}} - \frac{3}{2} \right) \right] F_{Ms}. \end{aligned} \quad (4.1)$$

We have absorbed the toroidal mean flow in the convective derivative as a constant Doppler shift, and neglected the equilibrium  $\mathbf{E} \times \mathbf{B}$  shear, which is consistent with the low flow ordering in Equation (3.3), and is justified in Chapter 7 with simulation results.

Substituting the expressions for  $\phi_1^{tb}$  and  $h_s$  in Equations (2.12) and (2.13) into Equation (4.1) gives a Fourier-analyzed gyrokinetic equation,

$$\begin{aligned} -i\omega h_s + \frac{2\pi v_{\parallel}}{L_{\theta}} \frac{\partial h_s}{\partial \theta} + i\mathbf{v}_{Ms} \cdot \mathbf{k}_{\perp} h_s &= -i\omega \frac{Z_s e F_{Ms}}{T_{0s}} \phi_1^{tb} J_0 \left( \frac{k_{\perp} v_{\perp}}{\Omega_s} \right) \\ &+ i\omega_{*s} \left[ 1 + \eta_s \left( \frac{m_s \mathcal{E}}{T_{0s}} - \frac{3}{2} \right) \right] \frac{Z_s e F_{Ms}}{T_{0s}} \phi_1^{tb} J_0 \left( \frac{k_{\perp} v_{\perp}}{\Omega_s} \right), \end{aligned} \quad (4.2)$$

where  $J_0$  is a Bessel function of the first kind that comes from gyroaveraging  $\bar{\phi}_1^{tb}$ . The perpendicular wavenumber  $\mathbf{k}_{\perp}$  is

$$\begin{aligned} \mathbf{k}_{\perp} = k_x \nabla x + k_y \nabla y &= \left[ k_x - k_y \left( \hat{s}\theta - \frac{r}{q} \frac{\partial \nu}{\partial r} \right) \right] \nabla x \\ &+ \frac{\partial \psi}{\partial r} \frac{1}{B_a} k_y \left[ \nabla \zeta + \left( \frac{\partial \nu}{\partial \theta} - q \right) \nabla \theta \right], \end{aligned} \quad (4.3)$$

where every function is evaluated at  $r_c$ . We have also introduced the drift frequency,  $\omega_{*s}$ , and the stability parameter,  $\eta_s$ ,

$$\omega_{*s} \equiv -\frac{c}{B} \frac{T_{0s}}{Z_s e L_{ns}} (\mathbf{k}_{\perp} \times \hat{\mathbf{b}}) \cdot \nabla r = \frac{c}{B_a} \frac{T_{0s}}{Z_s e L_{ns}} k_y, \quad \eta_s \equiv \frac{L_{ns}}{L_{Ts}}. \quad (4.4)$$

Note that the factor  $(\mathbf{k}_\perp \times \hat{\mathbf{b}}) \cdot \nabla r$  in  $\omega_{*s}$  is only proportional to  $k_y$ . The system of equations is closed by the first order turbulent quasineutrality condition in Equation (2.7),

$$\begin{aligned} \frac{e\phi_1^{tb}n_{0e}}{T_{0e}} \left( \frac{Z_i T_{0e}}{T_{0i}} + 1 \right) + 2\pi \int \frac{B}{|v_\parallel|} h_e J_0 \left( \frac{k_\perp v_\perp}{\Omega_e} \right) d\mathcal{E} d\mu \\ - 2\pi \int \frac{B}{|v_\parallel|} h_i J_0 \left( \frac{k_\perp v_\perp}{\Omega_i} \right) d\mathcal{E} d\mu = 0, \end{aligned} \quad (4.5)$$

where we used that  $\mathcal{J} = \partial(\mathbf{r}, \mathbf{v})/\partial(\mathbf{R}, \mathcal{E}, \mu, \varphi) \simeq B/|v_\parallel|$  is the Jacobian of the gyrokinetic transformation [88].

We proceed to demonstrate how the presence of large equilibrium gradients changes the perpendicular scales at which ETG can be strongly driven, and how in the presence of these steep gradients, magnetic shear can act to determine the poloidal location where the ETG mode has its maximum amplitude.

## 4.2 Slab Versus Toroidal ETG In Large Gradient Regions

In this section, we describe a novel type of toroidal ETG with anisotropic perpendicular wavenumbers. Equations (4.2) and (4.5) contain two branches of electron temperature gradient driven instability, slab [27, 28] and toroidal [107, 108]. These modes have been covered extensively [27, 28, 30, 33, 107, 108]. Here, we give a very brief overview. In the slab branch, the density perturbation is caused by a competition between the parallel streaming and the radial  $\mathbf{E} \times \mathbf{B}$  drift. For sufficiently large  $\eta_s$ , a large parallel compression causes  $\phi_1^{tb}$  to grow in time. For smaller values of  $\eta_s$ , the radial  $\mathbf{E} \times \mathbf{B}$  drift term dominates and we obtain stable electron drift waves. The toroidal instability is caused by magnetic drifts, rather than parallel streaming, creating a compression that again, gives rise to a destabilizing electric field for sufficiently large  $\eta_s$ . In both cases, at the onset of instability, increasing the temperature gradients causes the linear instability to be more virulent.

Motivated by the large temperature gradients in Figure 3.1(b), we proceed to demonstrate that

$$\frac{R_0}{L_{Te}}, \frac{R_0}{L_{Ti}} \gg 1, \quad (4.6)$$

has major implications for ETG stability. First, we present an intuitive, albeit non-rigorous argument that will turn out to be incorrect. We then develop a more careful argument, which reveals the distinctive new character of ETG modes in steep gradients, which is very different to the more familiar lower gradient regime typical of the core. Throughout this section, we shall assume that  $\theta_0 = 0$ . We will investigate the physics of  $\theta_0 \neq 0$  in Chapter 5.

First, we present the intuitive, albeit incorrect argument. For the electrons, since  $R_0/L_{Te} \gg 1$ , we naively expect that the ratio determining the relative strength of the drive frequency to the magnetic drift frequency to be large. Therefore, in the pedestal, one might naively think that the drive for toroidal ETG is weak and independent of  $k_\perp$ ,

$$\frac{\omega_{*e}\eta_e}{\mathbf{v}_{Me} \cdot \mathbf{k}_\perp} \sim \frac{R_0}{L_{Te}} \gg 1. \quad (4.7)$$

Here, we use  $\mathbf{v}_{Me} \cdot \mathbf{k}_\perp \sim k_\perp v_{te}^2/\Omega_e R_0$  and  $k_y \sim k_\perp$ . Comparing the size of the drive frequency to the parallel streaming frequency, we obtain

$$\frac{\omega_{*e}\eta_e}{k_\parallel v_{te}} \sim \frac{k_y}{k_\parallel} \frac{\rho_e}{L_{Te}}. \quad (4.8)$$

As we will show in Section 4.3, the ratios in Equations (4.7) and (4.8) must be of order unity for a large toroidal and slab ETG growth rate, respectively (see Figure 4.3). Thus, Equation (4.7) suggests that the magnetic drifts are small for every  $k_\perp$ , whereas in Equation (4.8),  $k_\parallel$  can become large to drive slab instability. One would therefore expect slab ETG to be the dominant electron microinstability at all scales.

The above argument, however, suffers from a deficiency. It is naive to make the assumption  $\omega_{*e}\eta_e/\mathbf{v}_{Me} \cdot \mathbf{k}_\perp \sim R_0/L_{Te}$  (see Equation (4.7)) in the presence of magnetic shear, because  $\mathbf{k}_\perp$  varies along a field line (see Equation (4.3)). At large values of  $|\theta|$ , the *radial* component of the magnetic drift frequency becomes increasingly large and can compete with the linear drive  $\omega_{*e}\eta_e$ , to allow the toroidal branch to become unstable. Toroidal modes, with  $\mathbf{v}_{Me} \cdot \mathbf{k}_\perp \sim \omega_{*e}\eta_e$ , are therefore possible because the competition between the slab and toroidal modes has a  $\mathbf{k}_\perp$  dependence, which arises from the fact that  $\mathbf{v}_{Me} \cdot \mathbf{k}_\perp$  depends on both  $k_x$  and  $k_y$ , whereas  $\omega_{*e}$  only depends on  $k_y$ . For convenience, we define the radial component of  $\mathbf{k}_\perp$  in Equation (4.3) as

$$K_x = k_x - k_y \left( \hat{s}\theta - \frac{r}{q} \frac{\partial \nu}{\partial r} \right). \quad (4.9)$$

We now show that toroidal ETG modes with  $k_\perp \sim K_x \gg k_y$  can indeed compete with the slab ETG at sufficiently small  $k_y \rho_i$ . Motivated by the eigenmodes in Figure 3.4 that are localized far along a field line, we will make  $K_x$  large by taking  $\hat{s}\theta \gg k_x/k_y = \hat{s}\theta_0$  and  $\hat{s}\theta \gg (r/q)\partial\nu/\partial r$ . Thus, for  $\hat{s}\theta$  large, we find

$$k_\perp \sim K_x \sim k_y \hat{s}\theta. \quad (4.10)$$

When we compare the size of  $\hat{s}\theta$  to other terms, we are actually comparing  $|\hat{s}\theta|$ ; for ease of notation, we will drop the modulus signs, but will continue to compare the absolute value. According to Equation (4.10), for  $\hat{s}\theta \gg 1$ , the magnetic drift term that drives toroidal ETG can become comparable to the drive term,

$$\frac{\omega_{*e}\eta_e}{\mathbf{v}_{Me} \cdot \mathbf{k}_\perp} \sim \frac{k_y R_0}{k_\perp L_{Te}} \sim \frac{1}{\hat{s}\theta} \frac{R_0}{L_{Te}} \sim 1. \quad (4.11)$$

Thus, for sufficiently small  $k_x$ , the toroidal mode must be driven far along the field line,

$$\hat{s}\theta \sim \frac{R_0}{L_{Te}} \gg 1. \quad (4.12)$$

Through detailed analysis in later sections, we will indeed see that this explains the toroidal ETG modes, which are often unstable at large distances along the field line (see Figure 3.4). Recall that here  $\theta$  is the ballooning coordinate, which has a range  $-\infty < \theta < \infty$ .

When Equation (4.11) is satisfied, we will demonstrate with a local gyrokinetic dispersion relation in Section 4.3 that when  $\mathbf{v}_{Me} \cdot \mathbf{k}_\perp \sim \omega_{*e}\eta_e$ , the toroidal ETG growth rate becomes comparable to the slab ETG growth rate. This would seem to suggest that toroidal ETG exists for all  $k_y$ . However, for large  $k_y$  and small  $k_x$ ,  $k_\perp \rho_e \sim \hat{s}\theta k_y \rho_e$  becomes so large that FLR effects from the electron gyromotion become important. Thus, if  $R_0/L_{Te} \gg 1$  and  $\hat{s}\theta \gg 1$ , for strongly driven toroidal ETG,  $K_x$  has a maximum of the order of

$$K_x \rho_e \sim \hat{s}\theta k_y \rho_e \sim 1. \quad (4.13)$$

If  $K_x \rho_e$  is much larger than in Equation (4.13), the growth rate will be strongly reduced by electron FLR effects. Motivated by Equation (4.13), for a toroidal ETG mode we expect ion FLR damping to be very strong at  $k_y \rho_e \ll 1$  with  $k_\perp \rho_e \sim 1$ . Thus, our

analytic treatment of toroidal ETG will assume  $h_i = 0$  because  $|J_0(k_\perp \rho_i)| \ll 1$  when  $k_\perp \rho_i \gg 1$ . Using Equations (4.11) and (4.13), we obtain a scale for  $k_y$ ,

$$k_y \rho_e \sim \frac{L_{Te}}{R_0}. \quad (4.14)$$

Given that the pedestal profiles have  $R_0/L_{Te} \gtrsim \rho_i/\rho_e$  in the steep pedestal regions, toroidal ETG can be unstable even at scales as large as  $k_y \rho_i \lesssim 1$ . Therefore,  $R_0/L_{Te} \gg 1$  extends the minimum  $k_y$  scale at which toroidal ETG modes can be strongly driven to ion gyroradius scales or larger.

To obtain the parallel width of a toroidal ETG mode  $\Delta\theta$ , we balance the parallel streaming term with the change in the magnetic drift over the mode width,

$$\frac{v_{te}}{qR_0} \frac{\partial h_e}{\partial \theta} \sim \Delta\theta \frac{\partial}{\partial \theta} (\mathbf{k}_\perp \cdot \mathbf{v}_{Me}) h_e. \quad (4.15)$$

This is based on the conjecture that the magnetic drift profiles limit the parallel width of the mode. The quantity  $\Delta\theta$  captures the width of the mode envelope, rather than the oscillations within it, which would be captured by  $k_\parallel$ . Note that we do not require that  $\Delta\theta \ll 1$ , because Equation (4.15) can be justified using the Mean Value Theorem, given that  $\partial/\partial\theta(\mathbf{k}_\perp \cdot \mathbf{v}_{Me})$  is evaluated at an appropriate location. We can obtain a scaling for the mode width by first assuming that

$$\frac{\partial h_e}{\partial \theta} \sim \frac{h_e}{\Delta\theta}, \quad \frac{\partial}{\partial \theta} (\mathbf{k}_\perp \cdot \mathbf{v}_{Me}) \sim \mathbf{k}_\perp \cdot \mathbf{v}_{Me}. \quad (4.16)$$

Because  $\Delta\theta$  is the mode width associated with  $h_e$ , it follows that  $\partial h_e/\partial\theta \sim h_e/\Delta\theta$ . We order  $\partial/\partial\theta(\mathbf{k}_\perp \cdot \mathbf{v}_{Me}) \sim \mathbf{k}_\perp \cdot \mathbf{v}_{Me}$  as it satisfies the equilibria we examine. Next, we assume that magnetic drifts balance the drive frequency, as in Equation (4.11),

$$\mathbf{k}_\perp \cdot \mathbf{v}_{Me} \sim \omega_{*e} \eta_e. \quad (4.17)$$

Combining Equations (4.16) and (4.17), we obtain a scaling for the mode width,

$$\Delta\theta \sim \sqrt{\frac{v_{te}}{qR_0\omega_{*e}\eta_e}} \sim \sqrt{\frac{1}{qk_y\rho_e} \frac{L_{Te}}{R_0}}, \quad (4.18)$$

where we use  $\omega_{*e}\eta_e \sim k_y\rho_e v_{te}/L_{Te}$ . Hence, higher values of  $R_0/L_{Te}$ ,  $k_y\rho_e$ , and  $q$  make the mode narrower. Using  $\hat{s}\theta \sim R_0/L_{Te}$ , we obtain

$$\frac{\Delta\theta}{\theta} \sim \hat{s} \sqrt{\frac{1}{qk_y\rho_e} \left(\frac{L_{Te}}{R_0}\right)^{3/2}}. \quad (4.19)$$

In the pedestal, the quantity  $\Delta\theta/\theta$  is small, whereas in the core,  $\Delta\theta/\theta$  is of order unity. Results from gyrokinetic scans in  $q$ ,  $R_0/L_{Te}$  and  $k_y\rho_e$  are in fair agreement with the scalings in Equation (4.18). We report these scans in Chapter 5.

To summarize thus far, pedestal toroidal ETG — where  $R_0/L_{Te} \gg 1$  — has a very different character to core toroidal ETG — where  $R_0/L_{Te} \sim 1$ . In the pedestal, toroidal ETG can be driven strongly at wavenumbers as small as  $k_y\rho_e \sim L_{Te}/R_0 \ll 1$ , but with a large effective radial wavenumber  $K_x\rho_e \sim 1$ , due to the mode being driven far along the field line,  $\hat{s}\theta \sim R_0/L_{Te} \gg 1$ . For pedestal toroidal ETG, the radial component of the magnetic drift is essential for instability. In contrast, core toroidal ETG only becomes unstable at much larger poloidal wavenumbers  $k_y\rho_e \sim 1$ , and has a much smaller radial wavenumber  $K_x\rho_e \ll 1$  due to  $\theta \approx 0$ . For core toroidal ETG, the in-surface poloidal magnetic drift is essential to the instability drive.

In Figure 4.1, we show the physical picture for the pedestal toroidal ETG instability. This can be compared with the standard toroidal ETG instability in Figure 1.6, which has  $K_x = 0$ .

Slab ETG is also shifted to larger perpendicular scales by  $R_0/L_{Te} \gg 1$ . Re-examining Equation (4.8), and requiring a strong slab drive,

$$\frac{\omega_{*e}\eta_e}{k_{\parallel}v_{te}} \sim \frac{k_y\rho_e}{k_{\parallel}R_0} \frac{R_0}{L_{Te}} \sim 1. \quad (4.20)$$

Thus, the scale for which slab ETG can be strongly driven is

$$k_y\rho_e \sim k_{\parallel}R_0 \frac{L_{Te}}{R_0}. \quad (4.21)$$

We place bounds on  $k_y\rho_e$  for the ‘pure’ slab ETG branch by considering two linear effects that can constrain the parallel mode extent. The first constraint on the slab ETG mode is that the mode is not too strongly FLR damped, which according to Equation (4.13), requires

$$\theta \lesssim \theta_{\max} = \frac{1}{\hat{s}} \frac{1}{k_y\rho_e}. \quad (4.22)$$

A mode that oscillates only a few times before reaching  $\theta_{\max}$  has a parallel wavenumber  $k_{\parallel} \sim k_y\rho_e\hat{s}/qR_0$ . Using Equation (4.21), we find that such a mode would have  $R_0/L_{Te} \sim \hat{s}/q$ . Electron temperature gradients smaller than this value would be FLR damped. Since the gradients in the pedestal satisfy  $R_0/L_{Te} \gg \hat{s}/q$ , we conclude that the FLR

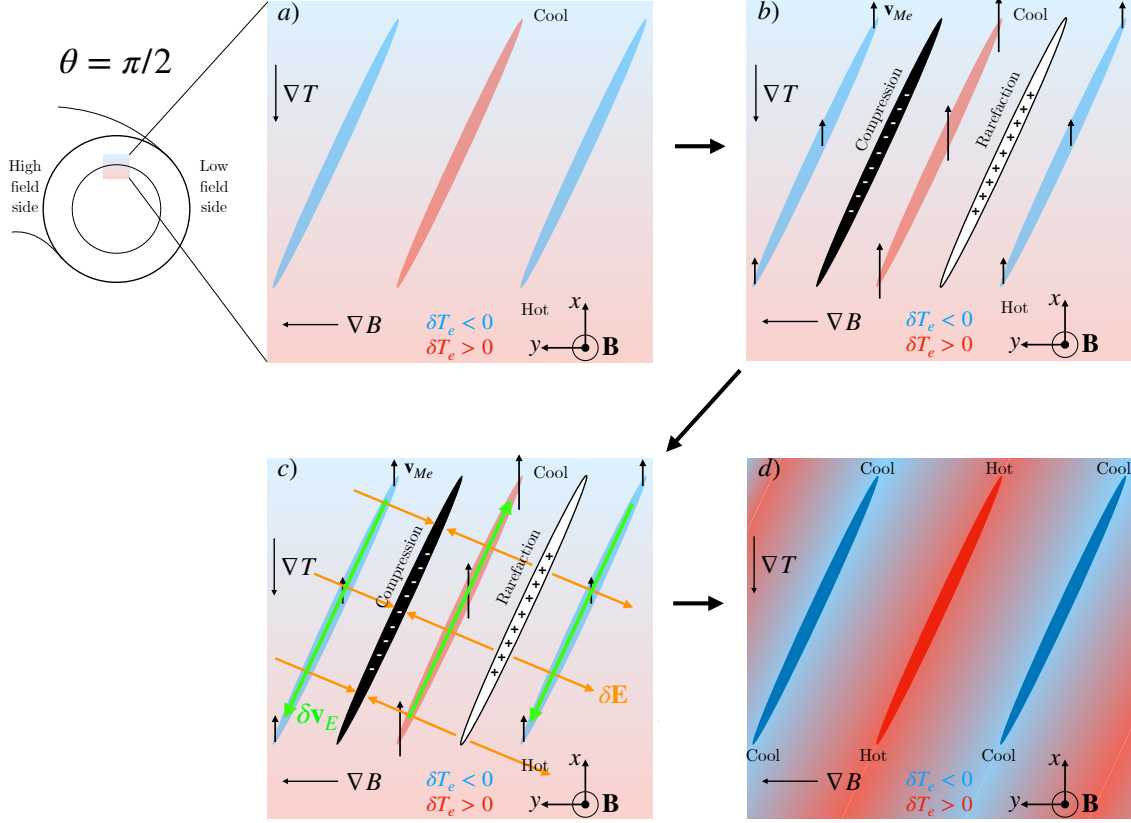


Figure 4.1: Mechanism for the pedestal toroidal ETG instability. (a) At  $\theta = \pi/2$ , consider a wave with both a poloidal and radial wavenumber, which creates regions of slightly hotter and colder temperature perturbations,  $\delta T_e$ , as shown by the red and blue contours. (b) The electron magnetic drift is larger in the regions where  $\delta T_e > 0$  and smaller where  $\delta T_e < 0$ . This causes regions where the plasma is compressed and regions in which it is rarified. In compressed regions there will be a net negative electric charge and in rarified regions a net positive electric charge. (c) The charge overdensities and underdensities create a perturbed electric field  $\delta \mathbf{E}$ , which creates a perturbed  $\mathbf{E} \times \mathbf{B}$  drift,  $\delta \mathbf{v}_E$ . This causes hot plasma to be sucked into the regions where  $\delta T_e > 0$ , and cool plasma to be sucked into the regions where  $\delta T_e < 0$ , creating a positive feedback loop. This creates the unstable state in (d), which will become turbulent. Note that this instability cannot occur without a radial wavenumber. Hence, the standard toroidal ETG instability, which relies on the  $y$  component of the magnetic drift, will be stable without a sufficiently large value of  $K_x$ .

damping constraint on the electron temperature gradient for the slab ETG mode is irrelevant in pedestals.

The second constraint on the slab ETG mode determines how far the mode can extend in the parallel direction while still retaining a parallel streaming frequency that is faster than the magnetic drift frequency. From Equation (4.11), the largest  $\theta$  value a mode can have before  $\mathbf{v}_{Me} \cdot \mathbf{k}_\perp$  and  $\omega_{*e}\eta_e$  become comparable is

$$\theta \lesssim \frac{1}{\hat{s}} \frac{R_0}{L_{Te}}. \quad (4.23)$$

A mode that oscillates only a few times before reaching this value of  $\theta$  has a parallel wavenumber of order

$$k_\parallel \sim \frac{\hat{s}}{qR_0} \frac{L_{Te}}{R_0}. \quad (4.24)$$

A slab ETG mode with such a  $k_\parallel$  is the mode with the smallest  $k_y\rho_e$  value because, for smaller values of  $k_y\rho_e$ , the mode would have to extend into the region of  $\theta$  where the magnetic drift is large. Thus, due to the magnetic drift condition, slab ETG modes must satisfy

$$k_y\rho_e \gtrsim \frac{\hat{s}}{q} \left( \frac{L_{Te}}{R_0} \right)^2. \quad (4.25)$$

Then, for a fast-growing ‘pure’ slab ETG mode, we require

$$\frac{\hat{s}}{q} \left( \frac{L_{Te}}{R_0} \right)^2 \lesssim k_y\rho_e \lesssim 1. \quad (4.26)$$

Even though our simple estimates suggest that slab ETG modes can grow for wavenumbers as small as  $k_y\rho_e \sim (\hat{s}/q)(L_{Te}/R_0)^2 \sim 1/30000$ , we should point out that kinetic ion physics is important at such large scales, and hence the slab ETG will be modified at these very long wavelengths.

In principle, the above arguments are also valid for toroidal and slab ITG in the collisionless limit with identical gradients. However, in the JET pedestal equilibrium we have studied,  $R_0/L_{Te} > R_0/L_{Ti}$ , which causes the ITG growth rates to decrease substantially. Furthermore, in the pedestal the electrons are sufficiently collisional to be non-adiabatic on ITG timescales; as we will show in Chapter 6, these electron collisions also decrease the ITG growth rate. Indeed, we will see that the less steep measured ion temperature gradients and collisions result in ITG being the subdominant mode

at all scales. For  $k_y \rho_i \lesssim 1$ , ITG is likely stable, and hence we do not expect ITG to cause significant transport in the equilibrium and radial location studied in this work. For other JET pedestal equilibria that we studied in less detail, it was also true that  $R_0/L_{Te} > R_0/L_{Ti}$  in the steep gradient region; these equilibria had qualitatively similar growth rate spectra to the equilibrium studied in this work (see Appendix A).

We now proceed to obtain an ETG dispersion relation using the approximations in the previous sections. Its solutions will provide useful insights on toroidal ETG stability, which will be used heavily in subsequent sections.

### 4.3 ETG Dispersion Relation

Formally solving Equation (4.2) for  $h_s$  gives

$$h_s = \frac{-\widehat{\omega}_s + \widehat{\omega}_{*s} \left[ 1 + \eta_s \left( \widehat{v}_{\parallel}^2 + \widehat{v}_{\perp}^2 - 3/2 \right) \right]}{-\widehat{\omega}_s + \widehat{k}_{\parallel s} \widehat{v}_{\parallel} + \sigma \widehat{v}_{\parallel}^2 + \widehat{\omega}_{\nabla B s} \widehat{v}_{\perp}^2 / 2} \frac{Z_s e}{T_{0s}} \phi_1^{tb} F_{Ms} J_0 \left( \sqrt{2b_s} \widehat{v}_{\perp} \right), \quad (4.27)$$

where we replace the parallel operator with  $k_{\parallel}$ , which is a number,

$$ik_{\parallel} h_s \equiv \widehat{\mathbf{b}} \cdot \nabla h_s, \quad (4.28)$$

and we define  $b_s$  and  $\widehat{v}$  as

$$b_s = \frac{k_{\perp}^2 T_{0s}}{m_s \Omega_s^2}, \quad \widehat{v} = \frac{v}{v_{ts}}. \quad (4.29)$$

We have non-dimensionalized quantities using the modulus of the curvature magnetic drift frequency  $\omega_{\kappa s}$ ,

$$\sigma \equiv \frac{\omega_{\kappa s}}{|\omega_{\kappa s}|}, \quad \widehat{\omega} \equiv \frac{\omega}{|\omega_{\kappa s}|}, \quad \widehat{\omega}_{\nabla B s} \equiv \frac{\omega_{\nabla B s}}{|\omega_{\kappa s}|}, \quad \widehat{\omega}_{*s} \equiv \frac{\omega_{*s}}{|\omega_{\kappa s}|}, \quad \widehat{k}_{\parallel} \equiv \frac{k_{\parallel} v_{ts}}{|\omega_{\kappa s}|}, \quad (4.30)$$

where

$$\omega_{\kappa s} \equiv \frac{v_{ts}^2 \mathbf{k}_{\perp}}{\Omega_s} \cdot \left( \widehat{\mathbf{b}} \times \left( \nabla \ln B + \frac{4\pi}{B^2} \frac{\partial p_0}{\partial r} \nabla r \right) \right), \quad \omega_{\nabla B s} \equiv \frac{v_{ts}^2 \mathbf{k}_{\perp}}{\Omega_s} \cdot (\widehat{\mathbf{b}} \times \nabla \ln B). \quad (4.31)$$

We write the total magnetic drift frequency as

$$\mathbf{v}_{Ms} \cdot \mathbf{k}_{\perp} = \omega_{\kappa s} \widehat{v}_{\parallel}^2 + \omega_{\nabla B s} \frac{\widehat{v}_{\perp}^2}{2}. \quad (4.32)$$

It is important to note that Equation (4.27) is valid for any value of  $\theta_0$ , since in this work we are paying particular attention to the radial component of  $\mathbf{k}_{\perp}$  (see Equation (4.3))

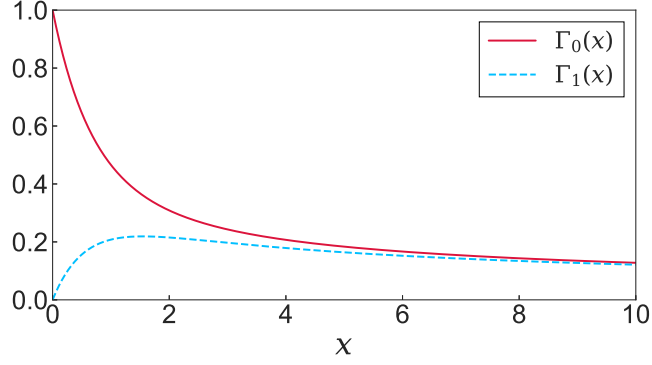


Figure 4.2: The functions  $\Gamma_0$  and  $\Gamma_1$  that appear in Equation (4.34).

due to its importance for the toroidal ETG instability in steep temperature gradient regions. Thus,  $b_s$ ,  $\omega_{\kappa s}$ , and  $\omega_{\nabla B_s}$  depend on  $\theta_0$ ; this differs from many previous works where only the  $\nabla y$  component of the magnetic drift frequency was retained.

As a simplified model, we will take  $k_{\parallel}$  to be a number. We obtain the ETG dispersion relation by substituting Equation (4.27) into quasineutrality, as demonstrated in Appendix C. For a single ion species, this gives

$$\frac{T_{0e}}{T_{0i}} Z_i + 1 - \sum_s D_s = 0, \quad (4.33)$$

where  $D_s$  is given by

$$D_s = iZ_s^2 \frac{T_{0e} n_{0s}}{T_{0s} n_{0e}} \int_0^{\infty} d\lambda \frac{\Gamma_0(\hat{b}_s^{\sigma})}{(1+i\sigma\lambda)^{1/2}} \frac{1}{(1+i\hat{\omega}_{\nabla B_s}\lambda/2)} \exp\left(i\lambda\hat{\omega} - \frac{(\lambda\hat{k}_{\parallel})^2}{4(1+i\sigma\lambda)}\right) \\ \times \left[ -\hat{\omega} + \hat{\omega}_{*s} \left( 1 + \eta_s \left\{ \frac{1}{1+i\hat{\omega}_{\nabla B_s}\lambda/2} - \frac{3}{2} \right. \right. \right. \\ \left. \left. \left. + \frac{2(1+i\sigma\lambda) - (\hat{k}_{\parallel}\lambda)^2}{4(1+i\sigma\lambda)^2} - \hat{b}_s^{\sigma} \frac{1 - \Gamma_1(\hat{b}_s^{\sigma})/\Gamma_0(\hat{b}_s^{\sigma})}{1+i\hat{\omega}_{\nabla B_s}\lambda/2} \right\} \right) \right]. \quad (4.34)$$

The functions  $\Gamma_{\nu}$  and  $\hat{b}_s^{\sigma}$  are defined as

$$\Gamma_{\nu}(x) = I_{\nu}(x) \exp(-x), \quad \hat{b}_s^{\sigma} \equiv \frac{b_s}{1+i\hat{\omega}_{\nabla B_s}\lambda/2}, \quad (4.35)$$

where  $I_{\nu}$  is a modified Bessel function of the first kind. We plot  $\Gamma_0$  and  $\Gamma_1$  in Figure 4.2; the function  $\Gamma_0$  will be used extensively in this work.

We have numerically solved Equation (4.33) in the adiabatic ion limit,  $h_i = 0$ ,

$$\frac{T_{0e}}{T_{0i}} Z_i + 1 - D_e = 0. \quad (4.36)$$

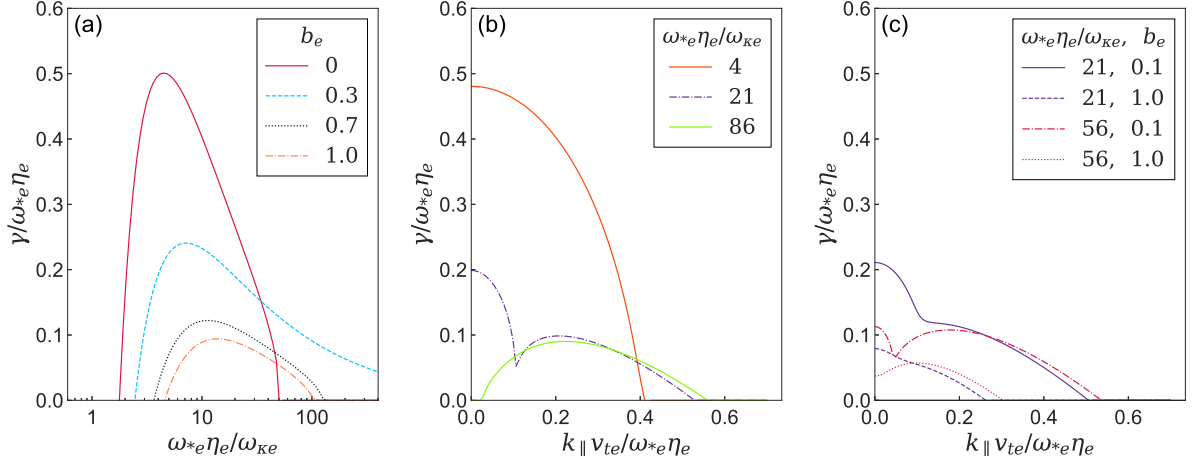


Figure 4.3: Solutions to Equation (4.36) with  $\eta_e = 4.28$ . (a): Growth rates for different  $\omega_{*e}\eta_e$  and  $b_e$  with  $k_{\parallel} = 0$ . (b): Growth rates versus  $k_{\parallel}$  for different values of  $\omega_{*e}/\omega_{\kappa e}$  with  $b_e = 0$  and  $\omega_{\kappa e} > 0$ . (c): Growth rates  $k_{\parallel}$  for different values of  $\omega_{*e}/\omega_{\kappa e}$  and  $b_e$ . Here, we set  $\omega_{\kappa e} = \omega_{\nabla B_e}$ . In (a), we only plot the growth rate for  $\omega_{*e}\eta_e/\omega_{\kappa e} > 0$  because we find that all solutions are damped for  $\omega_{*e}\eta_e/\omega_{\kappa e} < 0$ .

We justify setting  $D_i = 0$  when  $k_{\perp}\rho_i \gg 1$  because  $\Gamma_0(\hat{b}_i^{\sigma})$  in Equation (4.34) is small. For information on the numerical techniques used to solve Equation (4.36), refer to Appendix C. In Figure 4.3, we solve Equation (4.36), performing a scan in  $\omega_{*e}\eta_e/\omega_{\kappa e}$  and  $k_{\parallel}v_{te}/\omega_{*e}\eta_e$ . Note that while for Figure 4.3 we have set  $\omega_{\kappa e} = \omega_{\nabla B_e}$ , when we solve Equation (4.36) with the geometry for the discharge 92174 in forthcoming sections, we use the correct values of  $\omega_{\kappa e}$  and  $\omega_{\nabla B_e}$  (for example, see Figures 5.4, 5.5 and 5.12). For the toroidal ETG mode, we observe two stability limits in  $\omega_{*e}\eta_e/\omega_{\kappa e}$ . Figure 4.3(a) shows that for  $b_e = 0$ , toroidal ETG instability only occurs when  $1.4 \lesssim \omega_{*e}\eta_e/\omega_{\kappa e} \lesssim 42$ , and we found no instability when  $\omega_{*e}\eta_e/\omega_{\kappa e} < 0$ .

We observe in Figure 4.3(b) and (c) that increasing  $k_{\parallel}$  causes the ETG instability to transition from the toroidal ETG branch to the slab ETG branch for the values of  $\omega_{*e}\eta_e/\omega_{\kappa e}$  where the toroidal mode is unstable. Generally, increasing  $b_e$  strongly decreases the growth rate for both the toroidal and slab branches, although small increasing values of  $b_e$  can increase the growth rate, shown by comparing the  $\omega_{*e}\eta_e/\omega_{\kappa e} = 21$  values in Figure 4.3(b) and (c).

The  $h_i = 0$  limit is generally an accurate description of toroidal and slab ETG instability in the JET pedestal discharges we analyzed, as will be described in Chapter 5. This is not surprising given that for the toroidal ETG instability we require  $K_x\rho_e \sim 1$ ,

which means that  $h_i \approx 0$  because of the large argument of  $J_0$  (see Equation (4.27)). For the fastest growing slab ETG instability we usually find that  $k_y \rho_i \gg 1$ , again resulting in  $h_i \approx 0$ . However, the  $h_i = 0$  approximation might not always be justified for  $k_y \rho_i \sim 1$  slab ETG instability, where FLR damping has not substantially decreased the size of the ion kinetic response.

In the next section, we proceed to use gyrokinetic simulations to study ETG stability in the pedestal. Of particular interest, consistent with the predictions of this section, we will find both toroidal and slab ETG modes at scales  $k_y \rho_i \sim (\rho_i / \rho_e) L_{Te} / R_0 \lesssim 1$ , and long poloidal wavelength toroidal ETG being unstable at  $\hat{s}\theta \sim R_0 / L_{Te}$  (for  $\theta_0 = 0$ ).

# Chapter 5

## ETG Stability in the Pedestal

In this chapter, we describe ETG instability in electrostatic gyrokinetic simulations of JET shot 92174 at  $r/a = 0.9743$ .

The layout of this chapter is as follows. We first discuss the character of the toroidal and slab ETG instability in the pedestal in Section 5.1. In Section 5.2, we describe the parallel dynamics of the toroidal ETG mode, detailing how its parallel location and mode width are determined. In Section 5.3, the effects of a nonzero  $\theta_0$  for the toroidal ETG mode are analyzed, including an estimate for the quasilinear diffusion coefficient. Then in Section 5.4, we study the critical temperature gradient for the toroidal ETG mode described in Chapter 4.

### 5.1 Toroidal ETG Versus Slab ETG Instability

Gyrokinetic simulations show toroidal and slab ETG instability as the fastest growing modes for  $k_y \rho_i \gtrsim 0.1$  for JET shot 92174. Unlike ETG instability in the core, where the linear growth rate typically peaks at  $k_y \rho_e \sim 1$ , we find instances of maximum toroidal ETG growth rates at spatial scales as large as  $k_y \rho_i \sim (\rho_i/\rho_e)L_{Te}/R_0 \lesssim 1$ , strongly supporting the arguments in Chapter 4. We emphasize that very similar modes have been seen in previous works [74, 78–82], but have not been explained until now. For  $\theta_0 \neq 0$ , we find toroidal ETG as the fastest growing mode at all spatial scales between  $k_y \rho_i \sim 1$  and  $k_y \rho_e > 1$ , which we will discuss in Section 5.3. In Figure 5.3, we show the growth rates of modes with  $\theta_0 = 0$ , where we find two dominant ETG modes: for this specific pedestal location, the toroidal ETG branch is the fastest growing mode for

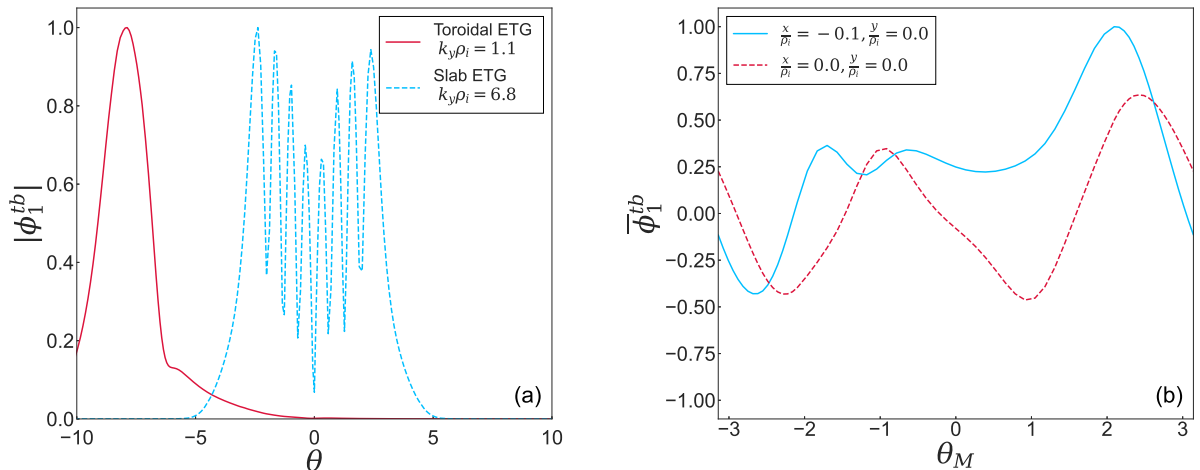


Figure 5.1: (a): Ballooning eigenmodes for toroidal and slab ETG in GS2 simulations. (b): Toroidal ETG eigenmodes in  $\theta_M$  space with  $k_y \rho_i = 1.1$ , using the transformation in Equation (5.1) at two locations: (1)  $x/\rho_i = -0.1, y/\rho_i = 0.0$ , and (2)  $x/\rho_i = 0, y/\rho_i = 0$ . Location (1) is where the mode amplitude is maximum.

$1 \lesssim k_y \rho_i \lesssim 5$ . Once  $k_y \rho_i$  is sufficiently large ( $k_y \rho_i \approx 5$ ), the toroidal ETG is FLR damped, and the slab ETG branch grows faster. The slab ETG branch is not FLR damped as quickly as the toroidal branch because the slab branch generally satisfies  $K_x \sim k_y$ .

We use several criteria to distinguish between the toroidal and slab ETG modes in the pedestal. First, as predicted in Chapter 4, toroidal ETG modes have  $\Delta\theta/\theta \ll 1$ , and have a  $\theta$  location that satisfies  $\hat{s}\theta \sim L_{Te}/R_0$  for  $|\theta_0|$  sufficiently small. Parameter scans can also be used to determine whether the location along a field line of a suspected toroidal ETG mode changes as predicted by Equation (4.12). In contrast, slab ETG modes tend to have a much larger  $k_{\parallel}$  (at a fixed  $k_y \rho_i$ ), and to have eigenmodes that are centered around  $\theta = 0$ . In Figure 5.1, we show both toroidal and slab ETG eigenmodes in (a). To go from ballooning coordinate  $\theta$  to the physical poloidal angle  $\vartheta$ , where  $-\pi \leq \vartheta \leq \pi$ , we use the ballooning transform,

$$\begin{aligned} \bar{\phi}_1^{tb}(\vartheta, x, y) = & \sum_{p=-\infty}^{\infty} \phi_1^{tb}(\vartheta - 2\pi p) \exp\left(ik_y x \hat{s} \left(\vartheta - 2\pi p - \frac{r}{\hat{s}q} \frac{\partial \nu}{\partial r}\right) - ik_y y\right) \\ & + \sum_{p=-\infty}^{\infty} \phi_1^{tb*}(\vartheta - 2\pi p) \exp\left(-ik_y x \hat{s} \left(\vartheta - 2\pi p - \frac{r}{\hat{s}q} \frac{\partial \nu}{\partial r}\right) + ik_y y\right), \end{aligned} \quad (5.1)$$

where  $*$  denotes a complex conjugate. In Figure 5.1(b), the toroidal ETG eigenmode is plotted against the Miller angle  $\theta_M$  for  $x/\rho_i = 0, y/\rho_i = 0$  and for  $x/\rho_i = -0.1, y/\rho_i =$

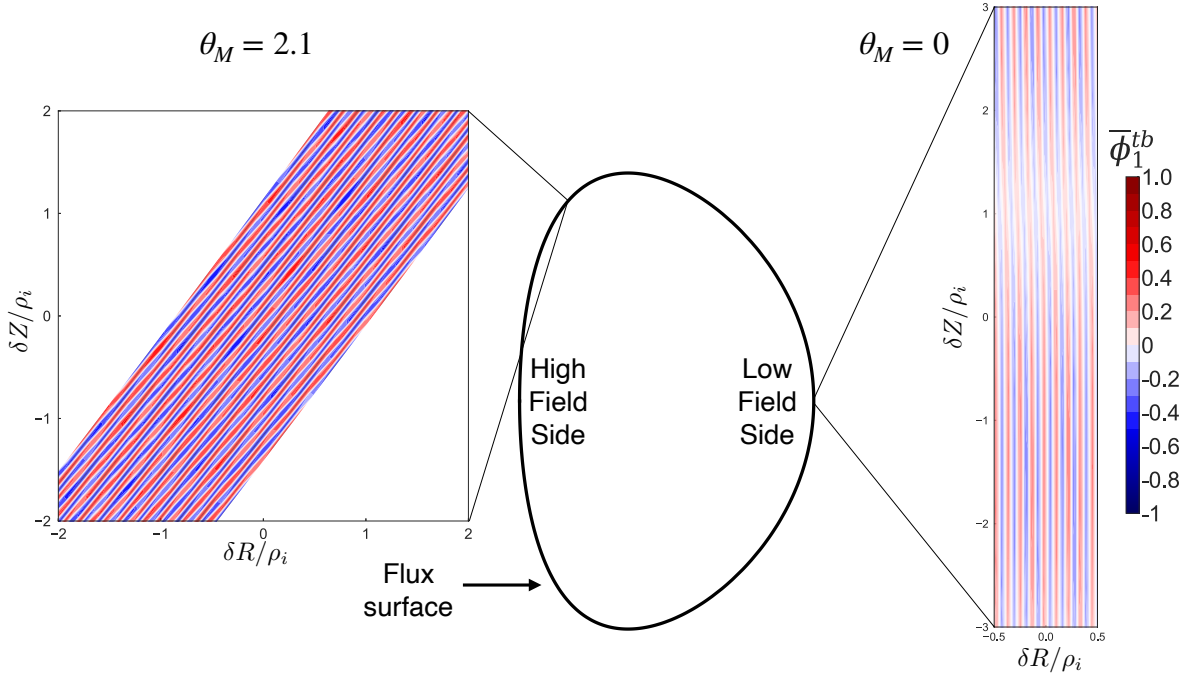


Figure 5.2: Real space images at the outboard midplane ( $\theta_M = \vartheta = 0$ ), and at  $\vartheta = 1.6$ ,  $\theta_M = 2.1$ , of a single toroidal ETG ballooning mode with  $k_y \rho_i = 1.1$  and  $\theta_0 = 0.0$  from GS2 simulations, demonstrating a relatively large radial wavenumber at both  $\theta_M$  locations, and that the mode has a larger amplitude at  $\theta_M = 2.1$  than at the outboard midplane. These were obtained using the transformation in Equation (5.1). We define the coordinates  $\delta R = R - R_M(r_c, \theta_r)$  and  $\delta Z = Z - Z_M(r_c, \theta_r)$ , where  $\theta_r = -0, 2.1$  is the Miller poloidal angle of the image. The gyroradius  $\rho_i$  is evaluated on the usual  $r/a = 0.9743$  flux surface at the outboard midplane. Both plots are normalized to the same colorbar. Each box is evaluated on the same  $x-y$  grid, and therefore each box is the same size in these variables. The maximum absolute mode amplitude at  $\theta_M = 0$  is about 25% of the mode amplitude at  $\theta_M = 2.1$ . The specific  $\theta_M = 2.1$  location was chosen as this was the location of the maximum value of  $\bar{\phi}_1^{tb}$ , which can be seen in Figure 5.1(b). The diameter of the flux surface normalized to the ion gyroradius is large:  $2r_c/\rho_i \simeq 660$ . Hence, the box at  $\theta_M = 2.1$  has a radial width roughly equal to  $1/165$  of the flux surface diameter, and the box at  $\theta_M = 0.0$  has a radial width roughly equal to  $1/660$  of the flux surface diameter.

0.0. We have normalized the mode such that the maximum of  $\overline{\phi}_1^{tb}$  is 1, and we have chosen the mode's phase such that the maximum is located at  $y = 0$ . The maximum value of  $\overline{\phi}_1^{tb}$  occurs at  $x/\rho_i = -0.1$ . In Figure 5.2, we show the real space picture of the mode at the outboard midplane ( $\theta_M = 0$ ) and where the amplitude is maximum, at  $\theta_M = 2.1$ . As expected, the toroidal ETG modes have  $K_x \gg k_y$  at both the outboard midplane and at  $\theta_M = 2.1$ , and the maximum amplitude is far away from the outboard midplane. To make the plots in Figure 5.2, we first evaluated Equation (5.1) for  $k_y\rho_i = 1.1$  on a uniform  $x, y$  grid. We then performed a change of variables from  $x, y$  to  $R, Z$  using the Miller formulas for  $R_M$  and  $Z_M$ . Finally, we changed from  $\vartheta$  to  $\theta_M$  variables. Figure 5.2, where we have plotted a toroidal ETG mode with  $\theta_0 = 0$ , demonstrates how the wavenumbers  $K_x$  and  $k_x$  can differ dramatically due to the presence of magnetic shear. At both the outboard midplane and at  $\theta_M = 2.1$ , this mode has  $\lambda_x \simeq 0.1\rho_i$ , and so  $K_x\rho_i \simeq 65$ , which is consistent with the requirement that  $K_x\rho_e \sim 1$  for the toroidal ETG mode. Here,  $\lambda_x$  is the radial mode wavenumber. Since  $k_\perp$ , which is non-trivial (see Equation (4.3)), enters the Bessel function arguments and not simply  $k_x$  and  $k_y$ , the distinction between  $k_x$  and  $K_x$  is crucial for the character of the mode.

To investigate the character of the toroidal and slab ETG modes, we have performed a scan in equilibrium gradients, as shown in the linear gyrokinetic spectrum in Figure 5.3. Our simulations indicate that the fastest growing toroidal ETG modes are driven strongly by  $R_0/L_{Te}$  because they depend strongly on this parameter, as shown in Figure 5.3(a). Conversely, these modes are relatively insensitive to  $R_0/L_n$ , and do not depend on  $R_0/L_{Ti}$ . Modifying  $R_0/L_n$  mainly affects the slab ETG growth rate, determining at which  $k_y\rho_i$  it will exceed the toroidal ETG growth rate. Kinetic ion physics is usually unimportant for toroidal ETG instability because  $k_\perp\rho_i \gg 1$ . This is demonstrated by the linear spectrum for the toroidal ETG being unchanged when the non-adiabatic part of the ion distribution function is artificially set to zero,  $h_i = 0$ , shown in Figure 5.3(b). The simulation results in Figure 5.4 also show higher  $R_0/L_{Te}$  and smaller  $T_{0i}/T_{0e}$  shifting the maximum growth rate of the toroidal ETG instability to a smaller  $k_y\rho_i$ , as predicted by Equation (4.14). Unlike the wavenumber of the fastest growing modes, the size of the maximum growth rate in the range of wavelengths shown

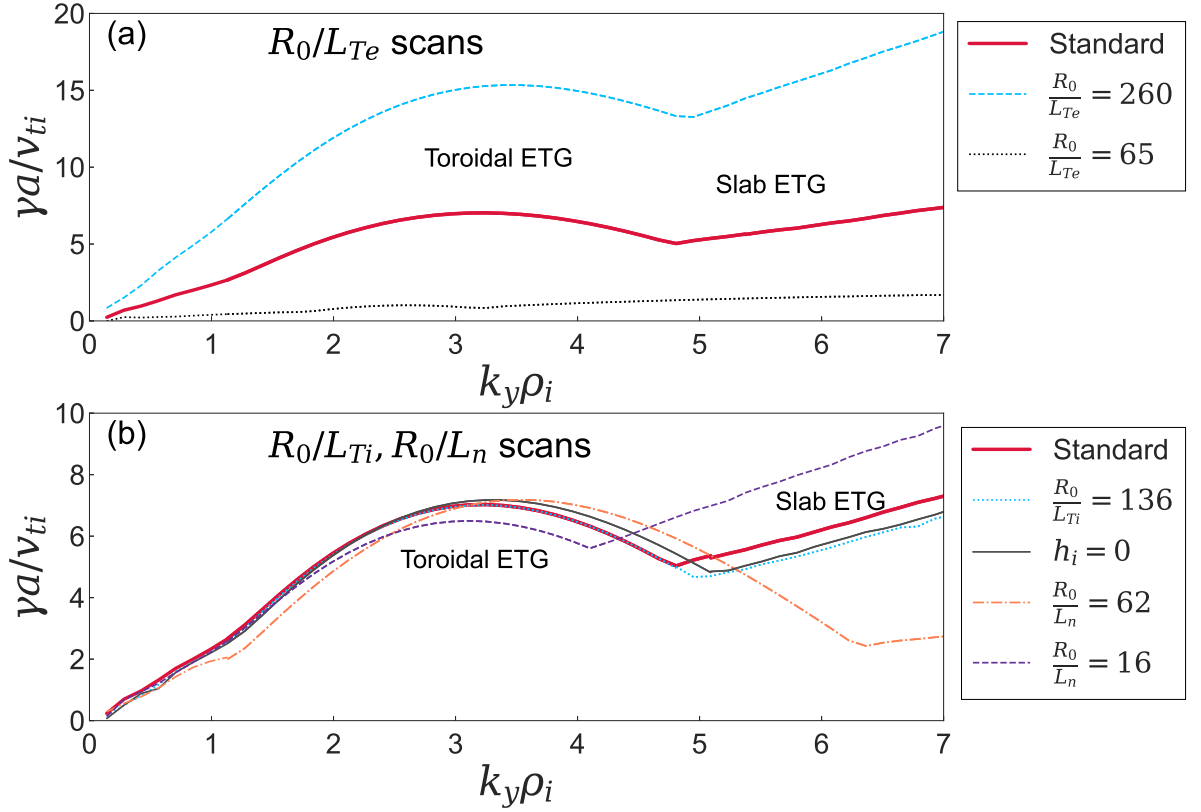


Figure 5.3: Electrostatic GS2 growth rates for JET shot 92174 for  $0.15 \leq k_y \rho_i \leq 7.0$  and sensitivity scans, all with  $\theta_0 = 0$ . (a):  $R_0/L_{Te}$  scans. (b):  $R_0/L_{Ti}$  and  $R_0/L_n$  scans. ‘Standard’ denotes simulations performed with the following parameters:  $R_0/L_{Te} = 130$ ,  $R_0/L_{Ti} = 34$ ,  $R_0/L_n = 31$ . All of the fastest growing ‘Standard’ modes at scales  $k_y \gtrsim 0.1$  are ETG-like instabilities.

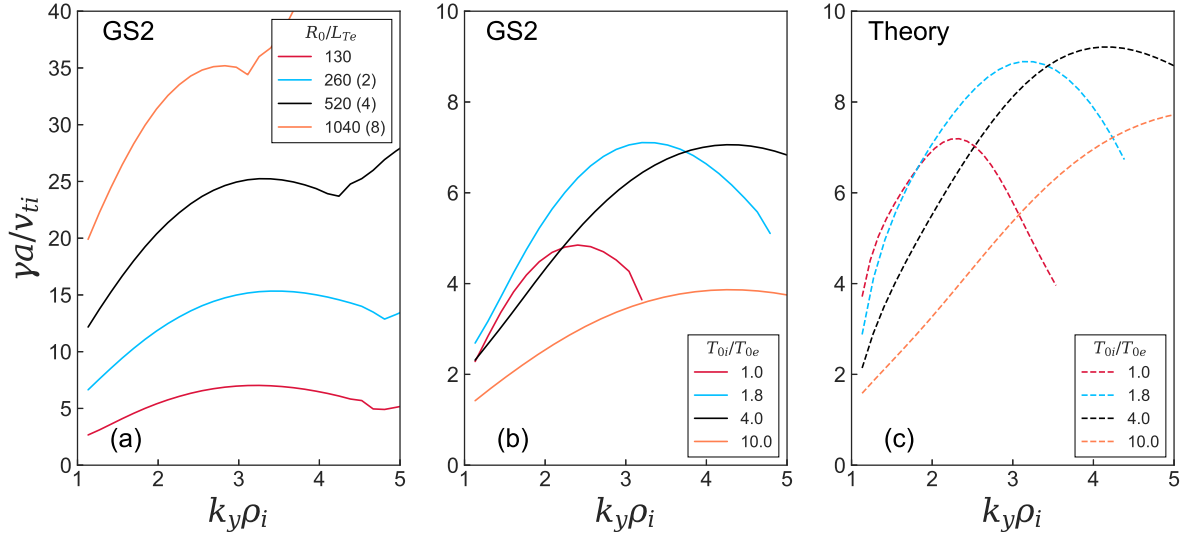


Figure 5.4: Growth rates. (a): GS2 scan in  $R_0/L_{Te}$ , (b): GS2 scan in  $T_{0i}/T_{0e}$ , and (c): Theory scan in  $T_{0i}/T_{0e}$ . These scans show the value of  $k_y\rho_i$  for the peak growth rate of the toroidal ETG mode shifting. For  $T_{0i}/T_{0e}$  scans,  $T_{0i}$  was fixed and  $T_{0e}$  was allowed to vary. (b): Growth rates from GS2 simulations with consistent collisionality. (c): The collisionless dispersion relation in Equation (4.36) was solved, along with a value of  $k_{\parallel}$  associated with the largest Fourier coefficient  $\hat{\phi}^{tb}(k_{\parallel})$  for each  $k_y\rho_i$  mode that was extracted from linear simulations, described in Section 5.2 and Equation (5.2). Numbers in parentheses in the legend for (a) are the multiples of the correct  $R_0/L_{Te}$  value.

depends on  $T_{0e}/T_{0i}$  in a non-trivial way. We show in Figure 5.4 that this dependence is consistent with a theory that we describe in Section 5.2.

For  $k_y\rho_i \gtrsim 1$ , the modes are unlikely to be a TEM since  $\omega_{be} \ll \gamma_{\text{ETG}}$  for  $k_y\rho_i \gtrsim 1$ , where  $\omega_{be} = v_{te}\sqrt{r_c/q_c^2 R_c^3}$  is the electron bounce frequency and  $\gamma_{\text{ETG}}$  is the ETG growth rate. In this equilibrium, we find that  $\omega_{be}a/v_{ti} \simeq 1.5$ , which is comparable to  $\gamma_{\text{ETG}}a/v_{ti}$  only when  $k_y\rho_i \simeq 0.5$ . Furthermore,  $\omega_{be}/\nu_{ee} \simeq 1.9$ , and so we expect the passing and trapped electron particle distributions to be fairly well equilibrated.

To understand the  $\theta$  location of the toroidal ETG eigenmodes, we solve the dispersion relation in Equation (4.36) locally for JET shot 92174 at each value of  $\theta$  by choosing  $k_y$  and setting  $k_{\parallel} = 0$ , and by using  $\omega_{ke}$ ,  $\omega_{\nabla Be}$ , and  $b_e$  from the Miller equilibrium. This is an approximation that assumes the mode's growth rate is local in  $\theta$ . Note that  $\mathbf{k}_{\perp}$  in Equation (4.3) is a function of  $\theta$ . By solving the dispersion relation, we obtain a set of frequencies as a function of  $\theta$ . Figure 5.5(c) shows the growth rates along  $\theta$  with  $k_{\parallel} = 0$  (for the present discussion, consider only the curve labeled 'Standard;'; the curve labeled

‘ $\omega_{Me} \rightarrow -\omega_{Me}$ ’ will be discussed in Section 5.2). For  $\theta_0 = 0$ , we find that the maximum growth rates are at  $|\theta| \simeq 7.7$  with the standard sign of  $\omega_{\kappa e}$  and  $\omega_{\nabla Be}$ . This  $\theta$  location is very close to the  $\theta$  where GS2 toroidal ETG eigenmodes have their maximum amplitude, as shown by comparison of Figure 5.5(a) and (c). Therefore, the parallel location of the toroidal ETG is fairly well described by our model.

One prediction of Chapter 4 was that the toroidal ETG mode is driven most strongly at  $\hat{s}\theta \gg 1$  when  $R_0/L_{Te} \gg 1$ . This causes the  $k_y \hat{s}\theta \nabla x$  term in  $\mathbf{k}_\perp$  in Equation (4.3) to become particularly large. In Figure 5.1, we show that the toroidal ETG eigenmodes are indeed driven at  $\hat{s}\theta \gg 1$ . As an experiment, we set the  $k_y \hat{s}\theta \nabla x$  component of  $\mathbf{v}_{Me}$  to zero. As expected, the toroidal ETG mode was not driven, and slab ETG was the fastest growing mode.

In JET shot 92174, slab ETG instability is the fastest growing mode for  $k_y \rho_i \gtrsim 5$  when  $\theta_0 = 0$  — however, the ‘slab’ ETG we observe is not always the conventional slab ETG with  $\omega_{\kappa e} = \omega_{\nabla Be} = 0$ . By artificially turning the magnetic drift off in gyrokinetic simulations, we observed that the slab ETG growth rates were reduced by factors of order unity. As shown in Figure 5.6, the slab ETG eigenmodes have quite a wide  $\theta$  extent, especially for smaller  $k_y \rho_i$  where FLR effects are less strong, and hence the magnetic drift, which increases for increasing  $\theta$ , can have a strong impact on the character of the slab ETG in the pedestal. As  $k_y \rho_i$  increases, FLR effects become stronger and the slab ETG eigenmode becomes more localized near  $\theta = 0$ . Hence, when we refer to the ‘slab’ ETG in the pedestal simulations described in this work, we refer to the modes with a  $k_\parallel$  much larger than the toroidal ETG, but also sometimes with a significant magnetic drift contribution.

The toroidal ETG modes are not affected by kinetic ion physics due to their large radial wavenumber  $K_x \rho_i \gg 1$ , but the ions can modify the slab ETG modes slightly when  $k_y \rho_i \sim 1$ , as we demonstrate in Figure 5.3, where we show results with the full ion kinetic response and with  $h_i = 0$ . This is consistent with the fact that slab modes with  $k_y \rho_i \sim 1$  have  $K_x \rho_i \sim 1$ . We have checked that  $h_i$  becomes unimportant at larger values of  $k_y \rho_i$ .

Note that the slab ETG modes in Figure 5.6 are asymmetric. This asymmetry is not a result of our choice of  $\theta_0$  because we observe it in modes with  $\theta_0 = 0$ . Due to the

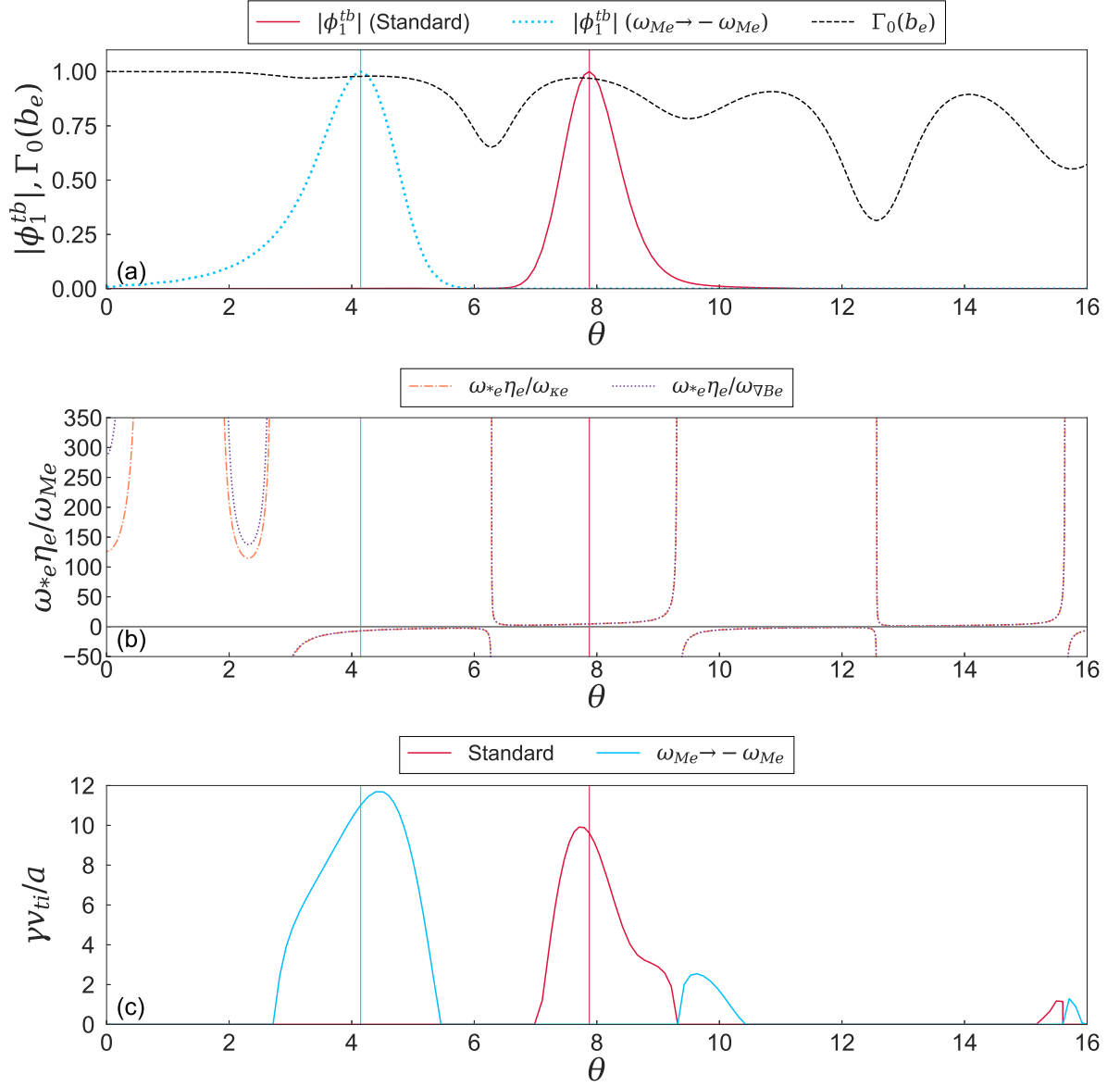


Figure 5.5: (a): Two eigenmodes obtained from two separate GS2 simulations, and the function  $\Gamma_0(b_e)$  for  $k_y \rho_i = 3.4$ . When  $\omega_{Me} \rightarrow -\omega_{Me}$ , the mode moves to a location where the sign of  $\omega_{Me}$  allows instability, where  $\omega_{Me}$  refers to both  $\omega_{\kappa e}$  and  $\omega_{\nabla Be}$ . (b) The quantities  $\omega_{*e}\eta_e/\omega_{\kappa e}$  and  $\omega_{*e}\eta_e/\omega_{\nabla Be}$ . The eigenmodes in (a) have their maxima in bad curvature regions, corresponding to  $\omega_{*e}\eta_e/\omega_{Me} > 0$ . (c): Finding the growth rates for the ETG dispersion relation in Equation (4.36) for two signs of  $\omega_{*e}\eta_e/\omega_{Me}$  in JET shot 92174. Note how the maximum growth rates in (c) roughly align with the eigenmode maximum in (a). Horizontal red and blue lines denote the eigenmode location for the two signs of  $\omega_{Me}$  in (a). Here,  $\omega_{*e} < 0$ ,  $\eta_e = 4.28$ ,  $k_y \rho_i = 3.4$ ,  $k_{\parallel} = 0$ ,  $\theta_0 = 0$ .

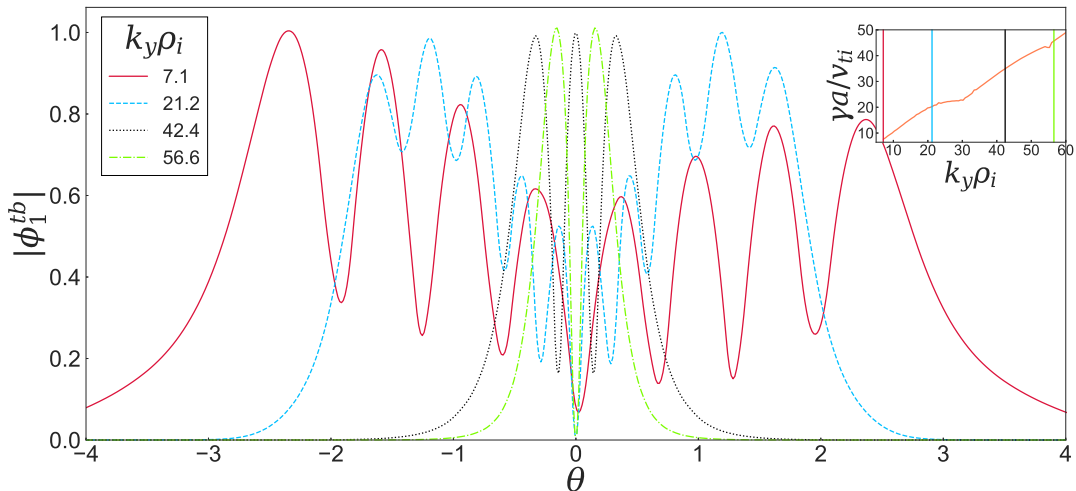


Figure 5.6: Electrostatic slab eigenmodes from GS2 for  $k_y \rho_i > 7.0$  instabilities at  $\theta_0 = 0.05$ . The corresponding linear growth rates are shown in the inset.

symmetry of the linear gyrokinetic equation described in [105], for  $\theta_0 = 0$ , if one obtains an asymmetric mode, there must be two modes with opposing asymmetry that grow at the same rate. We have run our simulations with a small value of  $\theta_0$  to avoid getting a linear combination of these two modes — the final result would depend on the initial conditions in this case.

Thus far, using the method described above to solve the dispersion relation in Equation (4.36), we found we could predict the parallel location of the toroidal ETG modes. We next describe the physics that determines the parallel location and width of the toroidal ETG mode in more detail.

## 5.2 Location And Width Of The Toroidal ETG Mode

We now discuss the parallel location and width of the toroidal ETG mode. The parallel location of the toroidal ETG mode is subject to four main constraints:

1. **The mode can only be driven in bad curvature regions**,  $\omega_{*e} \eta_e / \omega_{\kappa e} > 0$ , which eliminates roughly half of the parallel domain.
2. **The mode is only unstable when  $\mathbf{A} > \omega_{*e} \eta_e / \omega_{\kappa e} > \mathbf{C}$** . According to the results in Figure 4.3(a), for toroidal ETG instability the value of  $\omega_{*e} \eta_e / \omega_{\kappa e}$  must be above some critical value  $C$  for instability, but not larger than another critical value

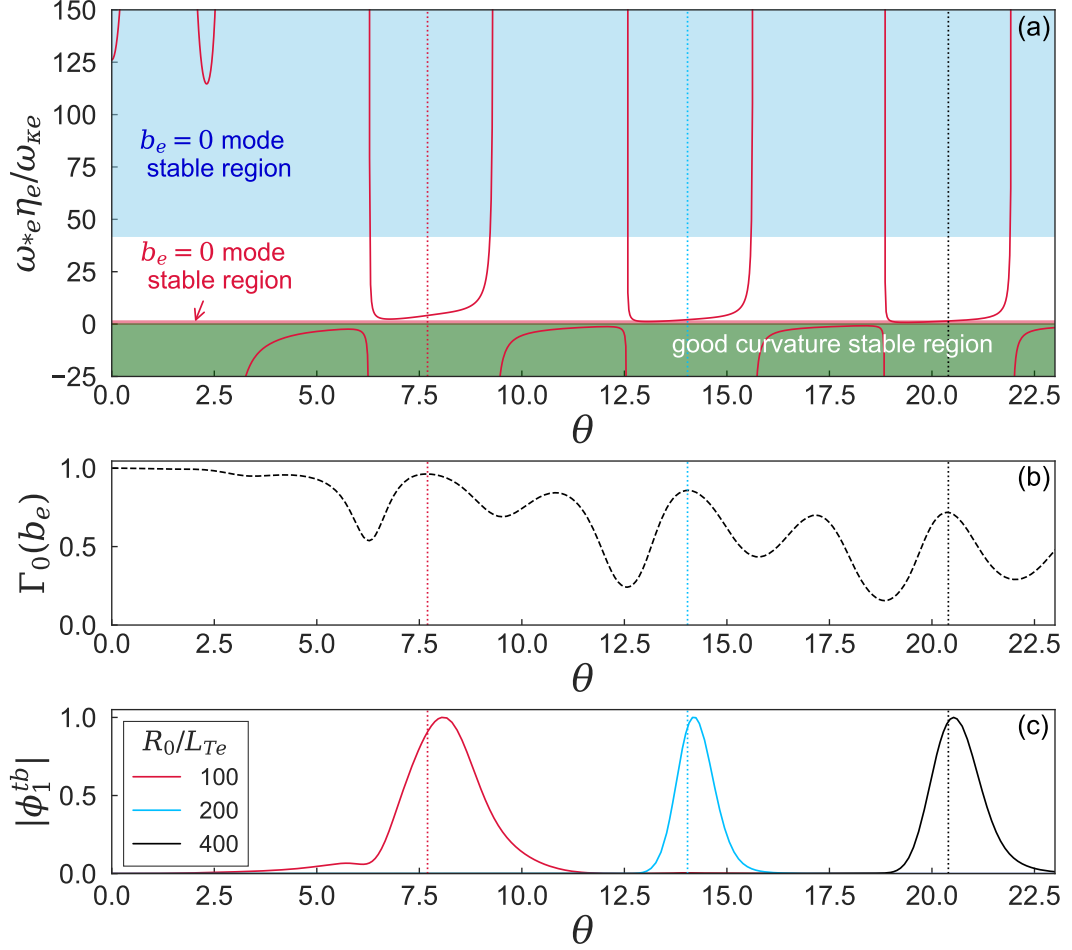


Figure 5.7: A stability plot for the toroidal ETG mode, combining theory and GS2 simulations. For (a), the small red  $b_e = 0$  stable region corresponding to  $0 < \omega_{*e}\eta_e/\omega_{\kappa e} \lesssim 1.8$ , is obtained from Figure 4.3. The blue  $b_e = 0$  stable region is also obtained from Figure 4.3, and corresponds to  $\omega_{*e}\eta_e/\omega_{\kappa e} \gtrsim 42$ . This is valid for  $\theta_0 = 0$  and  $k_y\rho_i = 1.1$ . (b): Quantity  $\Gamma_0(b_e)$  versus  $\theta$  for  $k_y\rho_i = 1.1$ . (c): The associated eigenmodes from GS2 with different temperature gradients, demonstrating that these modes are centered close to local maxima in  $\Gamma_0(b_e)$ , and that increasing  $R_0/L_{Te}$  moves the mode to larger  $\hat{s}\theta$ , predicted in Equation (4.14). Only for (c), we artificially lowered  $\hat{s} \rightarrow 1.68$  to make the mode more mobile in  $\theta$ . Dashed vertical lines show the local maxima of  $\Gamma_0(b_e)$  in bad curvature regions.

A. Consistent with Figure 4.3(a), we observe that no toroidal ETG modes with  $\theta_0 = 0$  can exist at  $|\theta| \lesssim 6$ ; this is because  $\omega_{*e}\eta_e/\omega_{\kappa e}$  is too large and the bad curvature region is too narrow, as shown in Figure 5.7(a) (note that for smaller values of  $R_0/L_{Te}$ , the  $\theta_0 = 0$  toroidal ETG mode *can* have its maximum amplitude at  $|\theta| \lesssim 6$  because  $\omega_{*e}\eta_e/\omega_{\kappa e}$  is smaller — see Section 5.4). Note that we discuss ‘good’ and ‘bad’ curvature using the quantity  $\omega_{*e}\eta_e/\omega_{\kappa e}$  rather than  $\omega_{*e}\eta_e/\omega_{\nabla Be}$  because in the regions where the toroidal ETG mode is typically most unstable (at large  $|\theta|$ ),  $\omega_{\kappa e}/\omega_{\nabla Be} \simeq 1$  (see Figure 5.5(b), for example). There are important exceptions, which occur for  $\theta_0 \neq 0$  with larger values of  $k_y\rho_i$ , which we discuss briefly in Section 5.4.

3. **The parallel extent of bad curvature regions must be sufficiently wide.** We require that the ‘bad curvature’ regions not be too narrow in the parallel direction; if this is the case, the mode acquires a large value of  $k_{\parallel}$  and becomes damped.
4. **The mode maximum is close to a local maximum in  $\Gamma_0(b_e)$ .** The maximum amplitude for the fastest growing toroidal ETG mode (at a given  $k_y\rho_i$ ) is usually centered close to a local maximum in  $\Gamma_0(b_e)$  (or equivalently a local minimum in  $b_e$ ) to limit FLR damping. We choose to plot the quantity  $\Gamma_0(b_e)$  rather than  $b_e$  to demonstrate the importance of FLR damping at different  $\theta$  locations. This is because  $\Gamma_0(b_e) \in [0, 1]$ , and therefore it is easier to convey the size of FLR damping, whereas  $b_e$  is unbounded and can become extremely large. Furthermore, the term  $\Gamma_0(b_e)$  appears directly in the dispersion relation in Equation (4.34), and thus is a good measure of the size of FLR effects.

As an experiment, we artificially reversed the signs of the magnetic drifts in GS2. As expected, the toroidal ETG modes only grew in regions that were previously ‘good curvature’ regions, which due to the sign reversal of  $\omega_{\kappa e}$ , are turned into ‘bad curvature’ regions. This is shown in Figure 5.5, being substantiated both by GS2 simulations (Figure 5.5(a)) and the results of our model ETG dispersion relation (Figure 5.5(c)).

Since  $\omega_{*e}\eta_e$  is fixed for a given  $k_y\rho_i$ , the  $\theta$  location will be such that  $\omega_{\kappa e}$  and  $b_e$  have the right value for maximum growth subject to FLR and curvature constraints. These

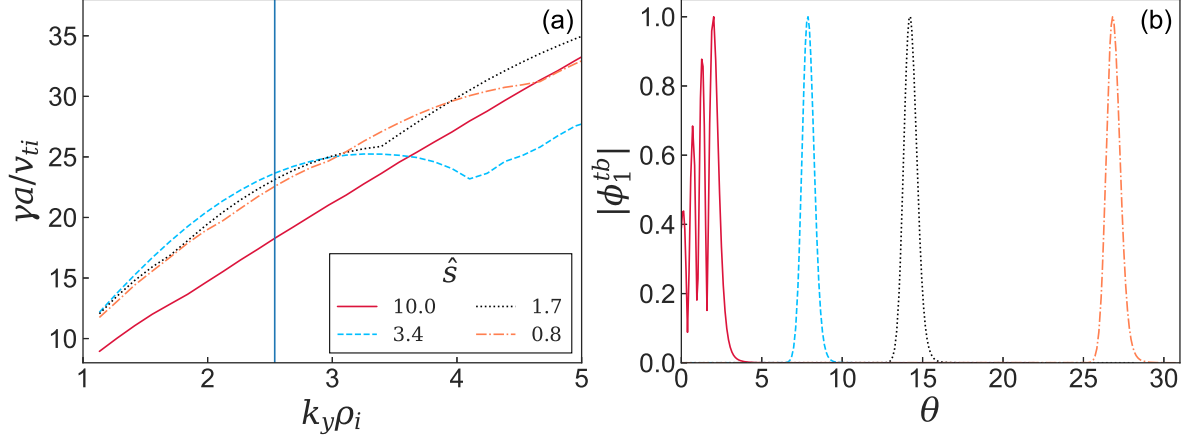


Figure 5.8: (a): Linear growth rates from GS2 for different  $\hat{s}$  values with  $R_0/L_{Te} = 520$ . (b): Corresponding eigenmodes for  $k_y \rho_i = 2.6$ . This is likely not an experimentally relevant temperature gradient; it was used to test the scaling of  $\theta$  with  $L_{Te}$ .

constraints are shown in Figure 5.7(a) and (b). According to Figure 5.7(a) and the above arguments, the smallest  $|\theta|$  that a mode with  $\theta_0 = 0$  can occupy is  $|\theta| \simeq 6.5$ . We denote this minimum  $\theta$  location as  $\theta_{\min}$ . The toroidal ETG mode cannot occupy a smaller  $|\theta|$  value because either  $\omega_{*e} \eta_e / \omega_{\kappa e} < 0$ ,  $\omega_{*e} \eta_e / \omega_{\kappa e}$  is too large, or the bad curvature region is too narrow.

From these considerations, there are several obvious parameters that can change where the mode is located. As already predicted in Equation (4.14), a larger  $R_0/L_{Te}$  causes a mode to be unstable at larger  $\theta$  values; in Figure 5.7(c) we show that increasing  $R_0/L_{Te}$  increases the  $\theta$  location of the mode. In Figure 5.7(c), we use a smaller value of  $\hat{s}$  (1.68 instead of 3.36), since we found that, for larger values of  $\hat{s}$ , increasing  $R_0/L_{Te}$  was not particularly effective at shifting the mode to larger values of  $|\theta|$  — this is because  $b_e$  increases nonlinearly with  $\hat{s}$ , and once  $\hat{s}$  is sufficiently large, a toroidal ETG mode becomes significantly more FLR damped as it moves along  $\theta$ . The parallel location of the modes with different values of  $R_0/L_{Te}$  agrees well with the curvature and FLR constraints discussed above. Smaller  $\hat{s}$  and  $k_y \rho_i$  also force the mode to larger  $\theta$  — as predicted in Equation (4.14), the shifting of modes due to  $\hat{s}$  and  $k_y \rho_i$  is shown in Figures 5.8 and 5.9, respectively.

Figure 5.8(a) illustrates that the toroidal ETG growth rate is relatively insensitive to  $\hat{s}$ , until  $\hat{s}$  exceeds a threshold value. Recall that  $\omega_{*e} \eta_e / \omega_{\kappa e} \sim R_0/L_{Te} \hat{s} \theta$ . This implies

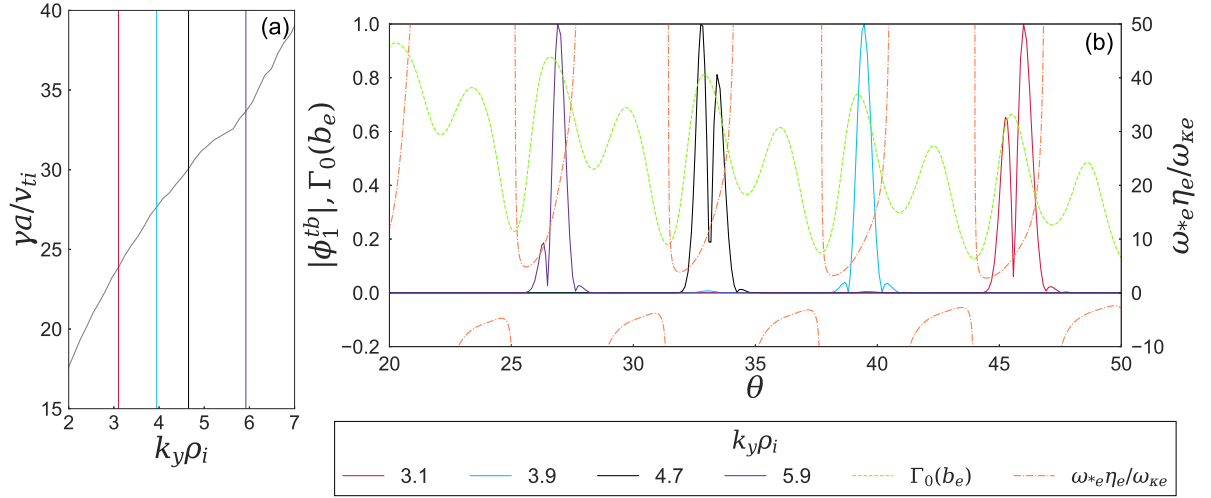


Figure 5.9: (a): Growth rates versus  $k_y \rho_i$ . (b): Corresponding eigenmodes (denoted by different values of  $k_y \rho_i$ ) and the functions  $\Gamma_0(b_e)$  and  $\omega_* \eta_e / \omega_{ke}$ . The toroidal ETG mode shifts due to changing  $k_y \rho_i$ , predicted by Equation (4.14). Here we have set  $\hat{s} = 0.45$  and  $R_0/L_{Te} = 520$ , allowing the mode to be very mobile in  $\theta$ . The values of  $\Gamma_0(b_e)$  are evaluated for  $k_y \rho_i = 5.9$ .

that if  $\hat{s}$  changes, a toroidal mode would move in  $\theta$  to have a  $R_0/L_{Te} \hat{s} \theta$  that maximizes its growth rate. As  $\hat{s}$  increases, the  $|\theta|$  location will decrease. However, the mode cannot be driven linearly unstable below  $\theta_{\min}$ , so at a critical value of  $\hat{s}$  the mode will become increasingly stabilized by FLR effects while the mode maximum remains at fixed  $\theta = \theta_{\min}$ . In Figure 5.8(a), we show that increasing  $\hat{s}$  beyond some critical  $\hat{s}$  indeed decreases the growth rate of the toroidal ETG mode. This increase in  $\hat{s}$  once the mode was at  $\theta_{\min}$  increased  $k_{\perp}$ , and hence caused its growth rate to be lower than the slab ETG mode — this occurred for a value of  $\hat{s}$  somewhere between  $\hat{s} = 3.4$  and  $\hat{s} = 10$  in Figure 5.8(b).

The  $\theta$  location of the mode also depends strongly on  $k_y \rho_i$ , as shown in Figure 5.9(b) where we ran GS2 simulations with a smaller value of  $\hat{s} = 0.45$  and an increased value of  $R_0/L_{Te}$ , which makes the location of the mode more sensitive to changes in  $k_y$ . Clearly, the eigenmodes are centered very close to a local minimum in  $b_e$ . The toroidal ETG modes are close to this minimum because of a competition between the size of the magnetic drift and FLR effects; as shown in Figure 4.3, the growth rates are very sensitive to  $b_e$ . Careful inspection of the growth rates in Figure 5.9(a) reveals that there is a change in mode type as the mode jumps to a new  $\theta$  location — this can be seen by discontinuities in  $\partial\gamma/\partial k_y$ .

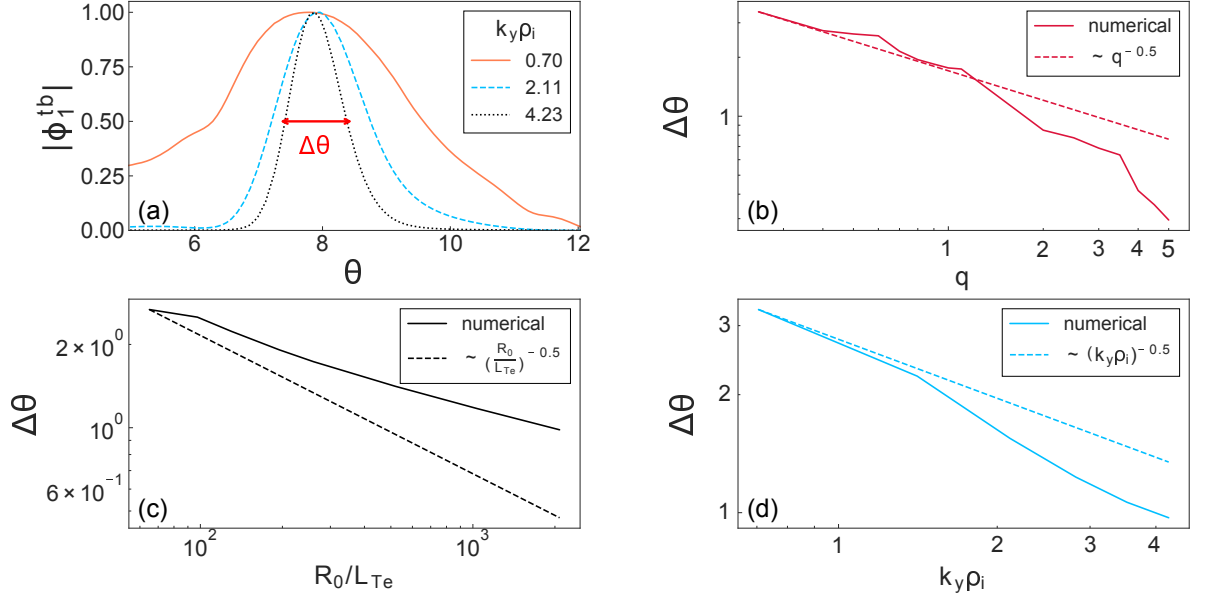


Figure 5.10: (a): Toroidal ETG eigenmodes for different values of  $k_y \rho_i$ , and numerical definition of  $\Delta\theta$  used in subsequent subplots. (b): Numerical (solid) and predicted (dashed)  $\Delta\theta$  versus  $q$  scaling, (c):  $\Delta\theta$  versus  $R_0/L_{Te}$  scaling, (d):  $\Delta\theta$  versus  $k_y \rho_i$  scaling.

We now examine the scalings for the mode width from Equation (4.18) by comparing them with toroidal ETG eigenmodes from GS2 simulations. We calculate the width  $\Delta\theta$  as the length in  $\theta$  for the half height of the mode; this is shown in Figure 5.10(a). Equation (4.18) predicts that the mode width  $\Delta\theta$  scales with  $R_0/L_{Te}$ ,  $k_y \rho_i$ , and  $q$  as  $\Delta\theta \sim \sqrt{L_{Te}/R_0 k_y \rho_e q}$ . Scans in these quantities, shown in Figure 5.10, demonstrate that increasing  $R_0/L_{Te}$ ,  $k_y \rho_i$ , and  $q$  narrows the toroidal ETG mode structure. However, the scaling exponents do not appear to be quantitatively correct. The theoretical scaling  $\Delta\theta \sim \sqrt{L_{Te}/R_0 k_y \rho_e q}$  in Equation (4.18) is not perfect because the mode changes location. Indeed, since the parallel location of the mode is sensitive to  $q$ ,  $k_y \rho_i$ , and  $R_0/L_{Te}$ , changing the location of the mode by changing these parameters changes the local derivative of  $\mathbf{v}_{Me} \cdot \mathbf{k}_{\perp}$ , and hence changes  $\Delta\theta$ . Note that we have fixed the numerical scaling with the data at the minimum value on the x-axis in Figure 5.10(b), (c), and (d), which falsely gives the impression that the fit is better for larger values of  $\Delta\theta$ . Finally, the slope in Figure 5.10(c) looks too shallow because as  $R_0/L_{Te}$  is increased, the mode jumps to larger values of  $|\theta|$ , where other physics parameters that are independent of  $R_0/L_{Te}$  also change (such as  $\mathbf{k}_{\perp} \cdot \mathbf{v}_{Ms}$ ).

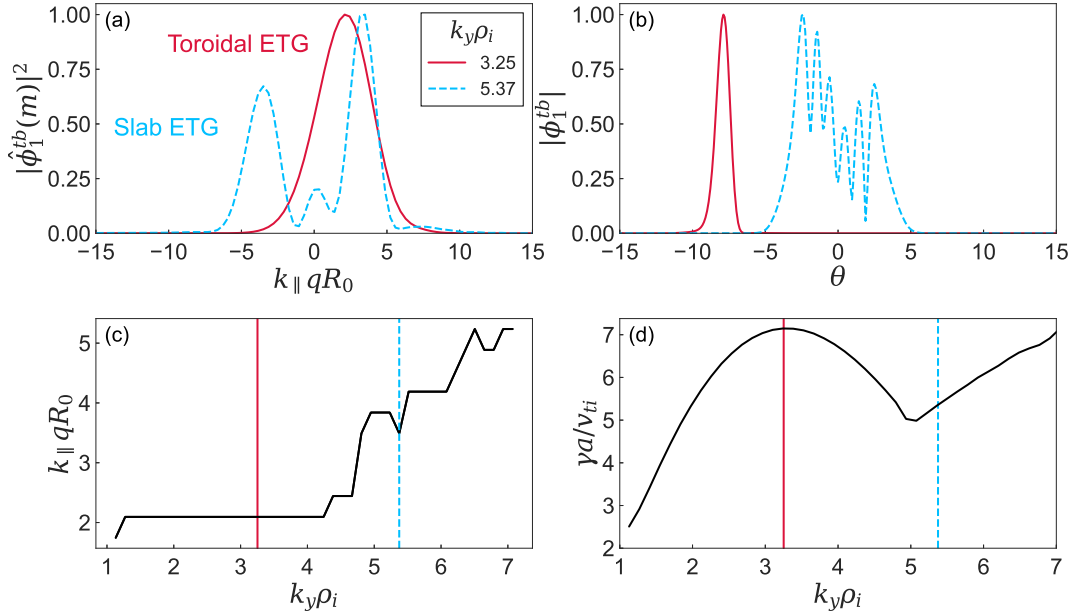


Figure 5.11: (a): The Fourier transformed coefficient  $|\hat{\phi}_1^{tb}(m)|^2$  spectrum for 2 modes from GS2 with different values of  $k_y \rho_i$ . The coefficient  $|\hat{\phi}_1^{tb}(m)|^2$  is normalized so that its maximum value is 1. (b): Eigenmodes. (c): The  $k_{\parallel}$  associated with the largest coefficient  $|\hat{\phi}_1^{tb}(m)|^2$  in (a). (d): Growth rates. All of these plots have  $\theta_0 = 0.02$ .

As the toroidal ETG instability is FLR damped at increasing  $k_y$ , the mode switches to the slab branch, with an accompanying increase in  $k_{\parallel}$ . The switch from toroidal to slab at fixed  $k_y$  is shown in the simple dispersion relation used to plot Figure 4.3(c). At this transition,  $k_{\parallel}$  for the slab mode is much larger than the toroidal mode and the eigenmodes move from being quite localized around a large value of  $\theta$ , to oscillating rapidly about smaller  $\theta$ , as shown in Figure 5.1(a).

To demonstrate this transition, we need to define  $k_{\parallel}$ . Our choice of  $\theta$  in Equation (2.11) is such that  $\theta$  is proportional to the length along the magnetic field line. Thus, Fourier analyzing in  $\theta$  is equivalent to obtaining the spectrum in  $k_{\parallel}$ .

To carry out the Fourier transform, we first interpolate  $\phi_1^{tb}(\theta)$  onto a regular  $\theta$  grid with gridspacing  $\Delta_{\theta}$ , since GS2's  $\theta$  grid is not usually regularly spaced. Next, we apply a Fast Fourier Transform [109] to obtain the Fourier transform of  $\phi_1^{tb}$ ,

$$\hat{\phi}_1^{tb}(m) = \sum_{\theta} \phi_1^{tb}(\theta) \exp(-im\theta) \Delta_{\theta}. \quad (5.2)$$

The sum in the discrete Fourier transform was performed over all values of  $\theta$  in the domain for eigenmodes from linear gs2 simulations; these values were typically  $-5\pi \leq \theta \leq 5\pi$ . The relation between  $m$  and  $k_{\parallel}$  is

$$k_{\parallel} = \frac{2\pi}{L_{\theta}} m. \quad (5.3)$$

Figure 5.11(a) shows that the power spectrum  $|\hat{\phi}_1^{tb}|^2$  changes significantly at the transition between toroidal and slab ETG. The toroidal ETG spectrum is Gaussian whereas the slab spectrum is more complicated, with at least two peaks. It is noteworthy that the toroidal ETG has a non-zero  $k_{\parallel}$  for its fastest growing mode since theory predicts toroidal ETG with the highest growth rate at  $k_{\parallel} = 0$ , shown in Figure 4.3. Previous studies of toroidal ETG have also found  $k_{\parallel} = 0$  as the fastest growing mode [23].

We now use Equation (5.2) to calculate the toroidal ETG growth rates for a range of  $k_y \rho_i$ . Our analytic model requires  $k_{\parallel}$  as an input, which we obtain from GS2 by choosing the value of  $k_{\parallel}$  that corresponds to the largest amplitude in the poloidal Fourier transform  $\hat{\phi}_1^{tb}$ . Once we have obtained  $k_{\parallel}$  from the GS2 data for each value of  $k_y \rho_i$ , we solve the model dispersion relation in Equation (4.36) for each value of  $\theta$ , inputting the correct value of  $k_{\perp}$ ,  $\omega_{\kappa e}$ , and  $\omega_{\nabla B e}$  at each  $\theta$  location. For each  $k_y \rho_i$  value, we take the growth rate from the  $\theta$  location with the highest growth rate to be the growth rate of the toroidal ETG mode for that  $k_y \rho_i$ . There is excellent agreement between the  $\theta$  location with the highest growth rate by solving Equation (4.36) and the eigenmode maximum from GS2. This method for calculating  $k_{\parallel}$  gave a toroidal ETG growth rate reasonably close to the values obtained from GS2 shown in Figure 5.12, as well as the  $k_y \rho_i$  location of the peak. Since the toroidal ETG mode is no longer the fastest growing instability for  $k_y \rho_i \gtrsim 5$ , the value of  $k_{\parallel}$  that we deduce from GS2 and we use to plot the values of the toroidal ETG growth rate in Figure 5.12 is not reliable for  $k_y \rho_i \gtrsim 5$ . To calculate the toroidal ETG growth rate for  $k_y \rho_i > 5.0$ , we simply evaluated the growth rate at  $\theta = 7.7$  with  $k_{\parallel}$  given by the slab ETG mode from GS2. To calculate the slab ETG growth rate, we found the value of  $k_{\parallel}$  for which the growth rate at  $\theta = 0.0$  was maximized. Surprisingly, this method also gives a very good approximation to the slab ETG growth rate even though slab ETG modes are very extended (see Figure 5.6).

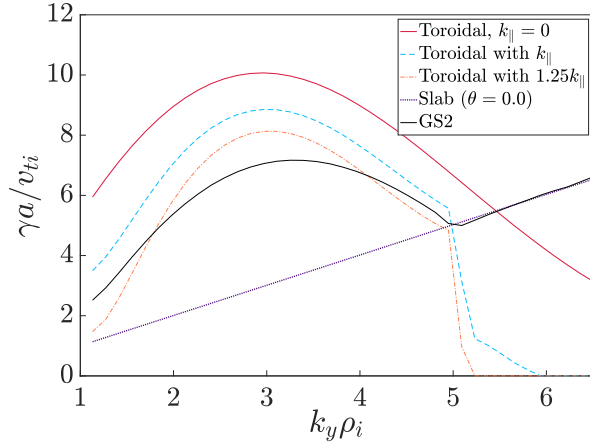


Figure 5.12: The growth rates obtained in theory and in GS2. For the toroidal ETG growth rate, we found the  $\theta$  with the highest growth rate for Equation (4.36), which occurred at  $\theta = 7.7$ , and for the slab ETG growth rate, we evaluated the dispersion relation at  $\theta = 0.0$  (note that  $\omega_{\kappa e}$  is nonzero at  $\theta = 0$ ). The  $k_{\parallel}$  input for the toroidal ETG was obtained by Fourier transforming the GS2 eigenmodes for each  $k_y$ , and for the ‘ $1.25k_{\parallel}$ ’ series, we multiplied all  $k_{\parallel}$  values by 1.25.

The theory presented in this work cannot self-consistently calculate  $k_{\parallel}$  and thus we have used solutions with a  $k_{\parallel}$  associated with the numerical simulations. Until now, our analysis has been performed with  $\theta_0 = 0$ . In the next section, we extend our analysis to toroidal ETG with a nonzero value of  $\theta_0$ .

### 5.3 Effects of $\theta_0$

We now consider ETG instability for  $\theta_0 \neq 0$ . The growth rate of microinstabilities and MHD ballooning instabilities has a complicated dependence on  $\theta_0$ . Previous works have found that nonzero  $\theta_0$  can substantially change the growth rates for toroidal ITG [93, 110], ETG [79, 80], and MTMs [76]. For MHD ballooning modes, it was found that for smaller pressure gradients, increasing  $|\theta_0|$  is stabilizing, but once the gradients become sufficiently large, increasing  $|\theta_0|$  is destabilizing [111].

As briefly discussed in Chapter 3, we find that increasing  $|\theta_0|$  can substantially increase the toroidal ETG growth rate, shown in Figure 5.13(a). For many values of  $\theta_0$ , the toroidal ETG mode can be the fastest growing mode not only at ion scales,  $k_y \rho_i \sim 1$ , but at scales smaller than the electron gyroradius:  $k_y \rho_e > 1$ . To be precise, we find

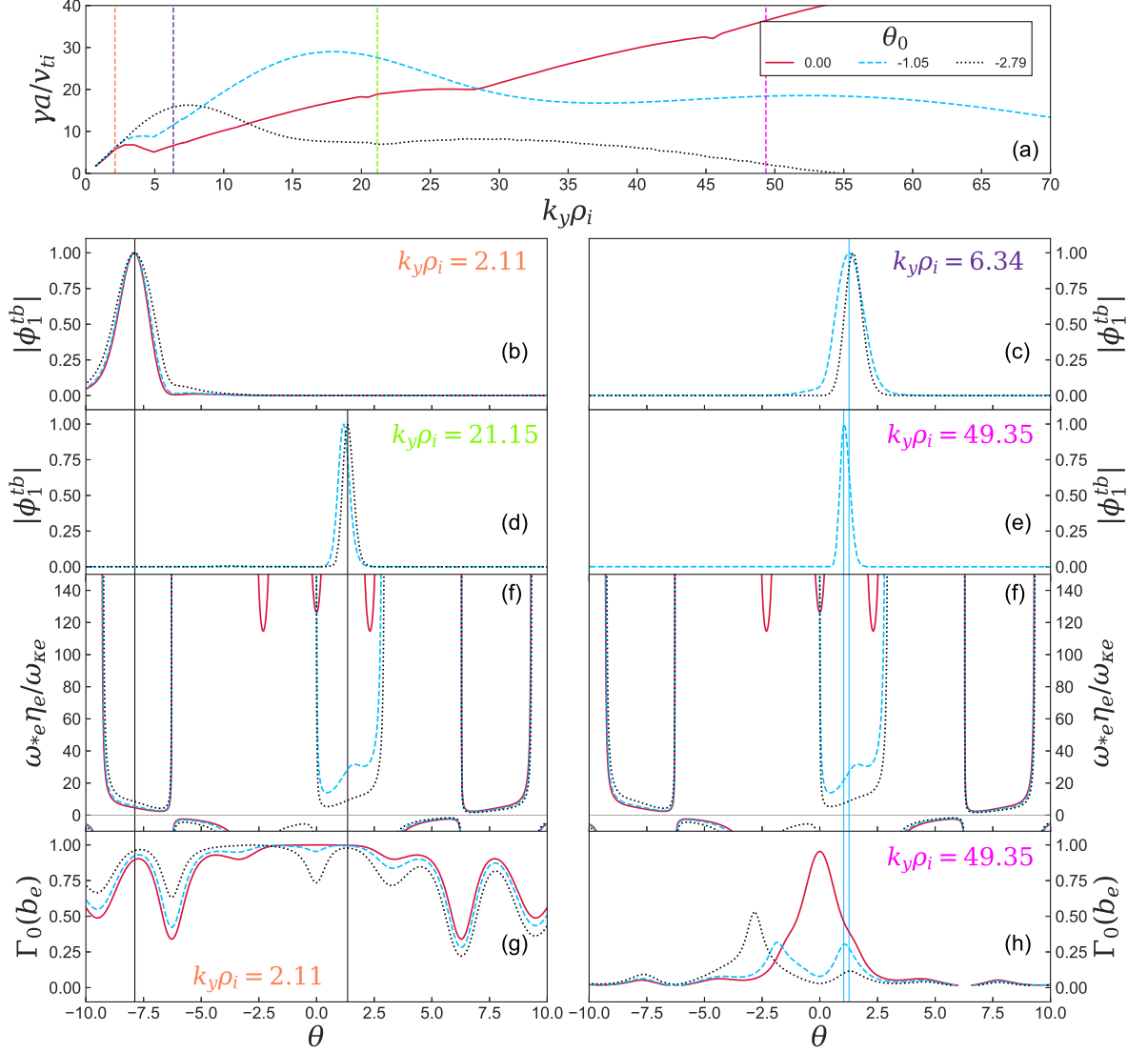


Figure 5.13: The effect of  $\theta_0$  on growth rates and eigenmodes. (a): Growth rates with three values of  $\theta_0$ . Vertical dashed lines indicate the  $k_y\rho_i$  values for the eigenmodes that are shown in (b), (c), (d), and (e). (b), (c), (d), and (e): Eigenmodes for  $k_y\rho_i = 2.11, 6.34, 21.15, 49.35$  and different  $\theta_0$ . (f):  $\omega_{*e}\eta_e/\omega_{ke}$  for different  $\theta_0$ ; for  $|\theta_0|$  sufficiently large, new good curvature regions near  $\theta = 0$  appear. (g) and (h):  $\Gamma_0(b_e)$  for different  $\theta_0$  at two values of  $k_y\rho_i$ . Vertical solid lines on rows 2 - 5 indicate the maximum amplitude of a selected toroidal ETG eigenmode for a given  $\theta_0$ ; if the eigenmode is not shown for a given  $k_y\rho_i$ , then the fastest growing mode for that  $k_y\rho_i$  is not a toroidal ETG mode. Rows 2-5 share the same  $\theta$  axis. Consistent coloring and linestyle series is used throughout the plot, determined by the legend in (a).

that at low values of  $k_y \rho_i$  ( $k_y \rho_i \lesssim 2$ ), the toroidal ETG has a similar growth rate for all values of  $\theta_0$ , whereas for larger values of  $k_y \rho_i$ , the toroidal ETG growth rate becomes very strongly dependent on  $\theta_0$ . We proceed to explain why.

Throughout this thesis, we limit the values of  $\theta_0$  to  $-\pi \leq \theta_0 < \pi$ . To understand why this is useful, recall that the effective radial wavenumber is given by

$$K_x = k_y \hat{s}(\theta_0 - \theta) - k_y \frac{r}{q} \frac{\partial \nu}{\partial r}. \quad (5.4)$$

Under the transformation  $\theta \rightarrow \theta + 2n\pi$ ,  $\theta_0 \rightarrow \theta_0 + 2n\pi$ , where  $n$  is an integer, using that  $\nu$  is  $2\pi$  periodic in  $\theta$ , the quantity  $K_x$  remains unchanged. Because we are using a ‘ballooning’  $\theta$  that can take any value  $-\infty < \theta < \infty$ , we can include the physics of any value of  $\theta_0$  by going to a sufficiently large value of  $\theta$ . We therefore conclude that these two linear modes are the ‘same’ mode, and so it is convenient to use the same angle  $\theta_0$  that is bounded by  $-\pi \leq \theta_0 < \pi$ , rather than assigning the two modes two separate values of  $\theta_0$  that differ by  $\pm 2n\pi$ . Note that this is not valid for nonlinear physics, since different values of  $k_x$  can interact via the nonlinear term.

For  $k_y \rho_i \lesssim 2$ , the location and growth rate of the toroidal ETG mode are fairly independent of  $\theta_0$ , as shown in Figure 5.13(a) and (b). For such small values of  $k_y \rho_i$ , FLR damping is weak at many  $\theta$  locations, that is,  $k_\perp \rho_e \ll 1$  (and hence  $\Gamma_0(b_e) \approx 1$ ) in many distinct bad curvature regions. Since  $\Gamma_0(b_e) \approx 1$  in multiple regions, the fastest growing mode will be located at the value of  $\theta$  where  $\omega_{*e} \eta_e / \omega_{\kappa e}$  is optimal. The value of  $\omega_{*e} \eta_e / \omega_{\kappa e}$  is modified by  $\theta_0$ , shown in Figure 5.13(f). The modification is particularly noticeable for  $|\theta| \lesssim 6$ , where there are regions of much smaller values of  $\omega_{*e} \eta_e / \omega_{\kappa e}$  when  $\theta_0$  is nonzero. For example, for  $\theta_0 = -1.05$ , Figure 5.13(f) shows that  $\omega_{*e} \eta_e / \omega_{\kappa e}$  has values as small as  $\omega_{*e} \eta_e / \omega_{\kappa e} \simeq 15 - 30$  for  $1 \lesssim \theta \lesssim 2$ . While this value of  $\omega_{*e} \eta_e / \omega_{\kappa e}$  is appropriate to have an unstable toroidal ETG mode, at larger values of  $|\theta|$  there exists an even smaller value of  $\omega_{*e} \eta_e / \omega_{\kappa e}$  (recall that smaller  $\omega_{*e} \eta_e / \omega_{\kappa e}$  typically gives higher growth rates as long as  $\omega_{*e} \eta_e / \omega_{\kappa e} \gtrsim 2 - 3$ , see Figure 4.3). Again considering the  $\theta_0 = -1.05$  mode, we see that  $\omega_{*e} \eta_e / \omega_{\kappa e} \simeq 3 - 10$  for  $-8 \lesssim \theta \lesssim -7$ . Because we are currently considering relatively small values of  $k_y \rho_i$ , the FLR damping at  $\theta = -7.7$  is not much stronger than at  $\theta = 1.5$  (see Figure 5.13(g)). Therefore, a mode at  $\theta \simeq -7.7$  grows faster than a mode at  $\theta \simeq 1.5$ . The  $k_y \rho_i = 2.11$  modes in Figure 5.13(b) (all

with  $\theta_0 \leq 0$ ) have their maximum amplitude at  $\theta = -7.7$  rather than  $\theta = 7.7$  because FLR damping is slightly weaker at  $\theta = -7.7$ . Because *both* the  $\omega_{*e}\eta_e/\omega_{\kappa e}$  profiles and the  $\Gamma_0(b_e)$  profiles are not strongly dependent on  $\theta_0$  for  $|\theta| \gtrsim 6$  (see Figure 5.13(f)), the location of the toroidal ETG modes and their associated growth rates are almost independent of  $|\theta_0|$  for  $k_y\rho_i \lesssim 2$ , although the sign of the  $\theta$  location does depend on  $\text{sign}(\theta_0)$ .

We now consider what happens for larger values of  $k_y\rho_i$ . Here, the  $\Gamma_0$  profiles are much more strongly dependent on  $\theta_0$ , as shown in Figure 5.13(h). For  $\theta_0 = 0$ , as  $k_y\rho_i$  increases the toroidal ETG mode cannot grow at a smaller value of  $|\theta|$  because either  $\omega_{*e}\eta_e/\omega_{\kappa e}$  is too large, or the bad curvature region is too narrow, causing the mode to have a stabilizing value of  $k_{\parallel}$ . Hence, the  $\theta_0 = 0$  toroidal ETG mode becomes increasingly FLR damped as  $k_y\rho_i$  increases and at  $k_y\rho_i \simeq 5$ , the slab ETG mode overtakes the FLR damped toroidal ETG mode to become the fastest growing mode (see Figure 5.13(a)). However, for nonzero  $\theta_0$ , the toroidal ETG mode *can* grow at a smaller value of  $|\theta|$  where FLR damping is much weaker, and have a high growth rate because  $\omega_{*e}\eta_e/\omega_{\kappa e}$  is sufficiently small. A consequence of the toroidal ETG mode moving to a bad curvature region with reduced FLR damping is that modes can be unstable in a wide range of poloidal locations, even close to the inboard midplane of the tokamak, a region that has traditionally been considered to have ‘good curvature’ for all values of  $\theta_0$  (see Figure 5.5(b), where even the toroidal ETG mode with  $\theta_0 = 0$  is unstable close to the inboard midplane). However, the maximum eigenmode amplitude for the fastest growing mode is typically close to  $\theta \bmod 2\pi \simeq \pm\pi/2$ , which is mainly due to local magnetic shear causing a local maximum in  $\Gamma_0$  at  $\theta \bmod 2\pi \simeq \pm\pi/2$ .

As shown in Figure 5.13(c), (d), and (e), for nonzero  $\theta_0$  and larger values of  $k_y\rho_i$ , the mode moves to a  $\theta$  location that satisfies  $\theta\theta_0 < 0$ . This can be explained by including  $\theta_0$  in the scaling for  $\omega_{*e}\eta_e/\omega_{\kappa e}$ ,

$$\frac{\omega_{*e}\eta_e}{\omega_{\kappa e}} \sim \frac{k_y}{k_{\perp}} \frac{R_0}{L_{Te}} \sim \frac{1}{\hat{s}(\theta_0 - \theta)} \frac{R_0}{L_{Te}} \sim 1. \quad (5.5)$$

At larger values of  $k_y\rho_i$  when a mode needs to move to a location with a smaller  $|\theta|$  value, it will choose the location where  $\theta\theta_0 < 0$  in order to make  $\omega_{*e}\eta_e/\omega_{\kappa e}$  small.

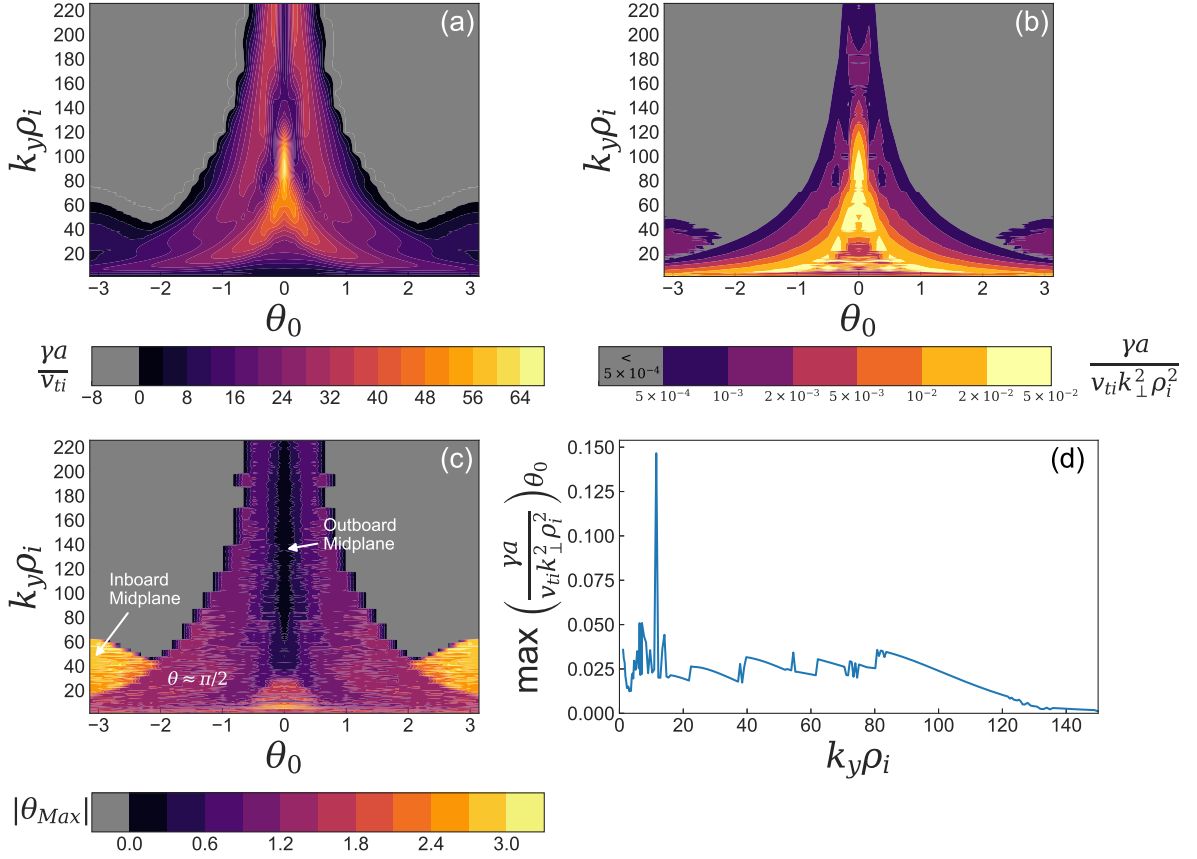


Figure 5.14: Growth rate-associated quantities from GS2 simulations. (a): Contour plot of growth rates versus  $\theta_0$  and  $k_y \rho_i$ . (b): Contour plot of  $\gamma/k_{\perp}^2$  versus  $\theta_0$  and  $k_y \rho_i$ . (c): Location of the maximum of  $|\phi_1^{tb}|$ ,  $\theta_{Max}$ . (d): The maximum value of  $\gamma/k_{\perp}^2$  (over all  $\theta_0$  values) for each value of  $k_y \rho_i$ .

To summarize, for smaller values of  $k_y \rho_i$  (here  $k_y \rho_i \lesssim 2$ ), FLR effects are relatively weak in multiple bad curvature regions, allowing the toroidal ETG mode to choose between multiple  $\theta$  locations in order to find the optimal value of  $\omega_{*e} \eta_e / \omega_{ke}$ . For the equilibrium considered in this work, this occurs for  $|\theta| \gtrsim 6$ . However, when  $k_y \rho_i$  is much larger and  $\theta_0 = 0$ , FLR damping prevents instability at higher values of  $|\theta|$ , even though bad curvature regions still exist there. For larger  $k_y \rho_i$  and  $\theta_0 \neq 0$ , instability becomes possible at lower  $|\theta|$  values due to modest FLR damping in select regions near  $\theta = 0$ .

To gauge the relative importance of toroidal and slab ETG modes for transport, we calculate the quantity  $\gamma/k_{\perp}^2$  for all modes at  $1 \lesssim k_y \rho_i \lesssim 230$  and  $|\theta_0| < \pi$ . The quantity  $\gamma/k_{\perp}^2$  is a rough quasilinear estimate for the transport diffusion coefficient of the mode. To estimate  $k_{\perp}$  for each mode, we find the  $\theta$  location with the largest eigenmode

amplitude, and calculate  $k_{\perp}$  at that location. In Figure 5.14(a), we show the growth rates versus  $\theta_0$  and  $k_y\rho_i$ . There is a notable maximum in the growth rate at  $k_y\rho_i \approx 80$  and  $\theta_0 = 0$  (which corresponds to a slab ETG mode). In Figure 5.14(b) we show the quantity  $\gamma/k_{\perp}^2$  — normalized and presented as the dimensionless parameter  $\gamma a/v_{ti}k_{\perp}^2\rho_i^2$  — versus  $\theta_0$  and  $k_y\rho_i$ . We observe that  $\gamma/k_{\perp}^2$  has its largest values across a wide range of  $k_y\rho_i$  and  $\theta_0$  scales,  $5 \lesssim k_y\rho_i \lesssim 100$  and  $|\theta_0| \lesssim 1.5$ . Most of these modes are toroidal ETG, although when  $\theta_0 = 0$  and  $k_y\rho_i \gtrsim 5$ , the fastest growing mode is a slab ETG mode. We stress that the quantity  $\gamma/k_{\perp}^2$  is only an approximate measure, and that nonlinear simulations in Part II of this thesis will show that these toroidal ETG modes cause at best a 15% change in the heat flux at the radial location we investigate in JET shot 92174. In Figure 5.14(c), we plot the  $|\theta|$  location of the maximum of  $|\phi_1^{tb}|$ , denoted as  $|\theta_{\text{Max}}|$ ; we see that modes with large values of  $\gamma/k_{\perp}^2$  tend to have  $0 \lesssim |\theta_{\text{Max}}| \lesssim \pi/2$ . In Figure 5.14(d), for each  $k_y\rho_i$  we plot the normalized value of  $\gamma/k_{\perp}^2$  that is maximum over  $\theta_0$ . This plot demonstrates that there is a comparable quasilinear diffusion coefficient estimate for all fastest growing modes between  $1 \lesssim k_y\rho_i \lesssim 100$ , and hence suggests that a wide range of  $k_y\rho_i$  values might be important for transport. In Appendix A, we show estimates of  $\gamma/k_{\perp}^2$  for the other three JET discharges we have examined, which demonstrate a qualitatively similar dependence of  $\gamma/k_{\perp}^2$  on  $\theta_0$  and  $k_y\rho_i$  as JET shot 92174 in Figure 5.14(b).

To ascertain how efficiently the toroidal ETG mode can transport heat, we also plot the ratio of the turbulent heat flux to the turbulent energy in Figure 5.15(a). We define the turbulent heat flux for a species  $s$  through the flux surface  $\psi$  as

$$Q_s^{tb}(t) = \left\langle \int \frac{mv^2}{2} \bar{h}_s(\mathbf{R}) \left( \mathbf{v}_E^{tb} \cdot \frac{\nabla x}{\langle |\nabla x| \rangle_{\psi}} \right) d^3v \right\rangle_D. \quad (5.6)$$

Here,  $\langle (\dots) \rangle_D$  is the flux tube spatial average over a volume  $D$  defined as  $\langle (\dots) \rangle_D = (1/D) \int (\dots) d^3r = (1/D) \int (\dots) J_r d\psi d\zeta d\theta$ , where  $\psi$  is integrated between the values  $-\Delta_{\psi}/2$  and  $\Delta_{\psi}/2$  (where  $\Delta_{\psi}$ , the flux tube radial extent, is large compared with the radial turbulent correlation length, but small compared with the device size), and  $\zeta$  and  $\theta$  are integrated between 0 and  $2\pi$ . The flux surface average  $\langle (\dots) \rangle_{\psi}$  is given by

$$\langle (\dots) \rangle_{\psi} = \frac{2\pi}{V'} \oint (\dots) \mathcal{J}_r d\theta, \quad (5.7)$$

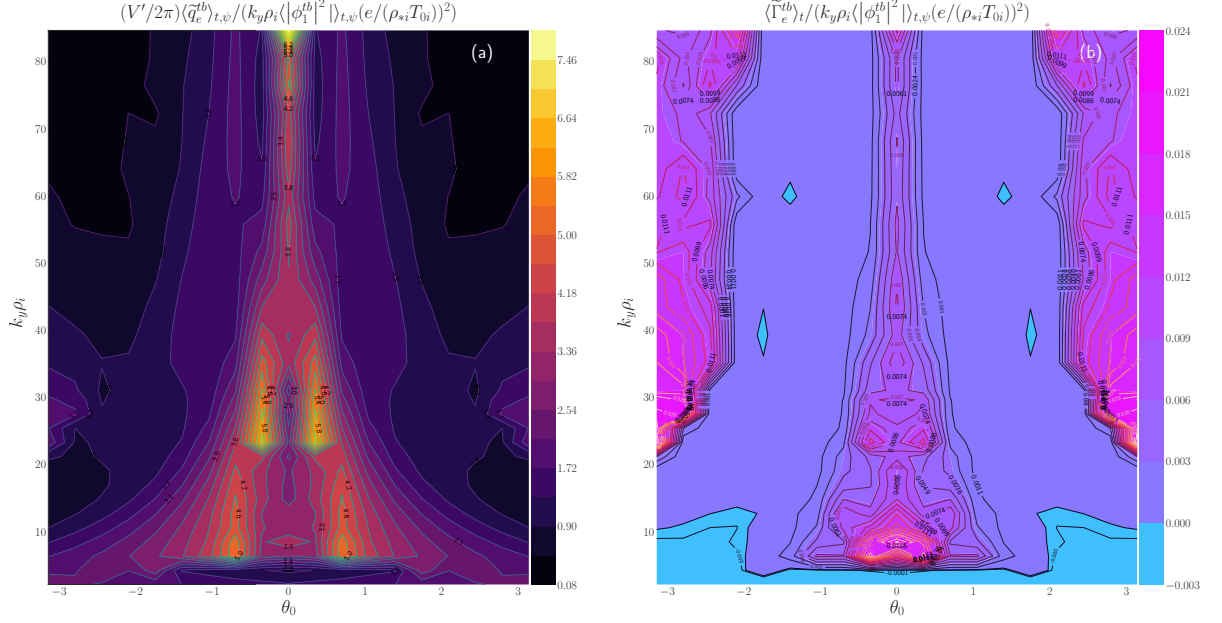


Figure 5.15: Quasilinear estimate for the normalized heat and particle fluxes. (a):  $(V'/2\pi)\langle\tilde{q}_e^{tb}\rangle_{t,\psi}/(k_y\rho_i\langle|\phi_1^{tb}|^2\rangle_{t,\psi}(e/(\rho_*iT_{0i}))^2)$ , (b):  $\langle\tilde{\Gamma}_e^{tb}\rangle_t/(k_y\rho_i\langle|\phi_1^{tb}|^2\rangle_{t,\psi}(e/(\rho_*iT_{0i}))^2)$ .

where  $V' = 2\pi \oint \mathcal{J}_r d\theta = D/(\Delta\psi)$ , and the quantity  $\mathcal{J}_r = 1/\mathbf{B}\cdot\nabla\theta$  is the spatial Jacobian. It is important to note that the quantity  $\langle|\nabla x|\rangle_\psi$  is flux surface averaged. After some tedious manipulations, we find

$$Q_s^{tb}(t) = - \sum_{k_x, k_y} \frac{ick_y(2\pi)^2}{\langle|\nabla r|\rangle_\psi B_a V'} \int \mathcal{J}_r d\theta \int d\epsilon d\mu \mathcal{J} \frac{m_s v^2}{2} h_{s, k_x, k_y} \phi_{1, -k_x, -k_y}^{tb} J_0 \left( \sqrt{2b_s} \hat{v}_\perp \right). \quad (5.8)$$

In order to understand the turbulence intensity distribution in  $k_x, k_y$ , and  $\theta$ , it is useful to define  $q_s^{tb}$  as

$$q_s^{tb}(k_x, k_y, \theta, t) = - \frac{ick_y(2\pi)^2}{\langle|\nabla r|\rangle_\psi B_a V'} \int d\epsilon d\mu \mathcal{J} \frac{m_s v^2}{2} h_{s, k_x, k_y} \phi_{1, -k_x, -k_y}^{tb} J_0 \left( \sqrt{2b_s} \hat{v}_\perp \right). \quad (5.9)$$

Here,  $q_s^{tb}$  is defined such that  $Q_s^{tb}(t) = \sum_{k_x, k_y} \int q_s^{tb}(k_x, k_y, \theta, t) J_r d\theta$ . We also choose to normalize the heat flux to its gyroBohm value,

$$Q_{\text{gB}} = \left( \frac{\rho_i}{a} \right)^2 p_{0i} v_{ti}, \quad (5.10)$$

define  $\tilde{Q}_s^{tb} \equiv Q_s^{tb}/Q_{\text{gB}}$ , and write the normalized perturbed electrostatic potential as  $\phi_1^{tb} e/(\rho_* i T_{0i})$ . Using these normalizations, we plot the quantity

$(V'/2\pi)\langle\tilde{q}_e^{tb}\rangle_{t,\psi}/(k_y\rho_i\langle|\phi_1^{tb}|^2\rangle_{t,\psi}(e/(\rho_{*i}T_{0i}))^2)$  versus  $k_y\rho_i$  and  $\theta_0$ , where we define

$$\tilde{q}_s^{tb} = \frac{q_s^{tb}}{Q_{gB}}. \quad (5.11)$$

We have introduced the time average  $\langle(\dots)\rangle_t = (1/T)\int(\dots)dt$ , where  $T \gg 1/\gamma$  and  $\gamma$  is the typical growth rate of an instability. If  $(V'/2\pi)\langle\tilde{q}_e^{tb}\rangle_{t,\psi}/(k_y\rho_i\langle|\phi_1^{tb}|^2\rangle_{t,\psi}(e/(\rho_{*i}T_{0i}))^2) \sim 1$ , according to this quasilinear estimate, the mode can efficiently transport heat. As Figure 5.15(a) shows,  $(V'/2\pi)\langle\tilde{q}_e^{tb}\rangle_{t,\psi}/(k_y\rho_i\langle|\phi_1^{tb}|^2\rangle_{t,\psi}(e/(\rho_{*i}T_{0i}))^2)$  can have values as large as 7, and thus we might expect the toroidal ETG mode to efficiently transport heat.

While significant heat might be transported by toroidal ETG modes, they are unlikely to transport particles because the ions are very close to adiabatic (see Figure 5.3(b)). However, since the ions are not fully adiabatic for the slab ETG at lower  $k_y\rho_i$  (see Figure 5.3(b)), the long wavelength slab ETG instability might cause particle transport. Finally, the ‘extended ETG’ modes, which are the fastest growing modes for  $0.1 \lesssim k_y\rho_i \lesssim 1$  (see Appendix B), can also have a large non-adiabatic ion response, and thus they too, may cause particle transport. To test these ideas, in Figure 5.15(b) we plot  $\langle\tilde{\Gamma}_e^{tb}\rangle_t/(k_y\rho_i\langle|\phi_1^{tb}|^2\rangle_{t,\psi}(e/(\rho_{*i}T_{0i}))^2)$ , where we define the turbulent particle flux as

$$\Gamma_s^{tb}(k_x, k_y, t) = \left\langle \int \bar{h}_s(\mathbf{R}) \left( \mathbf{v}_E^{tb} \cdot \frac{\nabla x}{|\nabla x|_\psi} \right) d^3v \right\rangle_\psi. \quad (5.12)$$

Figure 5.15(b) shows that  $\langle\tilde{\Gamma}_e^{tb}\rangle_t/(k_y\rho_i\langle|\phi_1^{tb}|^2\rangle_{t,\psi}(e/(\rho_{*i}T_{0i}))^2) \ll 1$ , where  $\tilde{\Gamma}_e^{tb}$  is the gyroBohm normalized form of Equation (5.12). Hence, none of the fastest growing modes in the linear spectrum will likely cause any substantial particle transport.

Next, we show how the values of  $\theta_0$ ,  $\theta_{\min}$ , and  $\hat{s}$  determine the critical temperature gradient of the toroidal ETG mode.

## 5.4 Critical $R_0/L_{Te}$

We now discuss the critical temperature gradient for the toroidal ETG instability that we are studying. We find critical  $R_0/L_{Te}$  values as large as  $R_0/L_{Te} \approx 32$  for toroidal ETG modes in the pedestal (see Figure 5.17(a), and Figure 5.18(a)), significantly larger than in the core. Unless mentioned otherwise, the quantity  $\eta_e$  will be kept fixed, to prevent the ETG from becoming stable due to  $\eta_e$  being less than its critical value.

We want to understand the dependence of the critical  $R_0/L_{Te}$  on different parameters. Recall from Figure 4.3(a) that there exists a stability boundary  $\omega_{*e}\eta_e/\omega_{\kappa e}$  for the toroidal ETG mode; that is, for instability we require

$$\frac{\omega_{*e}\eta_e}{\omega_{\kappa e}} > C. \quad (5.13)$$

For  $b_e = 0$ ,  $C \simeq 2$ . Given that  $\omega_{*e}\eta_e/\omega_{\kappa e} \sim R_0/\hat{s}L_{Te}$ , and that  $\hat{s}$  and  $R_0/L_{Te}$  are fixed parameters, the only free parameter in our scaling theory for the ratio  $\omega_{*e}\eta_e/\omega_{\kappa e}$  for a given equilibrium is  $\theta$  (note that  $C$  in Equation (5.13) is weakly dependent on  $\theta$ , because  $C$  depends on  $b_e$ , which in turn depends on  $\theta$ ). For the toroidal ETG mode to be unstable we then require

$$\frac{R_0}{\hat{s}L_{Te}} \frac{1}{C} \gtrsim \theta \gtrsim \theta_{\min}. \quad (5.14)$$

The quantity  $\theta_{\min}$  is determined by the profiles of  $\omega_{*e}\eta_e/\omega_{\kappa e}$  and  $\Gamma_0$  (see discussion at start of Section 5.2). If a simulation only resolves up to  $\theta < \theta_{\min}$  in ballooning space (or equivalently insufficiently large values of  $|K_x|$ ), a toroidal ETG mode might incorrectly appear to be stable.

Our numerical results have shown that  $\theta_{\min}$  is only very weakly dependent on  $R_0/L_{Te}$ , but can be strongly dependent on  $\theta_0$ , and on  $\hat{s}$  for large values of  $\hat{s}$ . For now we set  $\theta_0 = 0$ , but will soon consider the  $\theta_0 \neq 0$  case. Thus, from Equation (5.14) we obtain a critical gradient,  $R_0/L_{Te}^{\text{crit}}$ ,

$$\frac{R_0}{L_{Te}^{\text{crit}}} \approx \hat{s}\theta_{\min}C. \quad (5.15)$$

When the growth rate is relatively small and comparable to  $\nu_{ee}$ , and  $|\theta_0|$  is sufficiently small and  $\hat{s}$  is sufficiently large, a mode different from the toroidal ETG modes that we are studying often appears. This means that we are sometimes unable to directly show the toroidal ETG growth rate going to zero. When we artificially decrease the collision frequency (keeping all other parameters fixed) to  $\nu_{ee}a/v_{ti} \simeq 0.1$ , the toroidal ETG growth rates visibly go to zero. Therefore, we first discuss the low collisionality cases in which we can almost find  $R_0/L_{Te}^{\text{crit}}$  for the toroidal ETG mode before another mode (such as the mode due to high collisionality) appears. Following this, we discuss the simulations with the standard collisionality.

For the low collisionality case, we demonstrate the  $\hat{s}$  and  $\theta_{\min}$  scaling of the critical temperature gradient by performing a scan in  $R_0/L_{Te}$  for three different values of  $\hat{s}$ ,

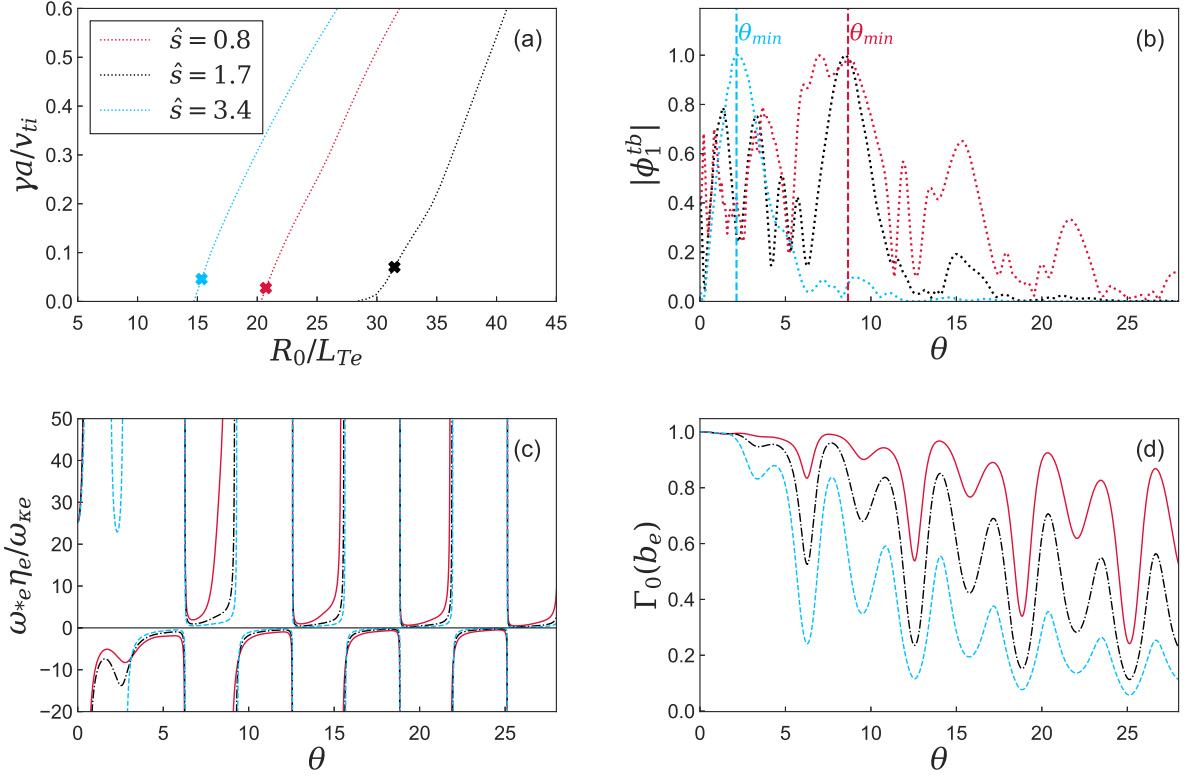


Figure 5.16: Stability plots of the toroidal ETG mode with  $k_y\rho_i = 2.8$  with lower collisionality. (a): Growth rate scan in  $R_0/L_{Te}$  with  $\eta_e$  and  $\eta_i$  fixed for three values of  $\hat{s}$ . (b): Eigenmodes corresponding to values of  $R_0/L_{Te}$  denoted by the colors in (a). (c): The quantity  $\omega_{*e}\eta_e/\omega_{\kappa e}$  for three values of  $\hat{s}$ , where  $R_0/L_{Te} = 26$ ,  $\eta_e = 4.3$ . (d): The quantity  $\Gamma_0(b_e)$  for three values of  $\hat{s}$ .

shown in Figure 5.16(a). Here,  $\eta_e$  and  $\eta_i$  are held fixed to avoid the  $\eta_s$  stability boundary. This scan is performed in GS2 for  $k_y\rho_i = 2.8$  with the standard pedestal equilibrium we have used before, except for changing the value of  $\hat{s}$ . In Figure 5.16(a), we see that  $\theta_{min} \simeq 2$  for  $\hat{s} = 3.4$ , as shown by the eigenmode in Figure 5.16(c). For this value of  $\hat{s}$ , the eigenmode can have a relatively small value of  $\theta_{min}$  because of the bad curvature region ( $\omega_{*e}\eta_e/\omega_{\kappa e} > 0$ ) that appears at  $\theta \simeq 2$  in Figure 5.16(c). Once  $\hat{s}$  is decreased, the smallest possible value for the mode appears to be  $\theta_{min} \simeq 8.5$ , as shown in Figure 5.16(b) and (c). Due to the scaling of  $R_0/L_{Te}^{crit}$  in Equation (5.15), a much larger value of  $\theta_{min}$  causes  $R_0/L_{Te}^{crit}$  to increase, shown in Figure 5.16(a). Both the cases  $\hat{s} = 0.8$  and  $\hat{s} = 1.7$  have the same value of  $\theta_{min} \simeq 8.5$ , but the  $\hat{s} = 1.7$  case has a much higher  $R_0/L_{Te}^{crit}$  due to its value of  $\hat{s}$  being larger. Thus, we have demonstrated that increasing both  $\hat{s}$  and

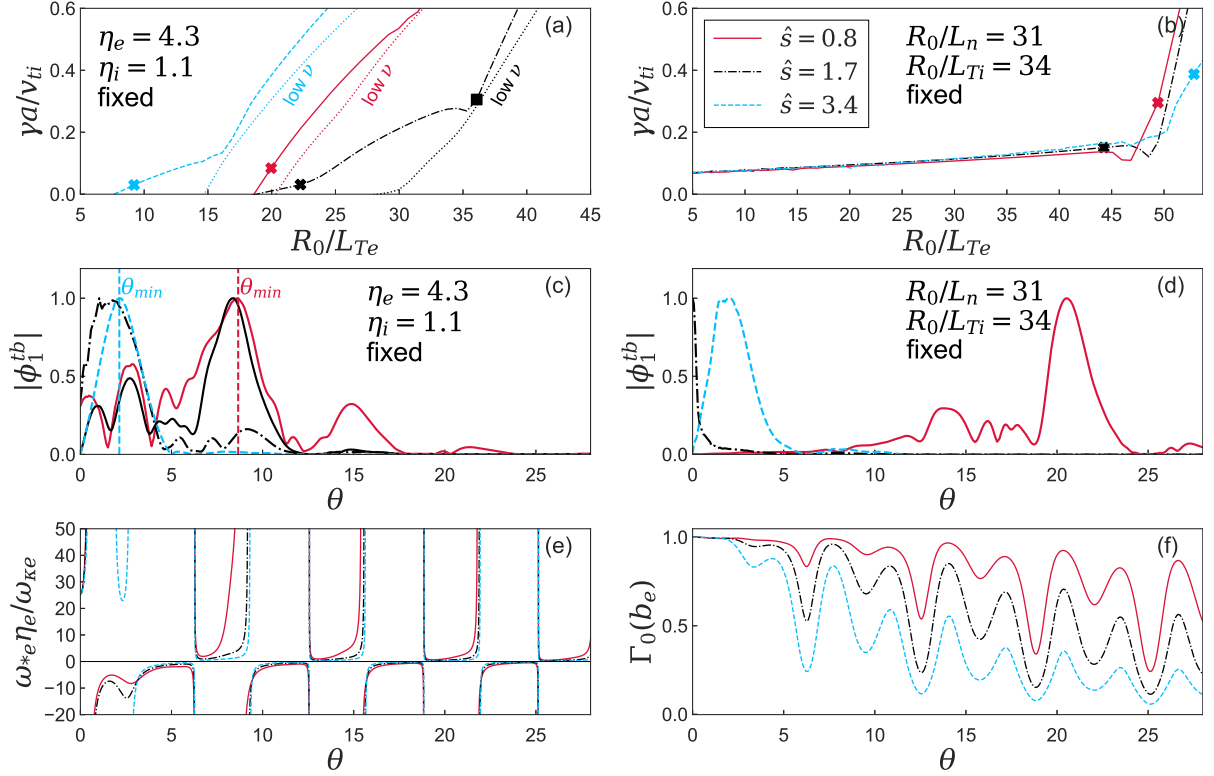


Figure 5.17: Stability plots of the toroidal ETG mode with  $k_y \rho_i = 2.8$ . (a): Growth rate scan in  $R_0/L_{Te}$  with  $\eta_e$  and  $\eta_i$  fixed for three values of  $\hat{s}$  with the standard and lowered collisionality (denoted by dotted lines labelled with ‘low  $\nu$ ’). (b): Growth rate scan in  $R_0/L_{Te}$  with  $R_0/L_n$  and  $R_0/L_{Ti}$  fixed for three values of  $\hat{s}$ . (c): Eigenmodes corresponding to values of  $R_0/L_{Te}$  denoted by the markers in (a). The black dash dotted eigenmode corresponds to the cross marker for  $\hat{s} = 1.7$  in (a), and the black solid eigenmode to the square marker for  $\hat{s} = 1.7$  in (a). (d): Eigenmodes corresponding to values of  $R_0/L_{Te}$  denoted by the markers in (b). (e): The quantity  $\omega_{*e} \eta_e / \omega_{ke}$  for three values of  $\hat{s}$ , where  $R_0/L_{Te} = 26$ ,  $\eta_e = 4.3$ . (f): The quantity  $\Gamma_0(b_e)$  for three values of  $\hat{s}$ .

$\theta_{\min}$  increases  $R_0/L_{Te}^{\text{crit}}$  for the toroidal ETG mode.

For the standard collisionality case, for  $\hat{s} = 1.7, 3.4$  we see that new modes appear at lower values of  $R_0/L_{Te}$  due to higher collisionality, shown in Figure 5.17(a). These modes are different from the toroidal ETG instability because these modes can have large amplitudes in good curvature regions (see the eigenmode corresponding to this ‘collisional’ mode for  $\hat{s} = 1.7$  in Figure 5.17(c), denoted by the dash dotted black line). These modes merit further investigation, but they are outside the scope of this work. Shown by the eigenmode with the solid black line in Figure 5.17(c) (corresponding to the square marker in Figure 5.17(a)), we see that before the fastest growing mode switches to the collisional mode as  $R_0/L_{Te}$  decreases, the toroidal ETG mode indeed has  $\theta_{\min} \simeq 8.5$ , as one would predict from the profile of  $\omega_{*e}\eta_e/\omega_{\kappa e}$  in Figure 5.17(c). In Figure 5.17(a), we see that  $\theta_{\min} \simeq 2$  for  $\hat{s} = 3.4$ , as shown by the corresponding eigenmode in Figure 5.17(c). For this value of  $\hat{s}$ , the eigenmode can have a relatively small value of  $\theta_{\min}$  because of the bad curvature region ( $\omega_{*e}\eta_e/\omega_{\kappa e} > 0$ ) that appears at  $\theta \simeq 2$  in Figure 5.17(e). Once  $\hat{s}$  is decreased to a value of  $\hat{s} = 1.7$ ,  $\theta_{\min}$  appears to also have a value of  $\theta_{\min} \simeq 2$  (shown in Figure 5.17(c)), yet  $R_0/L_{Te}^{\text{crit}}$  increases, in apparent contradiction to Equation (5.15), which predicts that  $R_0/L_{Te}^{\text{crit}}$  should decrease for smaller values of  $\hat{s}$  at fixed  $\theta_{\min}$ . However, this contradiction is due to the collisional mode that appears for smaller values of  $R_0/L_{Te}$ , which for  $\hat{s} = 1.7$  has a value of  $|\theta_{\min}|$  that is much smaller than for the toroidal ETG mode, where  $|\theta_{\min}| \simeq 8.5$ .

As mentioned above, there is another critical value of  $R_0/L_{Te}$  that occurs due to  $\eta_e$  being too small [112]. Figure 5.17(b) shows a scan in  $R_0/L_{Te}$  and  $\hat{s}$  with  $R_0/L_n$  and  $R_0/L_{Ti}$  fixed, allowing  $\eta_e$  to vary; here, the critical value of  $\eta_e$  for the toroidal ETG mode is  $\eta_e \approx 1.3$  (note that although the stability boundary is not visible in Figure 5.17(b), we checked that it indeed exists for the low collisionality case). Interestingly, for smaller values of  $R_0/L_{Te}$  we find a very weakly driven slab ITG mode.

The above arguments assumed that  $|\theta_0| \ll |\theta|$ . The critical temperature gradient is also modified by  $\theta_0$ . As discussed previously, larger values of  $|\theta_0|$  can allow a new region of bad curvature to appear at small values of  $|\theta|$ , as shown in Figure 5.18(d). Allowing  $\theta_0 \neq 0$ , for instability, we require

$$\frac{R_0}{L_{Te}} \gtrsim \hat{s}|\theta - \theta_0|C. \quad (5.16)$$

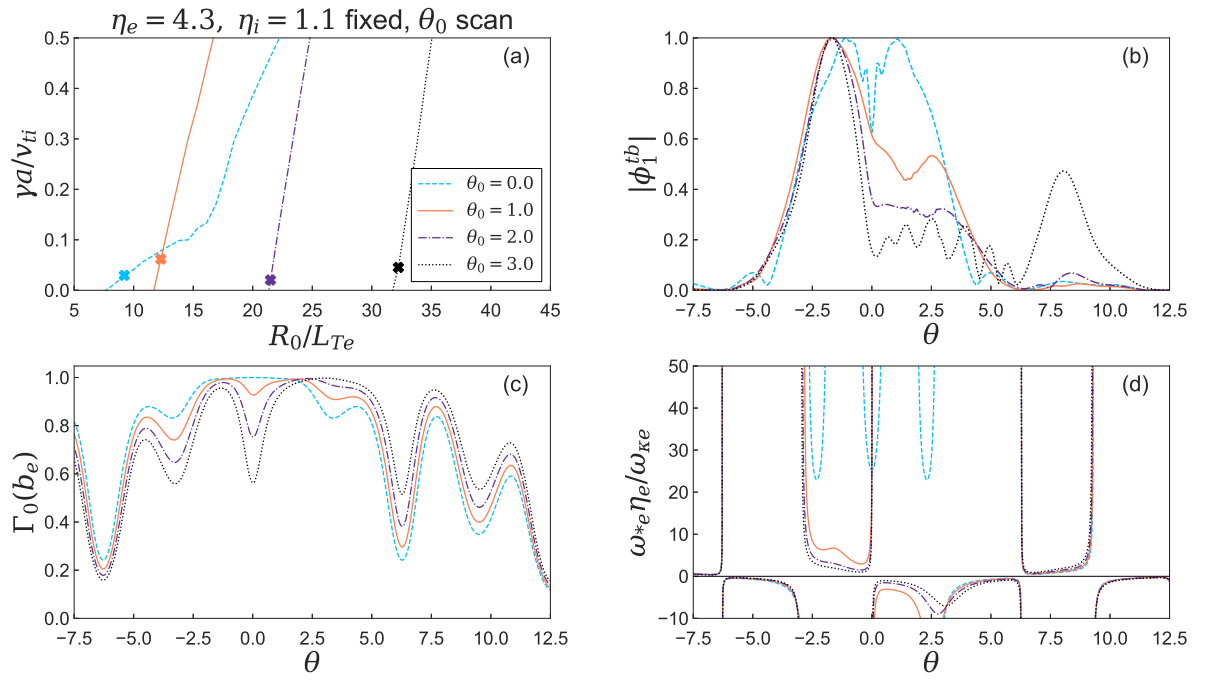


Figure 5.18: Stability plots of the toroidal ETG mode with  $k_y\rho_i = 2.8$ . (a): Growth rate scan in  $R_0/L_{Te}$  with  $\eta_e$  and  $\eta_i$  fixed for four values of  $\theta_0$ . (b): Corresponding eigenmodes at locations indicated by markers in (a). (c): The quantity  $\Gamma_0(b_e)$  for different values of  $\theta_0$ . (d): The ratio  $\omega_{*e}\eta_e/\omega_{\kappa e}$  for different values of  $\theta_0$ , using  $R_0/L_{Te} = 26$ .

We expect that for nonzero  $\theta_0$ ,  $\theta$  and  $\theta_0$  have opposite signs because the mode will grow faster where  $\omega_{*e}\eta_e/\omega_{\kappa e} \sim R_0/L_{Te}\hat{s}|\theta - \theta_0|$  is smallest, giving the critical temperature gradient

$$\frac{R_0}{L_{Te}^{\text{crit}}} \approx \hat{s}(|\theta_{\min}| + |\theta_0|)C. \quad (5.17)$$

Consistent with this idea, we see that for  $|\theta| \lesssim 6$  the only accessible bad curvature regions appear when  $\theta\theta_0 < 0$  and when  $|\theta_0|$  is sufficiently large. To demonstrate the scaling in Equation (5.17), we performed a scan in  $\theta_0$  and  $R_0/L_{Te}$  at fixed  $\hat{s}$ ,  $\eta_e$ , and  $\eta_i$ , shown in Figure 5.18(a); we observe that  $R_0/L_{Te}^{\text{crit}}$  indeed increases with  $\theta_0$  as expected. Furthermore, the assumption that  $\theta_{\min}\theta_0 < 0$  is also shown to be correct, as seen by the eigenmodes in Figure 5.18(b). Curiously, we note that the collisional mode that we found in Figure 5.18 only appears for  $\theta_0 = 0$  at smaller values of  $R_0/L_{Te}$ . For  $\theta_0 = 1.0, 2.0, 3.0$ , we cannot find such a mode.

Finally, we briefly discuss the effect of the difference between  $\omega_{\kappa e}$  and  $\omega_{\nabla Be}$  on toroidal ETG stability. Throughout this work, we have exclusively used  $\omega_{*e}\eta_e/\omega_{\kappa e}$  for our analysis, which is justifiable if  $\omega_{\kappa e} \simeq \omega_{\nabla Be}$  in the parallel vicinity of where the toroidal mode is most unstable. While this is true for  $|\theta| \gtrsim \pi$  (see Figure 5.5(b)), for  $|\theta| \lesssim \pi$ , the value of  $\omega_{\kappa e}/\omega_{\nabla Be}$  in bad curvature regions can be as large as 1.5 in a sufficiently-wide parallel region for some values of  $\theta_0$ . Thus, in the case where  $\omega_{\kappa e} \neq \omega_{\nabla Be}$ , we might expect a change in the linear stability boundary compared to the case where one artificially sets  $\omega_{\kappa e} = \omega_{\nabla Be}$ . Therefore, for certain values of  $k_y\rho_i$  and  $\theta_0$ , the stability boundary for the toroidal ETG mode might be increased when  $\omega_{\kappa e} > \omega_{\nabla Be}$ , which is consistent with previous work [113].

To summarize, we have demonstrated that the value of  $R_0/L_{Te}^{\text{crit}}$  for toroidal ETG depends on  $\hat{s}$ ,  $\theta_{\min}$ , and  $\theta_0$ . Most relevant to the Miller equilibrium of JET discharge 92174, scans in  $\theta_0$  at fixed  $\hat{s} = 3.4$  showed  $R_0/L_{Te}^{\text{crit}} \approx 8 - 32$ , depending on the value of  $\theta_0$ . This is a much higher value of  $R_0/L_{Te}^{\text{crit}}$  than is typically observed in the core (for example,  $R_0/L_{Ti}^{\text{crit}} \approx 3$  for Cyclone Base Case toroidal ITG). This new type of stability boundary for toroidal ETG directly results from the importance of the radial component of the magnetic drift, in contrast to the core, where the  $\nabla y$  component of the drift is usually considered more important.

# Chapter 6

## ITG Stability in the Pedestal

In this chapter, we discuss the ITG instability in JET shot 92174. Previous works have emphasized the importance of ITG instability in the pedestal [65, 77, 114–116]. In this work, we find that with the measured  $T_{0i}$  profiles, the ITG growth rate is extremely small compared with the ETG instability growth rate. This is due to  $R_0/L_{Ti}$  and  $\eta_i$  being relatively small, and electron collisions that decrease the ITG growth rates. If we increase the ion temperature profiles to make them equal to the electron temperature profiles and we ignore the  $\mathbf{E} \times \mathbf{B}$  shear, the ITG instability is the fastest growing mode at very large scales,  $k_y \rho_i \sim L_{Ti}/R_0$ . This finding is entirely consistent with Chapter 4’s results, as the same arguments can equally be applied to ITG (since  $R_0/L_{Ti} \gg 1$ ). While this section will discuss ITG for  $\theta_0 = 0$ , we also performed a scan in  $\theta_0$ , to see if any other  $\theta_0 \neq 0$  values could be unstable at  $k_y \rho_i \lesssim 1$  using the measured ion temperature profile. We found no significant increase in growth rates due to  $\theta_0$  with the measured ion profiles.

Due to the symmetry of the collisionless ITG and ETG dispersion relations when  $h_e = 0$  for ITG and  $h_i = 0$  for ETG, the growth rates of ITG and ETG are isomorphic:  $\gamma_{\text{ITG}} = \gamma_{\text{ETG}} \rho_e / \rho_i$  at wavenumbers  $k_{y\text{ITG}} = k_{y\text{ETG}} \rho_e / \rho_i$ . Here we investigate how the non-adiabatic electron response and a difference in equilibrium profiles in the pedestal break this isomorphism. According to the isomorphism, ITG instability is driven at  $k_y \rho_i \sim L_{Ti}/R_0 \ll 1$ , and the ETG instability is driven at  $k_y \rho_i \sim (\rho_i/\rho_e)L_{Te}/R_0$ , as demonstrated in Figure 6.1. In Figure 6.1, we show the growth rates of ITG at ‘ITG’ scales,  $k_y \rho_i \sim L_{Ti}/R_0$ , and the growth rates of ETG at ‘ETG’ scales,  $k_y \rho_i \sim (\rho_i/\rho_e)L_{Te}/R_0$ , for JET shot 92174. The isomorphism between ITG and ETG is confirmed, with the ‘ $T_{0i} =$

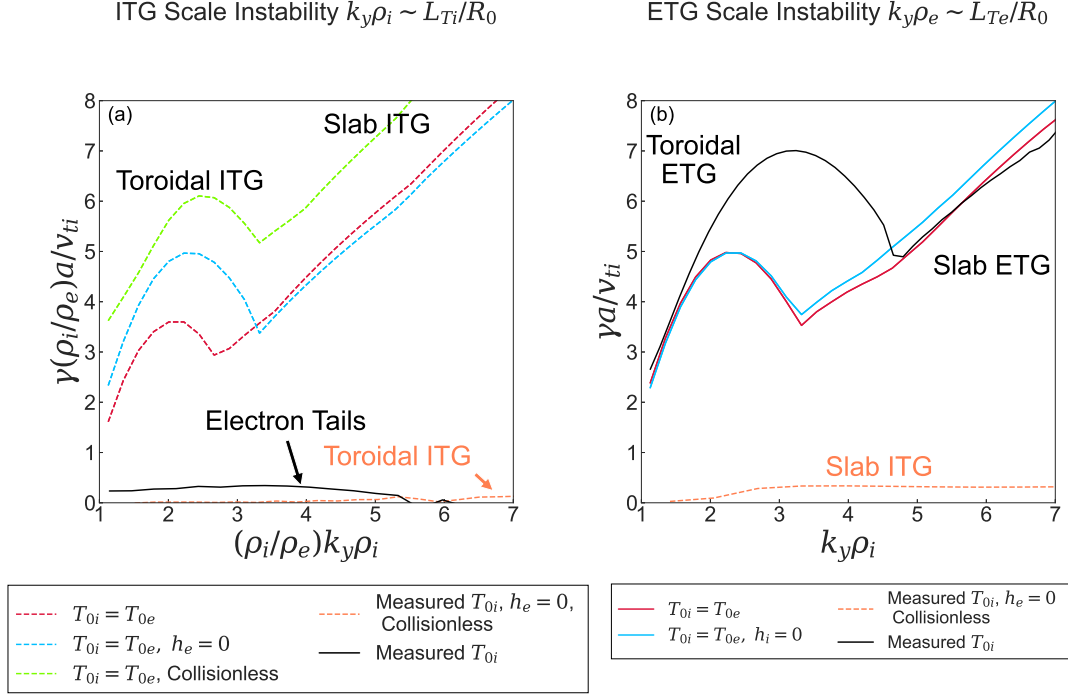


Figure 6.1: Linear ITG and ETG GS2 growth rates at (a):  $k_y \rho_i \sim L_{Ti}/R_0$  (ITG scales) and (b):  $k_y \rho_e \sim L_{Te}/R_0$  (ETG scales). Dashed series indicates an ITG mode, solid is a mode driven by electron temperature gradients. For the ITG scales, the growth rates and  $k_y \rho_i$  have been multiplied by  $\rho_i/\rho_e$ . The series ‘ $T_{0i} = T_{0e}$ ’ indicates that  $T_{0e} = T_{0i}$ ,  $L_{Ti} = L_{Te}$ ; ‘Measured  $T_{0i}$ ’ indicates that values of  $T_{0i}$  and  $L_{Ti}$  are taken from the measured ion profiles. Here,  $\rho_i/\rho_e \approx 82$  for the measured  $T_{0i}$  and  $T_{0e}$  profiles, and  $\rho_i/\rho_e \approx 61$  when  $T_{0i} = T_{0e}$ .

$T_{0e}, h_e = 0$ ’ and ‘ $T_{0i} = T_{0e}, h_i = 0$ ’ cases having the same isomorphic growth rates. Here, ‘ $T_{0i} = T_{0e}$ ’ means that both the ion and electron temperatures and their gradients are set equal to each other — specifically,  $T_{0e}$  is increased to match  $T_{0i}$ , and  $R_0/L_{Ti}$  becomes as large as  $R_0/L_{Te}$ . This affects the electron collision frequencies, which are decreased self-consistently. Note that the difference between the toroidal ETG growth rates in Figure 6.1(b) is mainly due to a different electron temperature, not a different collisionality.

Electron collisions have a significant effect on the toroidal and slab ITG growth rates. As shown in Figure 6.1(a), there is a substantial difference between the collisional and collisionless simulations, indicated by ‘ $T_{0i} = T_{0e}$ ’ and ‘ $T_{0i} = T_{0e}$ , Collisionless’ cases. In the simulations we have performed, electron collisions reduce the toroidal and slab ITG growth rates. It is not obvious that electron collisions should always decrease the

ITG growth rates, or whether this stabilization can be ascribed to trapped or passing electrons. At these scales,  $\nu_{ee}a/v_{ti} \sim 0.8 \gg \gamma_{\text{ITG}}a/v_{ti}$  and the modes with kinetic electron physics have a significant contribution of passing electrons due to the long electron ‘tails’ shown in Figure B.1 in Appendix B. Hence, at scales where there is ITG instability, the trapped electron response will be collisionally coupled to the large passing electron response.

We now describe gyrokinetic simulations with the measured ion profiles. Compared with the equal profile case, ‘ $T_{0i} = T_{0e}$ ,’ once measured equilibrium profiles are included, the ITG growth rates decrease substantially. In Figure 6.1(a), ‘Measured  $T_{0i}$ ’ is a simulation with the measured ion temperature profiles; the fastest growing modes at ITG scales are electron-driven modes with large electron tails [106] (see Appendix B), switching to a toroidal ETG mode once  $k_y\rho_i \gtrsim 0.1$ . In order to find the subdominant ITG instability, we must set  $h_e = 0$  (otherwise electron-driven modes dominate), as shown in the ‘Measured  $T_{0i}$ ,  $h_e = 0$ ’ line. The ITG instability barely grows in the runs with adiabatic electrons, although there were well-resolved toroidal ITG eigenmodes. Using GS2’s eigensolver function [117], we could not find any toroidal ITG instability for  $k_y\rho_i \sim L_{Ti}/R_0$  when using the measured profiles and kinetic electrons, indicating that ITG is stable at  $k_y\rho_i \ll 1$ . However, at ETG scales ( $k_y\rho_e \sim L_{Te}/R_0$ ), we did find weakly growing slab ITG modes by using adiabatic electrons, shown in Figure 6.1(b) (‘Measured  $T_{0i}$ ,  $h_e = 0$ ’), a result that was corroborated by very weakly growing slab ITG modes found using GS2’s eigensolver. Therefore, for the measured profiles, ITG is extremely subdominant in JET shot 92174. Moreover, we will see in Chapter 7 that the slab ITG is easily quenched by  $\mathbf{E} \times \mathbf{B}$  shear.

Heuristically, we can understand the stability of the toroidal ITG mode using a similar stability analysis performed for the toroidal ETG mode in Section 5.4. In Figure 5.17(b), we show the toroidal ETG mode being stabilized at  $\eta_e \simeq 1.3$  (we checked the toroidal ETG growth rates went to zero for the low collisionality case; in the correct collisionality case shown in Figure 5.17(b), a slab ITG mode appears before the toroidal ETG mode can be seen to be stabilized). Due to the isomorphism between toroidal ITG and toroidal ETG in the collisionless case where the other species is adiabatic, we can reasonably predict that toroidal ITG also has a similar critical  $\eta_i \approx 1$ . Examining the  $\eta_i$  profile in

Figure 3.1(c), we find that  $\eta_i \simeq 0.8 - 1.2$  in the steep gradient region of the pedestal ( $r/a \approx 0.97 - 0.99$ ). Hence,  $\eta_i$  is very close to (and likely slightly below) its critical value in all regions of the pedestal for  $\theta_0 = 0$ , and it is unsurprising that the toroidal ITG mode is very weakly-driven. A broader question that merits examination is the physics that keeps  $\eta_i$  close to its critical value, while  $\eta_e$  is far above its critical value (although this is subject to uncertainties in the ion temperature profile, which could change  $\eta_i$ ). Finally, the suppression of ITG instability in pedestals is not inconsistent with what has been observed in previous analyses; for example, [118] found that the ion heat diffusion was close to neoclassical in ASDEX-U inter-ELM pedestal discharges.

One might be concerned about the use of local simulations to analyze these large scale ITG modes. For JET shot 92174, at  $r/a = 0.9743$  the local equations require  $k_\perp \rho_i \gg \rho_i/L_{Te} = 0.12$  to be valid. Just as steep electron temperature gradients and FLR effects require toroidal ETG modes with wavenumber  $k_y \rho_e \sim L_{Te}/R_0$  to satisfy  $k_\perp \rho_e \sim 1$ , steep ion temperature gradients and FLR effects require toroidal ITG modes with wavenumber  $k_y \rho_i \sim L_{Ti}/R_0$  to satisfy  $k_\perp \rho_i \sim 1$ . Thus, even the long wavelength toroidal ITG does not violate  $k_\perp \rho_i \gtrsim 0.12$ . For example, we find that the toroidal ITG mode in Figure 6.1(a) with  $k_y \rho_i = 0.04$  ( $T_{0e} = T_{0i}, h_e = 0'$ ) has an eigenmode maximum at  $k_\perp \rho_i = 0.9$ , and so is far from violating the condition  $k_\perp \rho_i \sim 0.12$ . One might be concerned about the corresponding long wavelength slab ITG modes in Figure 6.1(a), since  $k_y \rho_i$  can be as small as  $k_y \rho_i \simeq 0.05$  for the fastest growing slab ITG instability; however, similar to the slab ETG instability, these eigenmodes are still quite extended in  $\theta$  for smaller values of  $k_y \rho_i$ . For a slab ITG mode with  $k_y \rho_i = 0.05$ , we find the eigenmode maximum occurring at a location where  $k_\perp \rho_i = 0.2$ , with many other peaks in the eigenmode with very similar amplitudes occurring at  $\theta$  locations where  $k_\perp \rho_i \gtrsim 1.0$ . There may be subdominant ITG modes at  $k_y \rho_i \sim L_{Ti}/R_0$  that are very narrow in  $\theta$ , and hence have  $k_\perp \rho_i \sim L_{Ti}/R_0$ ; such modes would likely be poorly described by a local prescription, and therefore we would not dare to include such modes in our analysis. To summarize, the radial profile variation would be much more important for modes where  $K_x \rho_i$  is sufficiently small, but we are examining modes that are typically much less extended in the radial direction than in the  $y$  direction, and hence we do not expect a big difference between local and global simulations for these  $K_x \gg k_y$  modes. Given

the particular importance of FLR damping for these modes in the pedestal, having an accurate gyroaveraging scheme is also useful, which can be more challenging to implement for global simulations [119].

To summarize, we find that with the measured ion temperature profiles, the ITG mode is stable for  $k_y \rho_i \ll 1$ , and there is very weakly-driven ITG at  $k_y \rho_i \sim 1$ . When the ion temperature profile is set equal to the electron profile and ITG modes become linearly unstable at very long wavelengths, the isomorphism between ITG with  $h_e = 0$  and ETG with  $h_i = 0$  holds. Electron collisions appear to decrease the ITG growth rate significantly. The detailed mechanism for this stabilizing impact of electron collisions requires further investigation.

# Chapter 7

## Flow Shear

In this work we chose to perform most simulations without  $\mathbf{E} \times \mathbf{B}$  shear, since in simulations with  $\mathbf{E} \times \mathbf{B}$  shear, the electrostatic modes were barely modified compared to the simulations without  $\mathbf{E} \times \mathbf{B}$  shear.

In this chapter, we present the results of gyrokinetic simulations with  $\mathbf{E} \times \mathbf{B}$  shear. We first briefly discuss the flow shear algorithm used for these simulations. We then discuss the validity of keeping  $\mathbf{E} \times \mathbf{B}$  shear, even though it is small in the low flow ordering. After that, in addition to the results we presented in Chapter 3 where KBMs were argued to be suppressed by  $\mathbf{E} \times \mathbf{B}$  shear, we show the effect of  $\mathbf{E} \times \mathbf{B}$  shear on KBMs, ETG modes, and ITG modes. We will see that while KBMs usually are easily suppressed by  $\mathbf{E} \times \mathbf{B}$  shear, ETG modes are barely affected. ITG instability is easily stabilized when using the measured ion temperature profile, but is not fully-suppressed when the ion temperature profile is made equal to the electron temperature profile.

In our local linear simulations with  $\mathbf{E} \times \mathbf{B}$  shear, we use a new  $\mathbf{E} \times \mathbf{B}$  shear algorithm [120], and also tested that the results were qualitatively similar with the previous GS2 algorithm [121]. With the newer algorithm, a typical simulation with  $\mathbf{E} \times \mathbf{B}$  shear contained a single poloidal mode, 150 radial wavenumbers with a spacing of  $\Delta k_x \approx k_y$ , and a  $\mathbf{E} \times \mathbf{B}$  shear value of  $\gamma_E a / v_{ti} = 0.56$ . With the previous algorithm, the range of  $k_x$  values was held fixed, but the  $\Delta k_x$  spacing was reduced by a factor of 10.

In the low flow ordering, if one retains the  $\mathbf{E} \times \mathbf{B}$  shear, one should also keep neoclassical corrections to the Maxwellian [16, 122], but for simplicity, we have neglected neoclassical corrections throughout this work. When analyzing high  $k_\perp$  modes for this

equilibrium, it is inconsequential whether or not the  $\mathbf{E} \times \mathbf{B}$  shear is kept, and we expect the neoclassical corrections to be similarly unimportant. However, for small  $k_\perp$ , we find the small  $\mathbf{E} \times \mathbf{B}$  shear can suppress instabilities and hence one might expect that neoclassical corrections are also important.

The parallel flow is one of the main physical features of neoclassical corrections. Therefore to estimate the effect of these corrections, we will use previous studies on the parallel velocity gradient (PVG) instability [123–128]. The PVG growth rate is

$$\gamma_{\text{PVG}} \sim \frac{du_{\zeta ip}}{dr} k_y \rho_i. \quad (7.1)$$

In regions where we see ITG stabilization by  $\mathbf{E} \times \mathbf{B}$  shear,  $k_y \rho_i \sim 0.1$ , and the PVG growth rate is much smaller than the  $\mathbf{E} \times \mathbf{B}$  shear rate. From the measured  $^{12}\text{C}^+$  rotation profiles at  $r/a = 0.974$ , we find that  $|du_{\zeta ip}/dr|a/v_{ti} \approx 1.4$ , and thus  $\gamma_{\text{PVG}}a/v_{ti} \approx 0.14$ . Therefore, given that  $\gamma_E a/v_{ti} = 0.56 > \gamma_{\text{PVG}}a/v_{ti}$ , this PVG mode is likely stabilized by the  $\mathbf{E} \times \mathbf{B}$  shear. Hence, we do not expect that the neoclassical flows will significantly modify a mode's growth rate, although the effect of neoclassical terms at these small scales merits further investigation.

The  $\mathbf{E} \times \mathbf{B}$  shear is usually more effective for low than for high  $k_\perp$  modes, as shown in Figure 7.1. This is because the growth rate of the electrostatic instabilities that we are investigating typically scales with  $\omega_{*s} \eta_s \sim k_y \rho_s v_{ts} / L_{Ts}$ , and because of the differences in a mode's radial extent for different instabilities. If the typical timescale for an instability,  $1/\gamma$ , is comparable to the  $\mathbf{E} \times \mathbf{B}$  shearing time,  $1/\gamma_E$ , the  $\mathbf{E} \times \mathbf{B}$  shear can be effective. However, when  $1/\gamma_E \gg 1/\gamma \sim L_{Ts}/k_y \rho_s v_{ts}$ , the  $\mathbf{E} \times \mathbf{B}$  shear is unable to shear the mode sufficiently quickly. Hence,  $\mathbf{E} \times \mathbf{B}$  shear suppresses modes at smaller  $k_y$ , and barely modifies short wavelength modes. Additionally, modes that are radially localized ( $K_x \gg k_y$ ) are harder to shear than those with a wider radial width; this is apparent when examining the middle term in Equation (7.3). If the time independent piece of  $|K_x|$  is already large, it will take a long time for flow shear to change  $|K_x|$  substantially, by which time the linear mode will have likely already grown for multiple e-folding times. Hence, modes with  $K_x \gg k_y$  are challenging to suppress with flow shear.

We now apply these two criteria (growth rate versus shearing rate, and radial extent of the mode) to explain our observations for which modes are suppressed by  $\mathbf{E} \times \mathbf{B}$  shear.

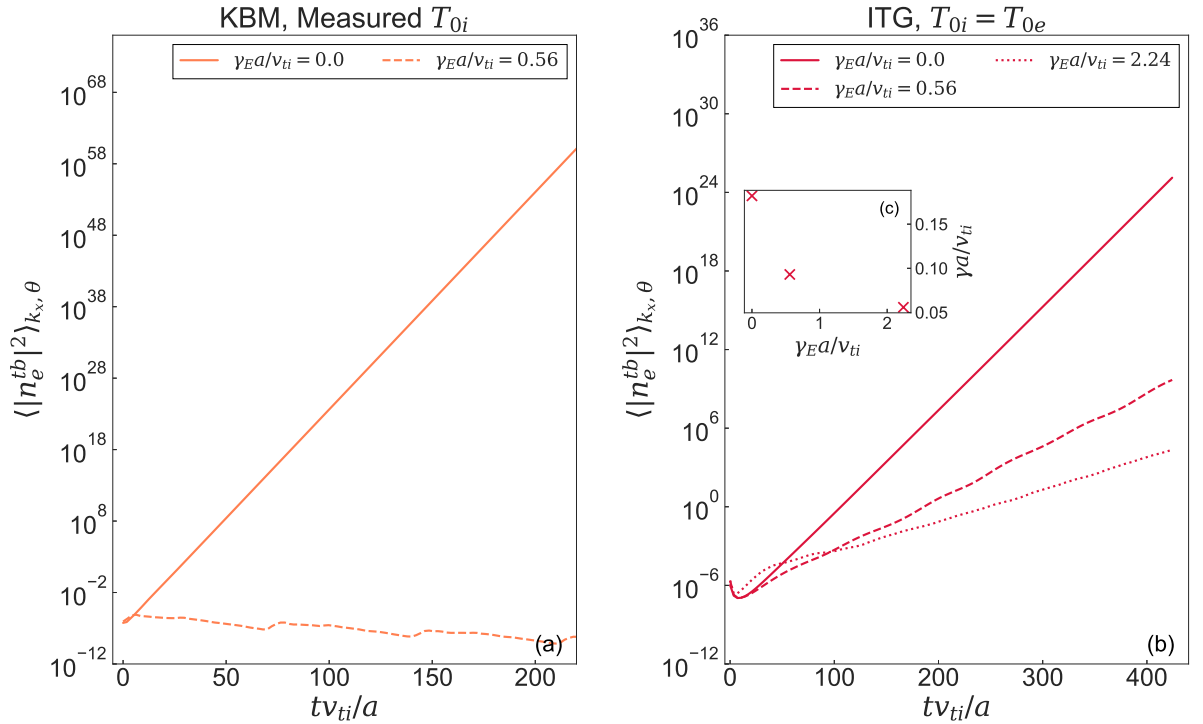


Figure 7.1: Density time traces of KBM and ITG instabilities with and without  $\mathbf{E} \times \mathbf{B}$  shear. (a): The KBM is suppressed by the  $\mathbf{E} \times \mathbf{B}$  shear consistent with the measured ion temperature profile. (b) The ITG is not fully suppressed by the  $\mathbf{E} \times \mathbf{B}$  shear when the ion temperature and gradient are equal to the electron temperature and gradient. The two separate values of  $\gamma_E a/v_{ti}$  correspond to its consistent value for the measured ion temperature profile ( $\gamma_E a/v_{ti} = 0.56$ ) and when the ion temperature profile is equal to the electron temperature profile ( $\gamma_E a/v_{ti} = 2.24$ ). (c): The effective growth rates of the ITG instability for the three separate values of  $\gamma_E a/v_{ti}$  in (b).

The KBM we discussed in Chapter 3 is easily suppressed by  $\mathbf{E} \times \mathbf{B}$  shear because it is radially extended and is stable for a wide range of  $\theta_0$  values (see Figure 3.3(d)). The KBM was shear suppressed even though  $\gamma_{\text{KBM}} > \gamma_E$ . This suppression is demonstrated in Figure 7.1(a), where the mode's average electron density is shown to decay in time.

Determining the effect of the  $\mathbf{E} \times \mathbf{B}$  shear on toroidal and slab modes separately is challenging. To understand why this is the case, it will be useful to define an 'effective'  $\theta_0$  that now depends on time,

$$\Theta_0(\gamma_E, t) = \theta_0 - k_y \frac{\gamma_E}{\hat{s}} t, \quad (7.2)$$

such that the time-dependent radial wavenumber is

$$K_x = k_y \left( \hat{s}(\theta_0 - \theta) - \frac{r}{q} \frac{\partial \nu}{\partial r} \right) - k_y \gamma_E t = k_y \left( \hat{s}(\Theta_0 - \theta) - \frac{r}{q} \frac{\partial \nu}{\partial r} \right). \quad (7.3)$$

The fact that the mode has different  $\Theta_0$  values at different times considerably complicates understanding the effect of  $\mathbf{E} \times \mathbf{B}$  shear on toroidal and slab ETG in the pedestal separately: for  $k_y \rho_i \gtrsim 5$  in the absence of  $\mathbf{E} \times \mathbf{B}$  shear, while for  $\theta_0 = 0$  the fastest growing modes are slab ETG modes, for  $\theta_0 \neq 0$  the fastest growing modes are almost always toroidal ETG modes. Since  $\mathbf{E} \times \mathbf{B}$  shear changes  $\Theta_0$  with time as described in Equation (7.2), if at  $t = 0$  a mode is a slab ETG mode (i.e. it has  $\theta_0 = 0$ ), after a period of time it will become a toroidal ETG mode. Therefore, we can only determine if the  $\mathbf{E} \times \mathbf{B}$  shear suppresses both slab and toroidal modes.

We now consider the effect of  $\mathbf{E} \times \mathbf{B}$  shear on the ITG instability. Our simulations indicate that the effectiveness of  $\mathbf{E} \times \mathbf{B}$  shear at suppressing ITG is sensitive to several parameters. We first test the effectiveness of  $\mathbf{E} \times \mathbf{B}$  shear with the measured ion temperature profiles, which requires using adiabatic electrons, since electron temperature gradient-driven modes are the fastest growing at all scales (see Figure 6.1). We test the  $\mathbf{E} \times \mathbf{B}$  shear on an ITG mode with  $k_y \rho_i = 0.7$ , which has a modest growth rate of  $\gamma a / v_{ti} \simeq 0.1$ . In simulations with  $\mathbf{E} \times \mathbf{B}$  shear, the mode is easily suppressed. This is expected, since  $1/\gamma_E \ll 1/\gamma$  for this ITG mode, and hence, both toroidal and slab ITG are suppressed by  $\mathbf{E} \times \mathbf{B}$  shear at  $k_y \rho_i = 0.7$  with the measured ion temperature profiles.

We also test the effectiveness of the  $\mathbf{E} \times \mathbf{B}$  shear at suppressing the ITG instability when the ion temperature profiles are made equal to the electron temperature profiles (that is,  $T_{0i} = T_{0e}$  and  $L_{Ti} = L_{Te}$ ). To investigate this, we perform GS2 simulations with  $\mathbf{E} \times \mathbf{B}$  shear for a single toroidal ITG mode with  $k_y \rho_i = 0.04$ . Recall that we estimate the radial electric field by balancing it with the pressure gradient as in Equation (3.3), which requires that  $\gamma_E$  is roughly proportional to the second derivative of the pressure gradient, as in Equation (3.4). Therefore, when we quadruple  $1/L_{Ti}$  for the case where the ion and electron temperature profiles are made equal, to be consistent with the temperature profile we must also roughly quadruple the value of  $\gamma_E$ . In Figure 7.1(b), we show the time trace of the density for three simulations of the ITG mode with  $T_{0i} = T_{0e}$ ,  $L_{Ti} = L_{Te}$ , where the value of  $\gamma_E$  varies in each simulation. We show the ITG mode in the absence

of  $\mathbf{E} \times \mathbf{B}$  shear, the mode with  $\gamma_E a / v_{ti} = 0.56$  (which is consistent with the measured ion temperature gradients) and the mode with  $\gamma_E a / v_{ti} = 2.24$  (which is consistent with the steepened ion temperature gradients). To calculate the effective growth rate, we used a similar technique to that in [129], which involves fitting the mode amplification in time. As shown in Figure 7.1(c), while the consistent value of  $\mathbf{E} \times \mathbf{B}$  shear,  $\gamma_E a / v_{ti} = 2.24$ , reduces the growth rate by 70 %, it does not fully suppress the ITG instability. We also found a range of additional parameters that determined how successfully the  $\mathbf{E} \times \mathbf{B}$  shear suppressed the high gradient ITG mode such as  $T_{0i}/T_{0e}$ ; more work is required to understand the resilience of strongly-driven pedestal ITG to  $\mathbf{E} \times \mathbf{B}$  shear.

We now discuss the ETG instability. We found that  $\mathbf{E} \times \mathbf{B}$  shear was insufficient to quench the ETG modes. Even tripling the value of  $\gamma_E$  at  $k_y \rho_i = 2.8$  barely changed the growth rates of the toroidal and slab ETG modes. The ineffectiveness of the  $\mathbf{E} \times \mathbf{B}$  shear for ETG modes is due to  $\gamma \gg \gamma_E$  for these modes. There is likely no experimentally-realizable value of  $\gamma_E$  that would suppress these ETG modes in the pedestal.

Thus, to summarize, we establish the following hierarchy for the efficiency of  $\mathbf{E} \times \mathbf{B}$  shear at reducing the growth rates of linear modes. KBMs are completely suppressed by  $\mathbf{E} \times \mathbf{B}$  shear, and ITG is also fully suppressed when using the measured ion temperature profiles. Using profiles with ion gradients as steep as the electron gradients, while the toroidal ITG growth rate is significantly reduced by  $\mathbf{E} \times \mathbf{B}$  shear, it is not necessarily stabilized. ETG is very resistant to  $\mathbf{E} \times \mathbf{B}$  shear.

# Chapter 8

## Linear Physics Discussion

In the steep gradient region of the fully developed pedestal of a JET H-mode discharge (92174) where measurements indicate that  $T_{0i} > T_{0e}$  and  $R_0/L_{Te} > R_0/L_{Ti}$ , local gyrokinetic simulations demonstrate that electron-driven modes are the fastest growing modes at all length scales perpendicular to  $\mathbf{B}$ . Linearly, KBMs are quenched by  $\mathbf{E} \times \mathbf{B}$  shear, as is ITG when the measured ion temperature profiles are used. This leaves ETG at  $0.1 \lesssim k_y \rho_i \lesssim 400$ .

Using  $R_0/L_{Te} \gg 1$ , we predicted that a novel type of toroidal ETG would be driven at  $k_y \rho_i \sim 1$  and  $K_x \rho_e \sim 1$ , which we have confirmed in gyrokinetic simulations. This toroidal ETG at  $k_y \rho_i \sim 1$  in the linear growth rate spectrum seems to be a robust feature of steep temperature gradient regions, having been seen in all three other pedestals we examined (see Figure A.1, and Appendix A for experimental information), as well as in other works: DIII-D [74, 82], NCSX [81], and ASDEX-U [78–80, 82]. It is also likely that a toroidal ITG mode of a similar nature has been observed at  $k_y \rho_i \sim L_{Ti}/R_0$  in [130].

A notable success of this inquiry is that a simple theoretical model predicted the linear growth rates of the toroidal and slab ETG and the poloidal location of the toroidal ETG mode fairly well. If the ion temperature profile is set equal to the electron temperature profile, ITG modes grow fastest for  $k_y \rho_i \lesssim 0.5$ , and ETG modes grow fastest for  $0.5 \lesssim k_y \rho_i \lesssim 400$ . With equal ion and electron temperature profiles, one might be concerned about significant transport caused by the toroidal ITG at scales as small as  $k_y \rho_i \sim L_{Ti}/R \ll 1$ , since nonlinearly these instabilities might produce large eddies that cause substantial heat transport. While the  $\mathbf{E} \times \mathbf{B}$  shear frequency is too small to damp the ETG, impurities are known to damp ETG [112, 131]. Therefore, further investigation

might explore the effect of impurities on toroidal ETG instability in pedestals. Work has already shown that impurities can produce non-negligible ion-scale pedestal transport [77, 93].

With the measured ion temperature profiles, it is likely that the nonlinear state of JET shot 92174's pedestal is dominated by electron-driven transport. Quasilinear estimates of  $q_e^{tb}/(k_y\rho_i(|\phi_1^{tb}|^2))$  and  $\gamma/k_\perp^2$  suggest that the novel toroidal ETG modes we have described in this work could transport significant electron heat flux. However, as we will see in following chapters, in nonlinear simulations the toroidal ETG modes transport almost no heat, despite quasilinear estimates suggesting they cause comparable heat transport to slab ETG modes. This is a result that we do not yet understand.

Careful work is required to resolve the toroidal ETG modes correctly in nonlinear simulations. For example, to resolve the fastest growing linear modes — toroidal ETG modes — from  $1 \lesssim k_y\rho_i \lesssim 100$  in a nonlinear simulation requires significant  $k_x$  resolution, as well as a sufficiently large number of independent  $\theta_0$  modes. In addition, the slab ETG modes require increasingly fine  $\theta$  grids to resolve at higher values of  $k_y\rho_i$ , which significantly increases computational cost. Caution is required in attempting to infer transport properties from these linear results: the observed modes span a wide range of perpendicular scales, and complex multiscale interactions could be important [132–136].

While in this work we have focused on a single radial location for a single discharge, we have also investigated the growth rates at various radial locations using gyrokinetic simulations. These simulations have demonstrated a significant sensitivity of the growth rates to the radial location because of the sensitivity of the instabilities to local gradients. Nevertheless, certain features such as (i) the dominance of ETG at all scales, and (ii) the toroidal ETG at  $k_y\rho_e \sim L_{Te}/R_0$  were robust features. Due to the sensitivity of microstability to the radial location, we caution against using the local growth rates at any given flux surface to infer global properties about the pedestal, such as its width or height. We have observed that some pedestals have consistently lower growth rates than others, but nonlinear simulations are required to connect gyrokinetic analysis with predictions of pedestal structure.

**Part II**  
**Nonlinear Physics**

# Chapter 9

## Nonlinear Simulations

In previous chapters, we focused exclusively on linear pedestal microinstability physics. We now study the nonlinear, turbulent state at scales similar to those for the linear ETG physics; that is,  $k_y \rho_i \gtrsim 1$ .

In this chapter, we first describe the challenges associated with nonlinear pedestal simulations of ETG turbulence, motivated by the linear physics described in previous chapters. Following this, we discuss the numerical set up for nonlinear simulations. We then show the numerical results. In particular, we show that pedestal ETG turbulence is strongly inhomogeneous in the poloidal angle.

In order to study the nonlinear dynamics, we keep the nonlinear term in the gyrokinetic equation so that the Fourier analyzed system becomes

$$\begin{aligned} & \frac{\partial h_{s,\mathbf{k}}}{\partial t} + \frac{2\pi v_{\parallel}}{L_{\theta}} \frac{\partial h_{s,\mathbf{k}}}{\partial \tilde{\theta}} + i\mathbf{v}_{Ms} \cdot \mathbf{k}_{\perp} h_{s,\mathbf{k}} - \frac{c}{B} \mathcal{G} \sum_{\mathbf{k}'} h_{s,\mathbf{k}-\mathbf{k}'} \phi_{1\mathbf{k}'}^{tb} J_0 \left( \sqrt{2b'_s} \hat{v}_{\perp} \right) \mathcal{K} \\ & = \frac{\partial \phi_{1\mathbf{k}}^{tb}}{\partial t} \frac{Z_s e F_{Ms}}{T_{0s}} J_0 \left( \sqrt{2b_s} \hat{v}_{\perp} \right) + i\omega_{*s} \left[ 1 + \eta_s \left( \frac{m_s \mathcal{E}}{T_{0s}} - \frac{3}{2} \right) \right] \frac{Z_s e F_{Ms}}{T_{0s}} \phi_{1\mathbf{k}}^{tb} J_0 \left( \sqrt{2b_s} \hat{v}_{\perp} \right), \end{aligned} \quad (9.1)$$

where  $\mathcal{K} = (k_y k'_x - k_x k'_y)$  and  $\mathcal{G} = (\nabla x \times \nabla y) \cdot \hat{\mathbf{b}}$ . We have introduced a new angle,  $\tilde{\theta}$ , which differs from the ballooning angle that we used in the linear physics chapters. While the ballooning angle has an infinite domain, the angle  $\tilde{\theta}$  is bounded. We define  $\tilde{\theta} = \theta + 2n\pi$  with the integer  $n$  chosen such that  $-\pi \leq \tilde{\theta} < \pi$

Performing nonlinear gyrokinetic simulations in the pedestal is particularly challenging:

- **Multiscale linear instability:** in the core, the scale separation between ITG and ETG instability means that nonlinear simulations can be performed using

appropriate scale-separated equations [135] with reasonable accuracy. However, in the pedestal there is no gap in the linear growth rate spectrum [49] and the range of scales to resolve is wide: there is ITG instability at wavelengths as long as  $k_y \rho_i \sim L_{Ti}/R_0 \ll 1$ , and ETG instability at wavelengths as short as  $k_y \rho_i \sim (5 - 10)\rho_i/\rho_e$ . Not only are such simulations expensive in terms of the range  $k_y$  wavenumbers, but also in  $k_x$ . As will be discussed shortly, the computing requirements of a fine  $k_x$  spacing and ensuring that turbulence at large values of  $|\tilde{\theta}|$  is well-described make simulations computationally costly. Altogether, this amounts to a wide range of scale lengths that need to be resolved if one wants to include the effect of ITG turbulence on ETG turbulence:  $L_{Ti}/R_0 \lesssim k_y \rho_i \lesssim 10\rho_i/\rho_e$ . Direct numerical simulations have been performed in the core at high numerical expense [132, 133]. Performing such simulations in the pedestal will be even more computationally expensive due to the wider range of instability. Since our stability analysis showed that ITG was mostly stabilized, we neglect most ITG scales by simulating only  $k_y \rho_i \gtrsim 1$ .

- **Large radial gradients:** in local flux-tube simulations, it is assumed that  $k_x L_T \gg 1$ . However, for modes with a large radial extent — for example, ETG streamers that have  $k_x \rho_e \approx 0$  — the steep radial gradients mean that within a single wavelength, the mode might sample an order of unity difference in temperature. In local simulations, however, this effect is neglected since the background temperature is kept constant. For example, for JET shot 92714 at  $r/a = 0.9743$ ,  $\rho_i/L_{Te} = 0.12$ . Assuming a linear temperature profile, a simulation with a radial extent of  $\Delta r = 2\rho_i$  would have a temperature difference of  $\Delta T_{0e} \simeq 0.24T_{0e}$  across the box, where  $T_{0e}$  is the equilibrium temperature at the flux tube center. Thus, at each side of the box, we would be making a 12 % error in the equilibrium temperature, while a ‘global’ approach where the temperature profiles are included might avoid such issues. However, there are other complications with global simulations [119] that we prefer to avoid for this work.

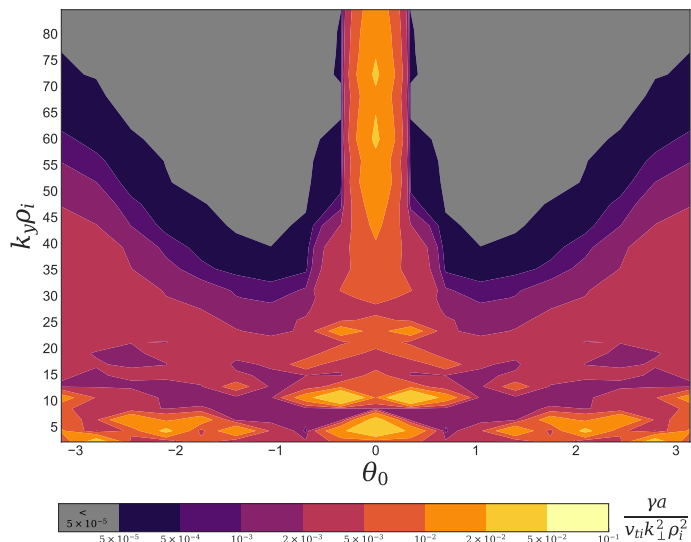


Figure 9.1: Quasilinear estimate of  $\gamma a / (v_{ti} k_{\perp}^2 \rho_i^2)$  for slab ETG modes using the same technique as in Figure 5.14(b). In this simulation, we set  $\mathbf{v}_{Me} = \mathbf{v}_{Mi} = 0$ .

## 9.1 Resolving Toroidal and Slab ETG Turbulence

In this section, we describe the numerical set up for our nonlinear pedestal simulations. Resolving the physics of interest in a nonlinear simulation requires carefully constructing the perpendicular wavenumber grid. The presence of strong magnetic shear can make it expensive to resolve both the slab and toroidal ETG dynamics. The magnetic shear affects the  $k_x$  grid configuration through the parallel boundary condition (PBC) [68]. The PBC arises from the physical requirement that tokamak turbulence be statistically identical at all locations with the same  $\tilde{\theta}$  value. We therefore require that fluctuations are identical at the end of our flux tube at  $\tilde{\theta} = \pm\pi$  for the same values of  $(\psi, \zeta)$ . Note that we do not impose periodicity for  $(\psi, \alpha)$  constant because the radial basis vectors vary at  $\tilde{\theta} = \pm\pi$ . Instead, we impose the following condition,

$$\overline{\mathcal{A}}\left(\psi, \alpha(\psi, \tilde{\theta} = \pi, \zeta), \tilde{\theta} = \pi\right) = \overline{\mathcal{A}}\left(\psi, \alpha(\psi, \tilde{\theta} = -\pi, \zeta), \tilde{\theta} = -\pi\right), \quad (9.2)$$

where  $\overline{\mathcal{A}}$  is any turbulent quantity, and we have suppressed any velocity space and time dependence. Fourier analyzing  $\overline{\mathcal{A}}$  in the perpendicular domain, the PBC becomes [68]

$$\mathcal{A}\left(\tilde{\theta} = \pi, k_x\right) = \mathcal{A}\left(\tilde{\theta} = -\pi, k_x - 2\pi \hat{s} k_y\right), \quad (9.3)$$

where we have ignored subtleties relating to a phase factor by setting it equal to 1. Since we are using the poloidal angle coordinate  $\tilde{\theta}$ , we also need to introduce a new coordinate  $\hat{\theta}_0 = k_x/(\hat{s}k_y)$ , which takes values  $-\infty < \hat{\theta}_0 < \infty$ , whereas the  $\theta_0$  variable we used until now is bounded:  $-\pi \leq \theta_0 < \pi$ . As discussed in Chapter 5, for linear physics, the coordinate pair  $(\theta, \theta_0)$  is more useful. However, the new coordinate pair  $(\tilde{\theta}, \hat{\theta}_0)$  is more useful for nonlinear simulations. This is because nonlinearly, two modes whose radial wavenumbers are connected by the parallel boundary condition (and hence their values of  $\hat{\theta}_0$  are separated by  $2\pi$  [68]) should be considered independent modes since they can interact via the nonlinear term in Equation (9.1). Because the nonlinear term depends on  $k_x$  and  $k'_x$ , all corresponding values of  $\hat{\theta}_0$  and  $\hat{\theta}'_0$  can be coupled nonlinearly, regardless of whether they are connected by the PBC. Therefore, in nonlinear simulations it is important to include values of  $|\hat{\theta}_0|$  larger than  $\pi$  as even two modes that satisfy  $\hat{\theta}_0 = \hat{\theta}_0 \pm 2n\pi$  can still interact. Using the definitions for  $\tilde{\theta}$  and  $\hat{\theta}_0$ ,  $K_x$  is given by

$$K_x = k_y \hat{s}(\hat{\theta}_0 - \tilde{\theta}) - k_y \frac{r}{q} \frac{\partial \nu}{\partial r}. \quad (9.4)$$

To control the number of ‘independent’ modes (that is, modes with different values of  $K_x$  at a given  $\tilde{\theta}$  and  $k_y$ ), we use a quantity called `jtwise`, which enters the definition of the value of the smallest nonzero  $k_x$  in the box,  $\Delta k_x$ ,

$$\Delta k_x = \frac{2\pi \hat{s}}{\text{jtwise} y_0}. \quad (9.5)$$

Here,  $2\pi y_0$  is the box size in the  $y$  direction. The number of independent modes  $\mathcal{I}$  for a given  $k_y$  is therefore

$$\mathcal{I}(k_y) = \frac{2\pi \hat{s} k_y}{\Delta k_x} = k_y y_0 \text{jtwise}. \quad (9.6)$$

Given that the smallest nonzero binormal wavenumber is given by  $\Delta k_y = 1/y_0$ ,  $\mathcal{I}$  is always an integer multiple of `jtwise`, and for  $k_y = \Delta k_y$ ,  $\mathcal{I}(\Delta k_y) = \text{jtwise}$ . In nonlinear simulations, both  $y_0$  and `jtwise` are input parameters, which control the radial box size  $2\pi x_0 = 2\pi/\Delta k_x$ ,

$$x_0 = \frac{\text{jtwise} y_0}{2\pi \hat{s}}. \quad (9.7)$$

For the specific spectra we are resolving, we need both a relatively large value of `jtwise` to resolve the structure in  $\theta_0$ , and a large maximum  $k_x$  on the grid (needed to resolve

modes with large radial derivatives and turbulence at large values of  $\tilde{\theta}$ ). This is computationally challenging to resolve since the maximum  $k_x$  in the box,  $k_{x,\max}$ , is proportional to the number of  $k_x$  modes, **nakx**, and the value of  $\Delta k_x$ ,

$$k_{x,\max} = \frac{\mathbf{nakx} - 1}{2} \Delta k_x \approx \frac{\mathbf{nakx} \pi \hat{s}}{\mathbf{jtwist} y_0}. \quad (9.8)$$

To determine the  $k_x$  and  $k_y$  ranges needed for a nonlinear simulation, recall that we plot  $\gamma/k_\perp^2$  versus  $\theta_0$  and  $k_y$  for a standard simulation in Figure 5.14(b). To study slab modes, we set  $\mathbf{v}_{Me} = \mathbf{v}_{Mi} = 0$  to obtain the ‘slab’ ETG values of  $\gamma/k_\perp^2$  in Figure 9.1. A small value of  $\Delta k_x$  is required because of the sensitivity of the growth rates to different  $\theta_0$  values, as can be seen in Figure 5.14(b) and Figure 9.1. Furthermore, since  $\gamma/k_\perp^2$  estimates indicate that there could be significant transport caused by  $k_y \rho_i \sim 1$  for both toroidal and slab ETG modes, we also need a relatively large value of  $y_0$  (ideally  $y_0 \sim \rho_i$ ) compared with standard ETG simulations. Analyzing the structure in  $\gamma/k_\perp^2$  at lower  $k_y \rho_i$  values, ideally we would like to have  $\mathbf{jtwist} \gtrsim 20$ . Demanding that  $k_{x,\max} \rho_e \approx 1$ , and rearranging Equation (9.8), we find that **nakx** becomes a relatively large number,

$$\mathbf{nakx} \approx \frac{k_{x,\max}}{\pi \hat{s}} \mathbf{jtwist} y_0 \simeq 160, \quad (9.9)$$

where we used  $\mathbf{jtwist} = 20$ ,  $y_0 = \rho_i$ ,  $\pi \hat{s} \simeq 10$ , and  $\rho_i/\rho_e \simeq 80$ . If we also wish to simulate a large number of  $k_y$  modes, such that  $1.0 \leq k_y \rho_i \leq 100.0$ , then **naky**, the number of  $k_y$  modes, becomes large: **naky**  $\approx 100$ . Finally, to resolve the slab ETG physics, we need a larger number of parallel grid points, typically **ntheta**  $\gtrsim 128$ , where **ntheta** is the number of parallel grid points. Thus, ideally we would have **nakx**  $\gtrsim 160$ , **naky**  $\gtrsim 100$ , and **ntheta**  $\gtrsim 128$ . These simulation resolutions are beyond our current computational resources, and hence we are required to make computational savings. However, by using large values of **nakx** and **naky** separately, we hope to demonstrate that we can believe some of the ‘low’ resolution simulations.

We proceed to explain why one should be cautious when performing simulations with large values of **jtwist** and  $y_0$ , as it limits the maximum  $|\hat{\theta}_0|$  value on the grid. Considering the case of  $\tilde{\theta} = \pi$  for an up-down symmetric equilibrium where  $\partial\nu/\partial r(\tilde{\theta} = \pi) = 0$ , then Equation (9.4) becomes  $K_x = k_y \hat{s}(\hat{\theta}_0 - \pi)$ . If  $\hat{\theta}_0 = \pi$  is not included in the grid, the simulation will not have a mode with zero radial wavenumber at  $\tilde{\theta} = \pi$ , and

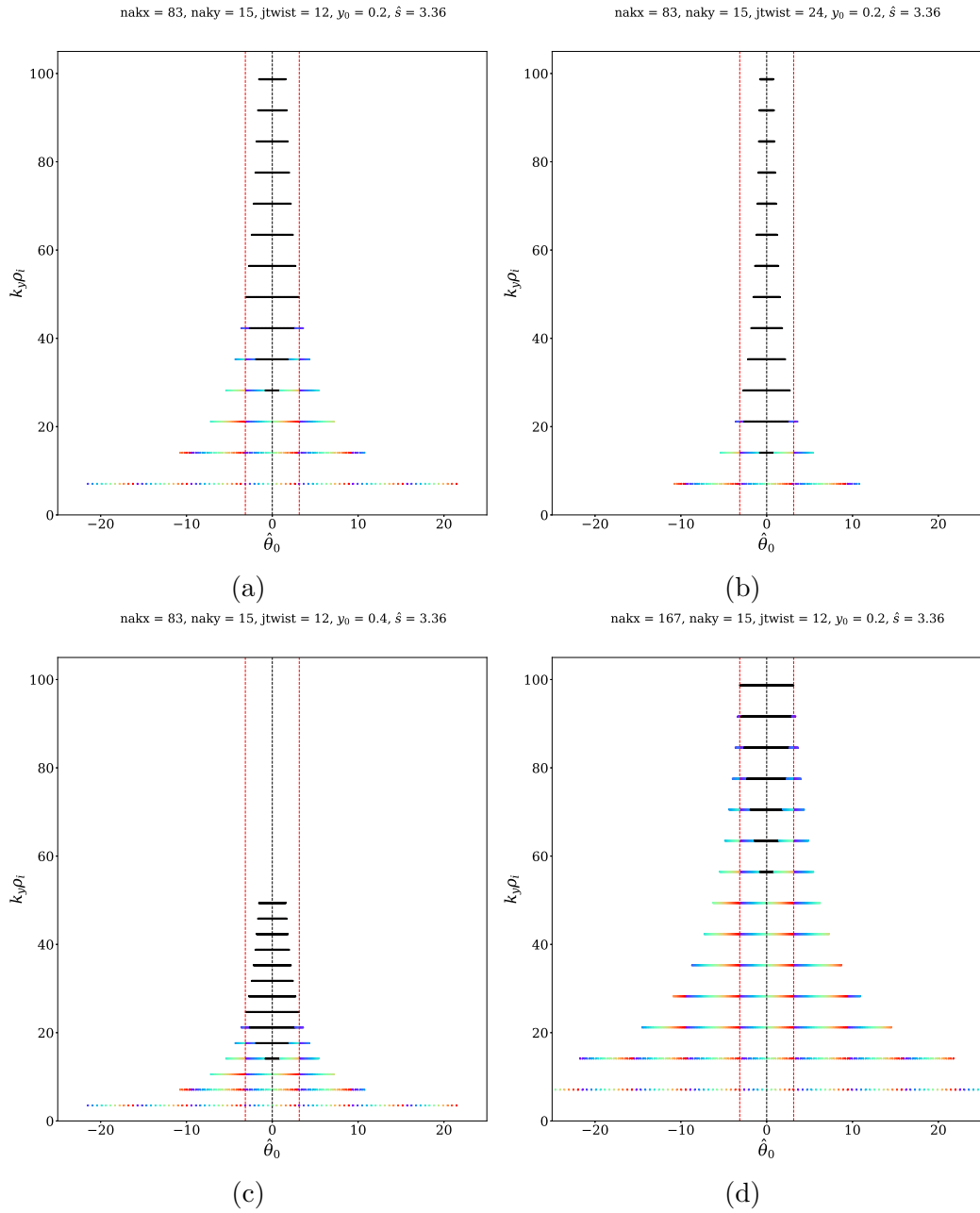


Figure 9.2: A representation of 4 different GS2 grids in  $\hat{\theta}_0$  and  $k_y$  variables. Each marker represents a ballooning mode. Black markers are unconnected, colored markers are connected via the parallel boundary condition to markers of the same color, which are separated by  $\Delta\hat{\theta}_0 = \pm 2\pi$ . Dashed red vertical lines are placed at  $\hat{\theta}_0 = \pm\pi$ . (a): A reference grid. (b): A grid with double the value of *jtwest*. (c): A grid with double the box length in the  $y$  direction. (d): A grid with roughly double the number of  $k_x$  modes.

hence will be unable to correctly resolve all of the physics at  $\tilde{\theta} = \pi$ ; this is particularly important for ETG turbulence because radially elongated modes have been observed to be important for ETG heat transport [23].

In Figure 9.2, we show how the  $\hat{\theta}_0$  modes included in a simulation can be affected by different values of  $y_0$ , `jt`**wist**, and `na`**kx**, the total number of simulated  $k_x$  modes. Figure 9.2(a) shows a representation of the perpendicular wavenumber for a fairly low resolution simulation grid. Each marker represents a ballooning mode; if it is black, it is not connected by the PBC. That is, there does not exist a value of  $\hat{\theta}_0, \hat{\theta}'_0$ , such that  $\hat{\theta}'_0 = \hat{\theta}_0 \pm 2\pi$ . If it has a color, it is connected to another ballooning mode with the same colored marker via the PBC: the same color marks values of  $\hat{\theta}_0$  separated by  $\pm 2\pi$ .

In Figure 9.2(b), we double `jt`**wist**, which limits the maximum  $|\tilde{\theta}|$  values that we can resolve, but decreases  $\Delta k_x$ . In Figure 9.2(c), we double  $y_0$ , which similarly to Figure 9.2(b), halves  $\Delta k_x$ , but also halves  $\Delta k_y$ , allowing us to resolve more fine structure in  $k_y$ . If we wish to resolve the modes with at larger  $|\tilde{\theta}|$  at higher values of  $k_y \rho_i$ , we need a grid that is shown in Figure 9.2(d), where we have doubled `na`**kx**.

In Figure 9.3, we show a physical picture of the  $\theta_0$  cutoff from two perspectives: increasing the value of  $k_y$  and increasing the value of  $\tilde{\theta}$ . Figure 9.3(a) shows a mode with  $K_x = 0$  fitting in the grid at  $\tilde{\theta} = \pi$  for  $k_y = \Delta k_y$ . The mechanism for the ‘shearing’ of the simulation box from a rectangle to a parallelogram with increasing  $\tilde{\theta}$  is similar to the shearing of an eddy that we discussed in Section 1.3.2: away from  $\tilde{\theta} = 0$ , the toroidal angle  $\zeta$  depends on the radial location for nonzero magnetic shear.

In Figure 9.3(b) and (c), we double and quadruple  $k_y$  compared with Figure 9.3(a), to show how modes are no longer able to span the entire radial extent of the box for larger values of  $k_y$  at  $\tilde{\theta} = \pi$ , and hence the  $K_x = 0$  mode is not included in the simulation for these larger values of  $k_y$ . In Figure 9.3(d),(e),(f), and (g), we show a perpendicular box shearing as  $\tilde{\theta}$  is increased. For simplicity, we assume that our equilibrium has  $\nu = 0$  such that  $K_x(\tilde{\theta}, \hat{\theta}_0) = 0$  at  $\tilde{\theta} = \hat{\theta}_0$ . In Figure 9.3(f), the  $\hat{\theta}_0 = \tilde{\theta}''$  mode is marginally resolved by the box. However, as shown in Figure 9.3(g), for  $\tilde{\theta} > \hat{\theta}_0 = \tilde{\theta}''$ , the box can no longer resolve the mode with the given  $k_y$ . Therefore, for this value of  $k_y$ , only the mode up to  $\hat{\theta}_0 = \tilde{\theta}''$  can be resolved, and for  $\tilde{\theta} > \tilde{\theta}''$ , we are missing the physics of modes

with  $K_x = 0$ . Thus, if  $\hat{\theta}_0$  cannot become larger than  $\pi$  for some value of  $k_y$ , modes with this  $k_y$  will not be resolved for high values of  $|\tilde{\theta}|$ .

In summary, to resolve the slab and toroidal ETG dynamics requires resolving a very wide range of perpendicular scales: ideally, we would simulate  $1 \lesssim k_y \rho_i \lesssim 100$  and  $k_x \rho_i \lesssim 100$ , where we also require  $\Delta k_x$  to be sufficiently small to reflect the strong  $\theta_0$  dependence of the mode. At larger values of  $k_y \rho_i$  and  $|\tilde{\theta}|$ , the physics of more radially extended modes will not be included without sufficient simulation resolution.

## 9.2 Hyperviscosity

Given that we wish to simulate a wide range of  $k_y \rho_i$  values (for instance,  $1 \lesssim k_y \rho_i \lesssim 100$ ) and that there is still virulent instability at  $k_y \rho_i \sim 100$ , we need hyperviscosity to suppress these small scale modes. This was motivated by the need to damp high  $k_y$  modes, but wanting to retain the effects of the toroidal ETG modes with large values of  $K_x$  and smaller values of  $k_y$ . We found that without hyperviscosity, the fluxes in a simulation would diverge at  $k_y \rho_i \sim 100$ . To address this, we implemented a hyperviscous option that could separately damp high  $k_y$  and  $k_x$ . The hyperviscous damping rate  $\gamma_h$  is given by

$$\gamma_h(k_x, k_y) \frac{a}{v_{ti}} = -D_{hx} (k_x \rho_i)^{n_x} - D_{hy} (k_y \rho_i)^{n_y}, \quad (9.10)$$

where  $D_{hx}$  and  $D_{hy}$  are dimensionless hyperviscous coefficients, and  $n_x$  and  $n_y$  are integers that we set equal to 4 for this work. Tests showed a much more satisfactory outcome for the effect of the hyperviscosity on the growth rate spectra, with modes at larger values of  $k_y \rho_i$  being preferentially damped. We proceed with this form of the hyperviscosity for all nonlinear simulations in this thesis. We found that damping in  $k_x$  was not necessary for convergence, but we usually kept a small value of  $D_{hx}$ . To determine the necessary value of  $D_{hy}$ , we found that damping the mode with the largest  $k_y \rho_i$  value to reduce its growth rate by around 80 percent of its undamped values was a satisfactory rule of thumb. After performing a simulation, depending on the form of the  $k_y$  cascade, the value of  $D_{hy}$  was modified to ensure that there was a viscous scale in the box at higher values of  $k_y \rho_i$ .

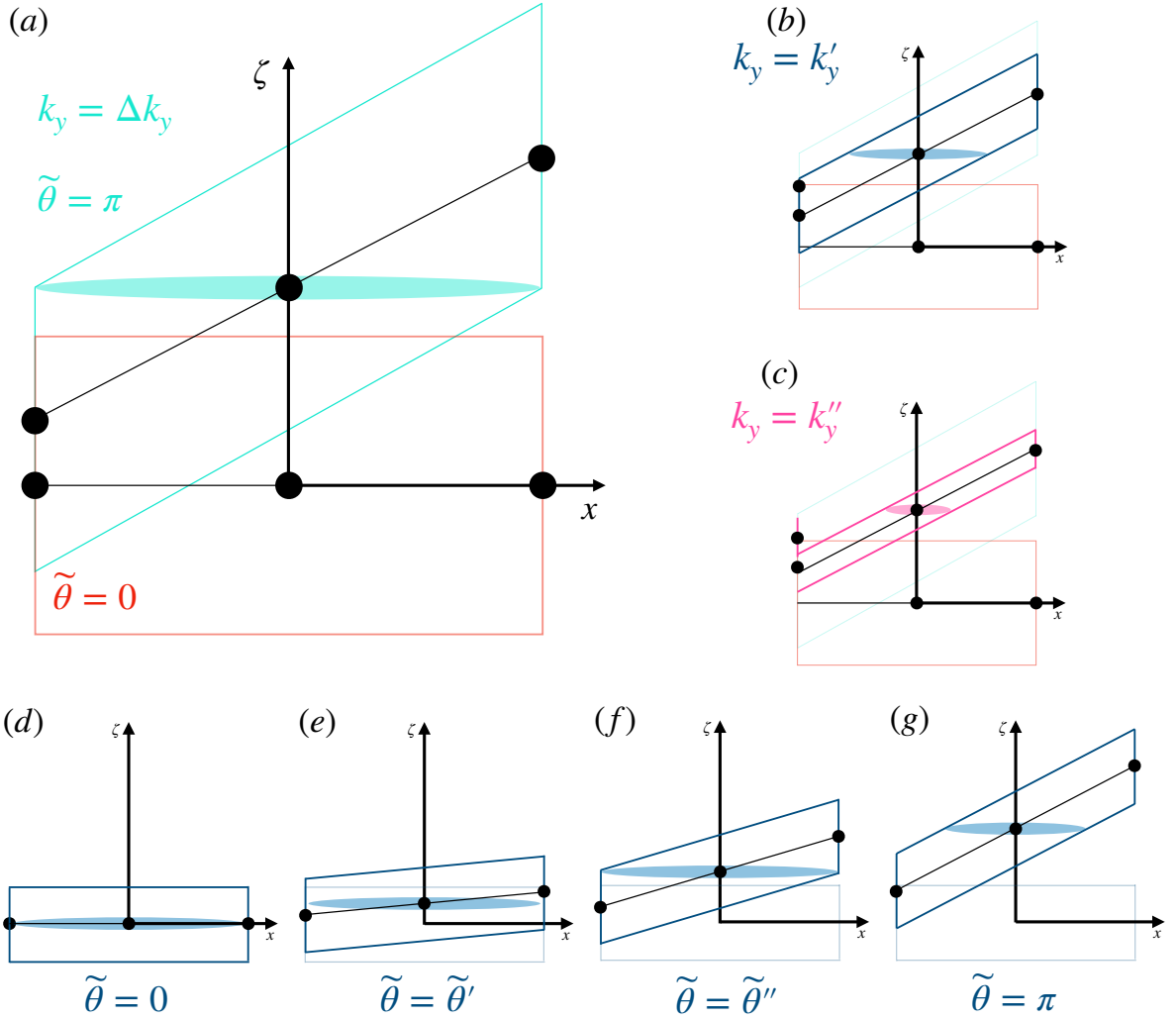


Figure 9.3: (a): The perpendicular grid at  $\tilde{\theta} = 0$  (red) and  $\tilde{\theta} = \pi$  (aqua). The  $\tilde{\theta} = \pi$  box shows a mode with  $K_x = 0$ ,  $k_y = \Delta k_y$ , which spans the entire box. (b): Blue box at  $\tilde{\theta} = \pi$  shows the effective box for a mode with  $k_y = k'_y > \Delta k_y$ . A mode with  $K_x = 0$  is unable to fit in the box, as it would require a length of  $2\pi x_0 \rho_r$ . (c): A box with an even larger  $k''_y > k'_y$ , where the maximum radial extent of a mode becomes even smaller. (d)-(g): boxes with a fixed value of  $k_y \rho_i$ , and  $\tilde{\theta}$  increasing from  $\tilde{\theta} = 0$  to  $\tilde{\theta} = \pi$ . In (f), at  $\tilde{\theta} = \tilde{\theta}''$ , the mode with  $K_x = 0$  barely fits in the box.

### 9.3 Numerical Results

We now introduce the nonlinear simulations covered in this chapter. The Base1 simulation is a compromise between the resolution required to resolve the physics of interest, and computational cost. The equilibrium is identical to that used for most of the linear physics: JET shot 92174 at  $r/a = 0.9743$ . The input parameters for all of the nonlinear simulations in this thesis are shown in Appendix D. This simulation has `ntheta` = 128, `naky` = 50, `nakx` = 67,  $y_0 = 1.0$ , `jt看ist` = 9, 20 passing pitch angles, 65 trapped pitch angles, 12 energy gridpoints,  $D_{hy} = 1.8 \times 10^{-10}$ , and  $D_{hx} = 2.0 \times 10^{-11}$ . We use a smaller collision frequency ( $\nu_{ee}a/v_{ti} \simeq 0.14$ ) than the linear physics, inspired by pedestal discharges with higher temperatures. This simulation can resolve scales  $1 \lesssim k_y \rho_i \lesssim 70$ . ‘Hero1’ is a higher resolution simulation than the Base1 simulation, with three times as many  $k_x$  modes. A plot of the connected modes for these two resolutions is shown in Figure 9.5. All simulations are electrostatic, keep both the kinetic electron and ion responses, and are performed without  $\mathbf{E} \times \mathbf{B}$  shear. Base1 and Hero1 simulation parameters are shown in Table 9.1. Hero1 is close to the upper limit of what we can simulate with our computational resources.

In Figure 9.4, we plot some diagnostic quantities for the Base1 simulation. Figure 9.4(a) shows time traces of the heat flux and the potential fluctuations, as well as the averaging time window. We choose to study the nonlinear state in the indicated time window. While at later times, it appears that the system could be tending towards a different saturated state, this is currently under investigation. The saturated state at an intermediate time that we study here is of interest because it is almost indistinguishable from the simulations we perform later in the absence of magnetic drifts, as we discuss in Chapter 10. We will briefly discuss the later time state of Base1 in Section 10.3. Note that the dip in the heat flux and potential at  $tv_{ti}/a \simeq 0.6$  occurs due to a halving of the simulation timestep, which is necessary to satisfy the Courant–Friedrichs–Lewy convergence condition. To obtain the power  $P_s$  through the flux surface requires integrating over the flux surface area,

$$P_s = Q_s^{tb} \int_S dS = \tilde{Q}_s^{tb} \frac{\rho_i^2}{a^2} n_{0i} T_{0i} v_{ti} \int_{-\pi}^{\pi} \int_{-\pi}^{\pi} \frac{|\nabla\psi|}{\mathbf{B} \cdot \nabla\theta} d\tilde{\theta} d\zeta, \quad (9.11)$$

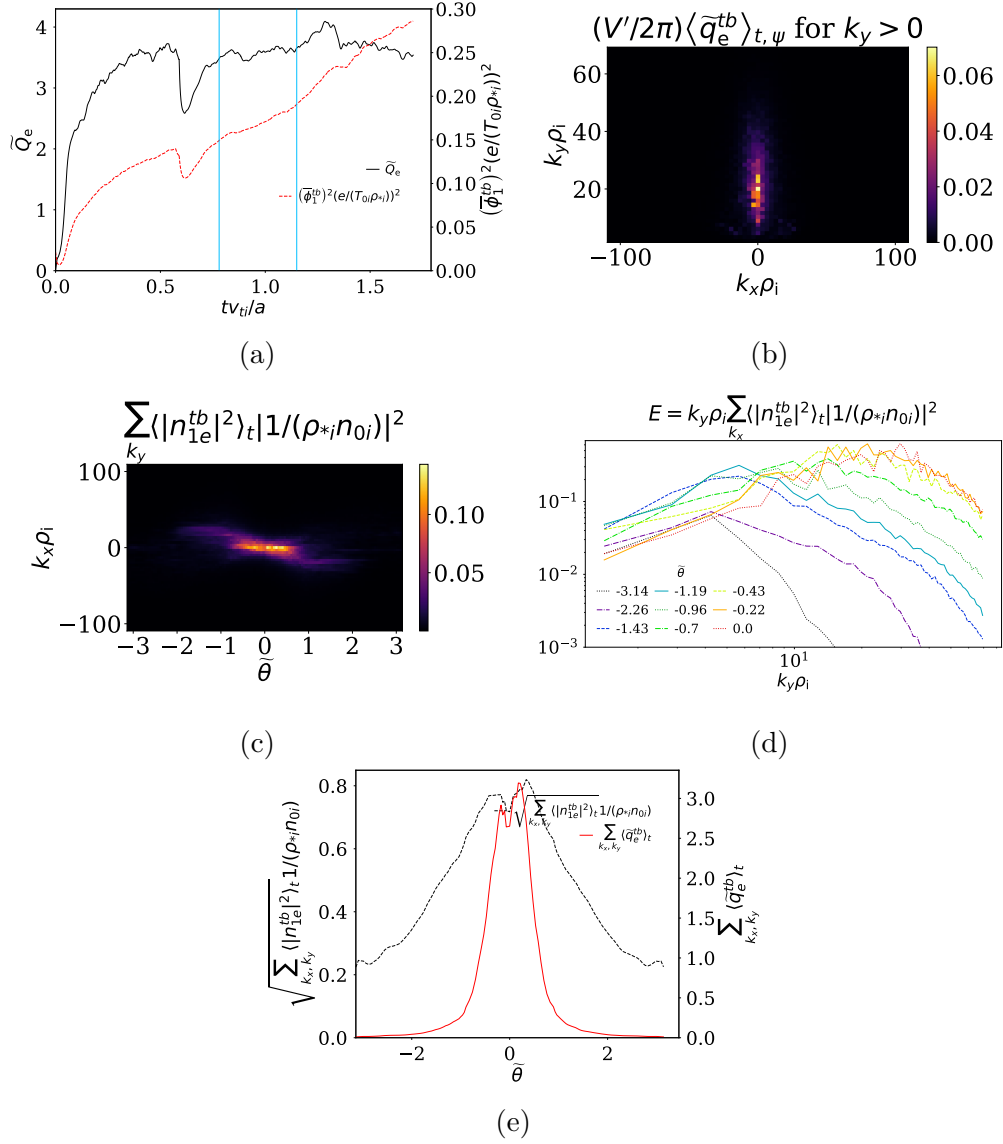


Figure 9.4: Quantities for Base1 simulation. (a):  $\tilde{Q}_e^{tb}$  and  $\phi_1^{tb}$  time traces with the time averaging window indicated by blue vertical lines, (b):  $\tilde{q}_e^{tb}$  spectrum in  $k_x, k_y$ , (c):  $|n_{1e}^{tb}|^2$  versus  $k_x$  and  $\tilde{\theta}$ , (d):  $|n_{1e}^{tb}|^2$  power spectrum versus  $k_y \rho_i$  at different  $\tilde{\theta}$  locations, (e):  $\tilde{Q}_e^{tb}$  and  $\sqrt{|n_{1e}^{tb}|^2}$  versus  $\tilde{\theta}$ .

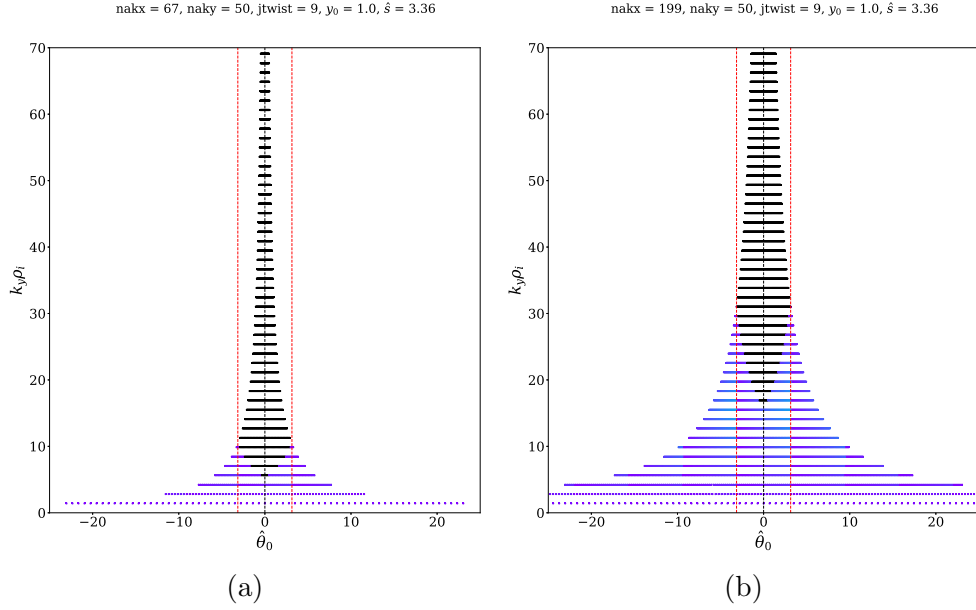


Figure 9.5: Connected modes plot for Base1 (a) and Hero1 (b).

which is straightforward to calculate since we are using a Miller equilibrium. Here,  $dS = |\nabla\psi|d\tilde{\theta}d\zeta/(\mathbf{B}\cdot\nabla\tilde{\theta})$  is the flux surface area element. For Base1, we find that  $P_e = 2.3$  MW, which is compatible with the experimental power through the pedestal. Figure 9.4(b) shows  $\tilde{q}_e^{tb}$  versus  $k_x \rho_i$  and  $k_y \rho_i$ ; we omit the ion heat flux because it is negligible. The maximum values of  $k_x \rho_i$  and  $k_y \rho_i$  are sufficiently large to resolve the heat flux with the simulation parameters. Figure 9.4(c) and (d) show the density perturbations versus  $k_x \rho_i$  and  $\tilde{\theta}$ , and the kinetic energy versus  $k_y \rho_i$  for different values of  $\tilde{\theta}$ , respectively. We choose to plot the turbulent density normalized as  $n_{1e}^{tb}/(\rho_{*i}n_{0i})$ . We see that the fluctuation amplitudes have a strong poloidal dependence, with the intensity falling off at larger values of  $|\tilde{\theta}|$ . This is also demonstrated in Figure 9.4(e), where we show the density and heat flux versus  $\tilde{\theta}$ . Clearly, the heat flux falls off even more strongly than the density fluctuations, which will be explained in Chapter 10. Both the density and heat flux are normalized to their maximum values. The decreasing turbulent amplitudes with increasing  $|\tilde{\theta}|$  can also be seen in Figure 9.4(e), where we plot the energy  $E = k_y \rho_i \langle \sum_{k_x} |n_{1e}^{tb}|^2 \rangle_t$  versus  $k_y \rho_i$  at different  $\tilde{\theta}$  locations. The energy is fairly constant at smaller  $|\tilde{\theta}|$ , and then decreases rapidly. This poloidal inhomogeneity is shown in plots of the turbulence in Figure 9.6(a) and (b), where we plot  $\overline{\phi}_1^{tb}$  versus  $x$  and  $\tilde{\theta}$ , and  $y$  and  $\tilde{\theta}$ , respectively.

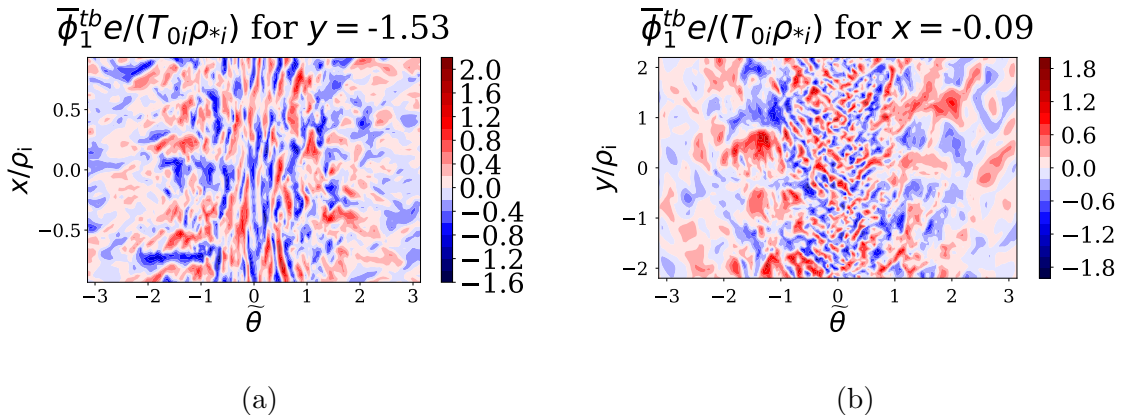


Figure 9.6: Parallel distribution of electrostatic potential for Base1. (a):  $\bar{\phi}_1^{tb}$  versus  $x$  and  $\tilde{\theta}$  at a fixed  $y$  location at the final timestep, (b):  $\bar{\phi}_1^{tb}$  versus  $y$  and  $\tilde{\theta}$  at a fixed  $x$  location at the final timestep.

Curiously, not only do the turbulence fluctuations amplitudes decrease at larger  $|\tilde{\theta}|$ , but the character of the turbulence also changes. At smaller values of  $|\tilde{\theta}|$ , the turbulence is more extended in  $x$ , and compressed in  $y$ , while also having a larger parallel wavenumber. Conversely, at higher values of  $|\tilde{\theta}|$ , the turbulence is more compressed in  $x$  and more extended in  $y$ , with a shorter parallel wavenumber. In the next chapter, we examine this poloidal inhomogeneity in more detail, which is due to slab ETG physics and magnetic geometry, but not the magnetic drifts.

### 9.3.1 Hero Simulation

Here, we introduce the Hero1 simulation, in order to demonstrate some confidence in our numerical results. By comparing Figure 9.5(a) and (b), one might be concerned that Base1 does not resolve any of the ETG physics beyond  $k_y \rho_i \approx 10$  at larger  $|\hat{\theta}_0|$  values, since none of the modes are connected by the parallel boundary condition. This might prevent turbulence from developing  $K_x = 0$  at larger values of  $|\tilde{\theta}|$  and higher values of  $k_y \rho_i$ . These two shortcomings can be seen in Figure 9.5(a), where for  $k_y \rho_i \gtrsim 10$ , there are no connected modes and modes at larger values of  $|\tilde{\theta}|$  are not resolved.

To determine the importance of modes at higher  $|\theta_0|$  that require connections, and higher  $|\tilde{\theta}|$  turbulence, we tripled the number of radial modes for Hero1 in comparison to Base1. For Hero1, we resolve all modes up to  $|\hat{\theta}_0| = \pi$  and  $k_y \rho_i \approx 30$ . Comparing Base1

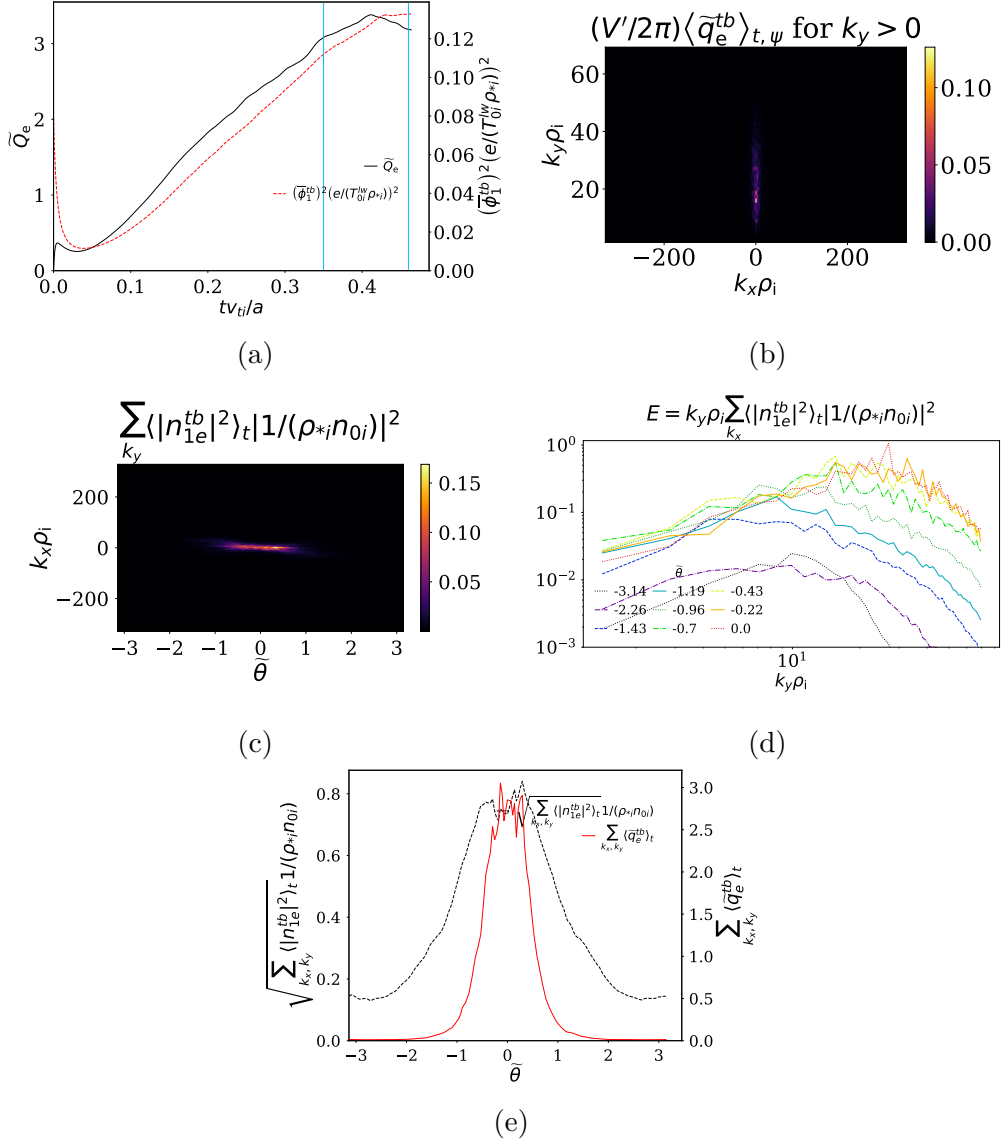


Figure 9.7: Quantities for Hero1 simulation. (a):  $\tilde{Q}_e^{tb}$  and  $\phi_1^{tb}$  time traces with time averaging window indicated by blue vertical lines, (b):  $\tilde{q}_e^{tb}$  spectrum in  $k_x, k_y$ , (c):  $|n_{1e}^{tb}|^2$  versus  $k_x$  and  $\tilde{\theta}$ , (d):  $|n_{1e}^{tb}|^2$  power spectrum versus  $k_y \rho_i$  at different  $\tilde{\theta}$  locations, (e):  $\tilde{q}_e^{tb}$  and  $\sqrt{|n_{1e}^{tb}|^2}$  versus  $\tilde{\theta}$ .

GS2 Pedestal Simulations							
Simulation	ntheta	naky	nakx	$y_0/\rho_i$	jt看ist	$D_{hy}$	$D_{hx}$
Base1	128	50	67	0.7	9	$1.8 \times 10^{-10}$	$2.0 \times 10^{-11}$
Hero1	128	50	199	0.7	9	$1.8 \times 10^{-10}$	$2.4 \times 10^{-13}$

Table 9.1: Nonlinear simulations discussed in this chapter.

in Figure 9.4 and Hero1 in Figure 9.7 the results are fairly similar. The steady state heat flux is comparable at  $\tilde{Q}_e^{tb} \simeq 3.5$ , and the poloidal distribution of the turbulence in Figure 9.7(c), (d), and (e) is comparable. Comparing Figure 9.4(d), with Figure 9.7(d), there is more energy at smaller scales in the Hero1 simulation. Note that the heat flux only just appears to saturate in Figure 9.7(a); we have refrained from running the simulation for longer due to computational resource constraints.

It appears that the connected modes and turbulence at larger values of  $|\tilde{\theta}|$  did not make a substantial difference to the fluxes or character of the turbulence. However, upon examining the connected modes for the Hero1 simulation in Figure 9.5 (b), there are still modes at higher  $k_y\rho_i$  and larger  $|\hat{\theta}_0|$  that have not been connected at least once, which one might be concerned could substantially change the simulations results. However, as we will show in more detail in Chapter 10, the pedestal geometry for this particular equilibrium tends to suppress turbulence at larger values of  $|\theta_0|$  and turbulence at  $|\tilde{\theta}| \gtrsim 1.5$ .

We now compare the turbulence properties at different  $\tilde{\theta}$  locations in more detail. In the left column of Figure 9.8, we plot  $\bar{\phi}_1^{tb}(x, y)$  at four poloidal locations. At different poloidal locations, the turbulence appears to have different statistical properties. With increasing  $|\tilde{\theta}|$ , the  $x$  correlation length decreases and the  $y$  correlation length increases, as shown by the correlation functions in the right column of Figure 9.8. We define the correlation function  $C_n$  as the Fourier transform of the absolute value squared of the density field  $n_{1e}^{tb}$ ,

$$C_n(x) = \frac{\left\langle \int_{-\infty}^{\infty} |n_{1e}^{tb}(k_x)|^2 \exp(-ik_x x) dk_x \right\rangle_t}{\left\langle \int_{-\infty}^{\infty} |n_{1e}^{tb}(k_x)|^2 dk_x \right\rangle_t}. \quad (9.12)$$

The increasing  $y$  correlation length with increasing  $|\tilde{\theta}|$  can also be seen in Figure 9.7(d) by a shift of the maximum value of  $E$  to smaller  $k_y\rho_i$  values at larger  $|\tilde{\theta}|$ . The discrete

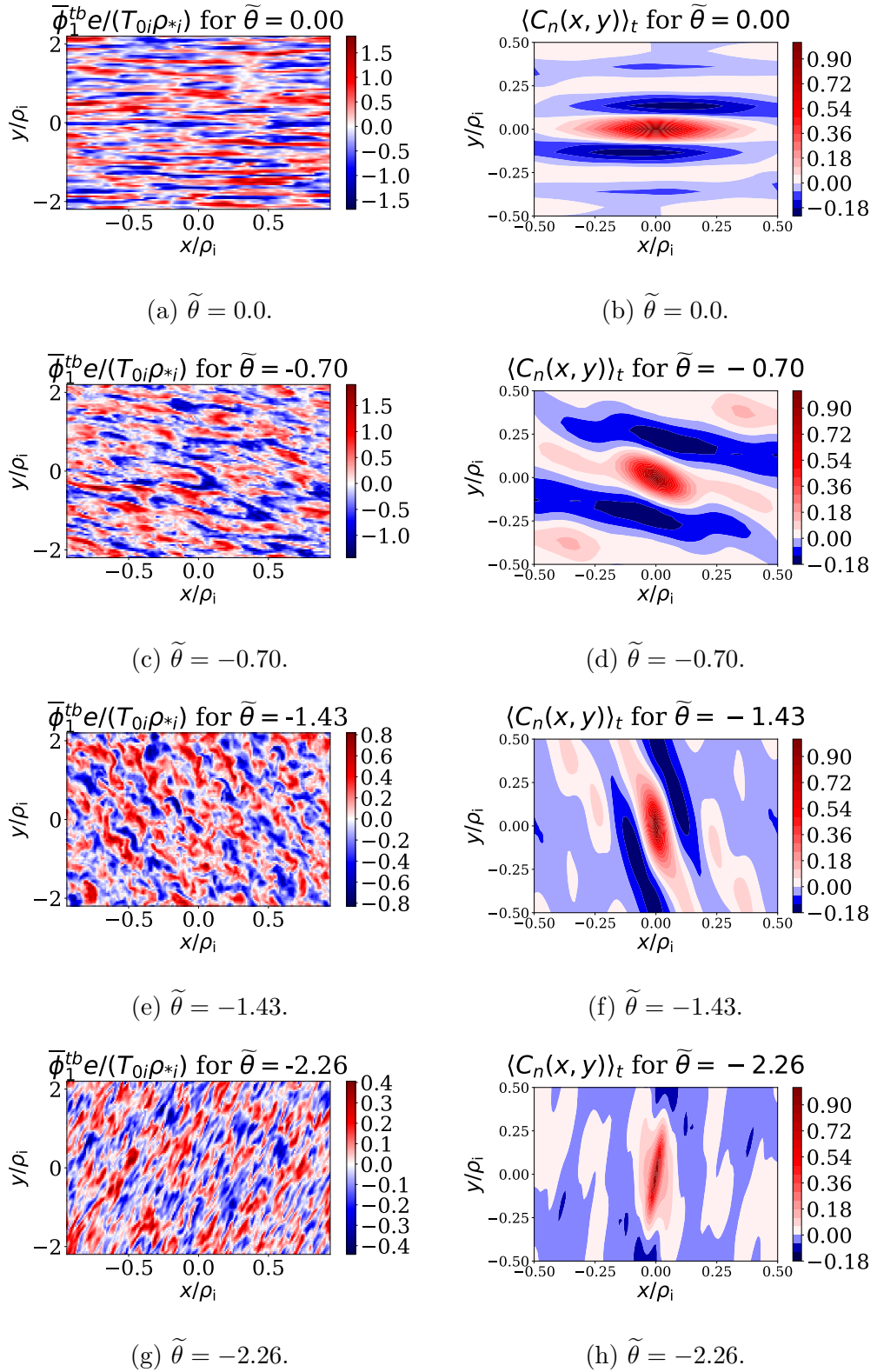


Figure 9.8: Turbulent fluctuations and correlation functions for Hero1. Left column:  $x - y$  plots for the perturbed density for different  $\tilde{\theta}$  locations at the final timestep. Right column: correlation functions at different  $\tilde{\theta}$  locations, where we have zoomed in for  $x$  and  $y$  to focus on the structures of interest.

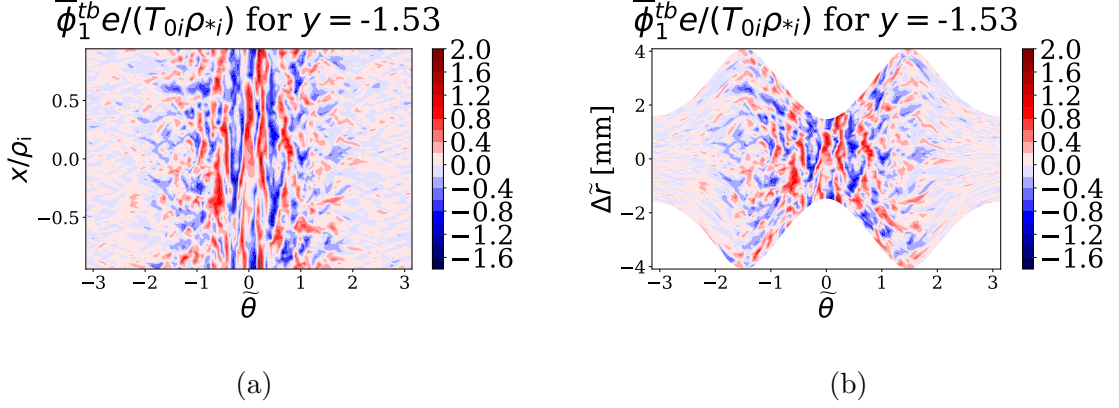


Figure 9.9: Potential fluctuations versus a radial coordinate and  $\tilde{\theta}$  on a single field line for Hero1. (a): Radial coordinate is the standard  $x$  variable. (b) Radial coordinate is  $\Delta\tilde{r}$ .

version of Equation (9.13) used for plots in Figure 9.8 is given by

$$C_n(x, y) = \frac{\left\langle \sum_{k_x, k_y} |n_{1e}^{tb}(k_x, k_y)|^2 \exp(-ik_x x - ik_y y) \Delta k_x \Delta k_y \right\rangle_t}{\left\langle \sum_{k_x, k_y} |n_{1e}^{tb}(k_x, k_y)|^2 \Delta k_x \Delta k_y \right\rangle_t}, \quad (9.13)$$

where  $\Delta k_x$  and  $\Delta k_y$  are the  $k_x$  and  $k_y$  grid spacings, respectively.

While the turbulence appears to become less radially extended with increasing values of  $|\theta|$ , to some extent this is an artefact of the flux tube representation. While a field line on a flux surface maintains a constant value of  $x$  as it moves in poloidal angle, due to plasma shaping, two different magnetic field lines separated by  $\Delta x$  do not maintain a constant distance  $\Delta\tilde{r}$  between two contiguous flux surfaces. Therefore, to give a better representation of the radial extension of the eddies at different poloidal locations, we can plot the turbulence fluctuations versus  $\tilde{\theta}$  and  $\Delta\tilde{r}$ , where we define  $\Delta\tilde{r}$  as

$$\Delta\tilde{r} = \frac{r_c}{a^2} \frac{1}{q_c} \frac{dr}{d\psi_N} \frac{1}{|\nabla r|} x. \quad (9.14)$$

Note  $\tilde{r}$  is not the Miller coordinate  $r$ , which is a flux function. In Figure 9.9, we compare the turbulence in both a  $x/\rho_i - \tilde{\theta}$  projection and a  $\Delta\tilde{r} - \tilde{\theta}$  projection. Due to shaping, the quantity  $\Delta\tilde{r}$  is roughly three times smaller at the inboard midplane than its maximum value along  $\tilde{\theta}$ . When examining Figure 9.9(b), there is the caveat: the coordinate  $\Delta\tilde{r}$  only accounts for the effects of flux expansion; it does not include the local magnetic shear, which is also important.

To ensure that the strong poloidal inhomogeneity is not a numerical artefact, we have performed resolution studies in `nakx`, `naky`, `y0`, and `jt看ist`. All of these simulations found a similar effect where the turbulent fluctuations have a maximum value for  $|\tilde{\theta}| \lesssim 1$ , and a heat flux with an even stronger poloidal angle dependence, similar to `Base1` and `Her01`.

In summary, we have discussed the exacting computational requirements for pedestal ETG simulations, given the wide range of scales in the linear physics that need to be resolved. We then performed nonlinear simulations of pedestal ETG turbulence that revealed a strong inhomogeneity in the poloidal distribution of the turbulence. In the next chapter, we investigate the role that magnetic drifts and FLR effects have in determining the character of pedestal ETG turbulence.

# Chapter 10

## Magnetic Drifts and FLR Effects in Pedestal ETG Turbulence

In this chapter, we describe how magnetic drifts and FLR effects influence the character of pedestal ETG turbulence. We first demonstrate that pedestal turbulence at  $r/a = 0.9743$  in JET shot 92174 is dominated by slab ETG, not the toroidal ETG instability that dominates the linear spectrum. We introduce simulations without the toroidal ETG instability and compare their properties to simulations with the full magnetic drifts. Despite the estimates of  $\gamma/k_{\perp}^2$  and  $q_e^{tb}/(k_y|\phi_1^{tb}|^2)$  in Chapter 5 suggesting that the toroidal ETG mode can transport significant heat, we find that it plays a minor role in turbulent transport in the equilibrium that we investigate. We also demonstrate how FLR effects strongly confine the turbulence to regions of low perpendicular wavenumber. We then show how this extends to a variety of different flux surface shapes. Finally, we briefly discuss the long time state of Base1.

GS2 Pedestal Simulations								
Simulation	ntheta	naky	nakx	$y_0/\rho_i$	jtwist	$D_{hy}$	$D_{hx}$	$v_{Ms}$
Base1	128	50	67	0.7	9	$1.8 \times 10^{-10}$	$2.0 \times 10^{-11}$	full
Slab1	128	50	67	0.7	9	$1.8 \times 10^{-10}$	$2.0 \times 10^{-11}$	zero
Hero1	128	50	199	0.7	9	$1.8 \times 10^{-10}$	$2.4 \times 10^{-13}$	full
Slab2	128	12	199	0.14	45	$1.8 \times 10^{-10}$	$3.9 \times 10^{-16}$	zero

Table 10.1: Nonlinear simulations discussed in this chapter that compare the effects of magnetic drifts.

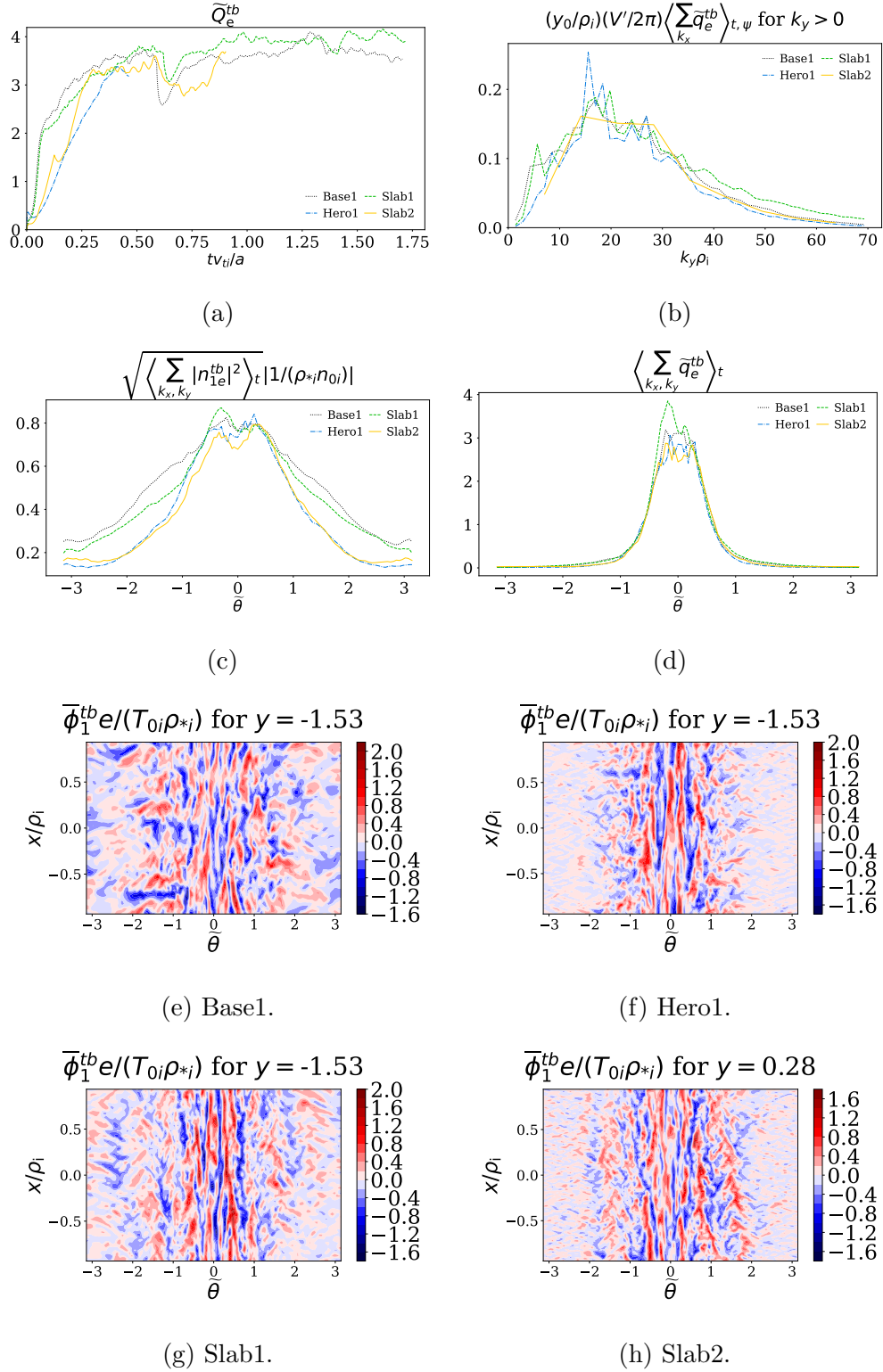


Figure 10.1: Comparison of Base1, Hero1, Slab1, and Slab2 simulations. (a):  $\tilde{Q}_e^{tb}$  versus time, (b):  $\tilde{q}_e^{tb}$  versus  $k_y$ , (c):  $|n_{1e}^{tb}|^2$  versus  $\tilde{\theta}$ , (d):  $\tilde{q}_e^{tb}$  versus  $\tilde{\theta}$ . In (e), (f), (g), and (h), we plot  $\bar{\phi}_1^{tb}$  versus  $x$  and  $\tilde{\theta}$  for Base1, Hero1, Slab1, and Slab2, respectively, evaluated at the final simulation timestep.

## 10.1 The Effect of Magnetic Drifts

In order to investigate the importance of toroidal ETG turbulence for the saturated state, we turn off the magnetic drift term in GS2 (by setting  $\mathbf{v}_{Me} = \mathbf{v}_{Mi} = 0$ ), while retaining all other physics that we have previously included. As mentioned in Chapter 9, for the simulations with magnetic drifts, we study the intermediate time state; the long time state is still under investigation. While we find some minor differences in the turbulence between the simulations with and without magnetic drifts, the fluxes are very similar and the turbulence is still confined to a narrow poloidal location. This leads to the conclusion that the turbulence in the pedestal we examine appears to be dominated by the slab ETG instability rather than the toroidal ETG instability. We introduce two simulations performed without magnetic drifts to compare with the Base1 and Hero1 simulations: Slab1 and Slab2. Slab1 is identical to Base1 apart from the magnetic drifts. Slab2 has the same  $\Delta k_x$  and  $k_{x,\max}$  as Hero1, but  $y_0$  is five times smaller, `naky` is five times smaller, and the magnetic drifts are turned off. Since we have reduced the box size  $y_0$  by a factor of five, to keep the same box size  $x_0$  (see Equation (9.5)), we decided to increase `jtwise` by a factor of 5. All 4 simulations, Base1, Slab1, Hero1, and Slab2 have the same value of  $k_{y,\max}$  and  $x_0$ . The grids for these four simulations are described in Table 10.1. In Figure 10.1, we compare Base1, Slab1, Hero1, and Slab2 simulations. As shown in Figure 10.1(b), (c), and (d), the heat flux versus  $k_y \rho_i$  and  $\tilde{\theta}$ , and the density fluctuations versus  $\tilde{\theta}$  are almost identical between the four simulations. The heat flux time traces in Figure 10.1(a) indicate similar values of saturated heat fluxes. The main difference between simulations with and without magnetic drifts appears qualitatively in the pictures of the turbulence versus  $x$  and  $\tilde{\theta}$ , shown in Figure 10.1(e), (f), (g), and (h), where in Base1 and Hero1, there are structures at larger  $|\tilde{\theta}|$  values that extend farther in  $\tilde{\theta}$ .

In summary, we find that turbulence in simulations with and without magnetic drifts is very similar for the equilibrium we examine. We have not yet understood why the slab ETG dominates nonlinearly over the toroidal ETG branch, or even if it dominates at long times since the nonlinear simulation with magnetic drifts shows a saturated heat flux, but some modes are still growing in size. For the purposes of this thesis, from

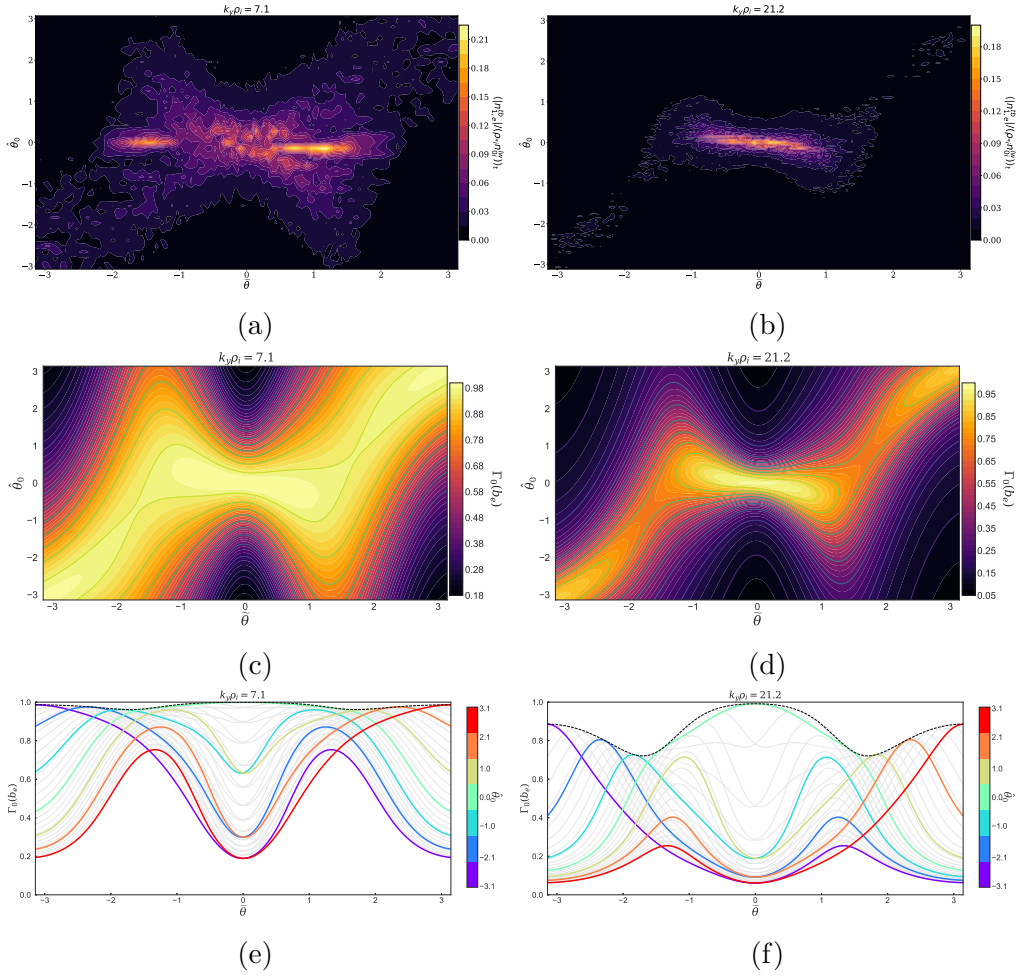


Figure 10.2: The first ballooning chain for Slab2 for time averaged density perturbations in (a):  $k_y \rho_i = 7.1$ , and (b),  $k_y \rho_i = 21.2$ . (c):  $\Gamma_0(b_e(\theta, \theta_0))$  for  $k_y \rho_i = 7.1$  and (d),  $k_y \rho_i = 21.2$ . (e) and (f): One-dimensional plots of (e) and (f), respectively, with certain  $\hat{\theta}_0$  values highlighted in color. Grey lines indicate other  $\hat{\theta}_0$  values.

this point we will focus on the nonlinear physics of slab ETG rather than toroidal ETG modes in the pedestal, although we briefly summarize tentative results for the long term behavior of simulations with magnetic drifts in Section 10.3. In the next section, we investigate how FLR effects determine slab ETG physics in the pedestal.

## 10.2 FLR Effects in Pedestal Turbulence

In this section, we demonstrate that ETG turbulence is confined to regions where  $b_e = (k_\perp \rho_e)^2/2$  has a low value. We do this by showing a strong correlation between regions of weak FLR damping and higher turbulent intensity, particularly at larger  $k_y \rho_i$  values.

This effect occurs for all the different geometries we investigate. In Figure 10.2(a) and (b), we show the pedestal turbulence versus  $\tilde{\theta}$  and  $\hat{\theta}_0$  for Slab1 at two values of  $k_y\rho_i$ . We only plot the density perturbations for  $-\pi \leq \hat{\theta}_0 \leq \pi$ , ignoring connections at higher values of  $|\hat{\theta}_0|$  (the turbulent intensity at higher values of  $|\hat{\theta}_0|$  is small). We compare the density fluctuations with a plot of  $\Gamma_0(b_e)$  versus  $\tilde{\theta}$  and  $\hat{\theta}_0$  at the two values of  $k_y\rho_i$  in Figure 10.2 (c) and (d). At a given  $\hat{\theta}_0$  value, the turbulence extends a distance in  $\tilde{\theta}$  before the value of  $\Gamma_0$  becomes too small, after which the turbulent intensity falls significantly. Figure 10.2 (e) and (f) show a one-dimensional cut of Figure 10.2 (c) and (d) for several selected values of  $\hat{\theta}_0$ ; these plots indicate that turbulence with certain values of  $\hat{\theta}_0$  close to zero is able to extend much farther in  $\tilde{\theta}$  without being significantly FLR damped. The dashed black line shows the maximum value of  $\Gamma_0$  for any  $\hat{\theta}_0$  value at each  $\tilde{\theta}$  location; this envelope will be discussed in detail shortly. We see that for  $k_y\rho_i = 21.2$ , modes with  $|\hat{\theta}_0|$  close to zero can have a larger value of  $\Gamma_0(b_e)$  that is close to the black dashed line for a relatively wide range of  $\tilde{\theta}$  values.

To test our hypothesis that FLR effects confine the turbulence, we perform simulations with different geometric configurations, which will have different  $\Gamma_0$  configurations in  $\tilde{\theta} - \hat{\theta}_0$  space. We use ‘Geo’ simulations that have a lower resolution and are used to scan different geometries at lower computational cost; their grid resolutions are the same as Slab2, except they have just under half of the number of radial wavenumbers. The simulation parameters are listed in Table 10.2. We emphasize that the ‘Geo’ simulations are not sufficiently high-resolution to make accurate quantitative comparisons of quantities such as the heat flux, but rather are meant to test the effect that the geometry has on the poloidal distribution of the turbulence. We have performed scans in `ntheta`, `naxx`, `naky`, and `jt看ist`, which showed that no qualitative change from the Geo results.

To motivate the different Geo simulation geometries, we pay close attention to two geometrical features of the pedestal equilibrium: the presence of strong local magnetic shear, and strong flux expansion. The local magnetic shear is the difference in the local pitch angle between two neighboring flux surfaces, whereas the global magnetic shear is the average over the flux surface. Flux expansion occurs when the physical distance between adjacent flux surfaces also varies as a function of poloidal angle. In the circular flux surface limit, the local magnetic shear is almost constant and hence almost equal to

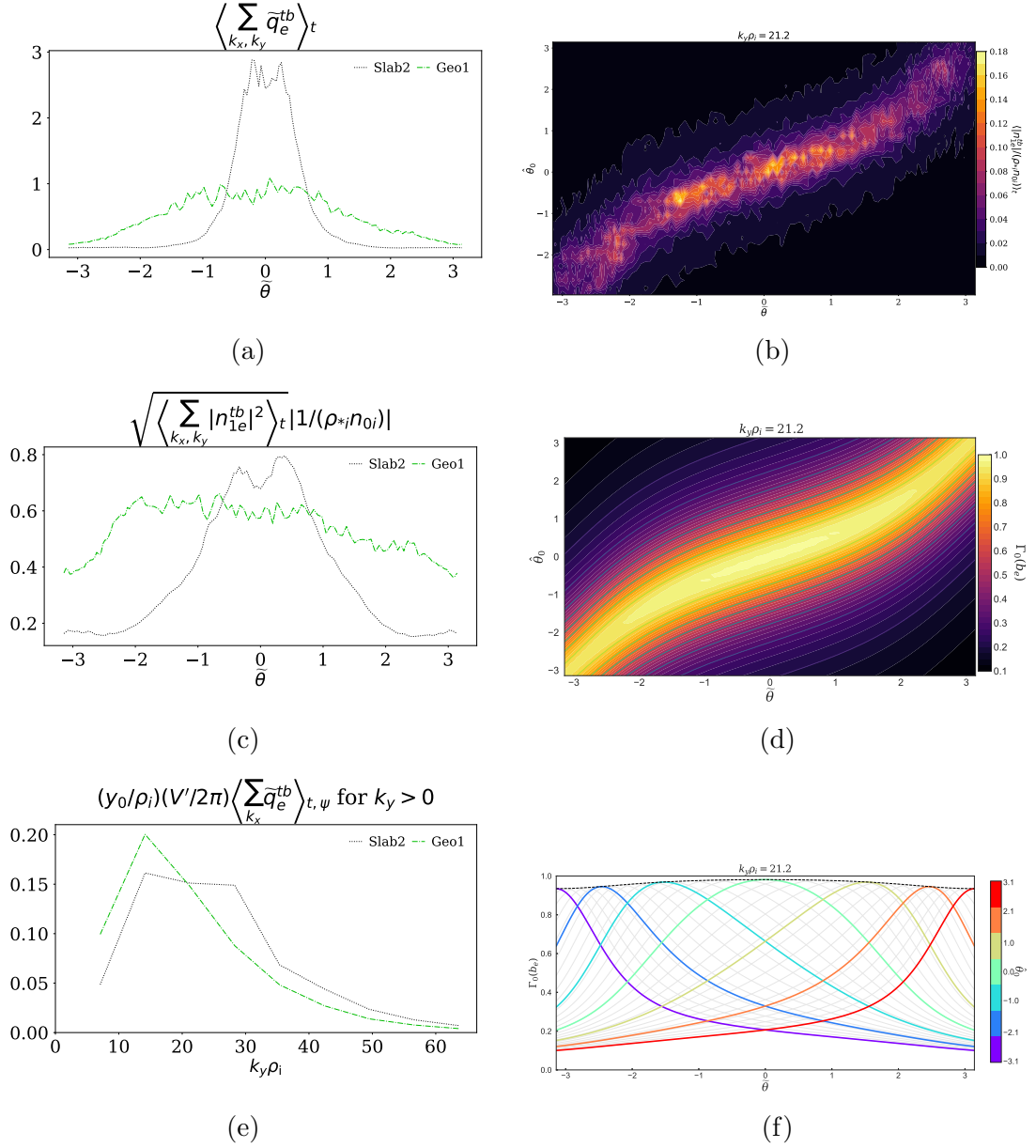


Figure 10.3: Left column: comparison of (a): heat flux versus  $\tilde{\theta}$ , (c): density fluctuations versus  $\tilde{\theta}$ , and (e): heat flux versus  $k_y \rho_i$  for Slab2 and Geo1. Right column: (b): density perturbations for Geo1 versus  $\hat{\theta}_0$  and  $\tilde{\theta}$ , (d):  $\Gamma_0$  for Geo1 versus  $\hat{\theta}_0$  and  $\tilde{\theta}$ , and (f):  $\Gamma_0$  for Geo1 versus  $\tilde{\theta}$  for a selection of  $\hat{\theta}_0$  values.

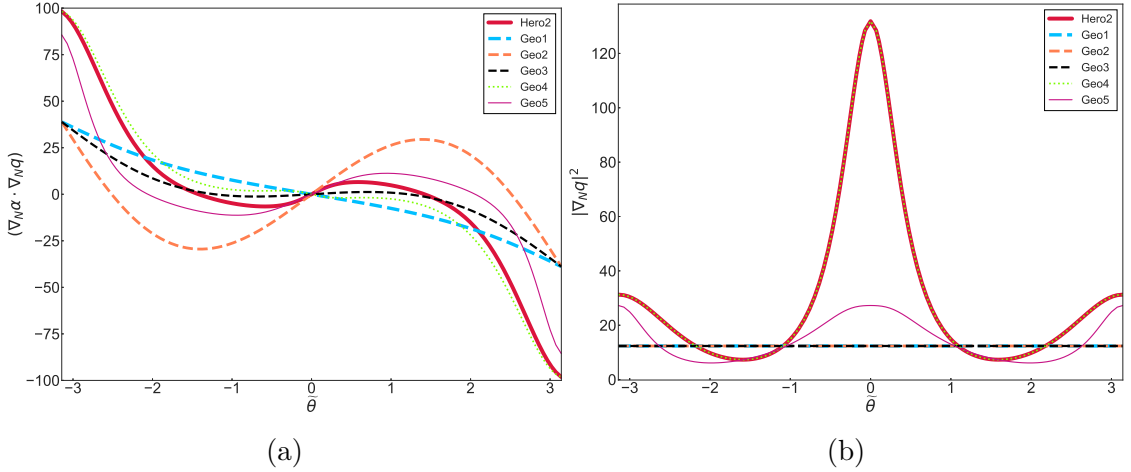


Figure 10.4: The geometric coefficients for the six geometries. (a):  $g_{21}$ , (b):  $g_{22}$ .

the global magnetic shear, and there is no flux expansion. The local magnetic shear and flux expansion enter the definition of the perpendicular wavenumber. It will be useful to write  $k_{\perp}$  in the following form,

$$|k_{\perp}|^2 = k_y^2 \left| g_2 + 2\hat{\theta}_0 g_{21} + \hat{\theta}_0^2 g_{22} \right|, \quad (10.1)$$

where  $g_2 = (d\psi_N/d\rho)^2 |\nabla_N \alpha|^2$ ,  $g_{21} = (d\psi_N/d\rho)^2 \nabla_N \alpha \cdot \nabla_N q$ ,  $g_{22} = (d\psi_N/d\rho)^2 |\nabla_N q|^2$ , and  $d\psi_N/d\rho = (\partial\psi/\partial r)(1/aB_a)$ . Here,  $\nabla_N = a\nabla$ . The  $\tilde{\theta}$  derivative of the coefficient  $g_{21}$  is roughly proportional to the local magnetic shear, and the quantity  $\sqrt{g_{22}}$  gives the flux expansion. As shown in Figure 10.4, for the circular flux surface, Geo1 ( $\delta = \delta' = \kappa' = \Delta' = \beta' = 0, \kappa = 1$ ),  $\partial_{\tilde{\theta}} g_{21}$  is roughly constant, and  $g_{22}$  is exactly constant. In contrast, for the pedestal geometry Slab2, both  $\partial_{\tilde{\theta}} g_{21}$  and  $g_{22}$  vary strongly with  $\tilde{\theta}$ . We now compare simulation results for Slab2 and Geo1, which both have  $\mathbf{v}_{Ms} = 0$ .

As shown in Figure 10.3(a), the heat flux is far less confined to the outboard midplane for the circular flux surface than for the pedestal geometry, where in the latter case  $\tilde{q}_e^{tb}$  is close to zero at  $|\tilde{\theta}| \gtrsim 1.5$ . Also shown in Figure 10.3(c), the fluctuation intensity falls off more slowly for Geo1 compared with Slab2. While the turbulence character in these two runs varies, their heat flux spectra are comparable, as shown in Figure 10.3(e). The weaker poloidal dependence of the density perturbations for Geo1 is also shown in Figure 10.3(b), where the turbulence is able to extend farther in  $\tilde{\theta}$ . As was also the case for Slab2 in Figure 10.2, the density perturbations in Figure 10.3(c) and the  $\Gamma_0$  profile

in Figure 10.3(d) are well correlated. Finally, comparing the one dimensional plots of  $\Gamma_0$  versus  $\tilde{\theta}$  in Figure 10.2(f) (Slab2) and Figure 10.3(f) (Geo1), for Slab2, certain  $\hat{\theta}_0$  values have a much longer  $\tilde{\theta}$  extent where  $\Gamma_0$  is relatively close to 1. In contrast, for the circular flux surface, no single  $\hat{\theta}_0$  mode is substantially wider in  $\tilde{\theta}$  than another. Clearly, the geometry has caused a significant difference in the character of the turbulence in the circular limit of uniform local magnetic shear and no flux expansion. Figure 10.2(e) and (f) show one dimensional plots of the quantity  $\Gamma_0(b_e)$  plotted for a selection of  $\hat{\theta}_0$  values versus  $\tilde{\theta}$  at a fixed value of  $k_y\rho_i$  for the pedestal geometry, and Figure 10.3(f) for the circular geometry. Several properties are apparent from these graphs:

1. There is a minimum non-zero value of  $k_\perp$  for each value of  $\tilde{\theta}$  for both the pedestal and circular geometries. That is, there is no value of  $\hat{\theta}_0$  such that  $k_\perp = 0$  for each  $\tilde{\theta}$  value; this is shown by the dashed black line in Figure 10.2(e) and (f), and Figure 10.3(f). The quantity  $k_{\perp\min}$  is given by differentiating  $|k_\perp|^2$  with respect to  $k_x$ , which gives that the minimum  $|k_\perp|$  value is  $k_x = -k_y\hat{s}g_{21}/g_{22}$ . At this value of  $k_x$ ,

$$|k_{\perp\min}|^2 = k_y^2 \left| g_2 - \frac{(g_{21}^2)}{g_{22}} \right|. \quad (10.2)$$

In general,  $k_{\perp\min} \neq k_y$ , even for a circular flux surface.

2. For the pedestal geometry,  $\tilde{\theta} = 0$  and  $\tilde{\theta} = \pm\pi$  are special points: that is,  $k_{\perp\min}$  is smaller at these locations than at other poloidal locations. This gives the prediction that the  $k_y$  peak of the spectra could be larger at  $\tilde{\theta} = 0$  and/or  $\tilde{\theta} = \pm\pi$ , and that the turbulent peak will occur at smaller values of  $k_y$  in between these  $\tilde{\theta}$  values. For the circular flux surface, while  $k_{\perp\min}$  is a maximum at  $\tilde{\theta} = 0$ , it has a much weaker  $\tilde{\theta}$  dependence than the pedestal geometry.
3. While  $k_{\perp\min}$  varies more with  $\tilde{\theta}$  for the pedestal case, the pedestal also has far fewer regions where a mode can extend far along  $\tilde{\theta}$  at fixed  $\hat{\theta}_0$  without the mode being strongly FLR damped. For example, as shown in Figure 10.2 (f), the range of  $\tilde{\theta}$  values for which  $\Gamma_0(b_e, \hat{\theta}_0 = 0.0) \gtrsim 0.5$  is roughly  $\Delta\tilde{\theta} \simeq 4$ , whereas for  $\hat{\theta}_0 = 1.0$ , the region for which  $\Gamma_0(b_e, \hat{\theta}_0 = 1.0) \gtrsim 0.5$  is much narrower:  $\Delta\tilde{\theta} \simeq 1$  (note that for  $\hat{\theta}_0 = 1.0$ , there are two distinct disconnected regions where  $\Gamma_0(b_e, \hat{\theta}_0 = 1.0) \gtrsim 0.5$ ,

whereas for  $\hat{\theta}_0 = 0.0$ , there is a single continuous region where  $\Gamma_0(b_e, \hat{\theta}_0 = 0.0) \gtrsim 0.5$ ). In contrast, the circular flux surface can accommodate extended modes along  $\tilde{\theta}$  for almost all  $\hat{\theta}_0$  values. For example, shown in Figure 10.3 (f), for  $\hat{\theta}_0 = 0.0$ ,  $\Delta\tilde{\theta} \simeq 4$ , and for  $\hat{\theta}_0 = 1.0$ ,  $\Delta\tilde{\theta} \simeq 3$ . Furthermore, for a given value of  $\hat{\theta}_0$ , there are no disconnected regions of  $\Gamma_0(b_e, \hat{\theta}_0) \gtrsim 0.5$ ; there is only one  $\tilde{\theta}$  location that satisfies  $\partial_{\tilde{\theta}}\Gamma_0(b_e, \hat{\theta}_0) = 0$  for each value of  $\hat{\theta}_0$ .

Motivated by the effect that local magnetic shear and local flux expansion appear to have on the poloidal distribution of the turbulence, we now introduce four additional geometries with varying local magnetic shear and local flux expansion that provide further examples of FLR effects confining the turbulence. These geometries were chosen to modify the geometric coefficients  $g_{21}$  and  $g_{22}$ , shown in Figure 10.4 to ascertain which effect was more important to the localization of the turbulence. Modifying the value of  $\beta'$  leaves  $g_{22}$  unchanged, but significantly changes the  $g_{21}$  profile. Modifying the quantities  $\Delta'$  and  $\kappa$  changes both  $g_{21}$  and  $g_{22}$ . Therefore, different combinations of  $\beta'$ ,  $\Delta'$ , and  $\kappa$  were used to test the effect of changing the local magnetic shear and flux surface expansion on the poloidal distribution of the turbulence. The pedestal geometry has a strongly varying  $g_{21}$  profile and  $g_{22}$  profile, whereas the circular geometry has a nearly linear  $g_{21}$  profile (weak and nearly constant local magnetic shear) and a constant  $g_{22}$  profile (no local flux surface expansion). The profile of  $g_{21}$  in the pedestal is such that  $\partial_{\tilde{\theta}}g_{21} < 0$  for  $|\tilde{\theta}| \gtrsim 0.5$ . The four additional geometries are an attempt to separate these distinct features of  $g_{21}$  and  $g_{22}$  into different simulations:

- Geo2: circular flux surface plus the pedestal value of  $\beta'$  (strong local magnetic shear, no flux surface expansion).
- Geo3: circular flux surface plus one third the pedestal value of  $\beta'$  (region of  $\partial_{\tilde{\theta}}g_{21} \approx 0$  for  $|\tilde{\theta}| \lesssim 1$ , no flux surface expansion).
- Geo4: pedestal flux surface but with  $\beta' = 0$  (region of  $\partial_{\tilde{\theta}}g_{21} \approx 0$  for  $|\tilde{\theta}| \lesssim 1$ , pedestal-like flux surface expansion).

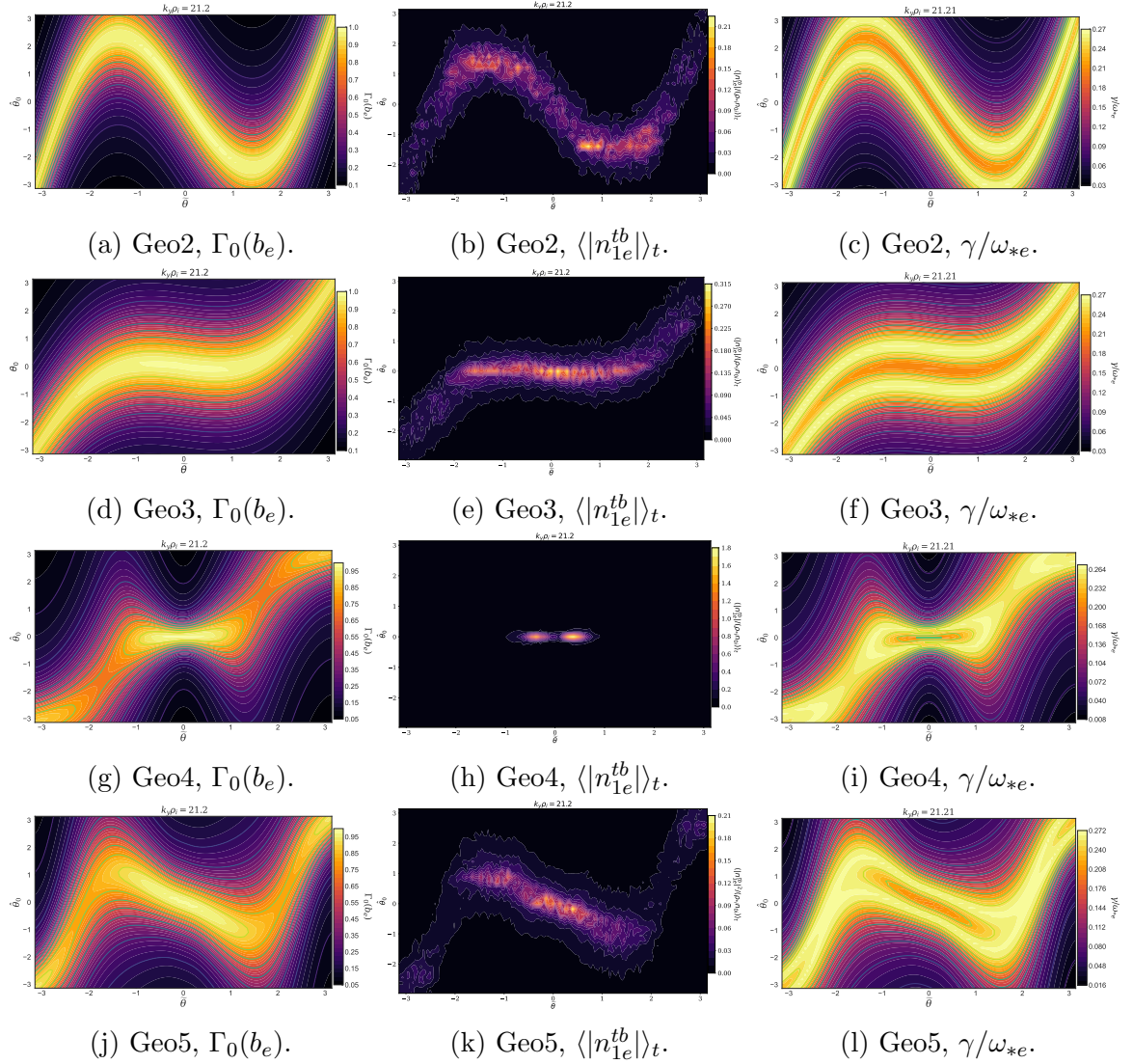


Figure 10.5: Left column:  $\Gamma_0(b_e)$  versus  $\tilde{\theta}$  and  $\hat{\theta}_0$ . Middle column:  $|n_{1e}^{tb}|$  versus  $\tilde{\theta}$  and  $\hat{\theta}_0$ . Right column:  $\gamma/\omega_{*e}$  versus  $\tilde{\theta}$  and  $\hat{\theta}_0$ . Top row: Geo2, second row: Geo3, third row: Geo4, fourth row: Geo5.

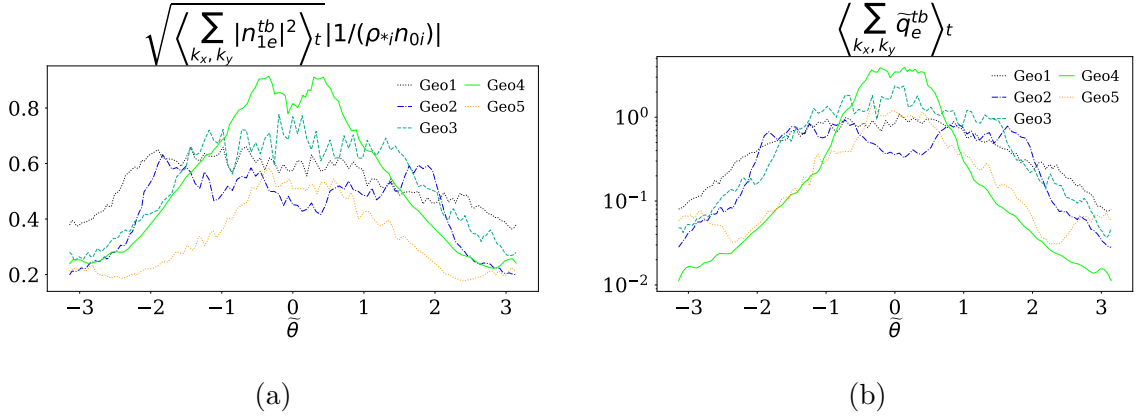


Figure 10.6: (a):  $n_{1e}^{tb}$  versus  $\tilde{\theta}$  for the five non-pedestal geometries, and (b):  $\tilde{q}_e^{tb}$  versus  $\tilde{\theta}$ .

- Geo5: pedestal flux surface but with  $\Delta' = 0$ ,  $\kappa = 1.0$  (some local magnetic shear, some local flux surface expansion, but both weaker than the pedestal-like flux surface expansion).

Plots of  $\Gamma_0(b_e)$  versus  $\hat{\theta}_0$  and  $\tilde{\theta}$  for these four geometries, shown in the left column of Figure 10.5, provide some intuition for how local magnetic shear and local flux expansion affect the values of  $\Gamma_0(b_e)$ . Comparing Geo2 and Geo3 in Figure 10.5(a) and Figure 10.5(d), which differ only by their local magnetic shear profiles, we see how the local magnetic shear ‘twists’ the  $\Gamma_0(b_e)$  profile in  $\hat{\theta}_0$ - $\tilde{\theta}$  space, while keeping the value of  $\Gamma_0(b_e)$  at  $(\tilde{\theta}, \hat{\theta}_0) = (0, 0), (\pm\pi, \pm\pi)$  roughly fixed. Similarly, comparing Geo3 and Geo4 in Figure 10.5(d) and Figure 10.5(g), which differ mainly by their local flux expansion, we observe that the flux expansion ‘expands’ the width of the  $\Gamma_0(b_e)$  profile in regions of larger  $|\nabla_N q|^2$  for  $\hat{\theta}_0 \neq 0$ . Finally, Geo5, which was chosen to have a comparable local magnetic shear profile to the pedestal but much weaker flux expansion, has a  $\Gamma_0(b_e)$  profile (Figure 10.5(j)) that is similar to the pedestal (Figure 10.2(d)), but has larger values of  $\Gamma_0$  for a wider range of  $\tilde{\theta}$  values.

Comparison of the density fluctuations for the pedestal and circular flux surface shapes revealed the correlation between high values of  $\Gamma_0(b_e)$  and a larger density fluctuation intensity. Observing the middle column of Figure 10.5 further supports this observation, where larger  $\Gamma_0$  values and stronger turbulence fluctuations are again, strongly correlated. As a plausibility check, we solved the collisionless slab ETG dispersion relation [137], as a function of  $\hat{\theta}_0$  and  $\tilde{\theta}$ , for Geo runs 2-5, shown in the right column

of Figure 10.5. The density fluctuations in the middle column are strongly correlated with the growth rates  $\gamma/\omega_{*e}$  in the right column of Figure 10.5. Note that our dispersion relation does not include the effects of magnetic shear (that is, in our treatment  $k_{\parallel}$  is independent of  $x$ ), and hence should not necessarily be expected to be an accurate predictor of the slab ETG growth rates in the pedestal, but rather used as a rough estimate.

The poloidal distribution of the heat flux also depends strongly on the geometry. In Figure 10.6(b), we plot the heat flux distribution for Geo simulations. In Figure 10.6(a), we plot the density of different configurations, which fall off less steeply than the heat flux, but have maxima at similar poloidal locations to the heat flux. We observe that the presence of significant local magnetic shear or flux expansion causes the heat flux to be smaller at  $|\tilde{\theta}| = \pi$  than the circular flux surface. Any up-down asymmetry in Figure 10.6 is due to insufficiently long time averaging. Despite the differences in the heat flux and density profiles, all six geometries (the standard pedestal and the 5 Geo configurations) have a region, centered around  $\tilde{\theta} = 0$ , of long radially elongated structures with a well-defined parallel wavenumber, shown in plots of  $\bar{\phi}_1^{tb}$  versus  $\tilde{\theta}$  and  $\Delta\tilde{r}$  in Figure 10.7. The only slight exception was Geo2, whose central region was not as well-defined as other geometries, although still existed somewhat. This is not surprising, given how relatively narrow a range of  $\tilde{\theta}$  values Geo2 has  $\Gamma_0(b_e) \approx 1$  around  $\tilde{\theta} = 0$  at fixed  $\hat{\theta}_0$  (see Figure 10.5(a)). We also plot  $\bar{\phi}_1^{tb}$  versus  $\tilde{\theta}$  and  $y$  in Figure 10.8, which demonstrates how the geometry modifies the  $y$  scales of the turbulence, although simulations with higher resolution in the  $y$  direction are needed to make quantitative comparisons. By comparing Figure 10.4 and Figure 10.6, magnetic geometries with a strong local flux expansion appear to confine the turbulent fluctuations and heat flux much more strongly around  $\tilde{\theta} = 0$ .

Our simulations reveal that large fluctuation amplitudes appear not simply in regions where  $\Gamma_0(b_e)$  is relatively large, but where  $\Gamma_0(b_e)$  is sufficiently large for a sufficiently long extent in  $\tilde{\theta}$  at a fixed value of  $\hat{\theta}_0$ . For the Geo2-5 simulations, comparison of the middle column of Figure 10.5 with the left column demonstrates that turbulence is localized to regions where it can have the longest parallel correlation length at fixed  $\hat{\theta}_0$ . The same is also true for Slab 2 (see Figure 10.2 (b) and (d)) and Geo1 (see Figure 10.3 (b))

and (d)). For example, for Geo1, the turbulence is the most uniform in  $\hat{\theta}_0$  and  $\tilde{\theta}$ ; we speculate that this is because  $\Gamma_0(b_e)$  is sufficiently large for a long extent in  $\tilde{\theta}$  for almost all  $\hat{\theta}_0$  values, and so there is not a strongly preferred  $\tilde{\theta}$  value where FLR damping is weaker. In contrast, Geo2 has relatively high fluctuation amplitudes at  $\tilde{\theta} \simeq \pm(1-2)$  and  $\hat{\theta}_0 \simeq \pm 1.5$ , which is precisely where  $\Gamma_0(b_e)$  can extend farthest in  $\tilde{\theta}$  at fixed  $\hat{\theta}_0$ . Thus, for Geo2, strong shaping confines the turbulence more strongly at certain  $\tilde{\theta}$  values. While we do not yet have a scaling theory for this phenomenon, heuristically, a comparison of the heat flux versus  $\tilde{\theta}$  profiles in Figure 10.6(b) with the respective  $\Gamma_0(\tilde{\theta}, \hat{\theta}_0)$  profiles for each simulation shows that the heat flux is largest in regions where the mode can extend farther in  $\tilde{\theta}$  at fixed  $\hat{\theta}_0$  without being strongly FLR damped. Thus, the scaling theory is likely to be a modified version of critical balance in [138], where eddies with a longer parallel extent can transport more heat.

In order to underscore the unusual character of the pedestal turbulence, we compare it with that of an ETG simulation with CBC-like (Cyclone Base Case) parameters (including magnetic drifts). In the CBC-like simulation, eddies extend coherently across  $\tilde{\theta} \in [-\pi, \pi]$ , in strong contrast with the pedestal runs we have performed where they have a relatively short parallel correlation length. Plots of  $\overline{\phi}_1^{tb}$  versus  $\Delta\tilde{r}$  and  $\tilde{\theta}$ , and versus  $y$  and  $\tilde{\theta}$  for the CBC-like ETG simulation are shown in Figure 10.7(g) and Figure 10.8(g). Both plots for the CBC simulation demonstrate elongated structures constrained to flux surfaces and extended in the parallel direction.

GS2 Pedestal Simulations									
Simulation	$\kappa$	$\kappa'$	$\delta$	$\delta'$	$\Delta'$	$\beta'$	$q$	$\hat{s}$	nakx
Slab2	1.55	0.95	0.26	0.74	-0.35	-0.12	5.08	3.36	199
Geo1	1.0	0.0	0.0	0.0	0.0	0.0	5.08	3.36	84
Geo2	1.0	0.0	0.0	0.0	0.0	-0.12	5.08	3.36	199
Geo3	1.0	0.0	0.0	0.0	0.0	-0.04	5.08	3.36	199
Geo4	1.55	0.95	0.26	0.74	-0.35	0.0	5.08	3.36	199
Geo5	1.0	0.95	0.26	0.74	0.0	-0.12	5.08	3.36	199

Table 10.2: Nonlinear simulations discussed in this chapter that compare magnetic geometries. All have  $\mathbf{v}_{Ms} = 0$ .

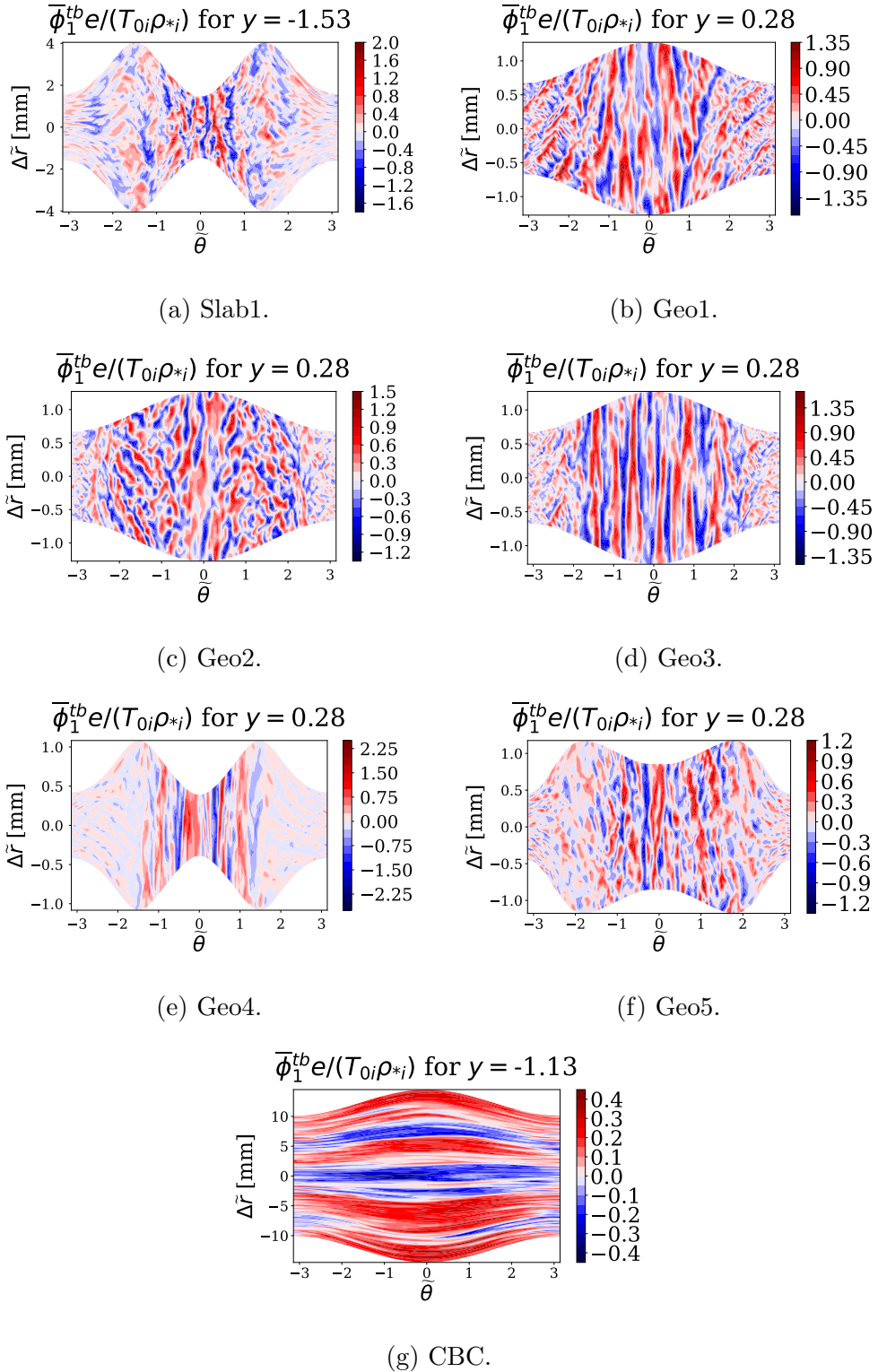


Figure 10.7: Comparison of potential fluctuations versus  $\tilde{\theta}$  and  $\Delta\tilde{r}$  for the six geometries and the CBC: (a) Full pedestal (Base), (b): Circular (Geo1), (c): Geo2, (d): Geo3, (e): Geo4, (f): Geo5, (g): ETG CBC.

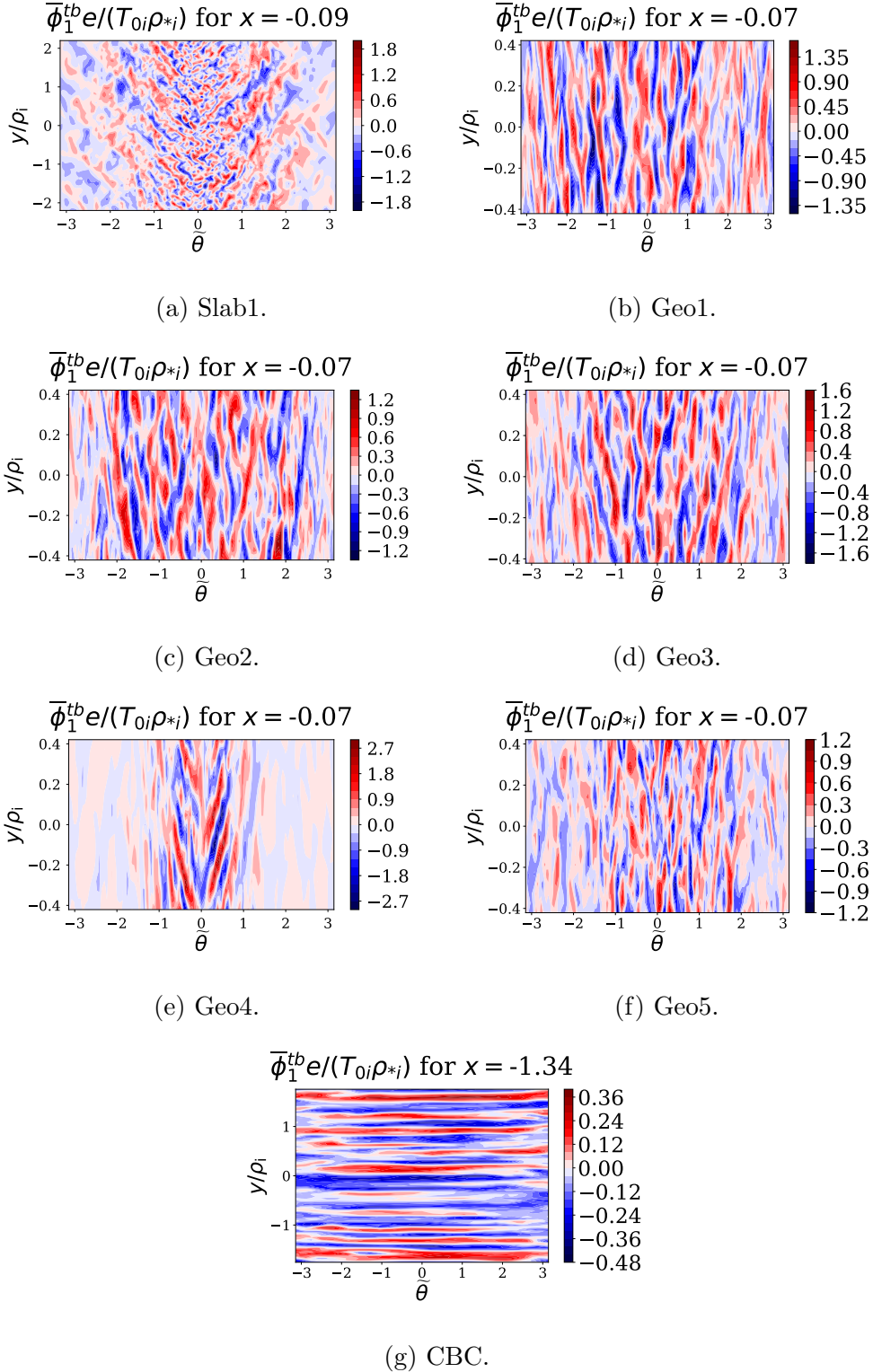


Figure 10.8: Comparison of potential fluctuations versus  $\tilde{\theta}$  and  $y$  for the six geometries: (a) Full pedestal (Slab1), (b): Circular (Geo1), (c): Geo2, (d): Geo3, (e): Geo4, (f): Geo5, (g): ETG CBC.

### 10.2.1 Heat Flux Poloidal Distribution

In this section, we describe the apparent mismatch between the poloidal distribution of the heat flux and the turbulent intensities, shown in Figure 10.6, which is due to a combination of factors: cross phase angles, temperature and potential perturbations, and the magnetic geometry. Using the definition for the turbulent heat flux  $q_s^{tb}(k_x, k_y, \tilde{\theta}, t)$  in Equation (5.9), we find that  $q_s^{tb}(\tilde{\theta}, t)$  can be written as

$$q_s^{tb}(\tilde{\theta}, t) = \frac{3\pi c}{\langle |\nabla r| \rangle_\psi B_a V'} \times \sum_{k_x, k_y} k_y \left[ |n_{1s, -k_x, -k_y}^{tb}| |\phi_{1, k_x, k_y}^{tb}| T_{0s} \sin(\xi_{\phi, n}) + |T_{1s, -k_x, -k_y}^{tb}| |\phi_{1, k_x, k_y}^{tb}| n_{0s} \sin(\xi_{\phi, T}) \right]. \quad (10.3)$$

Here,  $\bar{T}_{1s}^{tb} = \sum_{k_x, k_y} T_{1s, k_x, k_y}^{tb}$  is defined as

$$n_{0s} \bar{T}_{1s}^{tb} = \int d^3v \bar{h}_s \left( \frac{m_s v^2}{3} - T_{0s} \right). \quad (10.4)$$

The cross phase angles are given by  $\xi_{A,B} = \Theta_A - \Theta_B$ , where we have defined  $\Theta_A = \arg(A)$  so that  $A = |A| \exp(i\Theta_A)$ . In this work, the cross phase angle  $\xi_{A,B}$  depends on both  $k_x$  and  $k_y$ . We therefore need a cross phase angle  $\xi_{A,B} \neq n\pi$  where  $n$  is an integer to produce transport. In Figure 10.9, we plot the quantities that depend on  $\tilde{\theta}$  in Equation (10.3) versus  $\tilde{\theta}$ , to demonstrate how the combination of potential and temperature perturbations, and the cross phase angle, align to give the correct heat flux profile. This is evidenced by the quantity  $\sum_{k_x, k_y} k_y |\phi_1^{tb}| |T_{1e}^{tb}| \sin(\xi_{T,\phi})$  giving good agreement with  $\tilde{q}_e^{tb}$ . In Figure 10.9, we have suppressed the  $k_x$  and  $k_y$  indices, but all quantities in the summation except for  $k_y$  depend on both  $k_x$  and  $k_y$ . Note that agreement is not exact because we have neglected the contribution to  $\tilde{q}_e^{tb}$  due to density perturbations.

## 10.3 Toroidal ETG Turbulent State

While the nonlinear chapters in this thesis have focused on the turbulent slab ETG dominated state, in Section 9.3 we mentioned that the Base1 simulation might not yet be in a saturated state. Preliminary results suggest that the toroidal ETG modes become dynamically important at later times; for  $tv_{ti}/a \gtrsim 1.3$ , the heat flux in Figure 9.4(a)

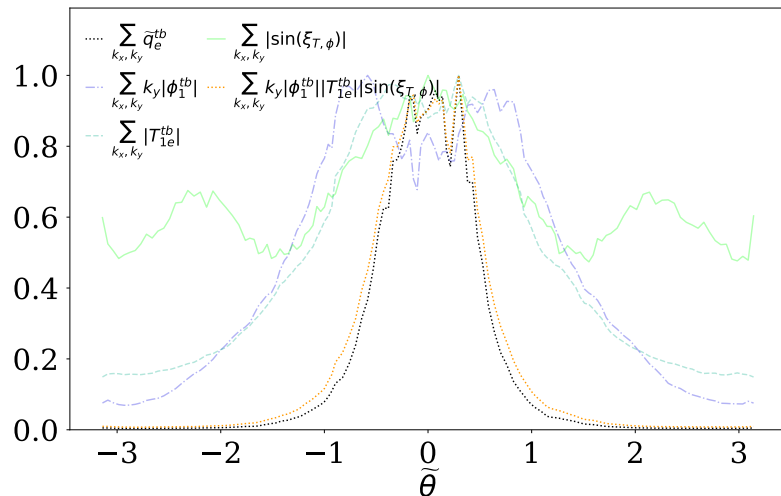


Figure 10.9: Poloidal distribution of the heat flux  $\tilde{q}_e^{tb}$  and quantities that enter the expression for the heat flux in Equation (10.3) for Slab2. Each of the quantities is normalized to its maximum value.

decreases while the potential continues to increase. In Figure 10.10, we compare the turbulence at these later timesteps in Base1 with saturated turbulence without magnetic drifts, Slab1. Comparing the heat flux versus  $k_x$  and  $k_y$  for Slab1 and Base1 in Figure 10.10(a) and (b) respectively, there is a small difference at  $k_y \rho_i \sim 1$  values, which for Base1 have small amplitudes at larger  $|k_x|$  values. In Figure 10.10(c) and (d), we compare the  $|\phi|^2$  spectra, which reveal a much starker difference: Slab1 has no large  $|k_x|$  but small  $k_y$  modes, in contrast to Base1. Clearly, in Base1, modes with smaller values of  $k_y \rho_i \sim 1$  have become dynamically important. It also instructive to compare the  $\Delta \tilde{r} - \tilde{\theta}$  and  $y - \tilde{\theta}$  projections, where the toroidal ETG modes with  $K_x \gg k_y$  are easily identifiable. In Figure 10.10(e) and (f), we compare the  $\Delta \tilde{r} - \tilde{\theta}$  projection; in Base1, there are additional toroidal ETG modes with relatively large  $K_x$  that extend far in  $\tilde{\theta}$ . In Figure 10.10(g) and (h), the  $y - \tilde{\theta}$  projection also reveals toroidal ETG modes with  $k_y \rho_i$  values much smaller than the slab in the central region. The numerical robustness of the long term state of these simulations is currently under investigation.

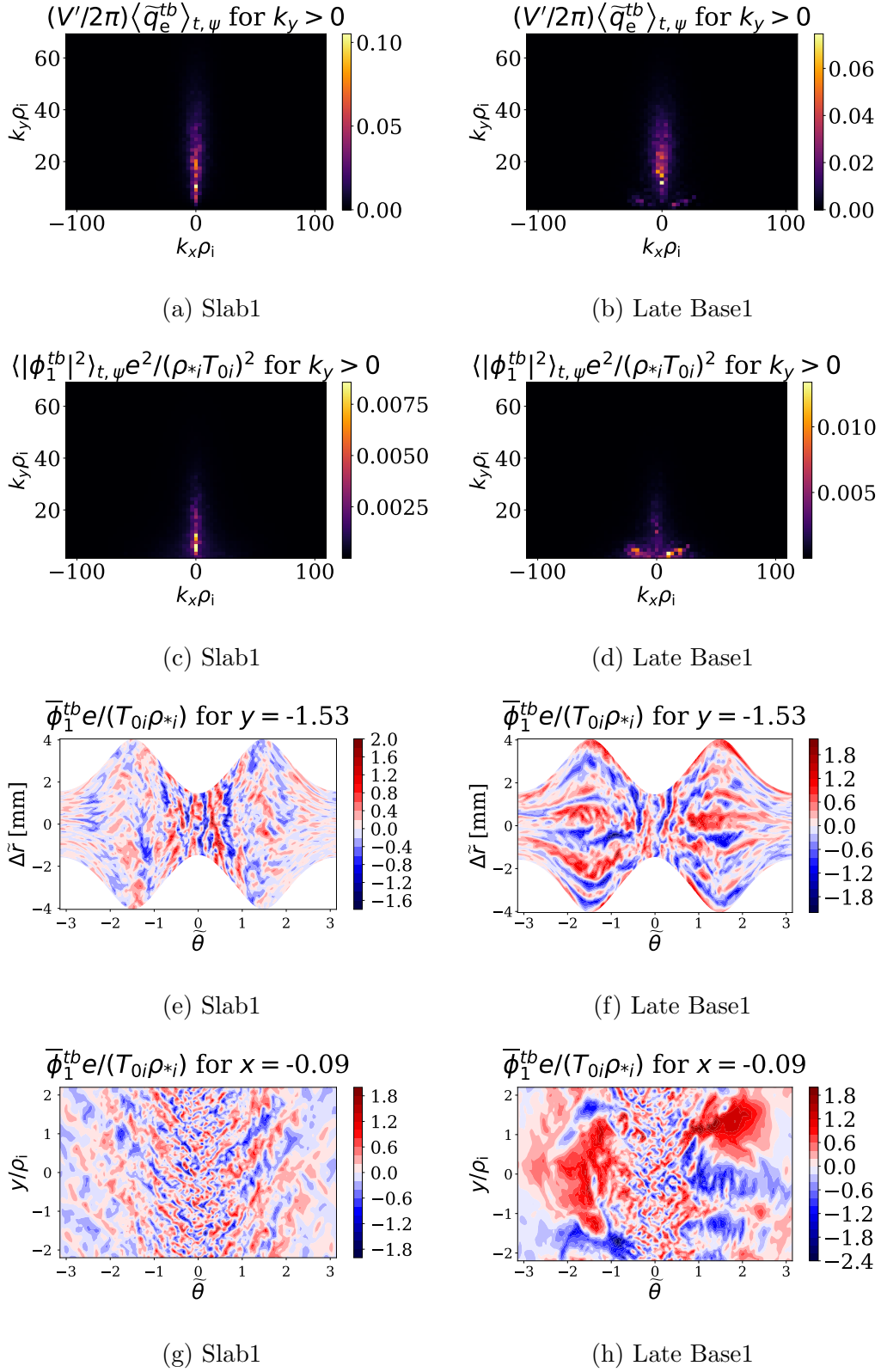


Figure 10.10: Comparison of turbulence properties for Slab1 versus Base1 in later timesteps for Base1.

## 10.4 Discussion

We have demonstrated that ETG pedestal turbulence for the equilibrium we have studied is dominated by slab ETG rather than toroidal ETG instability in the intermediate time state. The configuration of pedestal slab ETG turbulence in  $\hat{\theta}_0 - \tilde{\theta}$  space is very strongly constrained by FLR effects at larger values of  $k_y \rho_i$ , which limit its parallel extent, which in turn likely constrains how much transport the mode can produce. We find that local flux expansion causes FLR effects that are largely responsible for the strong confinement around  $\tilde{\theta} = 0$ . The character of pedestal ETG turbulence is markedly different to core ETG turbulence: in the pedestal, ETG turbulence is characterized by structures that are both narrow in  $\tilde{\theta}$  and highly inhomogeneous in  $\tilde{\theta}$ . In contrast, core ETG turbulence has long correlated structures that extend fully across  $\pi < \tilde{\theta} < \pi$ , and which are fairly homogeneous in  $\tilde{\theta}$ . Additionally, the very strong poloidal dependence of the heat flux can be straightforwardly explained by a combination of the field perturbations and the cross phase angle. Finally, the long time saturated state of pedestal turbulence may indeed reveal toroidal ETG turbulence, but more work is needed to confirm that the simulations are well-converged. Even if toroidal ETG turbulence is dynamically important for the long time saturated state, we do not yet understand why it is so inefficient at transporting heat; indeed, in our simulations, toroidal ETG turbulence appears to have decreased the turbulent heat flux.

# Chapter 11

## Conclusions

The steep temperature gradients and magnetic shear in the pedestal give rise to linear toroidal ITG and ETG microinstabilities whose characters are very different to the core. The toroidal ETG/ITG instability becomes more unstable at  $K_x \gg k_y$ , and the toroidal ETG mode is fastest growing mode for  $k_y \rho_i \gtrsim 1.0$  in the JET-ILW pedestal case we have examined. This mode is often most unstable at a relatively large ballooning coordinate  $\theta$ , and has a critical temperature gradient that is as large as  $R_0/L_{Te} \sim 30$ . Quasilinear estimates of  $\gamma/k_\perp^2$  and  $Q_e^{tb}/(k_y \rho_i |\phi_1^{tb}|^2)$  suggest that this toroidal ETG mode can efficiently transport heat. With the measured ion temperature profiles, we find that the ITG mode is stable for  $k_y \rho_i \ll 1$ , and is very-weakly driven at  $k_y \rho_i \sim 1$ . We have found that  $\mathbf{E} \times \mathbf{B}$  shear can fully suppress KBMs, and that it is also effective at stabilizing ITG. It is unable to stabilize ETG instability. For  $0.1 \lesssim k_y \rho_i \lesssim 1.0$ , ‘extended ETG’ modes span a wide range of perpendicular scales, and ‘electron tails’ at  $k_y \rho_i \lesssim 0.07$  are extremely extended in  $\theta$ . These two mode categories have not been investigated further in this thesis, but might also be important for transport.

Nonlinearly, we chose to study ETG physics at scales  $k_y \rho_i \gtrsim 1.0$ , since ITG is weakly-driven in the pedestal we have studied. We have shown that pedestal ETG heat transport is dominated by the slab ETG instability, despite this mode being linearly subdominant. Indeed, we found that in simulations without toroidal ETG instability, the heat transport increased by 15%. However, there is the caveat that our simulations with magnetic drifts need to be run for longer, which might reveal a new saturated state where toroidal ETG instability is dynamically important. Due to the magnetic geometry, pedestal ETG turbulence is statistically inhomogeneous in the poloidal angle. Using a variety of

geometric configurations, we have demonstrated that slab ETG turbulence is confined to regions of relatively small perpendicular wavenumber and where the mode can maximally extend in  $\tilde{\theta}$ , which are the regions that transport the most heat. In contrast to core ETG turbulence, which is statically homogeneous in  $\tilde{\theta}$  and is highly extended in  $\tilde{\theta}$ , pedestal ETG turbulence is narrow in  $\tilde{\theta}$  and has a different character at each  $\tilde{\theta}$  location.

Future investigation includes a scaling theory for the parallel extent of pedestal ETG turbulence, and an extension to electromagnetic physics. The long time state of nonlinear simulations also needs to be studied further, to determine the role of toroidal ETG turbulence. It would also be interesting to extend the work on toroidal ETG instability to stellarators, where the high aspect ratio,  $R_0/a \gg 1$ , can make  $R_0/L_{Te} \gg 1$ , even if  $a/L_{Te} \sim 1$ . We also need to better understand the conditions under which toroidal ETG heat transport is relatively weak in the pedestal, despite simple quasilinear estimates showing the mode can efficiently transport heat. Finally, given the importance of FLR damping in determining the spatial distribution of ETG turbulence, it would be interesting to extend this work to ITG and TEM turbulence. By understanding which parameters control pedestal turbulence, it may offer a route to optimizing turbulent heat transport.

# Appendix A

## Other Discharges

Discharge	82550	92167	92168	92174
Experimental Parameters				
$I_p$ [MA]	2.5	1.4	1.4	1.4
$B_{T0}$ [T]	2.7	1.9	1.9	1.9
$H_{98(y,2)}$	0.7	0.9	1.0	1.0
$n_G$	0.8	0.6	0.7	0.7
$R_D$ [electrons/s $\times 10^{22}$ ]	2.3	0.8	0.4	0.9
$q_{95}$	3.3	4.3	4.4	4.2
$Z_{\text{eff}}$	1.2	1.8	1.8	1.8
$P_{\text{NBI}}$ [MW]	14.4	17.4	17.6	17.4
$\beta_N$	1.1	2.2	2.6	2.5
Simulation Parameters				
$r/a$	0.9660	0.9784	0.9713	0.9743
$q$	3.65	5.14	5.07	5.08
$\hat{s}$	4.92	3.93	4.62	3.36
$a/L_{Te}$	57	41	29	42
$a/L_{Ti}$	12	19	16	11
$a/L_n$	23	8	10	10
$\kappa$	1.61	1.54	1.54	1.55
$\delta$	0.30	0.26	0.26	0.26
$a\beta'$	-0.09	-0.06	-0.07	-0.08
$dR_c/dr$	-0.17	-0.34	-0.36	-0.35
$a(d\kappa/dr)$	1.11	1.15	0.81	0.95
$a(d\delta/dr)$	0.97	0.85	0.67	0.74

Table A.1: Experimental and simulation parameters for the discharges in this work.

Here we present the results of gyrokinetic analysis for three other JET-ILW H-mode pedestal discharges. The basic experimental and simulation parameters for these JET-

ILW discharges in addition to the discharge discussed in the main text (shot 92174) are shown in Table A.1. Discharge 82550 is a very highly-fueled deuterium discharge with high triangularity and low ion temperature, 92167 is a highly-fueled deuterium discharge, 92168 is a weakly-fueled deuterium discharge, and 92174 is a highly-fueled deuterium discharge with deuterated ethylene ( $C_2D_4$ ) injection. In Table A.1, the quantity  $q_{95}$  is the safety factor measured at the location where the normalized poloidal flux is equal to 0.95. For more information on these data types, refer to the JET data handbook.

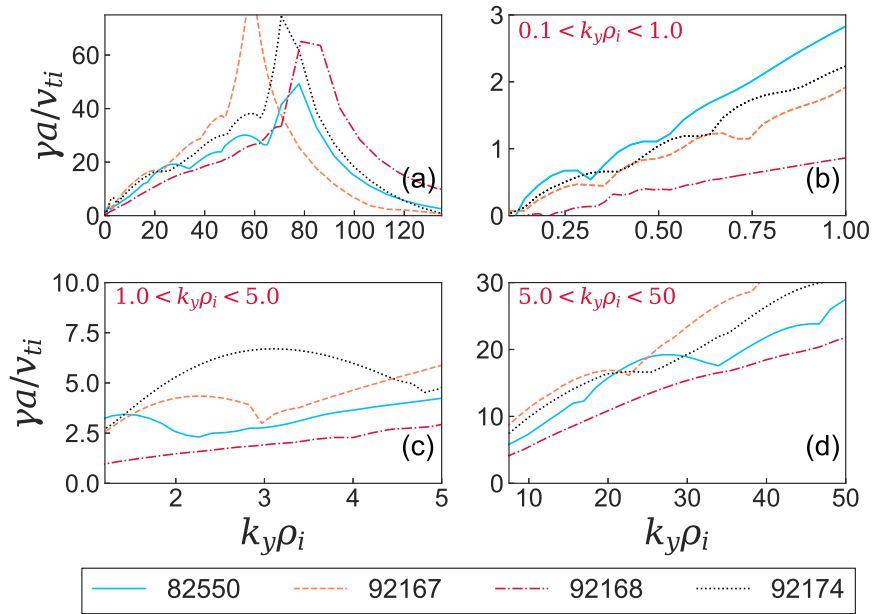


Figure A.1: GS2 gyrokinetic pedestal electrostatic growth rates for 4 JET equilibria with  $\theta_0 = 0$  for different ranges of  $k_y \rho_i$ . (a)  $1 \lesssim k_y \rho_i \lesssim 135$ . (b)  $0.1 \lesssim k_y \rho_i \lesssim 1.0$ . (c)  $1 \lesssim k_y \rho_i \lesssim 5$ . (d)  $5 \lesssim k_y \rho_i \lesssim 50$ .

Figure A.1 shows results from local gyrokinetic microinstability analysis at the radial location with the maximum pressure gradient (and therefore close to the maximum  $\gamma_E$ ) in the four JET-ILW H-mode pedestals described in Figure A.1. These are all electrostatic, linear GS2 simulations performed without  $\mathbf{E} \times \mathbf{B}$  shear and with  $\theta_0 = 0$ . While JET shot 92168 does not appear to have the characteristic toroidal ETG bump at  $k_y \rho_i \sim 1$ , an analysis of the eigenmodes demonstrates that toroidal ETG modes are indeed the fastest growing modes for  $1 \lesssim k_y \rho_i \lesssim 7$  with  $\theta_0 = 0$ .

In Figure A.2, we also plot quasilinear transport estimates for JET shots 82550,

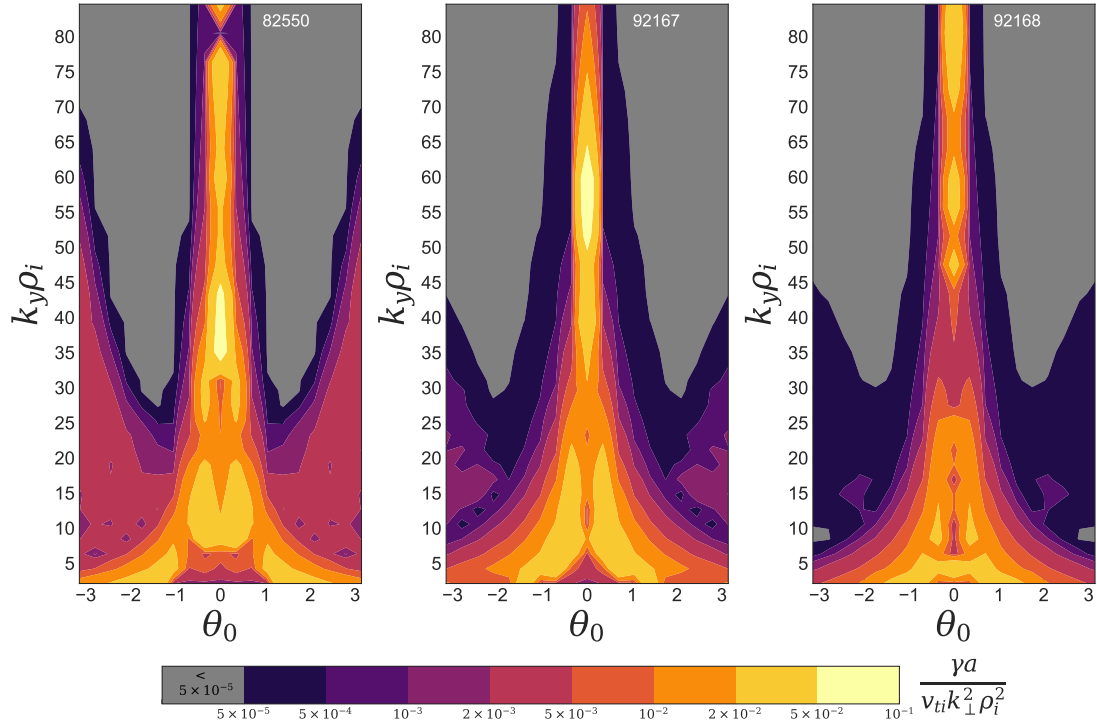


Figure A.2: Quasilinear estimates of  $\gamma a/v_{ti}k_{\perp}^2$  for JET shots 82550, 92167, and 92168.

92167, and 92168 using  $\gamma/k_{\perp}^2$ . These estimates demonstrate that  $\gamma/k_{\perp}^2$  depends non-trivially on  $\theta_0$ , similar to JET shot 92174, which is shown in Figure 5.14(b).

# Appendix B

## Electrostatic modes at $k_y \rho_i \lesssim 1.0$

For completeness, we briefly detail the electrostatic modes at  $k_y \rho_i \lesssim 1.0$ . We describe their eigenmode structure as well as growth rate sensitivity scans in temperature gradients and collisionality.

All of these simulations are performed with  $\theta_0 = 0.05$ . For  $0.1 \lesssim k_y \rho_i \lesssim 1.0$ , we observe modes that become increasingly extended in  $\theta$  with decreasing values of  $k_y \rho_i$ . For  $k_y \rho_i \approx 1$ , the fastest growing mode is still the toroidal ETG mode described throughout this work, shown in Figure B.1(a). Once  $k_y \rho_i$  decreases, the eigenmodes become more complicated and more extended in  $\theta$ , as shown by Figure B.1(b) and (c); we refer to these modes as ‘extended ETG.’ We also plot the quantity  $\omega_{*e} \eta_e / \omega_{\kappa e}$  when it is positive in Figure B.1(a), (b), and (c) — we observe that the extended ETG tends to have maxima of  $|\phi_1^{tb}|$  in bad curvature regions. This leads us to speculate that the extended ETG modes are a more complicated version of the toroidal ETG modes described throughout this work. The extended ETG modes in Figure B.1(b) and (c) have tearing parity for both  $\text{Re}(\phi_1^{tb})$  and  $\text{Im}(\phi_1^{tb})$ . We normalize the eigenmodes in Figure B.1(a), (b), (c), and (d) such that the maximum of  $|\phi_1^{tb}|$  is 1, and such that the value of  $\phi_1^{tb}$  is purely real at that location. In Figure B.1(f), we perform a growth rate sensitivity scan for these modes; the growth rate of these extended modes is very sensitive to  $R_0/L_{Te}$  and only slightly sensitive to  $R_0/L_{Ti}$  and collisions for smaller values of  $k_y \rho_i$ . The extended ETG modes are stable when run with adiabatic ions for  $k_y \rho_i \lesssim 0.2$ .

For  $k_y \rho_i \lesssim 0.1$ , we observe extremely extended eigenmodes, shown in Figure B.1(d) — the mode extends as far as  $\theta \approx 50$  before the typical  $|\phi_1^{tb}|$  value is less than 10% of the eigenmode maximum value. The modes are reminiscent of modes with extended

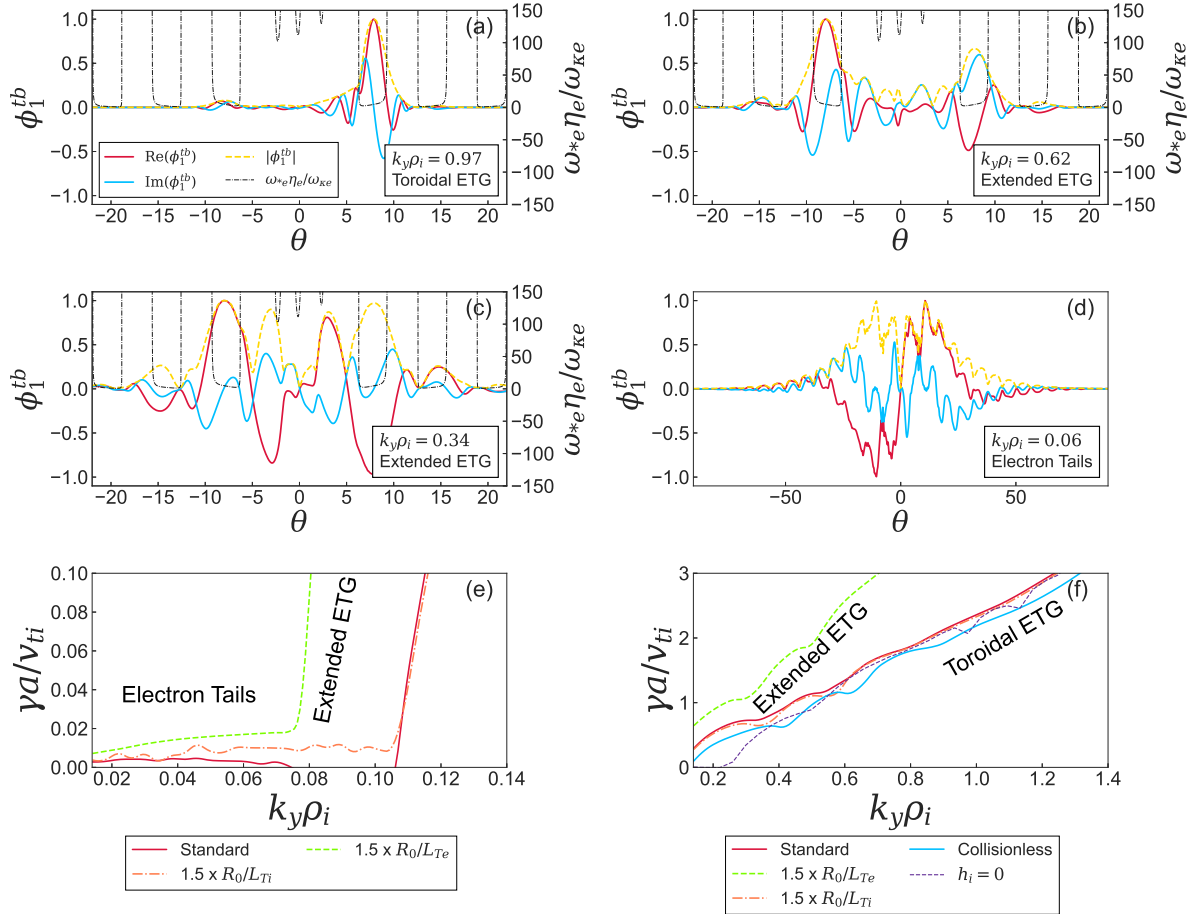


Figure B.1: Eigenmodes for  $k_y \rho_i \lesssim 1$  and  $\theta_0 = 0.05$  for JET shot 92174. In (a), (b), and (c), the quantity  $\omega_{*e} \eta_e / \omega_{ke}$  is plotted only when it is positive. In (a)-(d), the crimson lines are  $\text{Re}(\phi_1^{tb})$ , the blue lines are  $\text{Im}(\phi_1^{tb})$ , the gold dashed lines are  $|\phi_1^{tb}|$ , and the black dashed lines are  $\omega_{*e} \eta_e / \omega_{ke}$ . (a):  $k_y \rho_i = 0.97$ , toroidal ETG with large amplitude far down the field line. (b):  $k_y \rho_i = 0.62$ , extended ETG, (c):  $k_y \rho_i = 0.34$ , extended ETG, and (d):  $k_y \rho_i = 0.06$ : modes with electron tails. Growth rates for  $k_y \rho_i \lesssim 1.0$  modes with scans in temperature gradients, collisions, and kinetic/adiabatic ions: (e):  $k_y \rho_i < 0.14$  modes, and (f):  $0.14 < k_y \rho_i < 1.4$  modes.

electron tails [106]. There is no apparent relationship between the maxima of  $|\phi_1^{tb}|$  and bad curvature regions, unlike for the extended toroidal ETG modes. The mode shown in Figure B.1(d) has tearing parity for both  $\text{Re}(\phi_1^{tb})$  and  $\text{Im}(\phi_1^{tb})$ . Sensitivity scans in Figure B.1(e) show that these modes are very sensitive to  $R_0/L_{Te}$ , but insensitive to  $R_0/L_{Ti}$ . The modes with electron tails were stable for collisionless simulations.

# Appendix C

## Full Dispersion Relation

Using Equation (4.27) in the quasineutrality Equation (4.5), we find Equation (4.33) with

$$\begin{aligned}
D_s &\equiv \left( \frac{e\phi_1^{tb} n_{0e}}{Z_s T_{0e}} \right)^{-1} \int h_s d^3 v = \frac{2i Z_s^2 T_{0e} n_{0s}}{\pi^{1/2} v_{ts}^3 T_{0s} n_{0e}} \int_0^\infty d\lambda \int_0^\infty dv_\perp v_\perp \int_{-\infty}^\infty dv_\parallel \\
&\times \exp \left( i\lambda \left( \widehat{\omega} - \sigma \widehat{v}_\parallel^2 - \widehat{\omega}_{\nabla B_s} \frac{\widehat{v}_\perp^2}{2} - \widehat{k}_\parallel \widehat{v}_\parallel \right) - \widehat{v}_\parallel^2 - \widehat{v}_\perp^2 \right) \\
&\times \left[ -\widehat{\omega} + \widehat{\omega}_{*s} \left( 1 + \eta_s \left( \widehat{v}_\parallel^2 + \widehat{v}_\perp^2 - \frac{3}{2} \right) \right) \right] J_0^2 \left( \sqrt{2b_s} \widehat{v}_\perp \right),
\end{aligned} \tag{C.1}$$

where we have used [139]

$$\begin{aligned}
&i \int_0^\infty d\lambda \exp \left( i\lambda \left( \widehat{\omega} - \sigma \widehat{v}_\parallel^2 - \widehat{\omega}_{\nabla B_s} \widehat{v}_\perp^2 / 2 - \widehat{k}_\parallel \widehat{v}_\parallel \right) \right) \\
&= \frac{1}{-\widehat{\omega} + \widehat{k}_\parallel \widehat{v}_\parallel + \sigma \widehat{v}_\parallel^2 + \widehat{\omega}_{\nabla B_s} \widehat{v}_\perp^2 / 2}.
\end{aligned} \tag{C.2}$$

To find growing solutions and obtain a converged integral, we require that  $\text{Im}(\widehat{\omega}) > 0$ .

Evaluating the integral in  $\widehat{v}_\parallel$  gives

$$\begin{aligned}
D_s &= 2i \frac{Z_s^2 T_{0e} n_{0s}}{v_{ts}^2 T_{0s} n_{0e}} \int_0^\infty d\lambda \int_0^\infty dv_\perp v_\perp \frac{1}{(1 + i\sigma\lambda)^{1/2}} \exp \left( i\lambda \widehat{\omega} - \widehat{v}_\perp^2 (1 + i\widehat{\omega}_{\nabla B_s} \lambda / 2) \right) \\
&\times \exp \left( -\frac{(\lambda \widehat{k}_\parallel)^2}{4(1 + i\sigma\lambda)} \right) \\
&\times \left[ -\widehat{\omega} + \widehat{\omega}_{*s} \left( 1 + \eta_s \left( \frac{2(1 + i\sigma\lambda) - (\widehat{k}_\parallel \lambda)^2}{4(1 + i\sigma\lambda)^2} + \widehat{v}_\perp^2 - \frac{3}{2} \right) \right) \right] J_0^2 \left( \sqrt{2b_s} \widehat{v}_\perp \right).
\end{aligned} \tag{C.3}$$

The integral in  $\widehat{v}_\perp$  gives Equation (4.34), where we used the integrals

$$\int_0^\infty x J_0^2(ax) \exp(-bx^2) dx = \frac{1}{2b} I_0 \left( \frac{a^2}{2b} \right) \exp(-a^2/2b) = \frac{1}{2b} \Gamma_0 \left( \frac{a^2}{2b} \right), \tag{C.4}$$

and

$$\int_0^\infty x^3 J_0^2(ax) \exp(-bx^2) dx = \frac{-(a^2 - 2b)\Gamma_0\left(a^2/2b\right) + a^2\Gamma_1\left(a^2/2b\right)}{4b^3}, \quad (\text{C.5})$$

which is found by differentiating Equation (C.4) with respect to  $b$ .

We proceed to explain the numerical technique used to calculate the  $\lambda$  integral in Equation (4.34). The  $\lambda$  integral in Equation (4.34) along the real  $\lambda$  axis is highly oscillatory when  $\gamma \rightarrow 0$ , and standard numerical integration methods can make substantial errors in the low growth rate limit. Similarly, a straightforward change of variables such as  $\lambda \rightarrow i\bar{\lambda}$  will fail for nonzero  $k_{\parallel}$  and  $b_s$  due to exponential singularities caused by  $k_{\parallel}$  and  $b_s$  (at  $\lambda = \sigma i$  and  $2i/\widehat{\omega}_{\nabla B_s}$ , respectively). To avoid these problems, we introduce a numerically robust path of integration that avoids singularities and significantly reduces the number of oscillations.

In the limit  $\lambda \rightarrow \infty$ , the exponential in Equation (4.34) reduces to,

$$\exp \left[ i \left( \widehat{\omega} + \frac{\widehat{k}_{\parallel}^2}{4\sigma} \right) \lambda \right]. \quad (\text{C.6})$$

Thus, if we wish to minimize oscillations, we should choose our path such that the imaginary component of the exponential is constant. This is achieved with the integral path

$$\lambda = i \left( \widehat{\omega}^* + \frac{\widehat{k}_{\parallel}^2}{4\sigma} \right) \bar{\lambda} + a, \quad (\text{C.7})$$

where  $\bar{\lambda}$  is a new parameter and  $a$  is a constant that we need to choose to improve integral convergence. Therefore, we choose an integration path composed of two different paths,  $C_0$  and  $C_1$ . The first path,  $C_0$ , goes a short distance  $a$  along the real  $\lambda$  axis. The second path,  $C_1$ , is the one given in Equation (C.7). The total integration path is shown in Figure C.1. The integration path in Figure C.1 gives the same result as the original path because the integrand in Equation (4.34) decays as  $|\lambda| \rightarrow \infty$ . The constant  $a$  needs to be sufficiently large to avoid the singularities at  $\lambda = \sigma i$  and  $2i/\widehat{\omega}_{\nabla B_s}$ . A value  $a = 0.5$  is usually sufficiently large.

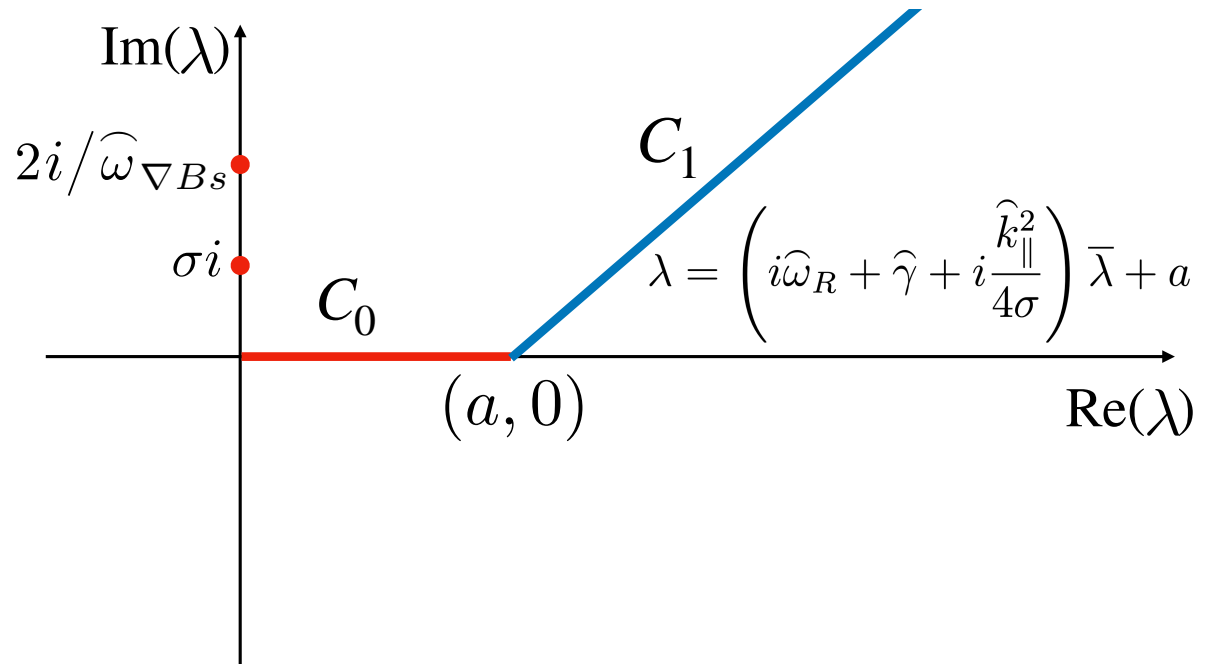


Figure C.1: Contour paths  $C_0$  and  $C_1$ , constructed to avoid the poles along the imaginary  $\lambda$  axis at  $\sigma i$  and  $2\sigma i$ , as well as minimizing oscillations.

# Appendix D

## Nonlinear Simulations Parameters

In Table D.1, we document the parameters for the nonlinear simulations discussed in this thesis.

GS2 Pedestal Simulations									
Simulation	ntheta	naky	nakx	$y0/\rho_i$	jt看ist	geometry	$D_{hy}$	$D_{hx}$	$v_{Ms}$
Base1	128	50	67	0.7	9	full	$1.8 \times 10^{-10}$	$2.0 \times 10^{-11}$	full
Slab1	128	50	67	0.7	9	full	$1.8 \times 10^{-10}$	$2.0 \times 10^{-11}$	zero
Hero1	128	50	199	0.7	9	full	$1.8 \times 10^{-10}$	$2.4 \times 10^{-13}$	full
Slab2	128	12	199	0.14	9	full	$1.8 \times 10^{-10}$	$3.9 \times 10^{-16}$	zero
Geo1	128	12	84	0.14	11	circle	$1.8 \times 10^{-10}$	0	zero
Geo2	128	12	84	0.14	11	circle*	$1.8 \times 10^{-10}$	0	zero
Geo3	128	12	84	0.14	11	circle*	$1.8 \times 10^{-10}$	0	zero
Geo4	128	12	84	0.14	11	full*	$1.8 \times 10^{-10}$	0	zero
Geo5	128	12	84	0.14	11	full*	$1.8 \times 10^{-10}$	0	zero

Table D.1: Nonlinear simulations discussed in this work. When the geometry is slightly modified from the circular flux surface or the full pedestal geometry, we use ‘circle\*’ or ‘full\*,’ respectively.

# References

- [1] J. Parisi and J. Ball. *The Future of Fusion Energy*. World Scientific, London, 2019.
- [2] H. Poincaré. Mémoire sur les courbes définies par une équation différentielle. *Journal de Mathématiques Pures et Appliquées*, 7:375, 1881.
- [3] T. C. Hender, J. C. Wesley, J. Bialek, and others. Chapter 3: MHD stability, operational limits and disruptions. *Nuclear Fusion*, 47(6):S128, 2007.
- [4] F. Troyon, R. Gruber, H. Saurenmann, S. Semenzato, and S. Succi. MHD-limits to plasma confinement. *Plasma Physics and Controlled Fusion*, 26(1A):209, 1984.
- [5] M. Murakami, J. D. Callen, and L. A. Berry. Some observations on maximum densities in tokamak experiments. *Nuclear Fusion*, 16(2):347, 1976.
- [6] M. Greenwald, J. L. Terry, S. M. Wolfe, and others. A new look at density limits in tokamaks. *Nuclear Fusion*, 28(12):2199, 1988.
- [7] S. Von Goeler, W. Stodiek, and N. Sauthoff. Studies of internal disruptions and  $m=1$  oscillations in tokamak discharges with soft-X-ray techniques. *Physical Review Letters*, 33(20):1201, 1974.
- [8] H. Zohm. Edge localized modes (ELMs). *Plasma Physics and Controlled Fusion*, 38(2):105, 1996.
- [9] P. B. Snyder, H. R. Wilson, J. R. Ferron, and others. Edge localized modes and the pedestal: A model based on coupled peeling–ballooning modes. *Physics of Plasmas*, 9(5):2037, 2002.

- [10] T. H. Stix. Current penetration and plasma disruption. *Physical Review Letters*, 36(10):521, 1976.
- [11] M. Lehnen, G. Arnoux, S. Brezinsek, and others. Impact and mitigation of disruptions with the ITER-like wall in JET. *Nuclear Fusion*, 53(9):093007, 2013.
- [12] S. I. Braginskii. Transport processes in a plasma. *Reviews of Plasma Physics*, 1:205, 1965.
- [13] P. Helander and D. J. Sigmar. *Collisional transport in magnetized plasmas*. Cambridge University Press, 2002.
- [14] P. C. Liewer. Measurements of microturbulence in tokamaks and comparisons with theories of turbulence and anomalous transport. *Nuclear Fusion*, 25(5):543, 1985.
- [15] J. Lee, F. I. Parra, and M. Barnes. Turbulent momentum pinch of diamagnetic flows in a tokamak. *Nuclear Fusion*, 54(2):022002, 2014.
- [16] F. I. Parra and M. Barnes. Intrinsic rotation in tokamaks: theory. *Plasma Physics and Controlled Fusion*, 57(4):045002, 2015.
- [17] A. H. Boozer. Physics of magnetically confined plasmas. *Reviews of Modern Physics*, 76(4):1071, 2005.
- [18] A. M. Dimits, G. Bateman, M. A. Beer, and others. Comparisons and physics basis of tokamak transport models and turbulence simulations. *Physics of Plasmas*, 7(3):969, 2000.
- [19] W. Horton and R. D. Estes. Fluid simulation of ion pressure gradient driven drift modes. *Plasma Physics*, 22(7):663, 1980.
- [20] R. J. Fonck, R. Howell, K. Jaehnig, and others. Ion thermal confinement in the enhanced-confinement regime of the TFTR tokamak. *Physical Review Letters*, 63(5):520, 1989.
- [21] A. J. Wootton, B. A. Carreras, H. Matsumoto, and others. Fluctuations and anomalous transport in tokamaks. *Physics of Fluids B*, 2(12):2879, 1990.

- [22] B. A. Carreras. Progress in anomalous transport research in toroidal magnetic confinement devices. *IEEE Transactions on Plasma Science*, 25(6):1281, 1997.
- [23] W. Dorland, F. Jenko, M. Kotschenreuther, and B. N. Rogers. Electron temperature gradient turbulence. *Physical Review Letters*, 85(26):5579, 2000.
- [24] R. E. Waltz. Three-dimensional global numerical simulation of ion temperature gradient mode turbulence. *Physics of Fluids*, 31(7):1962, 2002.
- [25] J. Wesson. *Tokamaks*. Oxford University Press, Oxford, 4th edition, 2012.
- [26] M. N. Rosenbluth and C. L. Longmire. Stability of plasmas confined by magnetic fields. *Annals of Physics*, 1(2):120, 1957.
- [27] L. I. Rudakov and R. Z. Sagdeev. On the instability of a nonuniform rarefied plasma in a strong magnetic field. *Soviet Physics Doklady*, 6:415, 1961.
- [28] B. Coppi, M. N. Rosenbluth, and R. Z. Sagdeev. Instabilities due to temperature gradients in complex magnetic field configurations. *The Physics of Fluids*, 10(3):582, 1967.
- [29] A. Jarmén, P. Andersson, and J. Weiland. Fully toroidal ion temperature gradient driven drift modes. *Nuclear Fusion*, 27(6):941, 1987.
- [30] S. C. Cowley, R. M. Kulsrud, and R. Sudan. Considerations of ion temperature gradient driven turbulence. *Physics of Fluids B: Plasma Physics*, 3(10):2767, 1991.
- [31] Y. C. Lee, J. Q. Dong, P. N. Guzdar, and C. S. Liu. Collisionless electron temperature gradient instability. *Physics of Fluids*, 30(5), 1987.
- [32] W. Horton, B. G. Hong, and W. M. Tang. Toroidal electron temperature gradient driven drift modes. *Physics of Fluids*, 31(10):2971, 1988.
- [33] F. Jenko, W. Dorland, M. Kotschenreuther, and B. N. Rogers. Electron temperature gradient driven turbulence. *Physics of Plasmas*, 7(5):1904, 2000.

- [34] H. Nordman, J. Weiland, and A. Jarmén. Simulation of toroidal drift mode turbulence driven by temperature gradients and electron trapping. *Nuclear Fusion*, 30(6):983, 1990.
- [35] F. Romanelli and S. Briguglio. Toroidal semicollisional microinstabilities and anomalous electron and ion transport. *Physics of Fluids B*, 2(4):754, 1990.
- [36] T. Dannert and F. Jenko. Gyrokinetic simulation of collisionless trapped-electron mode turbulence. *Physics of Plasmas*, 12(7):072309, 2005.
- [37] J. F. Drake, N. T. Gladd, C. S. Liu, and C. L. Chang. Microtearing modes and anomalous transport in tokamaks. *Physical Review Letters*, 44(15):994, 1980.
- [38] J. W. Connor, S. C. Cowley, and R. J. Hastie. Micro-tearing stability in tokamaks. *Plasma Physics and Controlled Fusion*, 32(10):799, 1990.
- [39] W. Guttenfelder, J. Candy, S. M. Kaye, and others. Electromagnetic transport from microtearing mode turbulence. *Physical Review Letters*, 106(15):155004, 2011.
- [40] J. W. Connor, R. J. Hastie, and J. B. Taylor. Shear, Periodicity, and Plasma Ballooning Modes. *Physical Review Letters*, 40(6):396, 1978.
- [41] W. M. Tang, J. W. Connor, and R. J. Hastie. Kinetic-ballooning-mode theory in general geometry. *Nuclear Fusion*, 20(11):1439, 1980.
- [42] N. A. Krall and M. N. Rosenbluth. Universal instability in complex field geometries. *Physics of Fluids*, 8(8):1488, 1965.
- [43] M. Landreman, T. M. Antonsen, and W. Dorland. Universal instability for wavelengths below the ion Larmor scale. *Physical Review Letters*, 114(9):095003, 2015.
- [44] M. Kotschenreuther, W. Dorland, M. A. Beer, and G. W. Hammett. Quantitative predictions of tokamak energy confinement from first-principles simulations with kinetic effects. *Physics of Plasmas*, 2(6):2381, 1995.
- [45] X. Garbet, P. Mantica, C. Angioni, and others. Physics of transport in tokamaks. *Plasma Physics and Controlled Fusion*, 46(12B):B557, 2004.

- [46] K. H. Burrell, T. N. Carlstrom, E. J. Doyle, and others. Physics of the L-mode to H-mode transition in tokamaks. *Plasma Physics and Controlled Fusion*, 34(13):1859, 1992.
- [47] F. Wagner, G. Becker, K. Behringer, and others. Regime of Improved Confinement and High Beta in Neutral-Beam-Heated Divertor Discharges of the ASDEX Tokamak. *Physical Review Letters*, 49(19):1408, 1982.
- [48] F. Ryter. H mode power threshold database for ITER. *Nuclear Fusion*, 36(9):1217, 1996.
- [49] J. F. Parisi, F. I. Parra, C. M. Roach, and others. Toroidal and slab ETG instability dominance in the linear spectrum of JET-ILW pedestals. *Nuclear Fusion*, 60(126045), 2020.
- [50] J. E. Kinsey, G. Bateman, T. Onjun, and others. Burning plasma projections using drift-wave transport models and scalings for the H-mode pedestal. *Nuclear Fusion*, 43(12):1845, 2003.
- [51] K. H. Burrell, S. L. Allen, G. Bramson, and others. Confinement physics of H-mode discharges in DIII-D. *Plasma Physics and Controlled Fusion*, 31(10):1649, 1989.
- [52] C. E. Bush, R. J. Goldston, S. D. Scott, and others. Peaked density profiles in circular-limiter H modes on the TFTR tokamak. *Physical Review Letters*, 65(4):424, 1990.
- [53] M. Greenwald, R. L. Boivin, F. Bombarda, and others. H mode confinement in Alcator C-Mod. *Nuclear Fusion*, 37(6):793, 1997.
- [54] M. Keilhacker, A. Gibson, C. Gormezano, and others. High fusion performance from deuterium-tritium plasmas in JET. *Nuclear Fusion*, 39(2):209, 1999.
- [55] M. Keilhacker, G. Becker, K. Bernhardt, and others. Confinement studies in L and H-type Asdex discharges. *Plasma Physics and Controlled Fusion*, 26(1A):49, 1984.

- [56] J. W. Connor, R. J. Hastie, H. R. Wilson, and R. L. Miller. Magnetohydrodynamic stability of tokamak edge plasmas. *Physics of Plasmas*, 5(7):2687, 1998.
- [57] G. T. A. Huysmans. ELMs: MHD instabilities at the transport barrier. *Plasma Physics and Controlled Fusion*, 47(12B):B165, 2005.
- [58] P. B. Snyder, N. Aiba, M. Beurskens, and others. Pedestal stability comparison and ITER pedestal prediction. *Nuclear Fusion*, 49(8):085035, 2009.
- [59] P. B. Snyder, R. J. Groebner, J. W. Hughes, and others. A first-principles predictive model of the pedestal height and width: development, testing and ITER optimization with the EPED model. *Nuclear Fusion*, 51(10):103016, 2011.
- [60] D. Lortz. The General “Peeling” Instability. *Nuclear Fusion*, 15(1):49, 1975.
- [61] J. A. Wesson. Hydromagnetic stability of tokamaks. *Nuclear Fusion*, 18(1):87, 1978.
- [62] P. A. Schneider, E. Wolfrum, R. J. Groebner, and others. Differences in the H-mode pedestal width of temperature and density. *Plasma Physics and Controlled Fusion*, 54(10):105009, 2012.
- [63] D. N. Hill. A review of elms in divertor tokamaks. *Journal of Nuclear Materials*, 241-243:182, 1997.
- [64] B. N. Rogers, J. F. Drake, and A. Zeiler. Phase Space of Tokamak Edge Turbulence, the L-H Transition, and the Formation of the Edge Pedestal. *Physical Review Letters*, 81(20):4396, 1998.
- [65] D. R. Hatch, M. Kotschenreuther, S. Mahajan, P. Valanju, and X. Liu. A gyrokinetic perspective on the JET-ILW pedestal. *Nuclear Fusion*, 57(3):036020, 2017.
- [66] J. Neuhauser, D. Coster, H. U. Fahrbach, and others. Transport into and across the scrape-off layer in the ASDEX Upgrade divertor tokamak. *Plasma Physics and Controlled Fusion*, 44(6):855, 2002.

- [67] I. Pusztai, S. Buller, and M. Landreman. Global effects on neoclassical transport in the pedestal with impurities. *Plasma Physics and Controlled Fusion*, 58(8):085001, 2016.
- [68] M. A. Beer, S. C. Cowley, and G. W. Hammett. Field aligned coordinates for nonlinear simulations of tokamak turbulence. *Physics of Plasmas*, 2(7):2687, 1995.
- [69] T. S. Hahm and K. H. Burrell. Flow shear induced fluctuation suppression in finite aspect ratio shaped tokamak plasma. *Physics of Plasmas*, 2(5):1648, 1995.
- [70] H. Biglari, P. H. Diamond, and P. W. Terry. Influence of sheared poloidal rotation on edge turbulence. *Physics of Fluids B: Plasma Physics*, 2(1):1, 1990.
- [71] D. Dickinson, C. M. Roach, S. Saarelma, and others. Kinetic Instabilities that Limit  $\beta$  in the Edge of a Tokamak Plasma: A Picture of an H -Mode Pedestal. *Physical Review Letters*, 108(13):135002, 2012.
- [72] J. C. Hillesheim, D. Dickinson, C. M. Roach, and others. Intermediate-k density and magnetic field fluctuations during inter-elm pedestal evolution in mast. *Plasma Physics and Controlled Fusion*, 58(1):014020, 2016.
- [73] Z. Lin, T. S. Hahm, W. W. Lee, W. M. Tang, and R. B. White. Turbulent transport reduction by zonal flows: Massively parallel simulations. *Science*, 281(5384):1835, 1998.
- [74] D. P. Fulton, Z. Lin, I. Holod, and Y. Xiao. Microturbulence in DIII-D tokamak pedestal. I. Electrostatic instabilities. *Physics of Plasmas*, 21(4):042110, 2014.
- [75] T. Görler, X. Lapillonne, S. Brunner, and others. The global version of the gyrokinetic turbulence code GENE. *Journal of Computational Physics*, 230(18):7053, 2011.
- [76] D. R. Hatch, M. Kotschenreuther, S. Mahajan, and others. Microtearing turbulence limiting the JET-ILW pedestal. *Nuclear Fusion*, 56(10):104003, 2016.

- [77] D. R. Hatch, M. Kotschenreuther, S. M. Mahajan, and others. Direct Gyrokinetic Comparison of Pedestal Transport in JET with Carbon and ITER-Like Walls. *Nuclear Fusion*, 59(8):086056, 2019.
- [78] D. Told, F. Jenko, P. Xanthopoulos, and others. Gyrokinetic microinstabilities in ASDEX Upgrade edge plasmas. *Physics of Plasmas*, 15(10):102306, 2008.
- [79] F. Jenko, D. Told, P. Xanthopoulos, F. Merz, and L. D. Horton. Gyrokinetic turbulence under near-separatrix or nonaxisymmetric conditions. *Physics of Plasmas*, 16(5):055901, 2009.
- [80] D. Told. *Gyrokinetic microturbulence in transport barriers*. PhD thesis, University of Ulm, 2012.
- [81] J. A. Baumgaertel, E. A. Belli, W. Dorland, and others. Simulating gyrokinetic microinstabilities in stellarator geometry with GS2. *Physics of Plasmas*, 18(12):122301, 2011.
- [82] M. Kotschenreuther, X. Liu, D. R. Hatch, and others. Gyrokinetic analysis and simulation of pedestals to identify the culprits for energy losses using ‘fingerprints’. *Nuclear Fusion*, 59(9):096001, 2019.
- [83] C. Giroud, N Aiba, A Chankin, and others. Optimisation of JET-DT and ITER operation by developing an understanding of the role of low-Z impurity on the H-mode pedestal. In *27th IAEA Fusion Energy Conference*, page 1, 2018.
- [84] J. B. Taylor and R. J. Hastie. Stability of general plasma equilibria - I formal theory. *Plasma Physics*, 10(5):479, 1968.
- [85] P. J. Catto. Linearized gyro-kinetics. *Plasma Physics*, 20(7):719, 1978.
- [86] T. M. Antonsen and B. Lane. Kinetic equations for low frequency instabilities in inhomogeneous plasmas. *Physics of Fluids*, 23(6):1205, 1980.
- [87] E. A. Frieman and L. Chen. Nonlinear gyrokinetic equations for low-frequency electromagnetic waves in general plasma equilibria. *The Physics of Fluids*, 25(3):502, 1982.

- [88] F. I. Parra and P. J. Catto. Limitations of gyrokinetics on transport time scales. *Plasma Physics and Controlled Fusion*, 50(6):065014, 2008.
- [89] I. G. Abel, G. G. Plunk, E. Wang, and others. Multiscale gyrokinetics for rotating tokamak plasmas: fluctuations, transport and energy flows. *Reports on Progress in Physics*, 76(11):116201, 2013.
- [90] F. L. Hinton and R. D. Hazeltine. Theory of plasma transport in toroidal confinement systems. *Reviews of Modern Physics*, 48(2):239, 1976.
- [91] E. J. Doyle, W. A. Houlberg, Y. Kamada, and others. Chapter 2: Plasma confinement and transport. *Nuclear Fusion*, 47(6):S18, 2007.
- [92] M. J. Leyland, M. N. A. Beurskens, L. Frassinetti, and others. The H-mode pedestal structure and its role on confinement in JET with a carbon and metal wall. *Nuclear Fusion*, 55(1):013019, 2015.
- [93] M. Kotschenreuther, D. R. Hatch, S. Mahajan, and others. Pedestal transport in H-mode plasmas for fusion gain. *Nuclear Fusion*, 57(6):064001, 2017.
- [94] E. Wolfrum, M. Beurskens, M.G. Dunne, and others. Impact of wall materials and seeding gases on the pedestal and on core plasma performance. *Nuclear Materials and Energy*, 12:18, 2017.
- [95] M. G. Dunne, S. Potzel, F. Reimold, and others. The role of the density profile in the ASDEX-Upgraded pedestal structure. *Plasma Physics and Controlled Fusion*, 59(1):014017, 2017.
- [96] C. F. Maggi, L. Frassinetti, L. Horvath, and others. Studies of the pedestal structure and inter-ELM pedestal evolution in JET with the ITER-like wall. *Nuclear Fusion*, 57(11):116012, 2017.
- [97] R. Pasqualotto, P. Nielsen, C. Gowers, and others. High resolution Thomson scattering for Joint European Torus (JET). *Review of Scientific Instruments*, 75(10):3891, 2004.

- [98] L. Frassinetti, M. N. A. Beurskens, R. Scannell, and others. Spatial resolution of the JET Thomson scattering system. *Review of Scientific Instruments*, 83(1):013506, 2012.
- [99] E. Delabie, N. Hawkes, T. M. Biewer, and M. G. O’Mullane. In situ wavelength calibration of the edge CXS spectrometers on JET. *Review of Scientific Instruments*, 87(11):11E525, 2016.
- [100] S. R. Haskey, B. A. Grierson, C. Chrystal, and others. Main ion and impurity edge profile evolution across the L- to H-mode transition on DIII-D. *Plasma Physics and Controlled Fusion*, 60(10):105001, 2018.
- [101] S. R. Haskey, B. A. Grierson, L. Stagner, and others. Active spectroscopy measurements of the deuterium temperature, rotation, and density from the core to scrape off layer on the DIII-D tokamak (invited). *Review of Scientific Instruments*, 89(10):10D110, 2018.
- [102] Y. Camenen, A. Bortolon, B. P. Duval, and others. Experimental demonstration of an up-down asymmetry effect on intrinsic rotation in the TCV tokamak. *Plasma Physics and Controlled Fusion*, 52(12):124037, 2010.
- [103] M. Barnes, W. Dorland, and T. Tatsuno. Resolving velocity space dynamics in continuum gyrokinetics. *Physics of Plasmas*, 17(3):032106, 2010.
- [104] R. L. Miller, M. S. Chu, J. M. Greene, Y. R. Lin-Liu, and R. E. Waltz. Noncircular, finite aspect ratio, local equilibrium model. *Physics of Plasmas*, 5(4):973, 1998.
- [105] A. G. Peeters and C. Angioni. Linear gyrokinetic calculations of toroidal momentum transport in a tokamak due to the ion temperature gradient mode. *Physics of Plasmas*, 12(7):072515, 2005.
- [106] K. Hallatschek and W. Dorland. Giant electron tails and passing electron pinch effects in tokamak-core turbulence. *Physical Review Letters*, 95(5):055002, 2005.
- [107] B. Coppi and F. Pegoraro. Theory of the ubiquitous mode. *Nuclear Fusion*, 17(5):969, 1977.

- [108] W. Horton, D. I. Choi, and W. M. Tang. Toroidal drift modes driven by ion pressure gradients. *The Physics of Fluids*, 24(6):1077, 1981.
- [109] J. W. Cooley and J. W. Tukey. An Algorithm for the Machine Calculation of Complex Fourier Series. *Mathematics of Computation*, 19(90):297, 1965.
- [110] P. Migliano, Y. Camenen, F. J. Casson, W. A. Hornsby, and A. G. Peeters. Ion temperature gradient instability at sub-Larmor radius scales with non-zero ballooning angle. *Physics of Plasmas*, 20(2):022101, 2013.
- [111] R. L. Miller, F. L. Waelbroeck, A. B. Hassam, and R. E. Waltz. Stabilization of ballooning modes with sheared toroidal rotation. *Physics of Plasmas*, 2(10):3676, 1995.
- [112] F. Jenko, W. Dorland, and G. W. Hammet. Critical gradient formula for toroidal electron temperature gradient modes. *Physics of Plasmas*, 8(9):4096, 2001.
- [113] C. Bourdelle, W. Dorland, X. Garbet, and others. Stabilizing impact of high gradient of  $\beta$  on microturbulence. *Physics of Plasmas*, 10(7):2881, 2003.
- [114] E. Wang, X. Xu, J. Candy, and others. Linear gyrokinetic analysis of a DIII-D H-mode pedestal near the ideal ballooning threshold. *Nuclear Fusion*, 52(10):103015, 2012.
- [115] S. Saarelma, M.N.A. Beurskens, D. Dickinson, and others. MHD and gyro-kinetic stability of JET pedestals. *Nuclear Fusion*, 53(12):123012, 2013.
- [116] H. Chen and L. Chen. On drift wave instabilities excited by strong plasma gradients in toroidal plasmas. *Physics of Plasmas*, 25(1):014502, 2018.
- [117] D. Dickinson, Jackson A., and C. M. Roach. An overview of recent gs2 optimisations and plans for further work.
- [118] E. Viezzer, E. Fable, M. Cavedon, and others. Investigation of inter-ELM ion heat transport in the H-mode pedestal of ASDEX Upgrade plasmas. *Nuclear Fusion*, 57(2):022020, 2017.

- [119] J. Guadagni and A. J. Cerfon. Fast and spectrally accurate evaluation of gyroaverages in non-periodic gyrokinetic-poisson simulations. *Journal of Plasma Physics*, 83(4):1, 2017.
- [120] N. Christen, M. Barnes, and F. I. Parra. Continuous-in-time approach to flow shear in a local  $\delta f$  gyrokinetic code. *In Preparation*.
- [121] G. W. Hammett, W. Dorland, N. F. Loureiro, and T. Tatsuno. Implementation of Large Scale  $E \times B$  Shear Flow in the GS2 Gyrokinetic Turbulence Code. *48th Annual Meeting of the Division of Plasma Physics*, 2006.
- [122] J. Lee, M. Barnes, F. I. Parra, E. A. Belli, and J. Candy. The effect of diamagnetic flows on turbulent driven ion toroidal rotation. *Physics of Plasmas*, 21(5):056106, 2014.
- [123] P. J. Catto, M. N. Rosenbluth, and C. S. Liu. Parallel velocity shear instabilities in an inhomogeneous plasma with a sheared magnetic field. *The Physics of Fluids*, 16(10):1719, 1973.
- [124] S. L. Newton, S. C. Cowley, and N. F. Loureiro. Understanding the effect of sheared flow on microinstabilities. *Plasma Physics and Controlled Fusion*, 52(12):125001, 2010.
- [125] M. Barnes, F. I. Parra, E. G. Highcock, and others. Turbulent transport in tokamak plasmas with rotational shear. *Physical Review Letters*, 106(17):175004, 2011.
- [126] A. A. Schekochihin, E. G. Highcock, and S. C. Cowley. Subcritical fluctuations and suppression of turbulence in differentially rotating gyrokinetic plasmas. *Plasma Physics and Controlled Fusion*, 54(5):055011, 2012.
- [127] J. Lee, M. Barnes, F. I. Parra, E. Belli, and J. Candy. Turbulent momentum transport due to neoclassical flows. *Plasma Physics and Controlled Fusion*, 57(12):125006, 2015.

- [128] J. Ball, S. Brunner, and B. F. McMillan. The effect of background flow shear on gyrokinetic turbulence in the cold ion limit. *Plasma Physics and Controlled Fusion*, 61(6):064004, 2019.
- [129] C. M. Roach, I. G. Abel, R. J. Akers, and others. Gyrokinetic simulations of spherical tokamaks. *Plasma Physics and Controlled Fusion*, 51(12):124020, 2009.
- [130] C. Bowman, D. Dickinson, L. Horvath, and others. Pedestal evolution physics in low triangularity JET tokamak discharges with ITER-like wall. *Nuclear Fusion*, 58(1):016021, 2018.
- [131] M. Reshko and C. M. Roach. Effects of impurities on electron temperature gradient modes. *Plasma Physics and Controlled Fusion*, 50(11):115002, 2008.
- [132] S. Maeyama, Y. Idomura, T. H. Watanabe, and others. Cross-scale interactions between electron and ion scale turbulence in a tokamak plasma. *Physical Review Letters*, 114(25):255002, 2015.
- [133] N. T. Howard, C. Holland, A. E. White, M. Greenwald, and J. Candy. Multi-scale gyrokinetic simulation of tokamak plasmas: Enhanced heat loss due to cross-scale coupling of plasma turbulence. *Nuclear Fusion*, 56(1):014004, 2016.
- [134] S. Maeyama, T. H. Watanabe, and A. Ishizawa. Suppression of Ion-Scale Microtearing Modes by Electron-Scale Turbulence via Cross-Scale Nonlinear Interactions in Tokamak Plasmas. *Physical Review Letters*, 119(19):195002, 2017.
- [135] M. R. Hardman, M. Barnes, C. M. Roach, and F. I. Parra. A scale-separated approach for studying coupled ion and electron scale turbulence. *Plasma Physics and Controlled Fusion*, 61(6):065025, 2019.
- [136] M. R. Hardman, M. Barnes, and C. M. Roach. Stabilisation of short-wavelength instabilities by parallel-to-the-field shear in long-wavelength  $\mathbf{E} \times \mathbf{B}$  flows. 2019. URL <http://arxiv.org/abs/1911.04999>.
- [137] R. J. Goldston and P. H. Rutherford. *Introduction to Plasma Physics*. CRC Press, 1st edition, 1995.

- [138] M. Barnes, F. I. Parra, and A. A. Schekochihin. Critically balanced ion temperature gradient turbulence in fusion plasmas. *Physical Review Letters*, 107(11):115003, 2011.
- [139] H. Biglari, P. H. Diamond, and M. N. Rosenbluth. Toroidal ion-pressure-gradient-driven drift instabilities and transport revisited. *Physics of Fluids B: Plasma Physics*, 1(1):109, 1989.